Magnetic molecules at hybrid interfaces

T, hν

Lorenzo Poggini

Magnetic molecules at hybrid interfaces

Dottorando   Tutori

Dott. Lorenzo Poggini   Dott. Matteo Mannini

                                                      Prof. Roberta Sesoli

                        Coordinatore
                        Prof. Andrea Goti

Alla mia famiglia

Index

1. Introduction

Molecular magnetism is a multidisciplinary research field where chemists and physicists have to work side by side on the design and characterisation of smart building blocks for innovative devices. The wide playground of chemistry research provided a series of different molecular magnetic building blocks that have been classified depending on the different and peculiar properties. These archetypal systems ranges from the simplest organic radicals (ORs) featuring ferromagnetic behaviour in a non-metal based system, to the more complex, Single Molecule Magnets (SMMs) exhibiting a variety of properties including memory effect and resonant quantum tunnelling, but also more exotic systems such as, Valence Tautomers (VT) and Spin Crossover (SCO), which can be switched between a diamagnetic and a paramagnetic state by external stimuli. All of them are very fascinating materials due to their magnetic properties and scientists from various fields have joined the research on molecular magnetism in order to explore the unprecedented properties of these new compounds. In this thesis work we explored the organization in nanostructures of several classes of molecular systems with the perspective of promoting the development of the new technology of molecular spintronic where these magnetic molecules can be used as active building blocks modulating the charge and spin transport. Here below we briefly introduce the reader to each family of magnetic molecules investigated during this research activity.

1.1 Molecular Magnetism from bulk to surfaces

Organic Radicals (ORs)

The interest in stable ORs origins from the presence of an unpaired electron localised in its function that one can use as efficient magnetic linker in molecular structures but potentially also in molecular devices exploiting the hyperfine interactions and the weak spin–orbit coupling. Organic radicals in fact are considered to be suitable media for spin transport;[1] thanks to their stability, they could be assembled on surfaces and used for the development of molecular devices,[2,3] sensors[4,5] and for non-volatile memory devices.[6] A particular class of organic radicals

1. Introduction

is constituted by the Nitronyl Nitroxide Radicals (NNRs) of general formula R-(4,4,5,5-tetramethylimidazoline- 1-oxyl-3-oxide) where R is the substituent which changes from one radical to another.[7] NNRs are purely organic paramagnetic molecules in which the unpaired electron is delocalized within an aromatic system including two N-O units.[7,8] NNRs are characterized by a $S = 1/2$ and they can be considered as the most simple magnetic molecules one can use to develop a hybrid system including a molecular magnetic layer and a magnetic surfaces. The unpaired electron in this system has stable in ambient conditions to be observed by conventional spectroscopic methods and in fact NNR can be isolated as pure compounds. Introduced by Ullman *et al.*[7,9] they have been widely studied starting from the nineties as relevant molecular building blocks being considered as valid candidates in the development of organic magnets,[10] but also for the design of Single Chain Magnets (SCMs)[11] as well as for the development of nanostructured magnetic surfaces.[12,13] Nanostructured NNRs molecules have been widely studied as monolayer[14] assembled by wet chemistry techniques as well as sub-monolayer obtained by thermal sublimation[15] (Figure 1). A characterisation by Scanning Tunnelling Microscopy (STM) has confirmed the high stability of NNR system and the retention of the unpaired electron. NNR monolayers have been studied also by special STM-based tools based on the spin noise detection approach.[16,17]
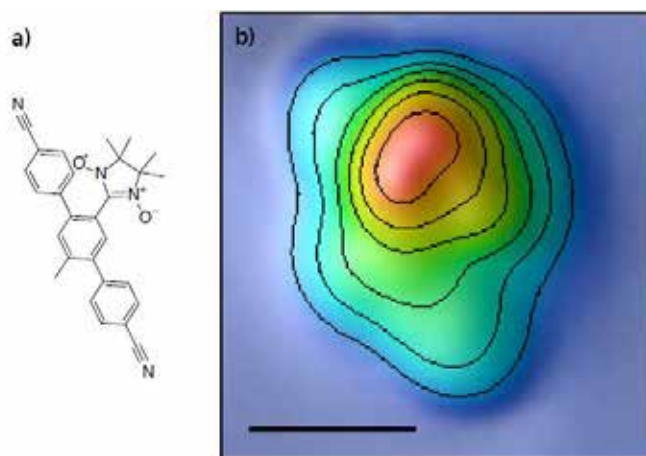
Figure 1. Chemical structure of the studied organic radical molecule ($C_{28}H_{25}O_2N_4$) High-resolution topography, contour lines are at height intervals of 50 pm. The scale bar corresponds to 1 nm. [15]

2

We mention here also that stable neutral organic biradicals recently attracted the interest of the community offering the possibility to study the tuning of the magnetic interactions through the appropriate design of a spacer and the biradical family.[18]

Several recent studies have been focused on the possibility to deposit NNR or other radicals under HV or UHV conditions.[19–25] Caro[19] *et al.* demonstrated for the first time the possibility to thermally evaporate NNRs in UV condition on NaCl (001). X-Ray Diffraction (XRD) and X-ray Photoelectron Spectroscopy (XPS) revealed a highly ordered thin film with 2D spherulitic growth, which was unprecedented for molecular organic compounds. Recently, organic molecular beam epitaxy (OMBE) technique has been adopted to deposit a pyrene derivative of NNR in UHV conditions on several surfaces ranging from Au (111),[20] $TiO_2(110)$, [21] and $Al_2O_3(11-20)$[22] identifying this system as a promising candidate for understanding thin film processes in purely organic-based magnets. Langmuir-Blodget technique has been also used to assemble functionalised radical molecules, including NNR, on various surface.[26,27] We have demonstrated that it is possible to obtain a 2D regular structure of radicals using the Self Assembly Monolayer (SAM).[14,28] Moreover, recent works have suggested that NNR function can be used to increase the spin polarisation of the current in molecular spintronics devices. [2,29]

In this thesis work we have focused our research on the realization of the first spin valve based on the use of NNR as a paramagnetic interface coupling the spin injection electrode $La_{0.7}Sr_{0.3}MnO_3$ (LSMO) and the organic semiconductor (OSC) layer with the aim to modify the spin injection efficiency of the manganite substrate.

Single Molecule Magnets (SMMs)

SMMs are molecular clusters or paramagnetic complexes characterised, at cryogenic temperatures, by a high spin ground state coupled with an easy axis anisotropy leading to the observation of a magnetic hysteresis at molecular level.[30] This behaviour results from slow relaxation of the magnetisation at low temperature that arises from the coexistence of two oppositely magnetised states separated by an energy barrier. Each single molecule shows therefore a magnetic bistability, intramolecular interactions playing a negligible role. Due to their unique magnetic behaviour, SMMs are investigated as elementary units for high-density data storage applications, quantum computing and spintronics.[31] The search for new SMMs with

1. Introduction

higher anisotropy barriers is then accompanied by attempts of organising these molecules on surface where the addressing and the control of a magnetic state at the single molecule level is possible.[32–34] The realization of SMM hybrid surfaces is not an easy task and became a critical issue like demonstrated for the dodecanuclear manganese complex (Mn$_{12}$)[35] where structural modifications induced by the substrate lead the molecules to lose their SMM character.[36] The first relevant success in the preparation of a hybrid surface where the SMM character was retained, was achieved by chemical grafting[37] a tetranuclear iron(III) complex[38] functionalized with a specific molecular linker group able to bind a gold surface using a wet chemistry approach.

SMM deposition has been achieved also using alternative techniques such as the electrospray beam deposition[39] and the molecular thermal sublimation methods.[40–43] These methods overcome the limitation of the chemical grafting procedure but require the thermal stability of molecules. This aspect reduces the number of SMMs suitable for this type of deposition. Thanks to their high stability and flatness, terbium(III) bis(phathalocyaninato) (TbPc$_2$) molecules, are probably the most studied SMM at the nanoscale.[31,44–54] For instance Ying-Shuang and co-workers demonstrated that the TbPc$_2$ molecules can appear chiral and after deposition on Iridium (111) this property can be switched by applying an external stimuli with STM tip.[55] This type of molecule is very suitable and can be functionalised with the pyrene in order to be grafted on graphene. This system has been characterised with Raman spectroscopy confirming the integrity of the system after wet deposition from solution.[44]
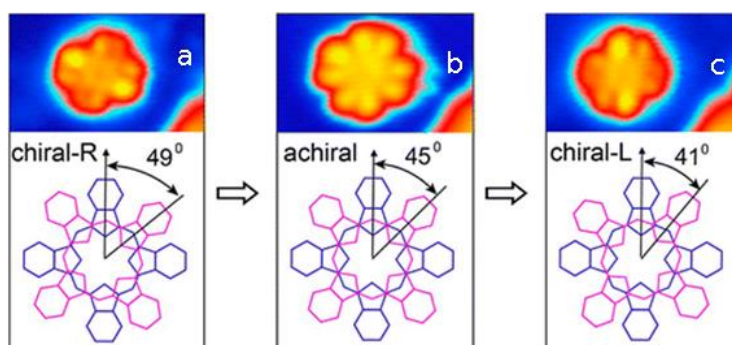
Figure 2. Chirality of TbPc$_2$ on Ir(111). STM images show two TbPc$_2$ molecules which are initially chiral (a, c) and become achiral in an eight-lobed state (b) after switching.[55]

4

Thiele and co-workers showed the general feasibility of establishing an all electrical control of a single nuclear spin through use of the hyperfine Stark effect and the approach should be transferable to other spin qubit devices with a large hyperfine interaction.[31]

In this work we present the results obtained adopting both the wet chemistry-based functionalization and the thermal sublimation of TbPc$_2$ complex. During the PhD we explored the deposition of this SMM on La$_{0.7}$Sr$_{0.3}$MnO$_3$ a widely employed spin injection electrode, and on Silicon (100). This peculiar molecular system has scientific and technological interest due to its slow relaxation of the magnetisation at relatively high temperatures for SMMs (15 K) and several recent works have been focused on the study on the understanding of the magnetic interaction between this complex and several surfaces, being this a prerequisite to be able to exploit these hybrid architectures in spintronic devices.[40,42] The control of the interaction between substrate and molecules could in fact open new perspectives for spintronics and data storage applications. On the other hand the surface interaction lead the SMM hybrid system some issues. When SMMs are organized in nanostructures on conducting surface a strong reduction of its magnetic hysteresis can be observed decreasing the richness of a SMM-based device.[56,57] On the other hand this interaction has been observed to cause the occurrence of relevant coupling with magnetic substrates, whose origin is still debated.[40–42,45] For this reason our work has been focused not only in the evaluation of occurring interactions between the molecular layer and the magnetic electrodes but also in maintaining the SMM behaviour in the final environment selected to develop new devices.

Valence Tautomers (VT)

The reversible conversion of the electronic state of switchable coordination systems at the single molecule level promises breakthrough outcomes for information storage and processing technologies.[58] In particular, the control of length and direction of the spin in paramagnetic switchable molecules represents a key feature to be used in quantum computation and nanosized spintronic applications.[59,60]

The class of compounds named Valence Tautomers (VT) comprises switchable compounds where an intermolecular redox isomerism occurs with a charge transfer

between a redox active ligand and a metallic centre thus leading to an entropically driven equilibrium between two molecular states that usually are distinguished by different colour, different magnetic behaviour and different refractive index. The conversion between these two states can be promoted by changing temperature but also with external stimuli like pressure variation or light irradiation.[61–63] Excluding the work described in this thesis work, in literature only one paper is present where chemically grafting strategies have been applied on Valence Tautomers. In this paper VT molecules have been chemisorbed on gold nanoparticles and small variation in the behaviour has been observed. That has been justified by the role of the solvent and by surface confinement effects thus highlighting that VT effects can be "tuned" by nanostructuration.[64]

Two cobalt-dioxolene complexes featuring a VT behaviour have been investigated in this thesis work. These coordination compounds are the simplest molecular systems displaying VT and have been modified here to promote their chemisorption on surface, the first step toward the realization of VT-based spintronic devices. Being in fact the retention of switchability in molecular-inorganic architectures obtained by the regular assembling of molecules on conductive surfaces a mandatory step towards their implementation in hybrid devices. In this thesis we focused the study on the deposition process of VT on gold surface paying attention to the retain of switchability after the deposition process. In particular we adapted the investigation tools often used for other magnetic molecules to VT systems demonstrating that also in-house apparatus can be used to study the VT process at the nanoscale.

Spin Cross-Overs (SCOs)

SCOs are another class of bistable molecules in which the reversible conversion between a low spin and a high spin state can be induced by a temperature variation, a light irradiation or other external stimuli.[65] In the literature several successful attempts of nano-structuration of SCO materials are present.[66–68] In these complexes switchability arises from the control of the spin state of the metal centre and these experiments confirmed the feasibility of obtaining bistable nano-assemblies of SCO systems like thin films and nanoparticles.[66,67] These studies, however, highlighted the non-innocent role played by the interaction with the surface in modifying the thermodynamics of the SCO equilibrium.[66,69] In particular, the deposition of sub-

monolayers of SCO systems on solid surfaces using ultra-high vacuum sublimation approach evidenced a strong influence of the substrate-molecule interaction on their switchability properties: while on Highly Oriented Pyrolytic Graphite supported SCO system preserves its bulk phase switchability features,[70] sub-monolayer deposits of several SCO systems on metallic substrates show the loss of their original SCO behaviour .[71–74] Indeed Miyamachi *et al.*[71] have reported the reversible switching of individual **[Fe(phen)₂](NCS)₂]** molecules by an STM tip between two high- and low-conduction states, which they assigned to the *HS* and *LS* states, respectively (Figure 3).
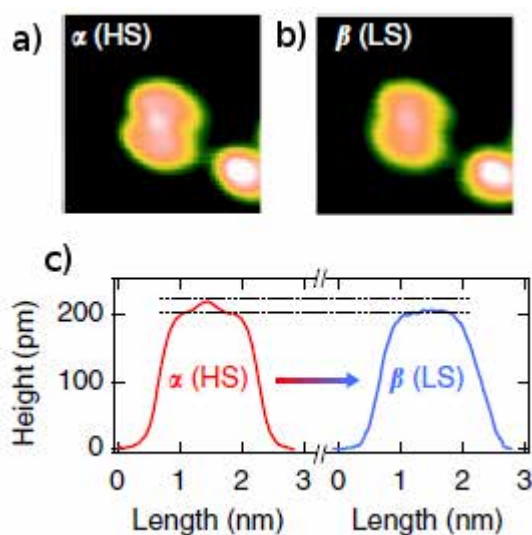
Figure 3. STM image of isolated [Fe(phen)₂](NCS)₂]molecules on a CuN/Cu(100) surface with α (*HS*) a) and β (*LS*) b) conformations and corresponding height profiles (c) along the molecular long axis acquired before and after the switching event.[71]

Switching to the *HS*(*LS*) state of the molecular junction was achieved by applying a certain threshold bias of negative (positive) polarity. Interestingly the effect was observed only when the molecules were decoupled from the metallic Cu(100) substrate by a thin insulating CuN layer highlighting the crucial role of the molecule-substrate interaction.

The SCO molecules studied in this thesis work are robust and chemically stable. We have demonstrated that they can be thermally evaporated to promote the interaction with surfaces. Additionally, the system investigated in this thesis features photomodulation of SCO properties: light irradiation at room temperature induces a

transformation in the chemistry of the ligand causing the SCO transition, [75] that has been here confirmed to occur also at the nanoscale.

1.2. Spintronics and molecular spintronics

The discovery of a Giant Magneto-Resistance (GMR) effect in nanostructures[76] has led to the new research field of Spintronic,[77] namely the use of spin state transport instead of charge transport as a new kind of electronics. The electron spin, has only two possible configurations (up or down), lending itself to the implementation of binary codes. The GMR effect consist in a "giant" variation in the resistance when two ferromagnetic layers (FM) separated by a non-magnetic conductive layer have their relative magnetisation paralely or antiparallely aligned. In GMR the conduction through this spacer is diffusive or ballistic, while, if the two ferromagnetic layers are separated by a thin insulator, the conduction occurs through quantum mechanical tunnelling effect. This magneto-resistance effect occurs when the insulating layer is only a few atomic layers in thickness. In this case there is a non-zero probability for the electrons to quantum tunnel through the insulating barrier and the effect is named as Tunnelling Magneto-Resistance (TMR). Its use in non-volatile Magnetic Random Access Memories (MRAM) has made TMR technology dominant over the GMR sensors. TMR is a pure interface effect and does not require spin transport in the non-magnetic layer.[78] TMR originates from the difference in the Density Of State (DOS) at the Fermi energy between spin-up and spin-down electrons. They can tunnel only from a given sub-band in the first FM layer to the same sub-band in the second FM layer, because of the conservation on the spin orientation. Most employed devices has a sandwich structure where, between two ferromagnetic electrodes, a non-magnetic material is placed. They are referred as Spin Valve (SV) and Magnetic Tunnel Junction (MTJ), when the non-magnetic material spacer is a semiconductor and a thin insulator (few nanometres), respectively.

One of the most challenging aspect in spintronic is an *efficient* transfer of spin polarisation.[79] The injection depends not only on the individual materials properties, but also on the interfaces.[80] This aspect has become relevant when the inorganic metals and semiconductors constituting the interlayer between the two electrodes have been replaced by a molecular layer. A newer field of research, the *organic*

spintronics,[81] has been in fact developed by following the interesting results obtained in organic electronics with molecular systems acting as charge carriers (organic semiconductors) leading to well-developed devices like organic light emitting diodes (OLED) and organic photovoltaic cells (OPV). Using a molecular layer as interlayer the versatility of chemistry can be fully exploited to improve and tune the transport effect.

Noticeably, the transport efficiency of the device is dominated by the resistance of the spacer and this aspect become particularly relevant for organic spintronics, since most organic materials are less conductive than the FM contacts.[79] A bypass to this problem has been achieved by introducing a large spin dependent resistance: i) placing a tunnel barrier between the FM contact and the spacer or ii) using of a fully spin-polarized ferromagnetic material, like lanthanum strontium manganite $La_{0.7}Sr_{0.3}MnO_3$ (LSMO).

Dediu and co-workers reported the first example of a molecular spin-valve observing a magneto-resistance at room temperature using both LSMO electrodes (Figure 4a).[82] The architecture was based on lateral spin devices where two ferromagnetic LSMO electrodes patterned by electron-beam lithography were bridged by a sexithiophene channel (Figure 4a). The archetypal molecular spin valve is a vertical device constituted by a bottom LSMO electrode, an OSC layer such as Al(III) tris(8-hydroxyquinoleine), Alq_3, acting as spin carrier, an AlO_x interlayer enrolled as tunnel barrier (not shown) and a metallic cobalt upper electrode (Figure 4b).[83,84]
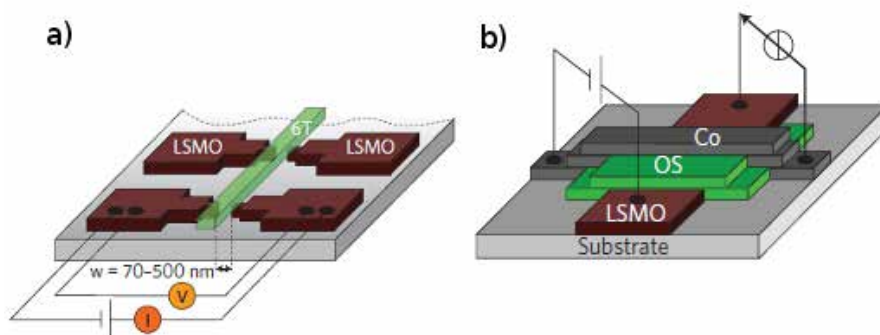

Figure 4. a) Lateral spin device as published by Dediu et al.[82] In this device, two ferromagnetic LSMO electrodes patterned by electron-beam lithography bridged by a 6T channel; b) Schematic of a typical vertical molecular spin valve.[84]

1. Introduction

In a molecular spin valve the LSMO contact is used as spin injector and the cobalt as spin detector. The cobalt magnetic layer is a soft magnetic material and its magnetisation can be easily changed by the application of a small magnetic field, or applying a voltage, while the LSMO layer is a hard magnetic material and its magnetisation is insensitive to moderate fields. In a molecular spin valve the distance between the FM contacts is very important, and to works properly, it should be smaller than the spin relaxation length,[85,86] thus evidencing that the conductivity of the OSC is a crucial point but even more important is the spin lifetime that is reduced if spin-orbit coupling effect occurs. Purely organic materials are attractive for building molecular spintronic devices because of their long spin relaxation lifetime (between a few milliseconds and a second).

A systematic understanding of these aspects is still lacking and there is a lot of unexplored aspects, though, for instance, it has been observed that a thin insulating layer (like AlO_x) deposited between the magnetic electrodes and the organic materials help to improve the device reproducibility and increase the MR. It is still not clear if this is connected to the suppression of surface states within the band-gap or to the reduction of the transition metal inter-diffusion into the organic layer or to the reduction of the resistance mismatch.[87]

Molecular spintronics is an extension of the organic spintronics, in which the OSC is replaced by a multifunctional molecular material with non-linear magnetic properties. The tunnelling probability of electrons will depend also on the specific and tuneable properties of the molecular layer such as a variable tunnel barrier of the material. It has been noticed that a spin filter junction with a ferromagnetic[88,89] semiconductor can promote a spin-polarized flow of tunnelling electrons. Using magnetic molecules deposited at the spin injection interface, one can imagine to develop newer devices where molecules, with metastable states related to the position of the magnetisation, could tune the spin injection. On the other hand it is also expected that the use of magnetic molecule can not only increase the spin injection gain, but also that magnetic molecules with a high spin state can act as molecular spin selector layer. In this way, by using a single layer of molecules it will be possible to select the spin direction of electrons without the use of spin injection electrode but simply acting on the molecular layer.

In the frame of the wide research field briefly described above, during this PhD thesis we have explored the possibility to use multifunctional magnetic molecules as

active interfaces for spintronics devices. The persistence of the molecular magnetic behaviour after deposition on non-magnetic and ferromagnetic electrodes is however a crucial point for any further development and it has been the main focus of this thesis work.

The thesis is organized as outlined in the following. Chapter 2 is devoted to a chemical investigation of the LSMO spin injection electrode focusing on the composition of the termination layer, the adsorbing site for a molecular layer and point out important information using a combination of *in-house* technique flanked by DFT calculations. Then in the same chapter we described a new protocol for assembling simple organic chain on the LSMO surface: important study finalized to the realization of the first spin valve based on magnetic molecules, functionalizing the LSMO surface with NNR and observing relevant magneto-resistance also when a paramagnetic layer is present. After that we moved on the investigation of the magnetic behaviour of a $TbPc_2$ complex on the same substrate (LSMO) but with two different deposition technique. In particular we focused our attention on the alteration of the magnetisation dynamics of $[TbPc_2]^0$ depending on the deposition protocol (i.e. via sublimation and via wet chemistry).

The chapter 3 is dedicated to the grafting of functionalized $[TbPc_2]^0$ molecules on silicon surface. A synchrotron characterisation evidenced an enhancement of the magnetic bistability of the complex due to the stabilization of cationic species of the complex by surface effects. This hypothesis was confirmed with a rigorous XPS characterisation of the complex. This rare behaviour makes this hybrid surface suitable for advanced spintronic applications as spin injection molecular layer.

Chapter 4 is devoted to the study of three optical switchable systems, two based on cobalt, dioxolene and ancillary ligands featuring a VT behaviour and the third on a SCO system based on an iron(II) complex with 1- pyrazolyl ligands. The first system is a cobalt dimer with a general formula **[CoLn-dioxo-R-dioxo-CoLn]** we used it to test an in house analysis at the nanoscale to fasten also the selection of VT candidates for molecular spintronics. The second one is a cobalt monomer **[CoLndiox]** opportunely functionalized to be able to chemisorb it on a gold surface forming a monolayer with a VT behaviour. This is the first study, in our knowledge, based on a VT system chemically grafted on conductive surface that retains its redox isomerism. The transition in temperature was followed by in-house XPS as well as by synchrotron-based X-ray absorption spectroscopy (XAS) analyses at the nanoscale.

1. Introduction

This unique behaviour of **[CoLndiox]** complex opens the possibility to introduce this system in a molecular spin vale where the properties could be modulated through light irradiation. The third complex belongs to class of SCO and is a very attractive system because of the presence of a diarylethene unit as ligand. The reversible modification of the ligand structure under UV-visible light modifies the ligand-field at room temperature thus promoting the conversion of the system from an high-spin configuration to diamagnetic low- spin at the coordinated Fe(II) ion. The reversible photoswitching of the spin states has been performed on surface after thermal deposition and monitored through magnetometry as well as by XPS at the Fe$2p$ edge, though synchrotron based experiments remain a key tool for the investigation of these complex magnetic nanostructure and have been widely employed throughout this thesis work.

Reference

(1)   Rocha, A. R.; García-Suárez, V. M.; Bailey, S. W.; Lambert, C. J.; Ferrer, J.; Sanvito, S. *Nat. Mater.* **2005**, *4*, 335–339.

(2)   Mas-Torrent, M.; Crivillers, N.; Mugnaini, V.; Ratera, I.; Rovira, C.; Veciana, J. *J. Mater. Chem.* **2009**, *19*, 1691.

(3)   Shekhah, O.; Roques, N.; Mugnaini, V.; Munuera, C.; Ocal, C.; Veciana, J.; Wo, C.; Wöll, C. *Langmuir* **2008**, *24*, 6640–6648.

(4)   Zheng, Y.; Miao, M.; Kemei, M. C.; Seshadri, R.; Wudl, F. *Isr. J. Chem.* **2014**, *54*, 774–778.

(5)   Yucel, B.; Sanli, B.; Akbulut, H.; Ozbey, S.; Benniston, A. C. *Org. Biomol. Chem.* **2012**, *10*, 1775–1784.

(6)   Simão, C.; Mas-Torrent, M.; Crivillers, N.; Lloveras, V.; Artés, J. M.; Gorostiza, P.; Veciana, J.; Rovira, C.; Arte, J. M. *Nat. Chem.* **2011**, *3*, 359–364.

(7)   Osiecki, J. H.; Ullman, E. F. *J. Am. Chem. Soc.* **1968**, *90*, 1078–1079.

(8)   Caneschi, A.; Ferraro, F.; Gatteschi, D.; le Lirzin, A.; Rentschler, E. *Inorg. Chim. Acta* **1995**, *235*, 159–164.

(9)   Toda, T.; Mori, E.; Murayama, K. *Bull. Chem. Soc. Jpn.* **1972**, *45*, 1904–1908.

(10)   Palacio, F.; Antorrena, G.; Castro, M.; Burriel, R.; Rawson, J.; Smith, J.; Bricklebank, N.; Novoa, J.; Ritter, C. *Phys. Rev. Lett.* **1997**, *79*, 2336–2339.

(11)   Caneschi, A.; Gatteschi, D.; Rey, P.; Sessoli, R. *Inorg. Chem.* **1991**, *30*, 3936–3941.

(12)   Fraxedas, J.; Caro, J.; Santiso, J.; Figueras, A.; Gorostiza, P.; Sanz, F. *Phys. status solidi* **1999**, *215*, 859–863.

(13)   Ruan, L. *J. Vac. Sci. Technol. B Microelectron. Nanom. Struct.* **1991**, *9*, 1134.

(14)   Mannini, M.; Sorace, L.; Gorini, L.; Piras, F. M.; Caneschi, A.; Magnani, A.; Menichetti, S.; Gatteschi, D. *Langmuir* **2007**, *23*, 2389–2397.

(15)   Zhang, Y.; Kahle, S.; Herden, T.; Stroh, C.; Mayor, M.; Schlickum, U.; Ternes, M.; Wahl, P.; Kern, K. *Nat. Commun.* **2013**, *4*, 2110.

(16)   Messina, P.; Mannini, M.; Caneschi, A.; Gatteschi, D.; Sorace, L.; Sigalotti, P.; Sandrin, C.; Prato, S.; Pittana, P.; Manassen, Y. *J. Appl. Phys.* **2007**, *101*, 053916.

(17)   Mannini, M.; Messina, P.; Sorace, L.; Gorini, L.; Fabrizioli, M.; Caneschi, a.; Manassen, Y.; Sigalotti, P.; Pittana, P.; Gatteschi, D. *Inorg. Chim. Acta* **2007**, *360*, 3837–3842.

1. Introduction

(18)   Ravat, P.; Borozdina, Y.; Ito, Y.; Enkelmann, V.; Baumgarten, M. *Cryst. Growth Des.* **2014**, *14*, 5840–5846.

(19)   Caro, J.; Fraxedas, J.; Jürgens, O.; Santiso, J. J.; Rovira, C.; Veciana, J.; Figueras, A.; Caro, B. J. *Adv. Mater.* **1998**, *10*, 608–610.

(20)   Savu, S.-A.; Biswas, I.; Sorace, L.; Mannini, M.; Rovai, D.; Caneschi, A.; Chassé, T.; Casu, M. B. *Chem. Eur. J.* **2013**, *19*, 3445–3450.

(21)   Kakavandi, R.; Savu, S.-A.; Caneschi, A.; Chassé, T.; Casu, M. B. *Chem. Commun.* **2013**, 10103–10105.

(22)   Abb, S.; Savu, S.-A.; Caneschi, A.; Chassé, T.; Casu, M. B. *ACS Appl. Mater. Inter.* **2013**, *5*, 13006–13011.

(23)   Choi, J.; Lee, H.; Kim, K.; Kim, B.; Kim, S. *J. Phys. Chem. Lett.* **2010**, *1*, 505–509.

(24)   Lee, H.; Yang, S.; Choi, J.; Park, Y.; Kim, S. *J. Phys. Chem. C* **2011**, *115*, 18736–18739.

(25)   Robin, A.; Marnell, L.; Bjork, J.; Dyer, M. S.; Bermudez, P. S.; Haq, S.; Barrett, S. D.; Persson, M.; Minoia, A.; Lazzaroni, R.; Raval, R. *J. Phys. Chem. C* **2009**, *113*, 13223–13230.

(26)   Bonosi, F.; Gabrielli, G.; Martini, G.; Ottaviani, M. F. *Langmuir* **1989**, *5*, 1037–1043.

(27)   Gallani, J. L.; Moigne, J. Le; Oswald, L.; Bernard, M.; Turek, P. *Langmuir* **2001**, 1104–1109.

(28)   Poggini, L.; Lunghi, A.; Caneschi, A.; Armelao, L.; Cortigiani, B.; Magnano, E.; Bondino, F.; Magnani, A.; Totti, F.; Gatteschi, D.; Sessoli, R.; Sorace, L.; Mannini, M. *Manuscript in Preparation*.

(29)   Ratera, I.; Veciana, J. *Chem. Soc. Rev.* **2012**, *41*, 303–349.

(30)   Gatteschi, D.; Sessoli, R.; Villain, J. *Molecular Nanomagnets*; Oxford University Press, 2006; p. 408.

(31)   Thiele, S.; Balestro, F.; Ballou, R.; Klyatskaya, S.; Ruben, M.; Wernsdorfer, W. *Science* **2014**, *344*, 1135–1138.

(32)   Misiorny, M.; Barnaś, J. *Phys. Rev. B* **2008**, *77*, 172414.

(33)   Misiorny, M.; Weymann, I.; Barnaś, J. *Europhys. Lett.* **2010**, *89*, 18003.

(34)   Cornia, A.; Mannini, M.; Sainctavit, P.; Sessoli, R. *Chem. Soc. Rev.* **2011**, *40*, 3076–3091.

(35)   Sessoli, R.; Gatteschi, D.; Caneschi, A.; Novak, M. A. *Nature* **1993**, *365*, 141–143.

(36)   Mannini, M.; Sainctavit, P.; Sessoli, R.; Cartier dit Moulin, C.; Pineider, F.; Arrio, M.-A.; Cornia, A.; Gatteschi, D. *Chem. Eur. J.* **2008**, *14*, 7530–7535.

(37) Mannini, M.; Pineider, F.; Sainctavit, P.; Danieli, C.; Otero, E.; Sciancalepore, C.; Talarico, A. M.; Arrio, M.-A.; Cornia, A.; Gatteschi, D.; Sessoli, R. *Nat. Mater.* **2009**, *8*, 194–197.

(38) Accorsi, S.; Barra, A.-L.; Caneschi, A.; Chastanet, G.; Cornia, A.; Fabretti, A. C.; Gatteschi, D.; Mortalo, C.; Olivieri, E.; Parenti, F.; Rosa, P.; Sessoli, R.; Sorace, L.; Wernsdorfer, W.; Zobbi, L. *J. Am. Chem. Soc.* **2006**, *128*, 4742–4755.

(39) Kahle, S.; Deng, Z.; Malinowski, N.; Tonnoir, C.; Forment-Aliaga, A.; Thontasen, N.; Rinke, G.; Le, D.; Turkowski, V.; Rahman, T. S.; Rauschenbach, S.; Ternes, M.; Kern, K. *Nano Lett.* **2012**, *12*, 518–521.

(40) Lodi Rizzini, A.; Krull, C.; Balashov, T.; Kavich, J. J.; Mugarza, A.; Miedema, P. S.; Thakur, P. K.; Sessi, V.; Klyatskaya, S.; Ruben, M.; Stepanow, S.; Gambardella, P. *Phys. Rev. Lett.* **2011**, *107*, 177205.

(41) Malavolti, L.; Poggini, L.; Margheriti, L.; Chiappe, D.; Graziosi, P.; Cortigiani, B.; Lanzilotto, V.; Buatier de Mongeot, F.; Ohresser, P.; Otero, E.; Choueikani, F.; Sainctavit, P.; Bergenti, I.; Dediu, V. a; Mannini, M.; Sessoli, R.; de Mongeot, F. B. *Chem. Commun.* **2013**, *49*, 11506–11508.

(42) Lodi Rizzini, a; Krull, C.; Balashov, T.; Mugarza, a; Nistor, C.; Yakhou, F.; Sessi, V.; Klyatskaya, S.; Ruben, M.; Stepanow, S.; Gambardella, P. *Nano Lett.* **2012**, *12*, 5703–5707.

(43) Malavolti, L.; Lanzilotto, V.; Ninova, S.; Poggini, L.; Cimatti, I.; Cortigiani, B.; Margheriti, L.; Chiappe, D.; Otero, E.; Sainctavit, P.; Totti, F.; Cornia, A.; Mannini, M.; Sessoli, R. *Nano Lett.* **2014**.

(44) Lopes, M.; Candini, A.; Urdampilleta, M.; Reserbat-Plantey, A.; Bellini, V.; Klyatskaya, S.; Marty, L.; Ruben, M.; Affronte, M.; Wernsdorfer, W.; Bendiab, N.; Affronte, Ḱ. M. *ACS Nano* **2010**, *4*, 7531–7537.

(45) Stepanow, S.; Honolka, J.; Gambardella, P.; Vitali, L.; Abdurakhmanova, N.; Tseng, T.-C.; Rauschenbach, S.; Tait, S. L.; Sessi, V.; Klyatskaya, S.; Ruben, M.; Kern, K. *J. Am. Chem. Soc.* **2010**, *132*, 11900–11901.

(46) Vitali, L.; Fabris, S.; Conte, A. M.; Brink, S.; Ruben, M.; Baroni, S.; Kern, K. *Nano Lett.* **2008**, *8*, 3364–3368.

(47) Biagi, R.; Fernandez-Rodriguez, J.; Gonidec, M.; Mirone, a.; Corradini, V.; Moro, F.; De Renzi, V.; del Pennino, U.; Cezar, J. C.; Amabilino, D. B.; Veciana, J. *Phys. Rev. B* **2010**, *82*, 224406.

(48) Ganzhorn, M.; Klyatskaya, S.; Ruben, M.; Wernsdorfer, W. *Nat. Nanotechnol.* **2013**, *8*, 165–169.

(49) Urdampilleta, M.; Klyatskaya, S.; Cleuziou, J.-P.; Ruben, M.; Wernsdorfer, W. *Nat. Mater.* **2011**, *10*, 502–506.

(50) Schwöbel, J.; Fu, Y.; Brede, J.; Dilullo, A.; Hoffmann, G.; Klyatskaya, S.; Ruben, M.; Wiesendanger, R. *Nat. Commun.* **2012**, *3*, 953.

1. Introduction

(51) Müllegger, S.; Tebi, S.; Das, A. K.; Schöfberger, W.; Faschinger, F.; Koch, R. *Phys. Rev. Lett.* **2014**, *113*, 133001.

(52) Kyatskaya, S.; Mascarós, J. R. G.; Bogani, L.; Hennrich, F.; Kappes, M.; Wernsdorfer, W.; Ruben, M. *J. Am. Chem. Soc.* **2009**, *131*, 15143–15151.

(53) Candini, A.; Klyatskaya, S.; Ruben, M.; Wernsdorfer, W.; Affronte, M. *Nano Lett.* **2011**, *11*, 2634–2639.

(54) Ganzhorn, M.; Klyatskaya, S.; Ruben, M.; Wernsdorfer, W. *ACS Nano* **2013**, *7*, 6225–6236.

(55) Fu, Y.-S.; Schwöbel, J.; Hla, S.-W.; Dilullo, A.; Hoffmann, G.; Klyatskaya, S.; Ruben, M.; Wiesendanger, R. *Nano Lett.* **2012**, *12*, 3931–3935.

(56) Margheriti, L.; Mannini, M.; Sorace, L.; Gorini, L.; Gatteschi, D.; Caneschi, A.; Chiappe, D.; Moroni, R.; de Mongeot, F. B.; Cornia, A.; Piras, F. M.; Magnani, A.; Sessoli, R. *Small* **2009**, *5*, 1460–1466.

(57) Margheriti, L.; Chiappe, D.; Mannini, M.; Car, P.-E.; Sainctavit, P.; Arrio, M.-A.; de Mongeot, F. B.; Cezar, J. C.; Piras, F. M.; Magnani, A.; Otero, E.; Caneschi, A.; Sessoli, R. *Adv. Mater.* **2010**, *22*, 5488–5493.

(58) Prasanna de Silva, A. *Molecular Logic-based Computation*; Monographs in Supramolecular Chemistry; Royal Society of Chemistry: Cambridge, 2012.

(59) Baadji, N.; Piacenza, M.; Tugsuz, T.; Della Sala, F.; Maruccio, G.; Sanvito, S. *Nat. Mater.* **2009**, *8*, 813–817.

(60) Wagner, S.; Kisslinger, F.; Ballmann, S.; Schramm, F.; Chandrasekar, R.; Bodenstein, T.; Fuhr, O.; Secker, D.; Fink, K.; Ruben, M.; Weber, H. B. *Nat. Nanotechnol.* **2013**, *8*, 575–579.

(61) Dapporto, P.; Dei, A.; Poneti, G.; Sorace, L. *Chem. Eur. J.* **2008**, *14*, 10915–10918.

(62) Beni, A.; Carbonera, C.; Dei, A.; Létard, J.-F.; Righini, R.; Sangregorio, C.; Sorace, L. *J. Braz. Chem. Soc.* **2006**, *17*, 1522–1533.

(63) Goswami, T.; Misra, A. *Chem. Eur. J.* **2014**, *20*, 13951–13956.

(64) Bin-Salamon, S.; Brewer, S.; Franzen, S.; Feldheim, D. L.; Lappi, S.; Shultz, D. A. *J. Am. Chem. Soc.* **2005**, *127*, 5328–5329.

(65) Gütlich, P.; Hauser, A.; Spiering, H. *Angew. Chem. Int. Ed.* **1994**, *33*, 2024–2054.

(66) Bousseksou, A.; Molnár, G.; Salmon, L.; Nicolazzi, W. *Chem. Soc. Rev.* **2011**, *40*, 3313–3335.

(67) Shepherd, H. J.; Molnár, G.; Nicolazzi, W.; Salmon, L.; Bousseksou, A. *Eur. J. Inorg. Chem.* **2013**, *2013*, 653–661.

(68) Kahn, O.; Jay Martinez, C. *Science* **1998**, *279*, 44–48.

(69) Mikolasek, M.; Félix, G.; Nicolazzi, W.; Molnár, G.; Salmon, L.; Bousseksou, A. *New J. Chem.* **2014**, *38*, 1834.

(70) Bernien, M.; Wiedemann, D.; Hermanns, C. F.; Krüger, A.; Rolf, D.; Kroener, W.; Müller, P.; Grohmann, A.; Kuch, W. *J. Phys. Chem. Lett.* **2012**, *3*, 3431–3434.

(71) Miyamachi, T.; Gruber, M.; Davesne, V.; Bowen, M.; Boukari, S.; Joly, L.; Scheurer, F.; Rogez, G.; Yamada, T. K.; Ohresser, P.; Beaurepaire, E.; Wulfhekel, W. *Nat. Commun.* **2012**, *3*, 938.

(72) Gopakumar, T. G.; Matino, F.; Naggert, H.; Bannwarth, A.; Tuczek, F.; Berndt, R. *Angew. Chem. Int. Ed.* **2012**, *51*, 6262–6266.

(73) Pronschinske, A.; Bruce, R. C.; Lewis, G.; Chen, Y.; Calzolari, A.; Buongiorno-Nardelli, M.; Shultz, D. A.; You, W.; Dougherty, D. B. *Chem. Commun.* **2013**, *49*, 10446–10452.

(74) Pronschinske, A.; Chen, Y.; Lewis, G. F.; Shultz, D. A.; Calzolari, A.; Nardelli, M. B.; Dougherty, D. B. *Nano Lett.* **2013**, *13*, 1429–1434.

(75) Milek, M.; Heinemann, F.; Khusniyarov, M. *Inorg. Chem.* **2013**, *52*, 11585–11592.

(76) Baibich, M.; Broto, J.; Fert, A.; Dau, F. Van. *Phys. Rev. Lett.* **1988**, *61*, 2472–2475.

(77) Žutić, I.; Fabian, J.; Sarma, S. *Rev. Mod. Phys.* **2004**, *76*.

(78) Felser, C.; Fecher, G. H.; Balke, B. *Angew. Chem. Int. Ed.* **2007**, *46*, 668–699.

(79) Sanvito, S. *Chem. Soc. Rev.* **2011**, *40*, 3336–3355.

(80) Sanvito, S. *Nat. Phys.* **2010**, *6*, 562–564.

(81) Sun, D.; Ehrenfreund, E.; Vardeny, Z. V. *Chem. Commun.* **2014**, *50*, 1781–1793.

(82) Dediu, V.; Murgia, M.; Matacotta, F. C.; Taliani, C.; Barbanera, S. *Solid State Commun.* **2002**, *122*, 181–184.

(83) Dediu, V. A.; Hueso, L. E.; Bergenti, I.; Taliani, C. *Nat. Mater.* **2009**, *8*, 707–716.

(84) Dediu, V.; Hueso, L.; Bergenti, I.; Riminucci, A.; Borgatti, F.; Graziosi, P.; Newby, C.; Casoli, F.; De Jong, M.; Taliani, C.; Zhan, Y. *Phys. Rev. B* **2008**, *78*, 115203.

(85) Pramanik, S.; Stefanita, C.-G.; Patibandla, S.; Bandyopadhyay, S.; Garre, K.; Harth, N.; Cahay, M. *Nat. Nanotechnol.* **2007**, *2*, 216–219.

(86) Chappert, C.; Fert, A.; Van Dau, F. N. *Nat. Mater.* **2007**, *6*, 813–823.

1. Introduction

(87)   Moussy, J.-B.; Tortech, L.; Rengnez, F.; Matzen, S.; Ott, F.; Guittet, M.-J.; Fichou, D. *J. Mater. Chem.* **2009**, *19*, 6973.

(88)   Epstein, R.; Stephens, J.; Hanson, M.; Chye, Y.; Gossard, a.; Petroff, P.; Awschalom, D. *Phys. Rev. B* **2003**, *68*, 041305.

(89)   Pejaković, D.; Kitamura, C.; Miller, J.; Epstein, A. *Phys. Rev. Lett.* **2002**, *88*, 057202.

18

2. Assembling magnetic molecules on LSMO the electrode

In this chapter we describe our research activity having as final aim the realization of a vertical Spin-Valve including magnetic molecules. In particular we selected as starting substrate the ferromagnetic mixed oxide $La_{0.7}Sr_{0.3}MnO_3$ (hereafter LSMO), already introduced in the previous chapter, which is one of the most used electrodes in this class of spintronic devices.

In the last years the electronic and magnetic structure of interfaces formed between an organic π-conjugated semiconductor and a ferromagnetic layer has been investigated for a large variety of systems.[1] Among the results, it has been shown that the formation of hybrid states with magnetic properties, or specific exchange interactions, has a clear impact on spin injection across the interface. This topic has a huge interest for both fundamental and applicative research related to organic-inorganic devices like magnetic tunnel junctions, spin valves, memristors and others, whose performance is strongly affected by the boundary region between the organic and inorganic phases.[2–8] Most important achievements have been hitherto obtained by interfacing organic materials with complex ferromagnetic metal oxides, in particular with the LSMO, whose large spin polarisation of the surface (nominally 100% at zero temperature), and its good stability under different conditions, may represent a significant advantage with respect to the use e.g. of *3d* FM thin films.[7]

Using molecules as building blocks for electronic devices offers ample possibilities for new device functionalities due to a chemical tunability much higher than that of standard inorganic materials. As mentioned earlier, monolayers of magnetic molecules are attracting broad interest thanks to their potential technological applications as building block units in new devices for data storage and molecular spintronics.[9] SAM-based strategies [10] are among the most used techniques to achieve a bidimensional organization of molecules absorbed on surface but a prerequisite of the SAM formation is the presence of a functional group suitable to bind to a specific surface. According to this, focusing on the LSMO surface we had to design a specific coordination strategy to promote chemisorption of magnetic molecules on this manganite surface.

2. Assembling magnetic molecules on LSMO the electrode

Before proceeding with this task it is important to know the surface properties of LSMO electrodes including the stoichiometry of the topmost layers of this substrate, which is expected to exhibit relevant deviation from bulk stoichiometry thus altering reactivity and magnetism of the surface and consequently the interaction with magnetic molecules deposited on it.

2.1 Surface chemistry of LSMO

The composition of the termination layer in manganites is clearly a key issue for interfaces prepared in vacuum environment and is equally relevant for innovative devices prepared from self-assembly in solution, where molecules are designed to be chemically grafted on the electrodes.[11]
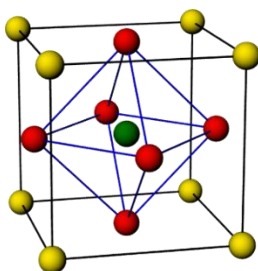

Figure 1. Unit cell of LSMO.

In the unit cell of $La_{1-x}Sr_xMnO_3$ (Figure 1) the manganese atom (green) is surrounded by an oxygen octahedron (red). The atoms at the yellow sites can be either lanthanum or strontium. The surface of oxide ferromagnetic electrodes requires a detailed characterisation because the stoichiometry of the perovskite-structured LSMO surface may deviate significantly from the nominal values, thereby affecting the surface magnetic properties e.g. by the generation of a magnetically dead layer or a complex magnetic configuration.[12,13] Previous studies evidenced that the surface of $La_{1-x}Sr_xMnO_3$ thin films is usually enriched in strontium over a wide range of the temperatures and oxygen partial pressures chosen for the film growth and regardless of the sign or magnitude of strain induced by the growth substrates.[14–17] This condition has been observed, e.g. by X-ray electron spectroscopy techniques, independently of the stoichiometry of the LSMO films as well as for other $La_xA_yMnO_3$ (A=Sr,Ca,Pb) manganites.[18–20] In particular, for the topmost layers different situations have been proposed. It has been suggested that

the Sr segregation is responsible for a significant restructuring of the LSMO surface region through the formation of a Ruddlesden Popper phase, i.e. $(La,Sr)_{n+1}Mn_nO_{3n+1}$ with n=1, or for the formation of a uniform strontium oxide (SrO) monolayer.[21,22] However other studies performed for LSMO films of different composition and on different substrates suggest also the presence of a MnO_2 terminating atomic layer.[23–25] It has been recently shown that for LSMO thin films of few nanometers the termination layer depends also on the nature of the substrate.[26]

For this reasons we performed a detailed analysis of the surface chemical composition of LSMO epitaxial thin films (thickness 40 nm) grown on $NdGaO_3$(110) by Channel Spark Ablation (CSA). These substrates have been provided by the group of Dr. Valentin A. Dediu of the ISMN-CNR in Bologna.

The combination of Low Energy Ion Scattering measurements (LEIS), a technique extremely sensitive to the chemical composition of the topmost surface layer (see Chapter 5.2.), and Angular-Resolved X-ray Photoemission Spectroscopy (AR-XPS. Chapter 5.4.1) have been used in this thesis to define the LSMO surface stoichiometry. While the latter technique has been already used to determine the Sr/La concentration profile of the LSMO film from the surface to the bulk,[27,28] the use of LEIS is practically unprecedented on this type of materials.

Before any surface investigation, we developed a specific cleaning procedure of the LSMO thin films consisting in a sonication in acetone and 2-propanol for 10 min followed by an annealing in ultra-high vacuum (UHV) at 523 K and at pressure lower than 10^{-9} mbar for 30 min. This procedure assures the removal of water and other volatile contaminants from the surface.
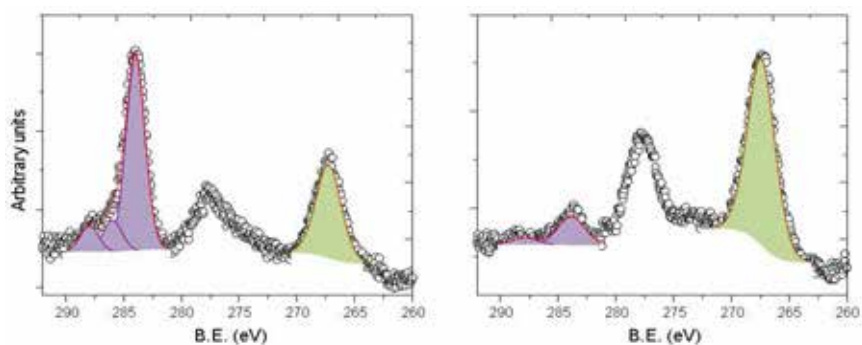

Figure 2. XPS spectra of LSMO in C*1s* and Sr*3p3/2* regions before and after annealing procedure, respectively; C components are filled in violet and Sr in green.

This cleaning procedure was validated in situ by means of XPS spectroscopy. From a comparison between XPS spectra (Figure 2) in the region of C$1s$ and Sr$3p_{3/2}$, acquired before and after annealing, we found that the ratio between the areas of adventitious carbon to that of strontium decreased from 7.53 to 0.73 with our treatment, confirming its efficiency.

Additionally an STM investigation carried out on a LSMO after this cleaning process (Figure 3) evidenced a sort of "grain-like" surface with average height of ca. 1 nm with RMS roughness of 0.29 nm, with most outgrowths showing lateral dimension of ca. 1.5 nm.
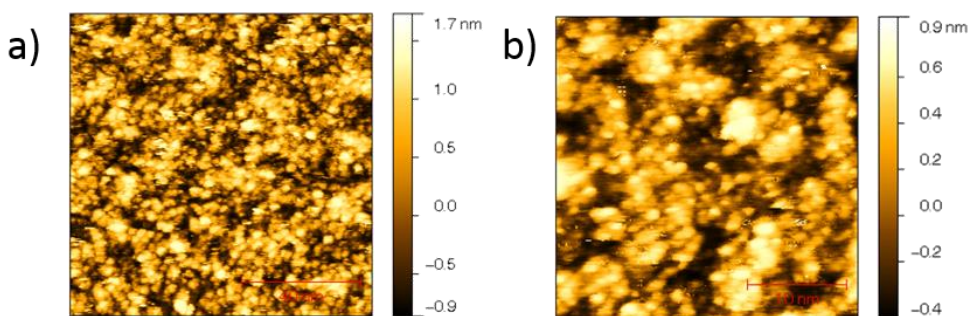
Figure 3. STM images of 12 nm LSMO on STO; 100x100nm^2 (a) and 30x30 nm^2 (b) both acquired with 50mV bias and 40pA of current.

We notice that being the available LSMO surface characterized by this roughness high resolution imaging of the adsorbates we planned to chemisorb on it will not be possible.

2.1.2 LEIS characterisation of the LSMO surface

The LEIS spectra were acquired in the UHV system described in Chapter 5.2. The scattering data were recorded using a He$^+$ ions accelerated at 1 keV on the LSMO film surface and the resulting spectra are shown in Figure 4. Primary He$^+$ ions were chosen in order to reduce the sputtering efficiency, thus permitting a soft depth profile analysis of the material. The small evolution of the LEIS spectra across the whole sequence indicates negligible alteration of the stoichiometry through sputtering by the He$^+$ ions at the imposed energy, confirming that they are fully indicative of the chemical composition of the topmost layers. The assignment of each

peak to the elements of the surface is achieved by evaluating the final kinetic energy E_i of the backscattered ions using the scattering equation for elastic collision events (Chapter 5.2, Eq. 13). On the basis of the above mentioned equation, the most intense peaks can be assigned to oxygen (400 eV), manganese (756 eV) and strontium (822 eV) respectively.
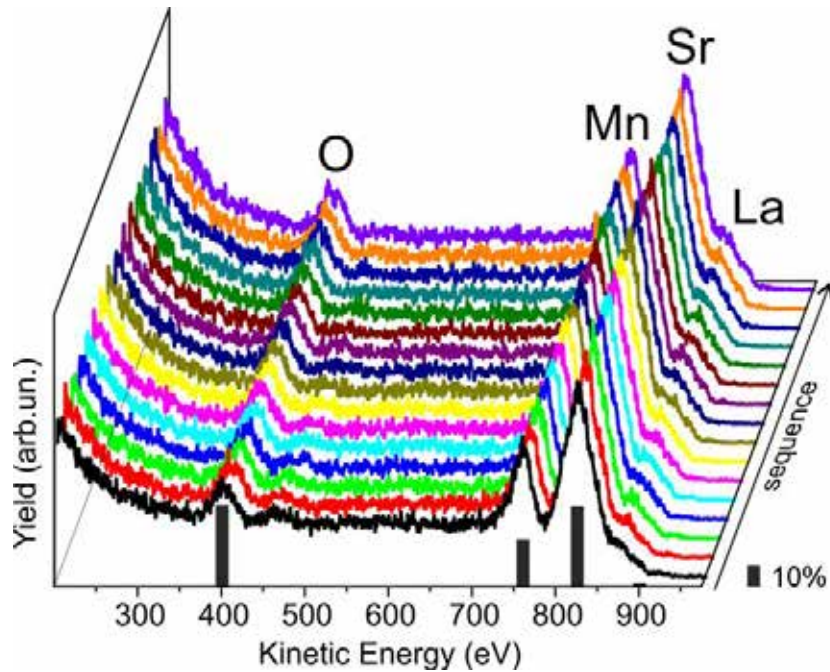
Figure 4. LEIS spectra for LSMO film surface (He⁺, 1000 eV) as a function of time.

The peak of lanthanum, expected in this case around 903 eV, shows up as a very small shoulder nearby the Sr peak, and increases very slightly along the sequence of the spectra despite the high differential scattering cross-section of La. This can be justified only considering that La is not present on the topmost layers of the surface.

Although the use of LEIS technique to extract chemical composition of the surface is not employed as routinely as for XPS, a semiquantitative indication of the surface stoichiometry can been achieved by estimating the differential cross-section for each element according to literature procedures.[29] The peaks areas were evaluated after subtracting a linear background. The differential cross-sections of the investigated elements, estimated by adopting a Thomas-Fermi-Moliere interacting potential and using the "Magic Formula" by Ziegler, Biersack and Littmark ,[30] were used to correct the contribution of the different element in the LEIS spectra and then to evaluate

2. Assembling magnetic molecules on LSMO the electrode

the elemental composition (see chapter 5.2).[30] It turns out that the composition of the topmost layer of the sample strongly deviates from the $La_{0.7}Sr_{0.3}MnO_3$ bulk phase, as shown in Figure 4 by the bars indicating the relative amount of the LSMO ion species for the first LEIS spectrum. We notice that the lack of an adequate standard for each element and the strong matrix effect in the scattering phenomenon, combined with the difficulties in background subtraction, does not allow a precise estimation of the uncertainty for our analysis. However, despite the limitations of this approach, a large disproportion between the amount of atoms of La and Sr in favour of the latter is achieved. In the first scan, considering also the contributions by oxygen and manganese, we obtain a nominal stoichiometry of $La_{0.07}Sr_{1.89}Mn_{1.12}O_{1.93}$. This result is confirmed along the whole series of the spectra, the peak intensities varying not more than 5% from their initial value. In particular, the La content, although slightly increasing with the sputtering time, remains very far from the bulk value of 0.7 reaching at the end of spectra series (15 scans) a nominal stoichiometry of $La_{0.12}Sr_{1.79}Mn_{1.07}O_{2.03}$. In Table 1 is reported the variation of surface stoichiometry for each LEIS scan in function of the time.

Table 1. Variation of surface stoichiometry during LEIS measurements as a function of time.

Stoichiometry			
La	Sr	Mn	O
0.07	1.89	1.12	1.93
0.07	1.94	1.15	1.83
0.09	1.95	1.20	1.76
0.11	1.91	1.19	1.79
0.10	1.89	1.11	1.90
0.10	1.79	1.14	1.96
0.12	1.90	1.19	1.79
0.11	1.86	1.11	1.92
0.12	1.91	1.10	1.87
0.11	1.77	1.03	2.09
0.12	1.80	1.13	1.95
0.10	1.79	1.05	2.06
0.11	1.74	1.08	2.07
0.13	1.73	1.09	2.06
0.12	1.77	1.05	2.06
0.12	1.79	1.07	2.03

N° of scan

...

Further information about the change of the stoichiometry from the surface to the bulk region may be achieved through LEIS measurements by increasing the mass and the kinetic energy of the primary ions. Figure 5 shows a set of LEIS spectra measured on a fixed area of the sample, in which Ne^+ ions were used as probe, and their energy was gradually varied from 600 and 1500 eV, followed by a last spectrum with the initial energy (E_i^0=600 eV). La, Sr and Mn peaks have been identified (in agreement with Eq. 13, Chapter 5.2) and the element percentage was evaluated. With these conditions, the peak of Mn is only visible for the higher energies, while oxygen cannot be detected due to its low mass with respect to Ne. A strong increase in the La/Sr concentration ratio is observed by increasing the energy of the primary beam and the associated sputtering efficiency of the Ne^+ ions, thus providing qualitative indications on the depth profile of the chemical composition. The La/Sr ratio varies from 0.25 at the lowest energy towards an almost stoichiometric value of 1.5 for the highest employed energy, as shown in the inset of Figure 5.
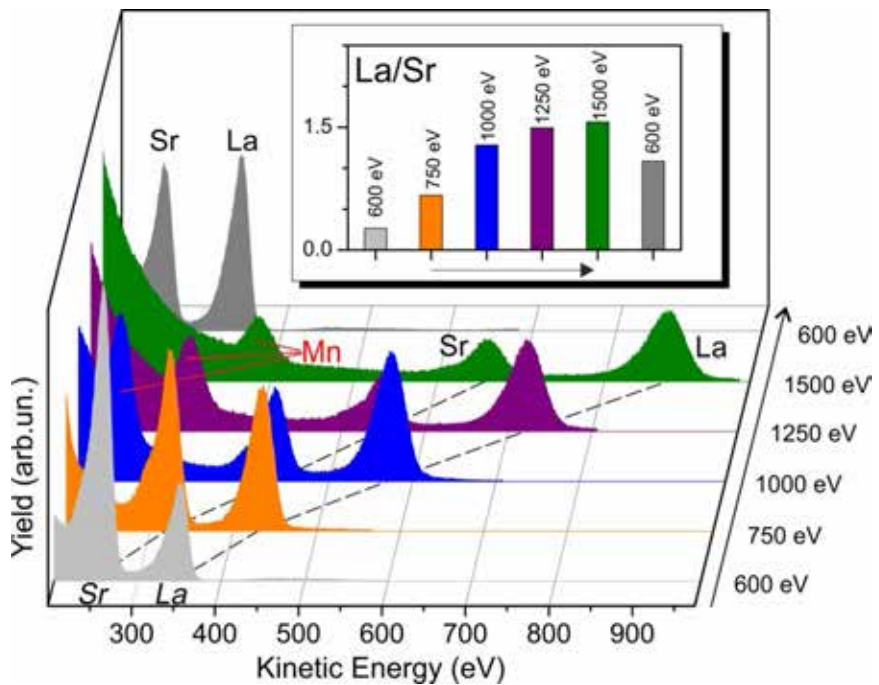

Figure 5. LEIS spectra measured using Ne^+ as primary source with kinetic energy varied from 600 eV to 1500 eV and back to 600 eV on the same position of the sample surface. Color code indicate the different kinetic energy. The positions of the La, Sr and Mn peaks are indicated by dashed and red straight lines, respectively.

In Figure 5 are reported the LEIS spectra obtained using different kinetic energies of the Ne$^+$ ions. La and Sr related signal are clearly identified in each spectrum, Mn is evident only at high energy while the oxygen signal is not visible within this primary energy range. The increased La/Sr ratio observed for E_i^0=600 eV in the last spectrum of the series with respect to the first one supports this analysis. Such evidences are in strong agreement with a small content of La on the topmost layer of the LSMO film and confirm that the topmost layers of LSMO are constituted almost exclusively by strontium and manganese oxides, while a gradual enrichment in La is observed sampling at increasing depth. Moreover, the presence of Mn on the surface denotes a situation different from the case of a termination layer containing exclusively of SrO proposed in Ref. 22, an information strictly related to the spin injection efficiency of our LSMO electrodes across the boundary with the organic layer. It is noteworthy that this evidence through LEIS measurements is very direct and unprecedented in the wide literature on the subject.[23,24]

2.1.3 AR-XPS characterisation of the LSMO surface

In order to confirm LEIS data we have investigated LSMO by AR-XPS measurements, collecting core-level spectra representative of all elements at different take-off angles to vary the sensitivity from the bulk to the surface regions.[28] This approach has been successfully utilised in the past for several studies focused on the investigation of surface segregation in manganite systems.[18–22] The changes of the spectral line-shape for each element through the comparison of spectra recorded at θ=0° (normal emission) and θ=60° (grazing emission) are reported in Figure 6. In the case of Mn*2p* and La*3d* no significant angular dependence of the line shape is observed, while in the spectral regions of O*1s* and Sr*3d* an evolution with the angle is clearly detected. The spectral features were recognized by fitting the core level peaks with pseudo-Voigt curves for each component in the spectrum, while the inelastic background was subtracted by the Shirley method. The O*1s* lineshape, in agreement with previous investigations, consists of two components, one at 528.4 eV (filled in orange) attributable to oxygen in bulk LSMO phase, and the other at 530.4 eV (filled in violet), attributable to the outmost layers of the film, as the intensity of the latter component increases with increasing take-off angle.[31]

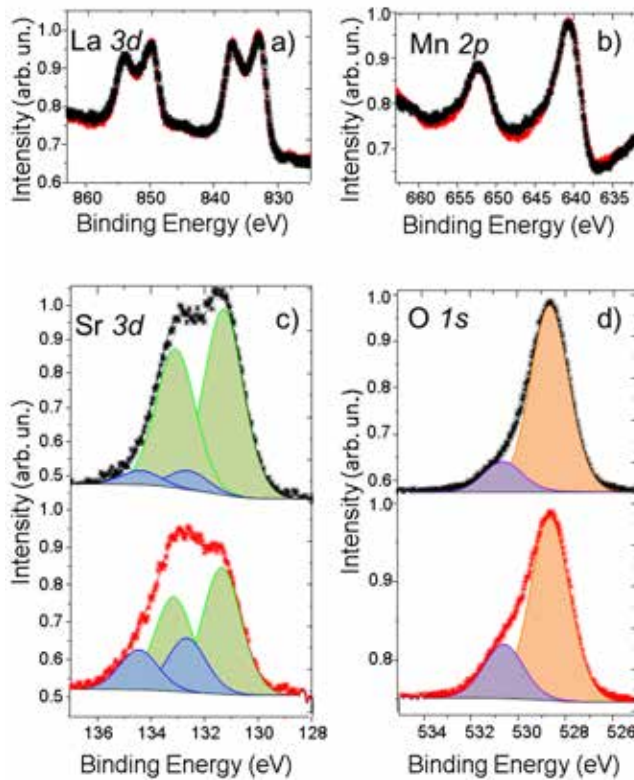**Figure 6. Comparison between core level spectra taken at normal (θ=0°, black) and grazing take-off angle (θ=60°, red). The intensity of the (a) La*3d* and (b) Mn*2p* spectra was normalized to better compare the line-shapes. (c) Sr*3d* peaks for θ=0° (top) and θ=60° (bottom); in both spectra green and blue area are relative to bulk and surface components, respectively. (d) O*1s* peaks for θ=0° (top) and θ=60° (bottom); bulk and surface components are indicated in orange and violet, respectively.**

Within the experimental resolution, there is no evidence of further contributions related to surface contaminations, thus indicating a surface quality similar to that of single crystals cleaved in vacuum. In analogy to what observed by several authors, the Sr*3d* peak is well described by two doublets with spin-orbit splitting 1.79 eV and full width half maximum 1.7 eV. The component at lower binding energy (Sr_{bulk}) is attributed to strontium contribution from bulk LSMO, while the other ($Sr_{surface}$) is related to states located near the surface. The dependence of the $Sr_{surface}/Sr_{bulk}$ ratio on the take-off angle ranges from 0.07 at 0° to 0.42 at 60°, thereby indicates large Sr enrichment in the top LSMO unit cells and the presence of SrO regions. The presence of La and Sr amounts at the surface region different from the bulk, in agreement with the LEIS results, is evident looking at the angular dependence of the Sr/La ratio

evaluated from the intensities of the Sr*3d* and La*3d* peaks, shown in Figure 7, which is increasing with the emission angle, as expected for Sr enrichment close to the surface. If the relative concentration of Sr with respect to that of La were independent of the depth into the sample, the Sr/La ratio would have been roughly constant. The strict correlation between the intensity of Sr and La peaks is indicative of Sr segregation involving mostly the substitution of the La ions in the LSMO lattice. Accordingly to previous similar studies,[21] the Sr/La intensity ratio has been used to evaluate quantitatively the deviation of the La and Sr composition from the bulk by fitting the data with the formula:

$$R = \frac{\sigma_{Sr}}{\sigma_{La}} \frac{T_{Sr}}{T_{La}} \frac{\sum_i f_i^{Sr} e^{\left(-id/\lambda_{Sr}\cos(\theta)\right)}}{\sum_j f_j^{La} e^{\left(-jd/\lambda_{La}\cos(\theta)\right)}} \qquad (1)$$

in which θ is the emission angle with respect to the surface normal, $\sigma_{Sr(La)}$ is the photoionization cross section, $T_{Sr(La)}$ is the transmission coefficient of the analyser, $\lambda_{Sr(La)}$ is the inelastic mean free path of the emitted electrons and $f_{i(j)}^{Sr(La)}$ is the atomic fraction of Sr and La, respectively.[28] Apart for the atomic fraction of the Sr and La ions, the other quantities were recovered from the literature: the cross sections for the excitation energy of 1253.6 eV (Mg Kα) were taken from Ref.32, while the mean free paths of the electrons in the LSMO were calculated according to the TPP-2M formula,[33] and the transmission coefficient of our electron analyser varies as the inverse of the kinetic energy of the emitted electrons. We use the following values for the Sr*3d* and La *3d* core levels: σ_{Sr} = 5.29, σ_{La} = 44.74, λ_{Sr} = 2.0 nm, λ_{La} = 1.0 nm. The interlayer spacing d is assumed to be 0.389 nm. The Sr and La atomic fractions were fitted, following the approach adopted in previous AR-XPS studies, by assuming for Sr an exponential segregation profile, while the La amount was correlated to the Sr value through the formulas:

$$f_i^{Sr} = \alpha + \beta e^{-id/\gamma} \qquad (2)$$

$$f_i^{La} = 1 - f_i^{Sr} \qquad (3)$$

where α is the bulk fraction of Sr in the material (nominally 0.3 in our case), β and γ are two parameters reflecting the excess of Sr across the lattice.
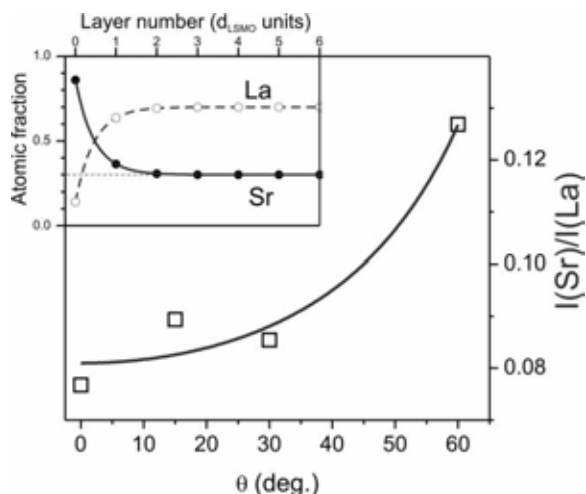
Figure 7. Squares: experimental values of the Sr*3d*/La3d intensity ratio vs. take-off angle. Solid line: best fit corresponding to the atomic concentration profiles of La and Sr shown in the inset. Details of the fitting procedure are reported in the text.

The curve shown in Figure 7 obtained from the fitting analysis, giving the values β = 0.56 and γ = 0.46 nm, denotes a good agreement with the experimental data. The corresponding distributions of the La and Sr atomic fractions, reported in the inset, show the prevailing presence of Sr in the surface layer of the lattice model while the nominal stoichiometry is almost completely recovered since the first underlying layer. This result provides a detailed characterisation of the Sr concentration profile in LSMO films deposited by CSA.

To shed further light on the topmost layers composition, and to support the experimental results, we performed periodic DFT calculations using a mixed Gaussian and plane waves approach (GPW) on several surface models. This theoretical study was part of Dr. S. Ninova PhD thesis.[34] We built surface models with [MnO_2] and [LaSrO] termination layers, shown in Figure 8, where the use of square brackets indicates the topmost layer. The slabs were modelled with a homogeneous distribution of the Sr ions and different termination layers ([MnO_2] and [LaSrO]), as well as with two other different models to reproduce the Sr segregation on the top layer, labelled as [LaSrO-nograd] and [LaSrO-grad], respectively.

2. Assembling magnetic molecules on LSMO the electrode
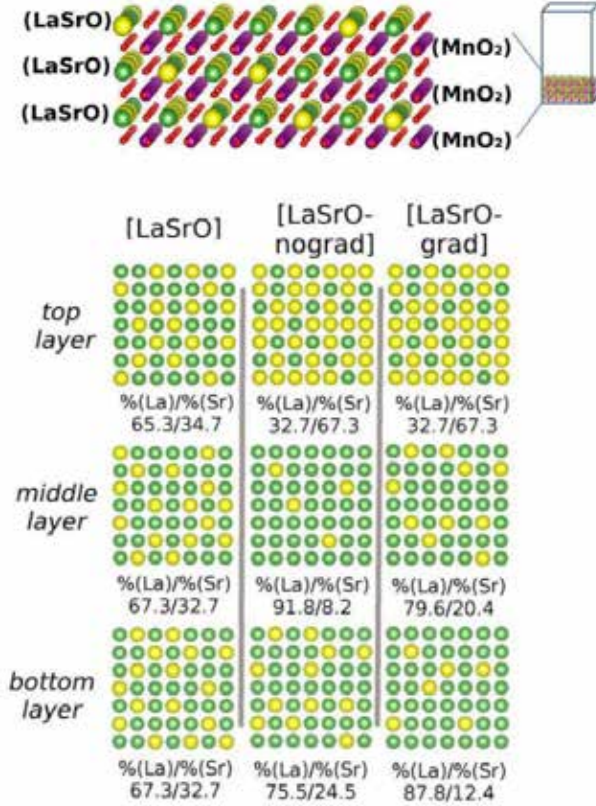
Figure 8. *Upper part*: The surface simulation cell (on the right) next to the model used for bulk and surfaces; *bottom part*: a schematic representation of the Sr ions distribution on the different (LaSrO)-layers. The Sr-ions are in yellow, and the La-ions in green.

The so called energy surface, E_{surf}, can be used as a criterion to give an estimation of the surfaces stability. In our case, surface energies have been computed for all the different surface models using the following equation:

$$E_{surf} = \frac{(E_{slab} - E_{bulk})}{A_{surf}} \qquad (4)$$

where A_{surf} is the surface area and for E_{bulk} we considered the energy computed for a homogeneous Sr bulk distribution in a 7×7×3 periodic supercell. The main indication arising from such a comparison is that the displacement of the Sr ions towards the surface lowers the E_{surf} term (see Table 2). In particular, a Sr gradient distribution presents the lowest E_{surf} term. These results support the experimental data, which suggest that La depletion is an energetic favourable process leading to a Sr segregated surface.

Table 2. Surface energies, E_{surf} computed at the DFT level.

Surface Model	E_{surf} [a], (Jm^{-2})	E_{surf} [b], (Jm^{-2})
[MnO$_2$]	2.853	2.861
[LaSrO]	2.633	2.644
[LaSrO-nograd]	2.369	2.379
[LaSrO-grad]	2.334	2.344

[a] E_{surf} computed without surface dipole correction.
[b] E_{surf} computed with surface dipole correction.

This multi-techniques approach suggests that the description of the terminating layer of LSMO films deposited on NdGaO$_3$(110) substrates by CSA should take into account the presence of a Sr and Mn rich oxide phase on the surface. LEIS can be fruitfully used as an additional tool for the straightforward investigation of the surface elemental composition of this material largely employed as spin valve electrode, thus opening the possibility of a deeper understanding of the properties LSMO-based spintronic devices and for the molecular functionalization of the LSMO films. The Sr segregation, although looking unavoidable in such complex oxide systems, in this case is limited to the topmost layers.

Once defined the chemical surface composition of LSMO spin injection electrode the next step for the realization of a spin valve device based on the chemisorption of magnetic molecules, is the deposition of these systems on the surface. However before the realization of a Spin-Valve device using wet chemistry and magnetic molecules, we considered an additional preliminary study focused on the grafting of simpler diamagnetic systems on surface.

2.2 2 Chemisorption of simple aliphatic systems on LSMO

Before the grafting of NNR and TbPc$_2$ we carried out a preliminary study to find the best procedure of the chemisorption, being the literature on LSMO functionalization[11] limited to only one article. In that work the grafting of an alkyl phosponic acid on LSMO is reported, even if the procedure used is not described in detail. In this thesis we considered as suitable linker groups for LSMO phosphonic acid and dietyl-phosponate moieties. These functional groups can be able to tether LSMO due to their known capacity to chemically bind metal oxides. In particular as

testing systems we employed the diethyl 12-iodododecyl-phosphonate (**1**) and 12-iodododecyl-phosphonic acid (**2**) systems reported in Figure 9. We decided to test an ethyl phosphonate and a phosphonic acid being available several articles describing the use of the latter system as linkers of nanoparticles based on metal oxides.[35–37] Considering that the acid functionalization cannot be compatible this SMMs or NNRs, we decided to test also the less commonly employed ethyl esters of the phosphonic acid.[38,39]
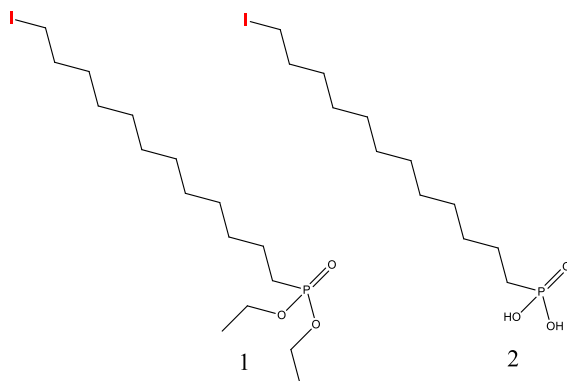

Figure 9. Diethyl-12-iodododecyl-phosphonate (1) and 12-iodododecyl-phosphonic acid (2).

The iodine functionalization present in both the two molecules has been selected in order provide an internal marker in XPS investigations. This aspect is very important because the XPS P*2p* peak at ca. 132.9 eV,[40] that could indicate the chemisorption of the molecule, is hidden by the Sr*3d* peak at ca. 133.5 eV[40] present in the LSMO substrate, making almost impossible the phosphorous identification. On the contrary the I*3d* peak, not overlapping to other signals, can be used to estimate the molecular content at the surface even if no direct indication can be inferred on the occurrence of a real chemisorption.

2.2.1 XPS characterisation of bulk alkyl systems

Before testing the grafting of **1** and **2** on LSMO surface a bulk characterisation of those molecules was planned. However we limited this characterisation only to compound **2** being the former too volatile to be easily measured in bulk without damaging the UHV environment of the XPS chamber. In Figure 10 are reported the XPS spectra of **2** in the bulk phase. In particular from the analysis of the selected regions of interest it is possible to distinguish the peak of P*2p* at 134.2 eV[40] and the presence of iodine peak at 620.1 eV with a spin-orbit splitting(ΔE_{SO}) of 11.5 eV. [40]
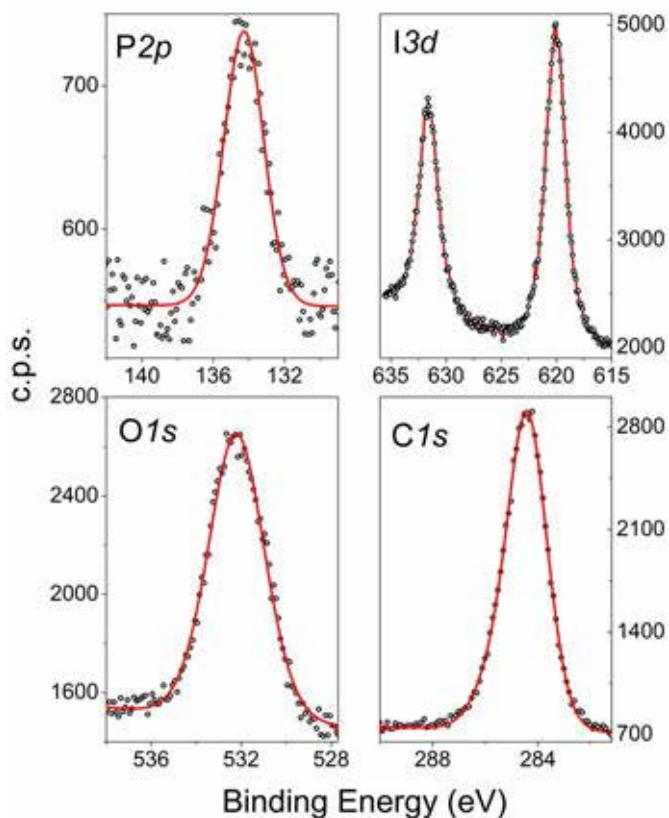
Figure 10. XPS spectra of 2 in bulk phase.

InTable 3 are reported the semiquantitative analysis of **2** drop cast on gold and the percentage are close to theoretical one especially for the P/I ratio.

Table 3. Semi quantitative analysis of 2 in the bulk phase.

	I	C 1s	P 2p		O
	%	%	%	P/I	%
2	7.1	67.4	6.9	0.9	18.7
Theoretical	5.9	70.6	5.9	1	17.6

2.2.2 XPS characterisation of the alkyl monolayers

The following chemisorbed monolayer of **2** on LSMO surface has been characterized by XPS. According to literature indications,[38,39] and locking forward to strategies compatible with the chemical grafting of SMMs and NNRs, we decided to adopt a procedure compatible with the chemistry of the reaction of the phosphonic group with the metal oxide as well as with the molecular stability. We used a 2 mM solution of the desired molecule dissolved in a methanol/dichloromethane 3:1 solution and we maintained the surface in incubation for 20 hours in the dark at 60°C. After the incubation time the surface was rinsed several times with methanol and dichloromethane and sonicated in same solvents mixture for 30 minutes and washed again to remove physisorbed molecules. In order to verify the effect of sonication we characterised the surface before and after the sonication. In Figure 11 are reported the spectra of the P$2p$ and Mn$2p$ regions analysed. Form these data is possible confirm the presence of the molecule at the LSMO surface due the appearance of the iodine components at 620.3 eV and its $\Delta E_{s.o.}$ at 631.8 eV near the Mn$2p$ peak at 642.3 eV.
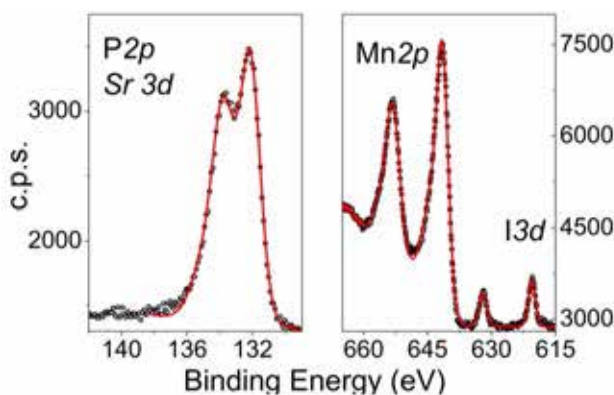
Figure 11. XPS spectra of monolayer of 2 on LSMO before sonication procedure.

As mentioned above the P$2p$ region is covered by Sr$3d$ thus making almost impossible the phosphorous identification and the observation of a chemical shift induced by chemisorption on the LSMO surface. Here below we mention that the sonication phase is fundamental to remove the physisorbed molecules leaving on surface only those strongly interacting with the LSMO substrate. This has been validated by an XPS characterisation performed before and after this treatment (see Figure 12).

Figure 12. XPS spectra in the Mn*2p* and I*3d* region on the pristine LSMO a), before b) and after c) sonic treatment for the 2 compound.

From this characterisation one can notice a decrease in intensity of I*3d* peaks after the sonication confirming the initial presence of physisorbed molecules removed with the sonication treatment. In order to have an estimation of the trend of desorption the ratio between areas of Mn*2p* and I*3d* regions was employed (Table 4). A decrease of ca. 50% of molecules initially present on LSMO surface can be estimated with this analysis, thus demonstrating that the sonication is a fundamental step to remove the excess of molecular layer present on the surface.

The same XPS characterisation has been carried out also for compound **1.** In Figure 13 are reported the regions of interest for a monolayer obtained by incubating an LSMO surface in a 2mM solution of compound **1**. The obtained characterisation evidence strong similarities with the previous case with the appearance of I*3d* peaks at 620.4 eV thus indicating that the two systems are equivalent passivating agents for LSMO.

2. Assembling magnetic molecules on LSMO the electrode

Figure 13. XPS spectra of monolayer of 1 on LSMO before sonication proceedings.
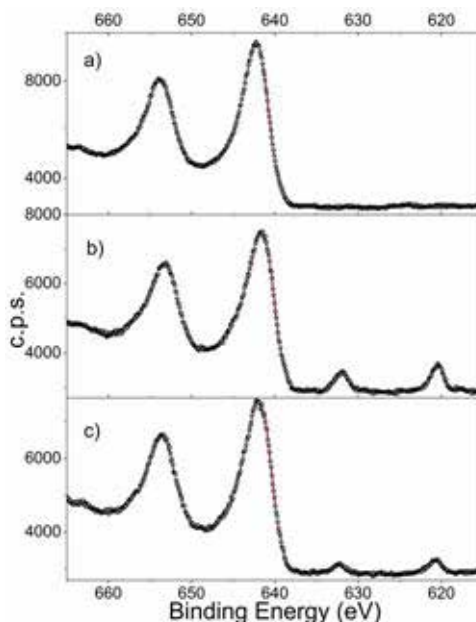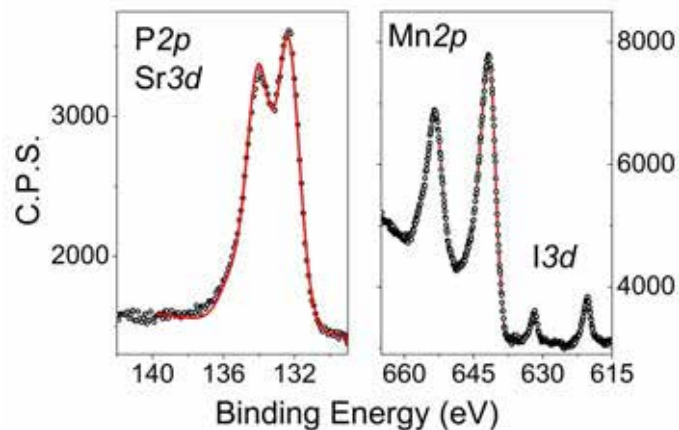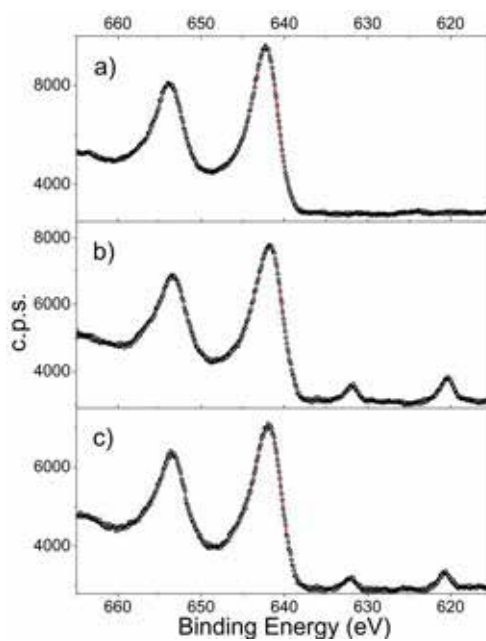

Figure 14. XPS spectra in the Mn*2p* and I*3d* region on the pristine LSMO a), before b) and after c) sonic treatment for the 1 compound.

After the sonication process the intensity peak of the iodine decreases of about 43% demonstrating that this treatment is mandatory also in this case.

Table 4. Areas ratio between areas under the Mn*2p* and I*3d* peaks.

	Before sonication	After sonication
Mn/I areas ratio for **1**	0.33	0.19
Mn/I areas ratio for **2**	0.35	0.18

From this characterisation it is possible to evidence that the chemisorption of compounds **1** and **2** on LSMO surface is equally efficient, thus one can assume that the deprotection of the phosphonic function that usually requires harsh conditions[41] can be avoided. Deposition of fragile systems like SMMs and NNRs functionalised with ethyl phosphonate units seems therefore feasible.

Tentatively it is possible to suppose that the surface catalyzes the elimination of ethyl groups bridged to phosphonate group thanks to LSMO catalytic properties[42] with a progressive impairment of P-OEt bond due to the formation of a bond with the oxide surface followed by the elimination of ethanol.[38,43]

Having characterized the termination layer of the LSMO substrate and having identified a protocol for grafting a molecular layer on it, one can proceed toward the grafting of NNRs systems on LSMO surface in order to start building the first Spin-Valve based on purely radical organic molecules.

2.3 Nitronyl-Nitroxide Radicals chemically grafted on LSMO surface

Due to the magnetic nature of LSMO surface, after the deposition of magnetic molecules, the presence of magnetic interaction between molecule and LSMO can occur. This interaction can alter the spin injection properties of the LSMO in an OSC based spin valve architecture. For this reason we started our activities of functionalization of LSMO with the simplest paramagnetic molecules, organic radicals.

2. Assembling magnetic molecules on LSMO the electrode

Purely organic molecules containing no metallic centres such as organic radicals can serve as an additional spin layer at the interface between a spin injecting electrode and an OSC layer due to the unpaired electron in the radical state of these molecules. This class of molecules, and in particular NNRs, results particularly interesting, since they feature long-range magnetic order[44] at low temperature and it has been theoretically and experimentally demonstrated that partial ordering of the molecules can be achieved also at the nanoscale.[45–47]

The idea was to chemically graft a particular class of NNR, using SAM strategies, able to create a direct bond with the surface. The decision to start from organic radicals to achieve a complete Spin-Valve, is given by the simple synthetic strategy required to realize the desired ethyl phosphonate functionalised NNR following the common strategies mastered in our laboratory. [44,48]
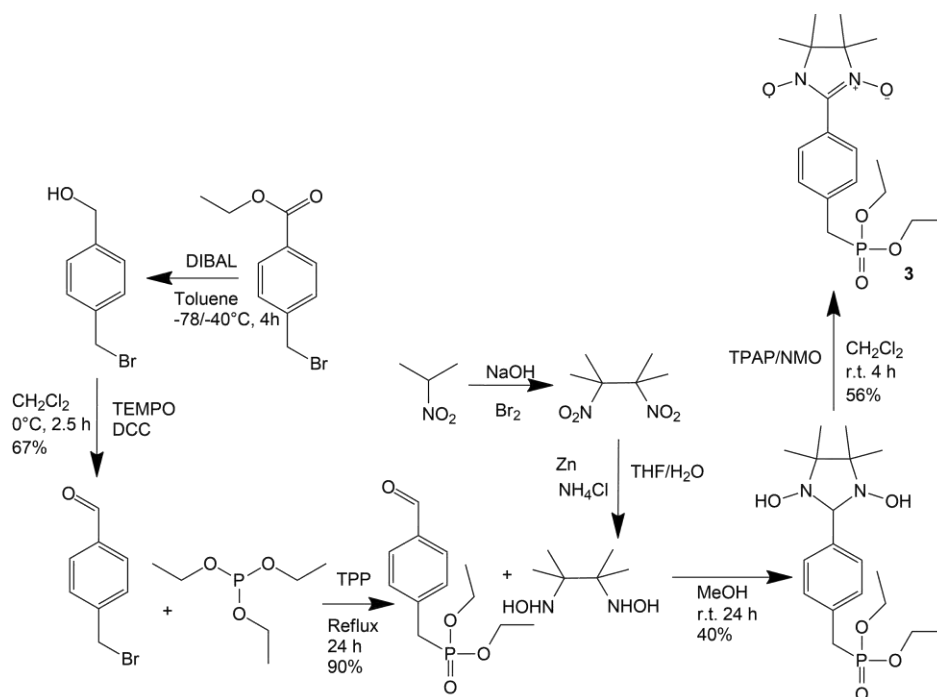
Figure 15. Synthetic scheme for the system (2-(diethyl 4-methylbenzylphosphonate)-4,4,5,5-tetramethylimidazoline- 1-oxyl-3-oxide (3).

The functionalised NNR system (2-(diethyl 4-methylbenzylphosphonate)-4,4,5,5-tetramethylimidazoline- 1-oxyl-3-oxide (**3**) was synthetized by following the procedure described in Figure 15 using the Arbusov reaction[49] in accord to literature procedures[50] to obtain the relative aldehyde followed by the usual steps of

condensation[51] and oxydation[48] to finally obtain the functionalised NNR. The resulting molecule was characterized with XPS, ToF-SIMS, ESI mass spectrometry and with FT-IR.

2.3.1 Bulk characterisations of the functionalised NNR system

The bulk characterisation was carried out using mass spectrometry techniques including ESI-MS and ToF-SIMS (Figure 16). These analyses indicated the presence of the molecular peak at 383.11 m/z with the expected isotopic distribution structure. ESI-MS was performed on a 10^{-5} M solution of NNR in methanol while ToF-SIMS was obtained using a dropcast sample on gold. From the latter characterisation it has been possible to identify fragmentation peaks typical of NNR systems:[45] 391.18 m/z $[M-O+H+Na]^+$, 369.18 m/z $[M-O+2H]^+$, 353.18 m/z $[M-2O+2H]^+$, 281.14 $[M-2Et-3O+4H]^+$.
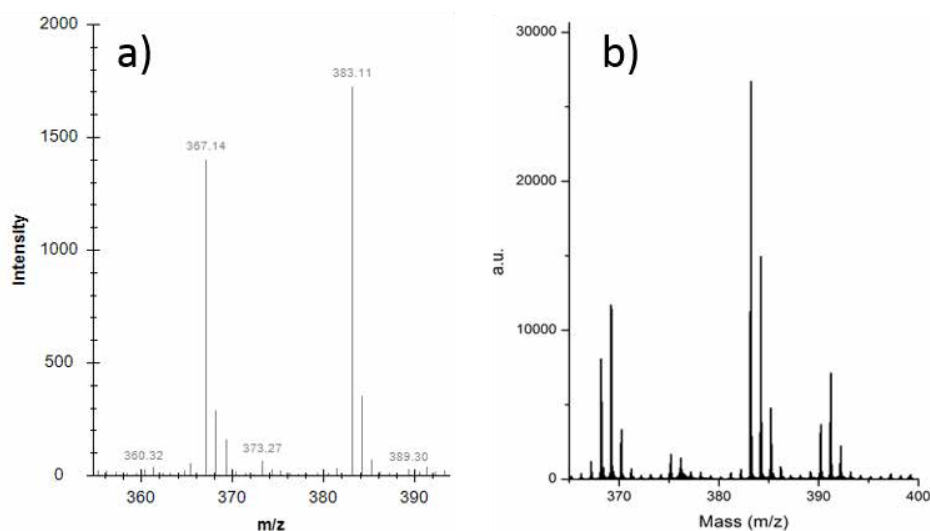
Figure 16. ESI-Mass and positive ToF-SIMS spectra of 3, a) and b) respectively.

The FT-IR spectrum (Figure 17a) presents fingerprint bands of the phosphonate group at: 1231 cm^{-1} ascribable to the stretching (P=O), 1167 cm^{-1} attributed to the stretching (C-P) and 900-1050 cm^{-1} coming from the stretching (P-OR), plus the the stretching N-O at 1393 cm^{-1} confirming the coexistence of the Nitronyl-Nitroxide radical function and of the phosphonate linker group.
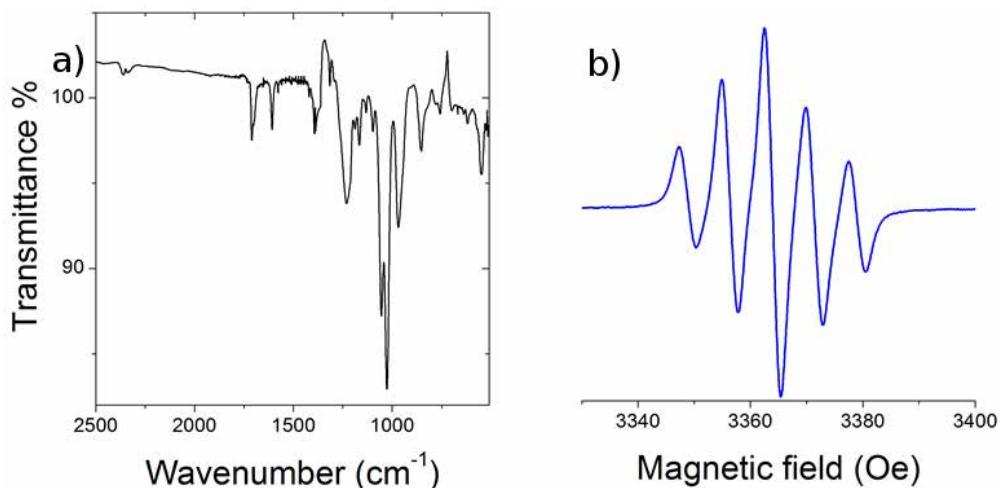
Figure 17. FT-IR spectrum of 3 in nujiol solution a) and room temperature X-band EPR spectrum b) in dichloromethane solution.

The recorded EPR spectrum (Figure 17b) of a 1mM solution in dichloromethane of NNR was in line with what expected for a Nitronyl-Nitroxide function showing the typical five lines shape centred around g = 2.009 with a relative intensity of 1:2:3:2:1 originated by two equivalent nitrogen nuclei ^{14}N (I = 1) with an approximate Hyperfine coupling of 7.5 G.[51,52]
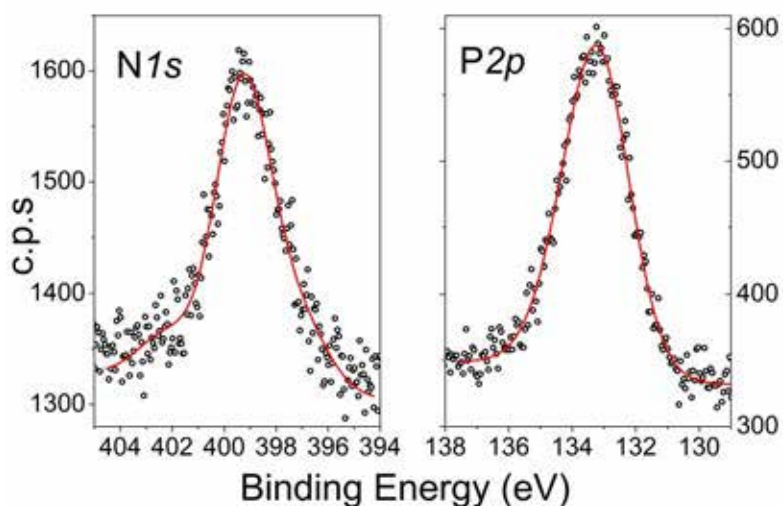
Figure 18. Massive phase N1s, P2p XPS spectra of 3 along with best-fit.

In Figure 18 are reported the XPS bulk spectra of this NNRs obtained by dropcast on gold. An agreement with the stoichiometry of the compound was found. In

particular we notice that the N/P ratio is 1.7 in good agreement with theoretical one of 2. The N*1s* peak was centred at 399.2 eV and the P*2p* peak was at 132.9 eV in agreement with [53,54] literature data.[55,56] The N*1s* region does not overlap with signals coming from the LSMO substrate and was therefore used like the finger print of deposition of NNR.

2.3.2 NNR Monolayer Characterisation

The same protocol employed to graft simple aliphatic chains on LSMO was here adopted; this surface was cleaned by sonication in acetone and 2-propanol for 10 min. In order to increase the density of the monolayer according to our previous experience on NNR[47] we increased concentration of the the incubation solution to 3 mM using a solvent mixture methanol/dichloromethane 3/1 and the surface incubation was carried out at 60°C for 20 hours in the dark to avoid light-induced damage. After the incubation the surface was rinsed several times with methanol and dichloromethane and sonicated in the same solvent mix for 30 minutes to remove physisorbed molecules. All the sample manipulation was carried out using a portable glove bag to minimize the air exposure.
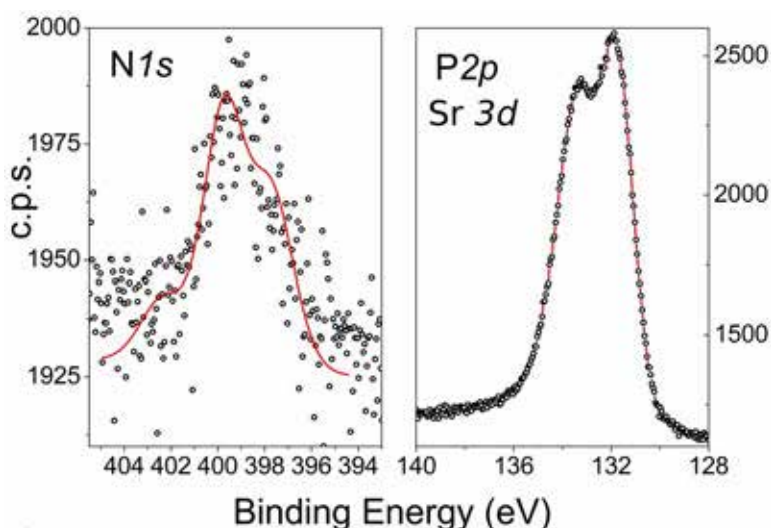
Figure 19. XPS spectra N*1s*, P*2p*/Sr*3d* of the SAM of 3.

In the XPS N*1s* region of functionalised LSMO surface was possible to identify a peak directly ascribable to a NNR functional group, centred at 399.3 eV, indicating

the successful deposition of molecules on surface. [47,55,56] For the deconvolution of the N*1s* peak was necessary to use three components due to a X-ray induced damage.[47] This damage was noticeable also in the massive sample but a negligible amount respect to the monolayer one. [47]

To confirm the deposition ToF-SIMS characterisation was carried out on the functionalised LSMO surface. In Figure 20 are reported the ToF-SIMS spectra of the 270-410 m/z region acquired on the monolayer deposit and in the massive phase. We notice that in the monolayer sample the [M]$^+$ peak at 383.11 m/z is absent that instead is evident in the massive phase. Moreover the peaks distribution at 331.18 m/z is present in the SAM sample while is absent in the massive phase indicating that a new species is formed on surface due to the deposition process. Indeed this distribution comes from a [M-2Et+4H]$^+$ ion and corresponds to a loss of the two ethyl groups of the phosphonic linker group due to a reaction occurred on the surface and indicating a the formation of a chemical bond between the phosphonic function and the LSMO surface. Clearly the NNR interact with the LSMO surface after the loss of the two ethyl groups.
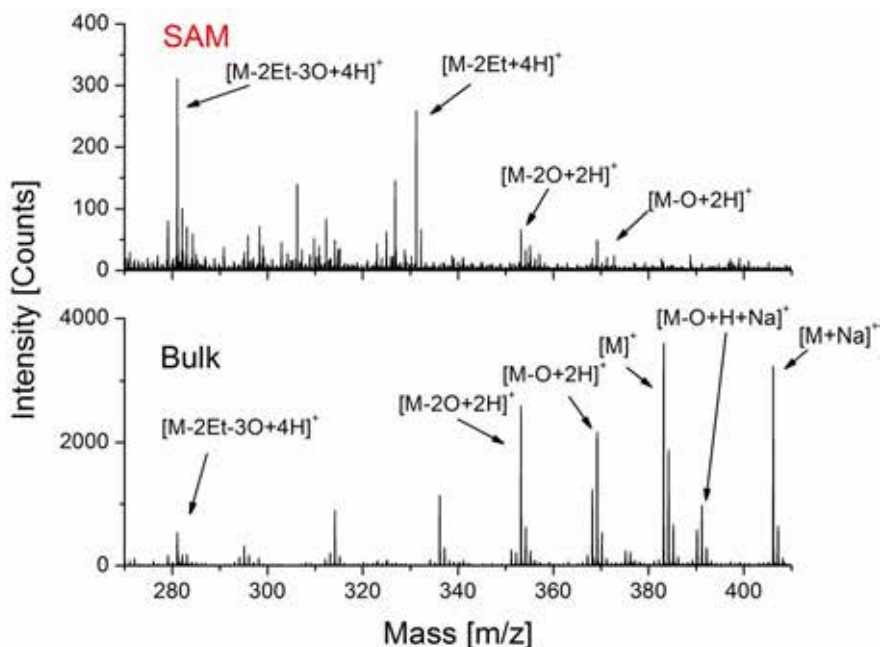
Figure 20. Comparison between SAM and bulk ToF-SIMS spectra in the region 270-410 m/z.

In addiction of those fingerprints other peaks were found confirming the effective chemisorption of functionalised NNR on LSMO surface. ToF-SIMS spectra of the

region from 253 to 261 m/z are reported: we notice that in the monolayer is present a molecular fragment, the ([M-NNR-Et+Sr]$^+$) in which a fragment of the molecule (without the two ethyl group of phosphonate linker) is directly bound to a strontium atom. This evidence confirms an effective chemical bond between molecules and surface.

On the other hand in the same region the bulk sample present another component, assignable to a molecular fragment containing the two ethyl groups still connected to the phosphorous ([C$_{12}$H$_{17}$NO$_3$P]$^+$). The absence of this peak in the SAM sample confirmed the good self-assembly procedure and effective washing protocol carried out.
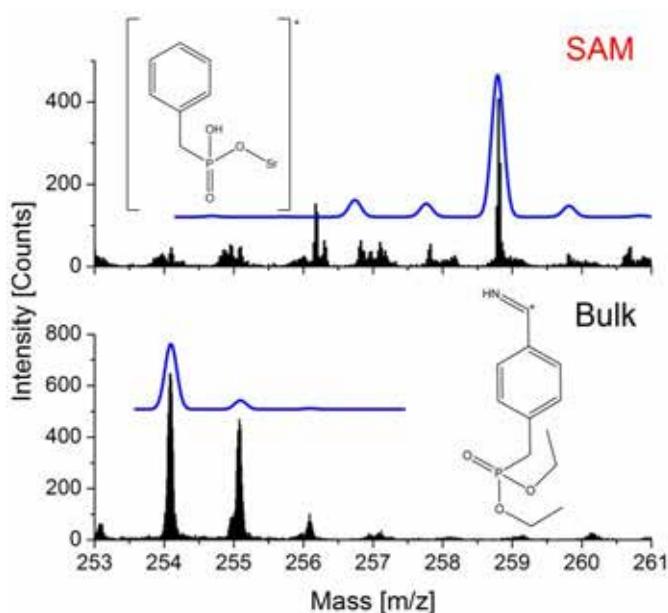
Figure 21. Comparison between SAM and bulk spectra in the region 253-261 m/z; lines above the experimental data represent the theoretical isotopic distribution.

2.3.3 NNR based spin valve

The NNR based spin valve was obtained using the SAM protocol described in previous chapter on a NGO substrate patterned with LSMO as spin injection

electrode. After the SAM incubation, on the functionalised surface 150 nm molecular film of Gaq$_3$ was thermal evaporated followed by deposition of the cobalt electrode (Figure 22).

An additional layer of Al$_2$O$_3$ (thickness 2nm) was interposed between the Co and Gaq3 layers to avoid interdiffusion of the metal inside the OSC and possible creation of short-circuits between the two ferromagnetic layers. LSMO and Co electrodes are characterized by different values of coercive fields in order to observe the spin-valve effect modifying selectively the magnetisation value of the single electrode
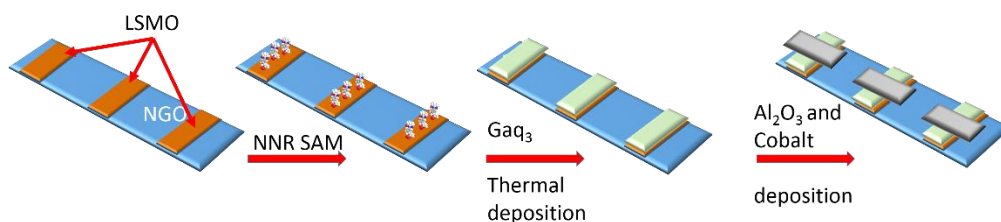
Figure 22. Schematic representation of the realization of the vertical sin valve.

Electric transport measurements on the OSVs have been performed interfacing a source-meter unit (SMU, Keithley 2601A) with a Physical Properties Measurement System (PPMS, by Quantum Design). The SMU can operate as a current source, measuring the current with a maximum resolution of 1 pA or as a current source measuring the voltage with a maximum resolution of 1 μV (in both 2 and 4 wire sensing probe mode).
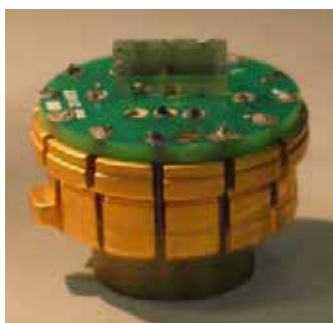
Figure 23. Sample-holder used for electric transport measurements with the device measured mounted on it.

This magneto transport study was part of Dr. G. Cucinotta PhD thesis.[57] The PPMS platform provides the possibility to apply a magnetic fields up to $\pm$ 90 kOe collecting

measurements in a range of temperatures from 1.9K to 350K. The SMU unit was connected to a pinned-head placed inside the variable temperature chamber of the PPMS as shown in Figure 23.

The device was constituted of a substrate (10mm x 5mm) where on it three organic spin valves (OSVs) are present. The OSVs are linked to pinholes at the base of the puck by means of an on purpose designed printed circuit board on which the OSVs are connected through gold wires. Once inserted in the chamber of the PPMS pinholes present on puck base assure electric connection with the PPMS pinned-head.
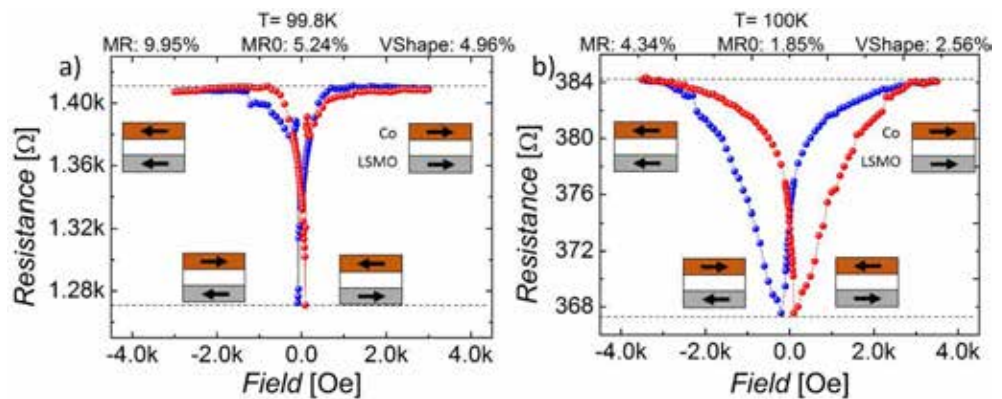
Figure 24. Comparison between the magneto-resistance of a "standard" spin valve (a) and one modified with NNR (b). Measurements are taken at 100K.

A schematic representation of the magnetic moments of the electrodes of the device is given in correspondence of the maxima and minima values of resistance. The magnetic field was directed in parallel to the device surface, while the electric measurements were collected in 2-wire sensing mode maintaining a fixed electric potential difference of 100 mV between the LSMO and Co. In Figure 24b the magnetoresistance measurement obtained at 100 K on an OSV with NNR is reported. A spin-valve effect was evident and a high resistance value, when both the magnetic moments of the electrodes are aligned with the magnetic field, was detected. Once the magnetic field reaches the value of the LSMO coercive field (≈±2.5 kOe), the device in an antiparallel configuration of the magnetic moments of the electrodes present the lowest resistance value. On continuing to decrease the field, once both the magnetic moments are again aligned to the external field, the resistance of the device returns again to its highest value. The magnetoresistance can be quantify as:

2. Assembling magnetic molecules on LSMO the electrode

$$MR = (R_{\uparrow\uparrow} - R_{\uparrow\downarrow}/R_{\uparrow\uparrow}) * 100 \hspace{2cm} \text{(5)}$$

where $R_{\uparrow\uparrow}$ and $R_{\uparrow\downarrow}$ are the resistances of the device when the magnetic moments of the electrodes are parallel and antiparallel respectively. This preliminary experiments demonstrate the presence of a spin-valve effect in OSV device comprising magnetic molecules and this represents the first report to the best of our knowledge. A comparison between standard OSV without magnetic molecules layer and the OSV with functionalised surface is reported in Figure 24, a) and b) respectively, both measured at 100K. The presence of a magnetic molecules layer on LSMO electrode seems to affects the shape of the field dependence of the resistance. In particular the value of magnetic field required to restore the high resistance state which is related to the change of the magnetisation at the interface with LSMO. In the device without NNR layer the magnetisation at the LSMO/Gaq3 is switched at H≈1 kOe and for the modified surface device the magnetic field required increases going to ≈2.5 kOe.

This result represents a confirmation of how important interfaces are in the transport properties of organic based devices opening the development of new OSVs based on magnetic molecules.

2.4 The terbium bis(phthalocyaninato) complex.

After the successful deposition of the simple NNR systems on the LSMO surface we moved to a more complicated magnetic molecule, a Tb-based SMM.

The Terbium bis(phthalocyaninato) complex ($TbPc_2$) represents the first example of mono-nuclear metal complexes with a SMM behaviour;[58–60] it is composed by a terbium ion inserted inside two phthalocyanine (Pc) ligands. The Pc are rotated with respect to each other by ca. 45° and the Tb ion is eight-fold coordinated by eight Nitrogen atoms. This peculiar structure induces, acting on the crystal field of the rare earth, a huge barrier for the reversal of the magnetisation with magnetic hysteresis observed at temperatures as high as 15 K.[61] For this reason $TbPc_2$ has been included in the molecular candidates for the realization of molecular spintronic devices based on SMMs.[9,62–65]

$TbPc_2$ can be synthesised as neutral $[TbPc_2]^0$ and anionic $[TbPc_2]^-$ powder.[66] By chemical oxidation of the neutral system[67] or by electrochemistry[68] is also possible

to achieve the [TbPc$_2$]$^+$ compound which is however rather unstable and can be stabilised using specific counterions.[68] In all the three different species (-/0/+) the oxidation number of the metal ion does not change: the extraelectrons/holes are localized on the ligands.[69] The Tb^{3+} ion has a ground state with L=S=3 and J=6. The two phthalocyanine ligands induce an exceptionally high energy gap between the ground pseudo-doublet J$_z$=$\pm$6 and the next higher doublet (J$_z$=$\pm$5), of the order of several hundreds of K.[70] This gives rise to a strong easy axis anisotropy with the axis perpendicular to the phthalocyanine planes. The neutral form [Pc$^{\bullet-}$Tb^{3+}Pc^{2-}]^0, however, has a hole delocalized on the two ligands, which provides an additional S=1/2 spin. On the other hand the anionic compound [Pc^{2-}Tb^{3+}Pc^{2-}]$^-$ has closed p shells because the two Pc ligands are doubly negatively charged and so only the magnetic moment of the Tb ion gives a contribution. The barrier opposing the reversal of the magnetisation changes with the oxidation state.[68] Ishikawa and Takamatsu [71] have theorised that the two forms [TbPc$_2$]$^{+/-}$ have different interplanar distance between the two Pc ligands. An increase of the crystal field applied to the Tb^{3+} is expected upon oxidation due to the reduction of bond length between N and Tb^{+3} of ca. 0.03 Å for the [TbPc$_2$]$^+$ state.

Standard magnetometry and magnetic circular dichroism (MCD) with visible light experiments on the three oxidation states , have shown the presence of a butterfly-shaped hysteresis, [68,72,73] originated by efficient tunnelling in zero field. Vitali *et al.*[74] performed scanning tunneling microscopy and spectroscopy experiment on isolated [TbPc$_2$]^0 molecules deposited on the Cu(111) surface and showed that the 4*f* states of the [TbPc$_2$]^0 molecules does not interact with the metal, while the ligand electronic states are heavily perturbed by the hybridization with the metal states till the disappearance of the ligand spin.

The chemical and thermal stability of the LnPc$_2$ systems (with Ln=Lu, Tb) allows the [TbPc$_2$]^0 to be thermal sublimated in high vacuum (HV) and ultra-high vacuum (UHV) conditions.[75,76] It is well known that in thin film of LnPc$_2$ sublimated on pure metal surfaces[74,77–79] the molecules lay flat where the two phthalocyanine are parallel to the surface.

This property, combined with the fact that these molecules tend to lie flat on metallic surfaces and graphite has prompted a large number of STM studies to probe the different orbitals. [80] The magnetic characterisation of hybrid surface has been mainly carried out using X-ray circular dichroism (XMCD), thanks to the high

sensitivity (in the order of sub-monolayer) and the high elements selectivity of this synchrotron-based technique.[81–83] The XMCD derived magnetisation curves acquired in sub-monolayer or monolayer samples thermally deposited on metal surfaces showed the absence of hysteresis.[76,77,84,85] On the other hand in a 200 nm thickness film the hysteresis opening is recovered.[76] In the thick film there is a different trend. The preferential orientation is a "standing-up" geometry were the Pc are perpendicular to the surface.[76] This type of phenomena is known for CuPc molecules were a reorientation process occurs during the films deposition. CuPc molecules lose their surface parallel orientation on Au(111) substrates after only 3nm and the perpendicular orientation is reached after ca. 10nm.[86] Hofmann *et al.*[87] using implanted muons at variable energy (from 0eV-30keV) demonstrated that a variation of molecular spin correlation time occurs in a thick film of $TbPc_2$ (ca. 100nm) on Au (111) depending on the distance from the gold surface. These changes in the magnetisation dynamics seems to correlate with structural changes induced by the re-orientation of the molecules, showing an important role of packing in the magnetic behaviour of this system.

Interestingly a molecule-surface antiferromagnetic (AF) interactions has been observed in sub-monolayer film of $TbPc_2$ thermally sublimated on nickel,[85] and in thin sublimated films on manganese.[84]

We have therefore decided to investigate the magnetic behaviour of thin films sublimated and chemically grafted on LSMO to evidence the presence of magnetic interaction with the ferromagnetic oxide. This characterisation was performed as preliminary steps for the use of the $TbPc_2$ as organic layer in spin valve devices.

2.4.1 Thermal evaporation of unfunctionalised $TbPc_2$ on LSMO

The LSMO surface corrugation does not allow an STM characterisation of sub-monolayer $TbPc_2$ films because the dimension of molecules are comparable with the dimension of "lentils" of LSMO. For this reason we focused our interest on the spectroscopic characterisation of this hybrid molecular-inorganic system with the aim of comparing the behaviour of $TbPc_2$ on this magnetic surface extending previous studies of the effect of the coupling of magnetic molecules on magnetic surfaces.[4,84,85,88–90]

The X-ray absorption spectroscopy characterisation of a thin TbPc$_2$ molecular layer deposited *in situ* was performed at the SIM-X11MA beamline at the Swiss Light Source (SLS) synchrotron facility. The LSMO substrate was a 12 nm LSMO film grown on strontium titanium oxide (STO) and was cleaned using the earlier reported procedure (Chapter 2.1).
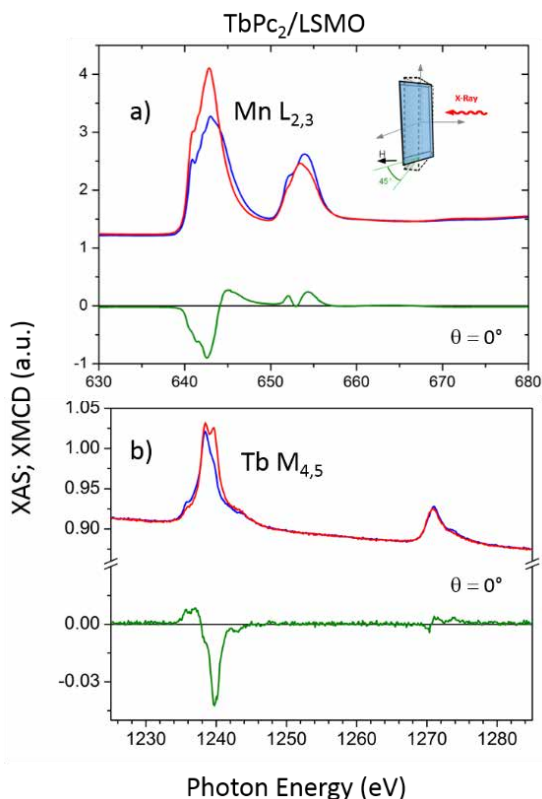
Figure 25. XAS and XMCD spectra of TbPc2/LSMO at the indicated edges measured, at T = 2 K, H = 3 kOe.

The molecular sublimation was carried out using the thermal evaporator described in Chapter 5.7.3. The XAS setup was equipped with a total electron yield detector and both linearly and circularly polarisations were employed.

The magnetic field was applied along the photon propagation at variable angle with the normal to the surface. The investigation of the hybrid surface was performed at both the Mn L$_{2,3}$ and Tb M$_{4,5}$ edges. The XAS spectra acquired at the Mn L$_{2,3}$ edges under 3 kOe of magnetic field and using the two circular polarisation (left, σ$^+$ and right, σ$^-$) at θ = 0° are reported in Figure 25a. The XMCD spectrum reported in

2. Assembling magnetic molecules on LSMO the electrode

Figure 25a has a similar features for LSMO films reported in the literature.[91,92] In Figure 25b is reported the XMCD spectra at Tb $M_{4,5}$ edges showing the expected strong dichroic signal of $TbPc_2$.[76] Linearly polarized light was also used in order to get information about the orientation of the molecules with respect to the surface.

The XNLD spectrum, obtained as the difference between vertically and horizontally polarized light absorption, both measured at $\theta = 45°$ (Figure 26), showed a small dichroic contribution indicative of a partial molecular orientation on the surface. By comparison with literature reports[76] it is possible to point out that this process induces a slightly preferential arrangement of the molecules with the easy axis of magnetisation in the plane of the surface, as expected for a standing configuration of the Pc ligands. This geometry in agreement with the literature data of simple metal-phthalocyanines on oxides.[93]
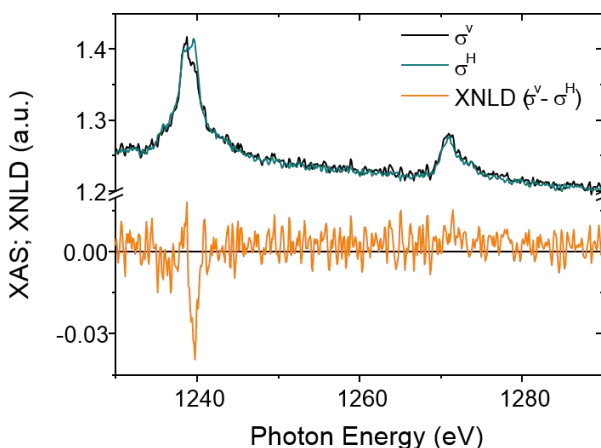
Figure 26. . XAS and XNLD spectra of TbPc2/LSMO at the indicated edges measured, at T = 2 K, H = 3 kOe.

To have a complete characterisation of the magnetic behaviour of this hybrid system the field dependence of the XMCD signal at the L_3 edge of Mn was recorded at $\theta = 0°$ and 45°. The hysteresis loops at Mn L_3 edge reported in Figure 27a show the expected angular dependence for a film with an in-plane magnetic anisotropy. On the other hand the hysteresis loops at the M_5 edge of Tb reported in Figure 27b show a small butterfly-shaped opening. This behaviour is similar to that observed for this type of molecule in the bulk phase or thick films.[72,76] The XMCD signal recorded at $\theta=45°$ is slightly larger than at $\theta=0°$, in agreement with the XNLD results. Unlike results obtained on other ferromagnetic substrates,[84,85,90] no observable

antiferromagnetic coupling (AF) between TbPc$_2$ molecules and the LSMO was detected with no correlation between the TbPc$_2$ hysteresis loops and those of the substrate (Figure 27a and b).

The collected data on the TbPc$_2$ sublimated on LSMO evidences that a preferential perpendicular orientation is obtained. This hybrid surface is characterized by the presence of a smaller butterfly shaped hysteresis loop respect to the one observed in the bulk phase. This effect has been previously observed in amorphous sample[72] and in diamagnetic glassy matrices[68] and can be directly ascribed to a different organization of molecules on the surface respect to the one occurring on bulk deposits or to an interaction of the deposited molecules with the surface.
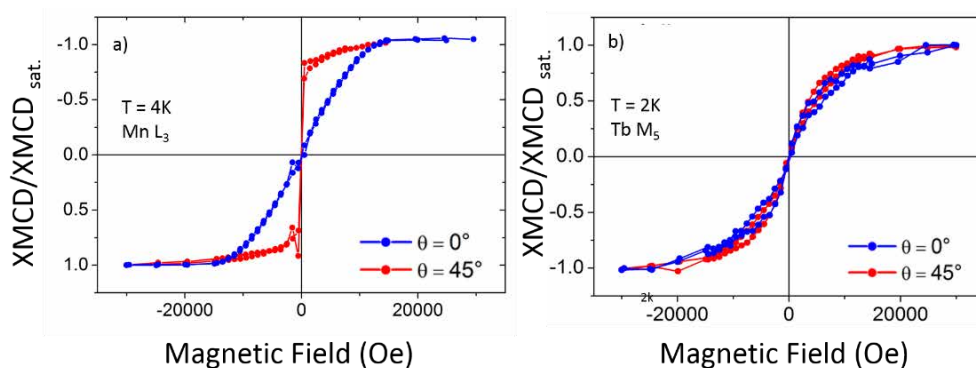
Figure 27. Field dependence of the XMCD signal measured at the maximum of the dichroic signal at the indicated edge for TbPc2/LSMO

Thus an alternative strategy has to be attempted, based on the chemical grafting of molecules using wet chemistry. In order to adopt this alternative approach molecules must be modified to promote specific interaction with the substrate and must be soluble and stable in the solvent selected for the grafting.

2.4.2 Grafting TbPc$_2$ functionalised systems on LSMO

In order to chemisorb TbPc$_2$ on LSMO we adopted a similar strategy respect to the one described earlier for NNRs. The TbPC$_2$ molecule suitable for the grafting, is constituted by a normal complex functionalised with a phosphonate group that is able to connect on metal oxides and hence on LSMO.

2. Assembling magnetic molecules on LSMO the electrode
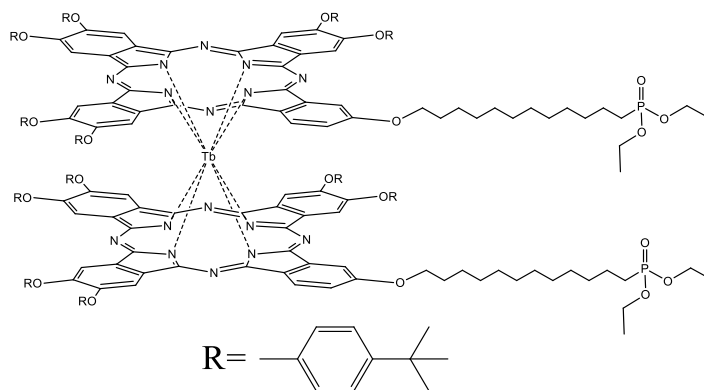
Figure 28. TbPc₂(PO₃Et₂)₂ chemical structure.

The chemical structure is reported in Figure 28 where the two phosphonate groups are connected directly with the two phthalocyanine ligands (hereafter TbPc$_2$(PO$_3$Et$_2$)$_2$).

This molecule has been designed and synthetized in the laboratories of Prof. E. Dalcanale at the University of Parma, who provided the material used in this thesis to perform bulk magnetic characterisations and grafting tests described in the following.

2.4.3 Bulk Magnetic Characterisations

Magnetic characterisation, performed with standard AC susceptometry, clearly indicates the SMM behaviour of the complex in its bulk phase. As already observed for other TbPc$_2$ complexes [72,76,89,] SMM behaviour with the presence of hysteresis in the magnetisation curves below 15K characterizes the new TbPc$_2$(PO$_3$Et$_2$)$_2$ derivative (Figure 29), thus indicating that the functionalization does not alter significantly the SMM behaviour of this double decker system.
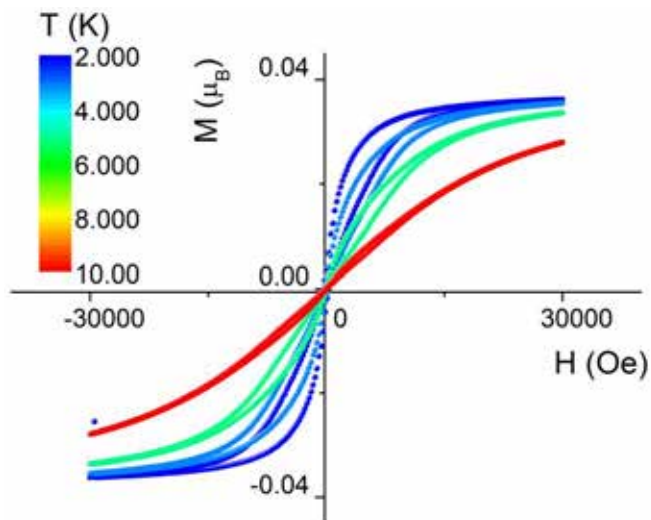
Figure 29. Magnetisation of [TbPc₂(PO₃Et₂)₂] as a function of the applied field at different temperatures.

A better estimation of the eventual changes in the hysteretic behaviour can be achieved by plotting the difference in the magnetisation scans (see Figure 30) obtained for increasing field M(H↑) and decreasing field M(H↓):

$$\Delta M(H) = |M(H \uparrow) - M(H \downarrow)| \qquad\qquad (6)$$

By comparing the integral of those plots with an analogous characterisation performed on the pristine $[TbPc_2]^0$ complex (Figure 31) it results evident that the functionalization induces a slight alteration of the SMMs properties: the irreversibility increases monotonically on decreasing the temperature, in contrast to the pronounced maximum observed for $[TbPc_2]^0$. The latter represents however an anomaly that we can tentatively assign to intermolecular interactions through the radical ligands that are strongly reduced in the bulky functionalised derivative.

2. Assembling magnetic molecules on LSMO the electrode
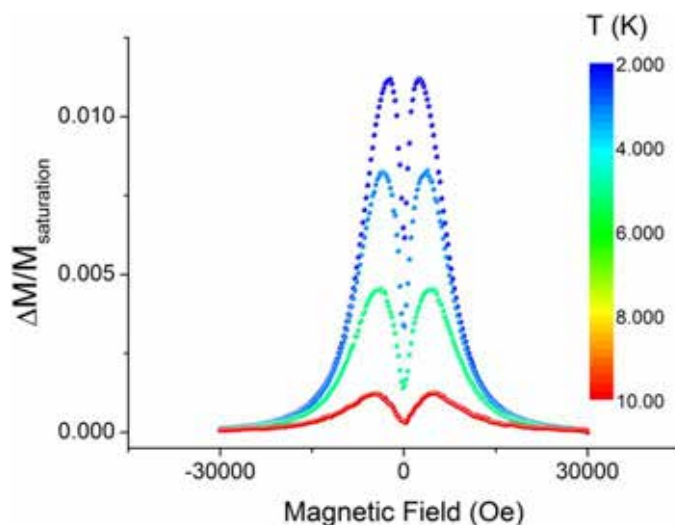
Figure 30. Hysteresis opening estimated as ΔM/Msaturation according to the procedure described in the text.

A more clear picture can be achieved by AC susceptometry. Zero static field AC susceptibility measurements as a function of temperature are shown in Figure 32. χ''T is characterised by a frequency dependent peak in the out-of-phase component occurring at relatively high temperatures. The extended Debye model[94] was adopted to analyse these data in the range 0.5Hz -10KHz allowing to extract the relaxation time, τ.
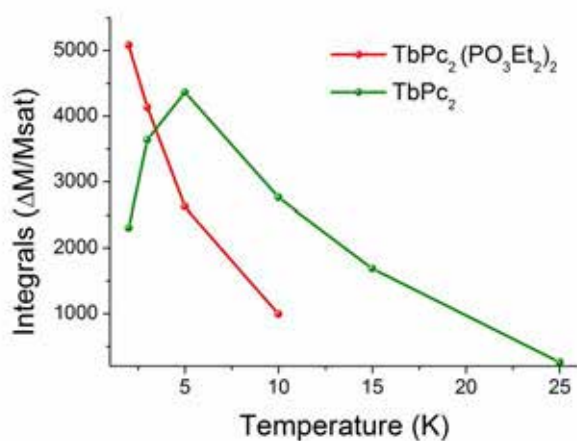
Figure 31. Comparison between the area under hysteresis curves as a function of the temperature for TbPc$_2$(PO$_3$Et$_2$)$_2$ and for microcrystalline TbPc$_2$.[72]
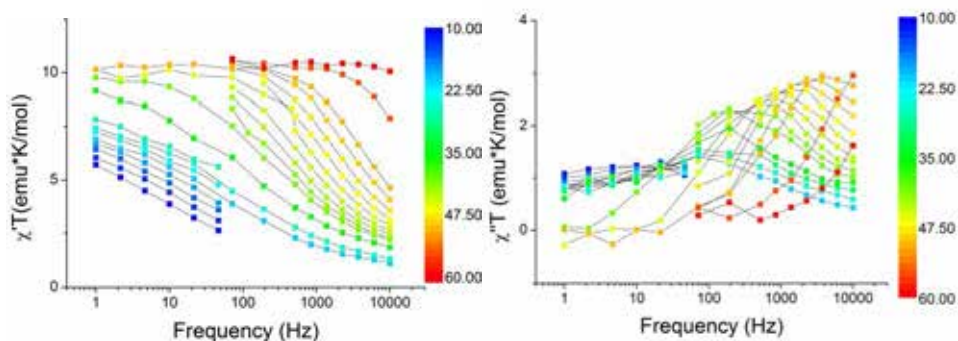
Figure 32. Frequency dependence of the χ'T product and χ''T product (left and right, respectively) as a function of temperature in zero static field left and right respectively.

The temperature dependence of τ is shown in Figure 34. A linear behaviour in the $\ln(\tau)$ *vs.* $1/T$ plot is observed at zero static field in the high temperature regime, $T>$ 40 K, providing the parameters τ_0 = 1.68±0.39*10^{-10}s and Δ/k_B=614±11 K for the best fit with the Arrhenius law, $\tau = \tau_0\exp(\Delta/k_BT)$.

The estimated energy barrier in the thermally activated process, 614 ($\pm$11 K) is smaller than that found for the crystalline phase of TbPc$_2$ (965 K)[95] but close to the value observed in similar conditions for amorphous unfunctionalised TbPc$_2$ system (856 K)[26], in agreement with the amorphous character of **TbPc$_2$(PO$_3$Et$_2$)$_2$** sample
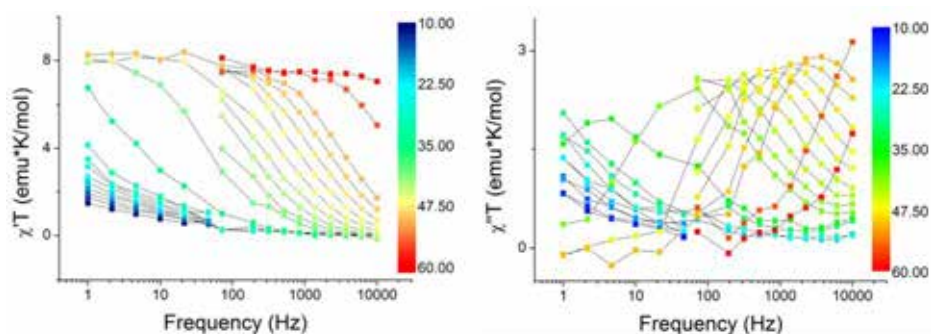
Figure 33. Frequency dependence of the χ'T product and χ''T product (left and right, respectively) as a function of temperature at 5000 Oe static field.

Below 40 K the relaxation becomes temperature independent, indicating the onset of a tunnel mechanism of relaxation, with a significant increase of the width of the distribution of the relaxation times.

55
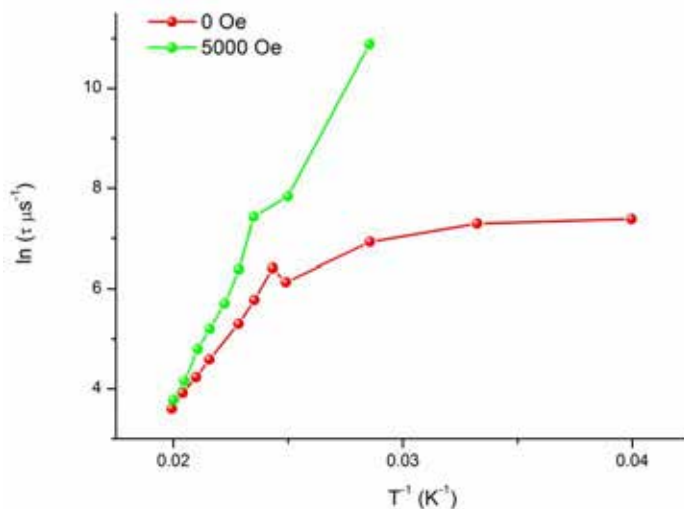
Figure 34. Arrhenius plot of the data extracted from AC measurements in zero field and in 5000 Oe static field.

The application of a static field of 5000 Oe (Figure 33) provides comparable high temperature behaviour as shown in Figure 34, but significantly affects the magnetic relaxation below 40 K, suppressing the tunnelling mechanism with τ exceeding the accessible timescale of the AC susceptometer. A single distribution of τ is observed in static field because distortions from idealised D_{4d} symmetry present in this amorphous material are less relevant when resonant quantum tunnelling is suppressed by the application of an external field. This AC characterisation reveals a significative effect of the tunnelling mechanism in the slow dynamics of the magnetisation of this system in zero field, in analogy to what previously found in the case of other functionalised and unfunctionalised TbPc2 complexes.[95,96]

2.4.5 XPS and mass bulk characterisation

A MALDI-ToF/ToF mass analysis was performed on the $TbPc_2(PO_3Et_2)_2$ complex (Figure 35) and an isotopic distribution patter in perfect agreement with the expected one and centred at 3603 m/z was found.

In Figure 36 is reported the UV-Vis spectrum of $TbPc_2(PO_3Et_2)_2$ solution in chloroform.
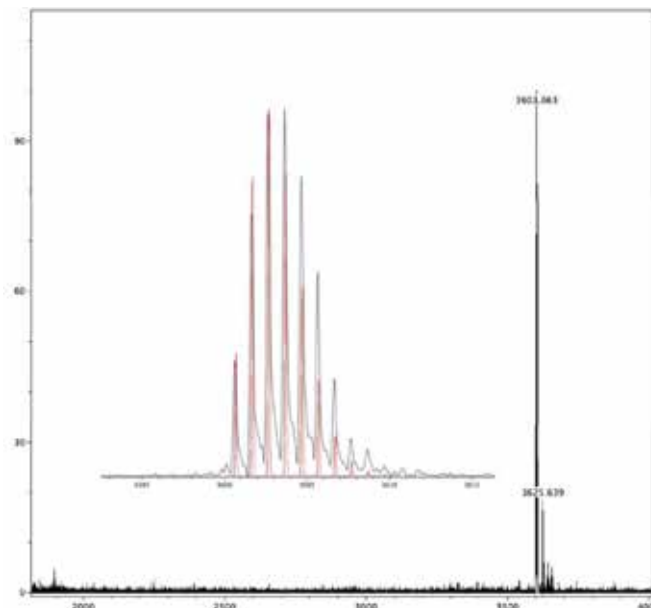
Figure 35. MALDI-ToF/ToF spectrum of TbPc$_2$(PO$_3$Et$_2$)$_2$ complex.

From the spectrum in Figure 36 was possible to notice the promotion of an electron from the first semi-occupied molecular orbital (SOMO) to the second LUMO and from the second fully occupied HOMO to the first LUMO with the Q band at 680 nm. At 330 nm and 360 nm the spectrum shows a typical split Soret band, resulting from the electronic transitions from the third occupied HOMO to the first LUMO. At 469 nm and 926 nm were found the two weak π-radical bands due to electronic transitions from the SOMO orbital to the degenerate LUMO.[97]
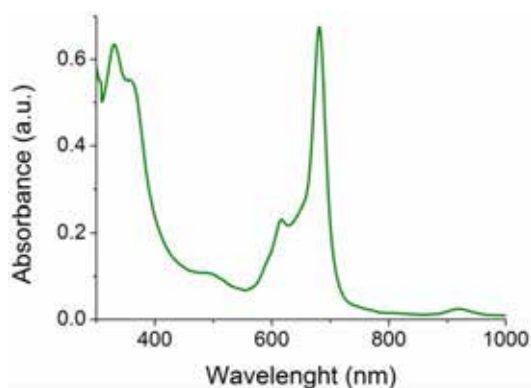
Figure 36. UV-Vis absorption spectrum of TbPc$_2$(PO$_3$Et$_2$)$_2$ in chloroform.

57

2. Assembling magnetic molecules on LSMO the electrode

The bulk phase of the TbPc$_2$(PO$_3$Et$_2$)$_2$ complex was characterised also by X-ray Photoelectron Spectroscopy (XPS) on a drop-cas sample on gold to acquire a reference for further studies on thin films. Tb$3d_{3/2}$, N$1s$ and P$2p$ signals have been included in a semiquantitative estimation of the element content (while C$1s$ and O$1s$ have been excluded being affected by spurious contaminations being the sample prepared *ex situ*). Regarding the Tb$3d$ region of interest, only the Tb$3d_{3/2}$ component can be used in this analysis, because the Tb$3d_{5/2}$ overlaps with carbon Auger lines KVV at 1233 eV (using Al monochromatic source as needed to reach this energy region). Even considering the experimental error of XPS and the presence of adventitious carbon contamination in this bulk sample, we can assert that the stoichiometry is respected. In Table 5 the XPS estimated atomic percentages and atomic ratios are reported.

Table 5. Theoretical and XPS estimated atomic percentages and ratios for TbPc$_2$(PO$_3$Et$_2$)$_2$ complexes in bulk.

	Tb$3d_{3/2}$	N$1s$		P$2p$		
	%	%	N/Tb	%	P/Tb	P/N
TbPc$_2$(PO$_3$Et$_2$)$_2$	5.1	79.9	15.6	15	2.9	0.18
theor.	5.3	84.2	16	10.5	2	0.13

The experimental atomic ratios are in agreement with the theoretical ones and in particular the ratio N/Tb clearly confirms that the molecular system is intact. As can be noticed a small excess of phosphorous in the bulk is present that could be originated by small fraction of precursors as contaminants in the measured sample.

The Tb$3d_{3/2}$ peak is centred at 1276.5 eV in agreement with literature data,[98] the N$1s$ is centred at 398.2 eV and in not shifted if compared with a literature data of 398.1 eV found on similar complexes[99] and is in line with a neutral TbPc$_2$ system.[98] P$2p$ and C$1s$ peaks was at 133.5 eV and 284.6 eV respectively, as expected for this type of organic compounds.[56]
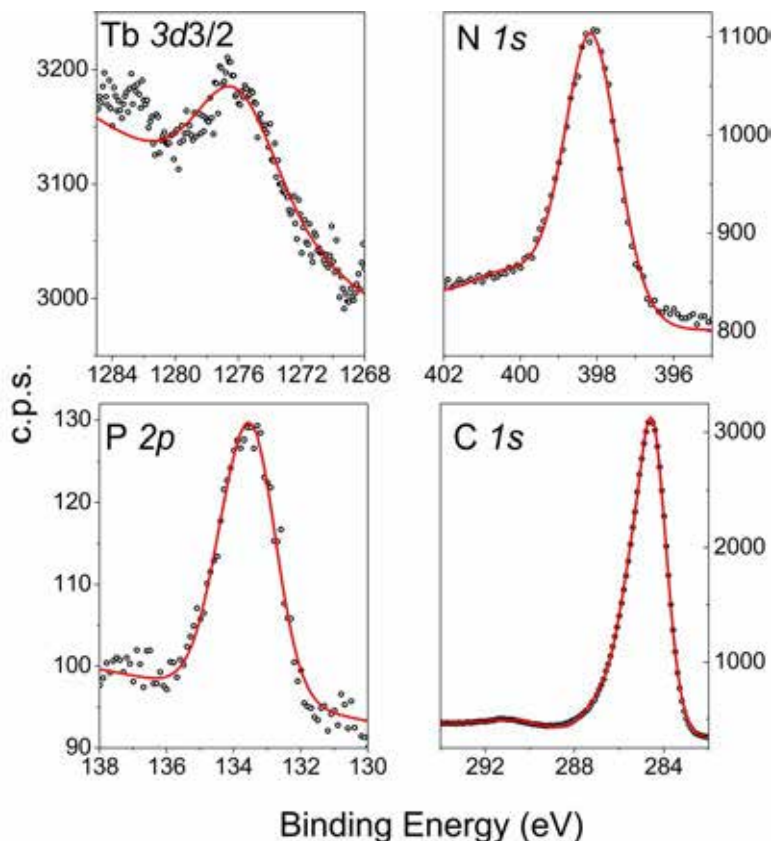
Figure 37. Tb$3d_{3/2}$, N$1s$, P$2p$ and C$1s$ XPS spectra of the bulk phase of TbPc$_2$(PO$_3$Et$_2$)$_2$ with best-fit components.

2.4.6 XPS Monolayer Characterisations

To deposit the functionalised TbPc$_2$ derivative on LSMO we slightly modified the procedure previously described for simple organic phosphonate molecules (See chapter 2.2).

Initially we tested a more rigorous cleaning procedure for LSMO based on oxygen plasma cleaning for 3 minutes at 15 W with a base pressure of 2×10^{-1} mbar in oxygen in order to promote a more efficient cleaning on the surface. After this treatment the LSMO has been immersed in a 2mM TbPc$_2$(PO$_3$Et$_2$)$_2$ mix of 3:1 Methanol/Dichloromethane and maintained in incubation under nitrogen flux at 60°C for ca. 20h in the dark. After that the slab was rinsed several times with pure

solvents, sonicated in the solvents solution for 30 minutes, rinsed a second time and dried under nitrogen flux. To avoid air exposure we used a portable glove bag filled with nitrogen gas.
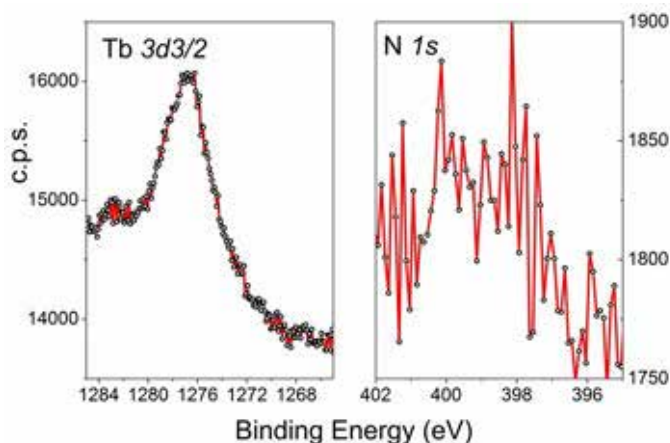
Figure 38. Tb $3d_{3/2}$ and N$1s$ XPS spectra of the SAM of TbPc$_2$(PO$_3$Et$_2$)$_2$ on LSMO

In Figure 38 are reported the most relevant XPS regions investigated after the incubation process. As anticipated the P$2p$ region is covered by the Sr$3d$ component thus making impossible the precise identification of peak position and a semiquantitative estimation of P$2p$. We notice that the peak relative of N$1s$ is very low in intensity unlike the terbium $3d_{3/2}$, where the peak is very high in intensity and it is centred at 1275.6 eV. The N/Tb ratio resulted to be close to zero, thus strongly reduced respect to the one observed in the bulk phase.

This dramatic evidence can be explained by considering i) an instability of the molecules in presence of the surface in the reaction condition or ii) a selective adsorption of contaminants onto the LSMO surface resulting not efficiently functionalisable with the designed molecules. A tentative justification of this anomaly can be due to the treatment with oxygen plasma and to a consequent activation of surface degradation process despite the high stability of terbium complex.

In order to overcame this problem we tested an alternative deposition procedure for TbPc$_2$(PO$_3$Et$_2$)$_2$ avoiding the oxygen plasma.
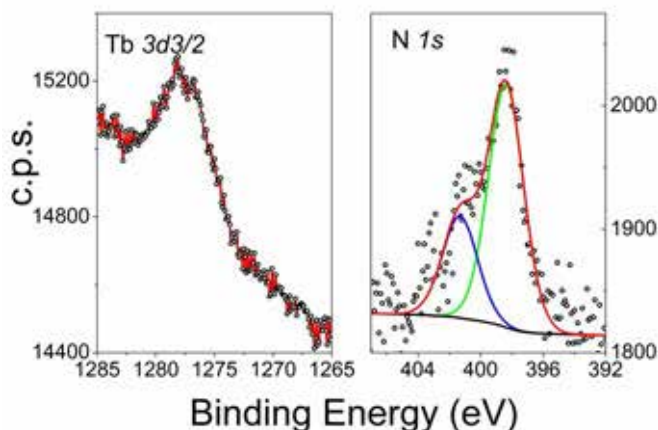
Figure 39. Tb *3d*₃/₂ and N*1s* XPS spectra of the SAM of TbPc₂(PO₃Et₂)₂ on LSMO obtained without oxygen plasma treatment.

In Figure 39 are reported the regions of interest of XPS spectra of a sample obtained without oxygen plasma treatment of LSMO surface. The N*1s* region shows a much stronger peak compared to the analogous of Figure 14, though a rough estimation of the N/Tb results in a value, ca 10, still smaller than the stoichiometric one. The N*1s* peak fit reveal two component at 398.3 eV and at 400.8 eV, the first is directly attributable to a nitrogen in the TbPc₂ environment[100] while the other one at higher energy (400.8 eV) clearly indicate a modification in the chemisorbed molecules, in analogy to hat observed for similar complexes chemisorbed on Si.[98] A partial oxidation of the double decker system cannot be excluded. However we underline that this second attempt confirm that the exclusion of the oxygen plasma treatment increased the stability of the complex at the surface level even if also in these conditions the intactness of the complex cannot be inferred by the XPS characterisation.

Additional experiments are required to clarify if intact TbPc₂ are grafted on the LSMO substrate before proceeding with the realization of a spin-valve based on this magnetic molecule.

2. Assembling magnetic molecules on LSMO the electrode

References

(1)   Zhan, Y.; Fahlman, M. *J. Polym. Sci. Part B Polym. Phys.* **2012**, *50*, 1453–1462.

(2)   Bergenti, I.; Dediu, V. A.; Prezioso, M.; Riminucci, A.; Naber, W. J. M.; Faez, S.; Wiel, W. G. Van Der. *Philos. Trans. A. Math. Phys. Eng. Sci.* **2010**, *369*, 3054–3068.

(3)   Steil, S.; Großmann, N.; Laux, M.; Ruffing, A.; Steil, D.; Wiesenmayer, M.; Mathias, S.; Monti, O. L. A.; Cinchetti, M.; Aeschlimann, M. *Nat. Phys.* **2013**, *9*, 242–247.

(4)   Wende, H.; Bernien, M.; Luo, J.; Sorg, C.; Ponpandian, N.; Kurde, J.; Miguel, J.; Piantek, M.; Xu, X.; Eckhold, P.; Kuch, W.; Baberschke, K.; Panchmatia, P. M.; Sanyal, B.; Oppeneer, P. M.; Eriksson, O. *Nat. Mater.* **2007**, *6*, 516–520.

(5)   Zhan, Y.; Holmström, E.; Lizárraga, R.; Eriksson, O.; Liu, X.; Li, F.; Carlegrim, E.; Stafström, S.; Fahlman, M. *Adv. Mater.* **2010**, *22*, 1626–1630.

(6)   Xiong, Z. H.; Wu, D.; Vardeny, Z. V.; Shi, J. *Nature* **2004**, *427*, 821–824.

(7)   Dediu, V. A.; Hueso, L. E.; Bergenti, I.; Taliani, C. *Nat. Mater.* **2009**, *8*, 707–716.

(8)   Prezioso, M.; Riminucci, A.; Bergenti, I.; Graziosi, P.; Brunel, D.; Dediu, V. A. *Adv. Mater.* **2011**, *23*, 1371–1375.

(9)   Bogani, L.; Wernsdorfer, W. *Nat. Mater.* **2008**, *7*, 179–186.

(10)   Ulman, A. *Chem. Rev.* **1996**, *96*, 1533–1554.

(11)   Tatay, S.; Barraud, C.; Galbiati, M.; Seneor, P.; Mattana, R.; Bouzehouane, K.; Deranlot, C.; Jacquet, E.; Forment-Aliaga, A.; Jegou, P.; Fert, A.; Petroff, F. *ACS Nano* **2012**, *6*, 8753–8757.

(12)   Curiale, J.; Granada, M.; Troiani, H. E.; Sánchez, R. D.; Leyva, A. G.; Levy, P.; Samwer, K. *Appl. Phys. Lett.* **2009**, *95*, 043106.

(13)   Lee, J.-S.; Arena, D. A.; Yu, P.; Nelson, C. S.; Fan, R.; Kinane, C. J.; Langridge, S.; Rossell, M. D.; Ramesh, R.; Kao, C.-C. *Phys. Rev. Lett.* **2010**, *105*, 257204.

(14)   Fister, T. T.; Fong, D. D.; Eastman, J. A.; Baldo, P. M.; Highland, M. J.; Fuoss, P. H.; Balasubramaniam, K. R.; Meador, J. C.; Salvador, P. A. *Appl. Phys. Lett.* **2008**, *93*, 151904.

(15)   Katsiev, K.; Yildiz, B.; Balasubramaniam, K.; Salvador, P. A. *Appl. Phys. Lett.* **2009**, *95*, 092106.

(16)   Jalili, H.; Han, J. W.; Kuru, Y.; Cai, Z.; Yildiz, B. *J. Phys. Chem. Lett.* **2011**, *3*, 801–807.

(17)   Monsen, Å. F.; Song, F.; Li, Z. S.; Boschker, J. E.; Tybell, T.; Wahlström, E.; Wells, J. W. *Surf. Sci.* **2012**, *606*, 1360–1366.

(18)   Choi, J.; Dulli, H.; Liou, S.-H.; Downben, P. A.; Langell, M. A. *Phys. Status Solidi* **1999**, 45–58.

(19)   Choi, J.; Zhang, J.; Liou, S.-H.; Downben, P. A.; Plummer, E. W. *Phys. Rev. B* **1999**, *59*, 453–459.

(20)   Borca, C. N.; Xu, B.; Komesu, T.; Jeong, H.-K.; Liu, M. T.; Liou, S. H.; Dowben, P. A. *Surf. Sci.* **2002**, *512*, L346–L352.

(21)   Dulli, H.; Dowben, P. A.; Liou, S.-H.; Plummer, E. W. *Phys. Rev. B* **2000**, *62*, R 14 629–R14 632.

(22)   Bertacco, R.; Contour, J. P.; Barthélemy, A.; Olivier, J. *Surf. Sci.* **2002**, *511*, 366–372.

(23)   Izumi, M.; Konishi, Y.; Nishihara, T.; Hayashi, S.; Shinohara, M.; Kawasaki, M.; Tokura, Y. *Appl. Phys. Lett.* **1998**, *73*, 2497.

(24)   Yoshimoto, M.; Maruta, H.; Ohnishi, T.; Sasaki, K.; Koinuma, H. *Appl. Phys. Lett.* **1998**, *187*, 150–153.

(25)   Katayama, M.; Nomura, E.; Kanekama, N.; Soejima, H.; Aono, M. *Nucl. Instruments Methods Phys. Res. B* **1988**, *33*, 857–861.

(26)   Yu, P.; Luo, W.; Yi, D.; Zhang, J. X.; Rossell, M. D.; Yang, C.; You, L.; Singh-Bhalla, G.; Yang, S. . Y.; He, Q.; Ramasse, Q. M.; Erni, R.; Martin, L. W.; Chu, Y. H.; Pantelides, S. T.; Pennycook, S. J.; Ramesh, R. *PNAS* **2012**, *109*, 9710–9715.

(27)   Oura, K.; Lifshits, V. G.; Saranin, A. A.; Zotov, A. V; Katayama, M. *Surface Science: An Introduction*; Springer, Ed.; Advanced texts in physics; Springer, 2003; Vol. 4, p. 452.

(28)   Fadley, C. S. *Prog. Surf. Sci.* **1984**, *16*, 275–388.

(29)   Brongersma, H. H.; Draxler, M.; de Deridder, M.; Bauer, P. *Surf. Sci. Rep.* **2007**, *62*, 63–109.

(30)   Ziegler, J.; Biersack, F.; Jochen, P. *The Stopping and Range of Ions in Solids*; Bromley, D., A., Ed.; Springer US, 1985.

(31)   Mannella, N.; Booth, C. H.; Rosenhahn, A.; Sell, B. C.; Nambu, A.; Marchesini, S.; Mun, B. S.; Yang, S.-H.; Watanabe, M.; Ibrahim, K.; Arenholz, E.; Young, A.; Guo, J.; Tomioka, Y.; Fadley, C. S. *Phys. Rev. B* **2008**, *77*, 125134.

(32)   Scofield, J. H. *J. Electron Spectros. Relat. Phenomena* **1976**, *8*, 129–137.

(33)   Tanuma, S.; Powell, C. J.; Penn, D. R. *Surf. Interface Anal.* **1993**, *20*, 77–89.

(34)   Ninova, S. Single-Molecule Magnets and surfaces at Density Functional level of theory: a study of their properties before and after adsorption, University of Florence, PhD Thesis, 2014.

(35)   Zenobi, M. C.; Luengo, C. V; Avena, M. J.; Rueda, E. H. *Spectrochim. Acta. A. Mol. Biomol. Spectrosc.* **2010**, *75*, 1283–1288.

2. Assembling magnetic molecules on LSMO the electrode

(36)   Botelho do Rego, A. M.; Ferraria, A. M.; El Beghdadi, J.; Debontridder, F.; Brogueira, P.; Naaman, R.; Rei Vilar, M. *Langmuir* **2005**, *21*, 8765–8773.

(37)   Yee, C.; Kataby, G.; Ulman, A.; Prozorov, T.; White, H.; King, A.; Rafailovich, M.; Sokolov, J.; Gedanken, A. *Langmuir* **1999**, *15*, 7111–7115.

(38)   Mingalyov, P. G.; Lisichkin, G. V. *Russ. Chem. Rev.* **2006**, *75*, 541–557.

(39)   Queffélec, C.; Petit, M.; Janvier, P.; Knight, D. A.; Bujoli, B. *Chem. Rev.* **2012**, *112*, 3777–3807.

(40)   Chastain, J.; Moulder, J. *Handbook of x-ray photoelectron spectroscopy: a reference book of standard spectra for identification and interpretation of XPS data*; Physical Electronics Division, P.-E. C., Ed.; 1995.

(41)   Jansa, P.; Baszczyňski, O.; Procházková, E.; Dračínský, M.; Janeba, Z. *Green Chem.* **2012**, *14*, 2282.

(42)   Resini, C.; Catania, F.; Berardinelli, S.; Paladino, O.; Busca, G. *Appl. Catal. B Environ.* **2008**, *84*, 678–683.

(43)   Queffélec, C.; Petit, M.; Janvier, P.; Knight, D. A.; Bujoli, B. *Chem. Rev.* **2012**, *112*, 3777–3807.

(44)   Caneschi, A.; Ferraro, F.; Gatteschi, D.; le Lirzin, A.; Rentschler, E. *Inorg. Chim. Acta* **1995**, *235*, 159–164.

(45)   Mannini, M.; Sorace, L.; Gorini, L.; Piras, F. M.; Caneschi, A.; Magnani, A.; Menichetti, S.; Gatteschi, D. *Langmuir* **2007**, *23*, 2389–2397.

(46)   Rajaraman, G.; Caneschi, A.; Gatteschi, D.; Totti, F. *J. Mater. Chem.* **2010**, *20*, 10747.

(47)   Poggini, L.; Lunghi, A.; Caneschi, A.; Armelao, L.; Cortigiani, B.; Magnano, E.; Bondino, F.; Magnani, A.; Totti, F.; Gatteschi, D.; Sessoli, R.; Sorace, L.; Mannini, M. *Manuscript in Preparation*.

(48)   Gorini, L.; Caneschi, A.; Menichetti, S. *Synlett* **2006**, *2006*, 948–950.

(49)   Arbuzov, B. A.; Zobova, N. N. *Synthesis* **1982**, *1982*, 433–450.

(50)   Loewe, R. S.; Ambroise, A.; Muthukumaran, K.; Padmaja, K.; Lysenko, A. B.; Mathur, G.; Li, Q.; Bocian, D. F.; Misra, V.; Lindsey, J. S. *J. Org. Chem.* **2004**, *69*, 1453–1460.

(51)   Osiecki, J. H.; Ullman, E. F. *J. Am. Chem. Soc.* **1968**, *90*, 1078–1079.

(52)   Toda, T.; Mori, E.; Murayama, K. *Bull. Chem. Soc. Jpn.* **1972**, *45*, 1904–1908.

(53)   Caro, J.; Fraxedas, J.; Jürgens, O.; Santiso, J. J.; Rovira, C.; Veciana, J.; Figueras, A.; Caro, B. J. *Adv. Mater.* **1998**, *10*, 608–610.

(54)   Busolo, F.; Franco, L.; Armelao, L.; Maggini, M. *Langmuir* **2010**, *26*, 1889–1893.

(55)   Viornery, C.; Chevolot, Y.; Léonard, D.; Aronsson, B.-O.; Péchy, P.; Mathieu, H. J.; Descouts, P.; Grätzel, M. *Langmuir* **2002**, *18*, 2582–2589.

(56)   Wagner, C. D.; Naumkin, A. V.; Kraut-Vass, A.; Allison, J. W.; Powell, C. J.; Rumble, J. R. J. NIST Standard Reference Database 20, Version 4.1 (web version).

(57)   Cucinotta, G. Determination Of Magnetic anisotropy Of Single Molecule Magnets in Different Environments, University of Florence, PhD Thesis.

(58)   Ishikawa, N.; Sugita, M.; Ishikawa, T.; Koshihara, S.-Y.; Kaizu, Y. *J. Am. Chem. Soc.* **2003**, *125*, 8694–8695.

(59)   Ishikawa, N.; Sugita, M.; Tanaka, N.; Ishikawa, T.; Koshihara, S.; Kaizu, Y. *Inorg. Chem.* **2004**, *43*, 5498–5500.

(60)   Ishikawa, N.; Sugita, M.; Wernsdorfer, W. *Angew. Chem. Int. Ed.* **2005**, *44*, 2931–2935.

(61)   Komeda, T.; Isshiki, H.; Liu, J.; Zhang, Y.-F.; Lorente, N.; Katoh, K.; Breedlove, B. K.; Yamashita, M. *Nat. Commun.* **2011**, *2*, 217.

(62)   Urdampilleta, M.; Klyatskaya, S.; Cleuziou, J.-P.; Ruben, M.; Wernsdorfer, W. *Nat. Mater.* **2011**, *10*, 502–506.

(63)   Thiele, S.; Balestro, F.; Ballou, R.; Klyatskaya, S.; Ruben, M.; Wernsdorfer, W. *Science* **2014**, *344*, 1135–1138.

(64)   Vincent, R.; Klyatskaya, S.; Ruben, M.; Wernsdorfer, W.; Balestro, F. *Nature* **2012**, *488*, 357–360.

(65)   Urdampilleta, M.; Klyatskaya, S.; Ruben, M.; Wernsdorfer, W. *Phys. Rev. B* **2013**, *87*, 195412.

(66)   Ivanov, A. V.; Svinareva, P. A.; Zhukov, I. V.; Tomilova, L. G.; Zefirov, N. S. *Russ. Chem. Bullettin, Int. Ed.* **2006**, *55*, 281–286.

(67)   Takamatsu, S.; Ishikawa, T.; Koshihara, S.; Ishikawa, N. *Inorg. Chem.* **2007**, *46*, 7250–7252.

(68)   Gonidec, M.; Davies, E. S.; McMaster, J.; Amabilino, D. B.; Veciana, J. *J. Am. Chem. Soc.* **2010**, *132*, 1756–1757.

(69)   Zhu, P.; Lu, F.; Pan, N.; Arnold, D. P.; Zhang, S.; Jiang, J. *Eur. J. Inorg. Chem.* **2004**, *2004*, 510–517.

(70)   Müllegger, S.; Tebi, S.; Das, A. K.; Schöfberger, W.; Faschinger, F.; Koch, R. *Phys. Rev. Lett.* **2014**, *113*, 133001.

(71)   Takamatsu, S.; Ishikawa, N. *Polyhedron* **2007**, *26*, 1859–1862.

(72)   Malavolti, L.; Mannini, M.; Car, P.-E.; Campo, G.; Pineider, F.; Sessoli, R. *J. Mater. Chem. C* **2013**, *1*, 2935.

2. Assembling magnetic molecules on LSMO the electrode

(73)   Gonidec, M.; Biagi, R.; Corradini, V.; Moro, F.; De Renzi, V.; del Pennino, U.; Summa, D.; Muccioli, L.; Zannoni, C.; Amabilino, D. B.; Veciana, J. *J. Am. Chem. Soc.* **2011**, *133*, 6603–6612.

(74)   Vitali, L.; Fabris, S.; Conte, A. M.; Brink, S.; Ruben, M.; Baroni, S.; Kern, K. *Nano Lett.* **2008**, *8*, 3364–3368.

(75)   De Cian, A.; Moussavi, M.; Fischer, J.; Weiss, R. *Inorg. Chem.* **1985**, *24*, 3162–3167.

(76)   Margheriti, L.; Chiappe, D.; Mannini, M.; Car, P.-E.; Sainctavit, P.; Arrio, M.-A.; de Mongeot, F. B.; Cezar, J. C.; Piras, F. M.; Magnani, A.; Otero, E.; Caneschi, A.; Sessoli, R. *Adv. Mater.* **2010**, *22*, 5488–5493.

(77)   Stepanow, S.; Honolka, J.; Gambardella, P.; Vitali, L.; Abdurakhmanova, N.; Tseng, T.-C.; Rauschenbach, S.; Tait, S. L.; Sessi, V.; Klyatskaya, S.; Ruben, M.; Kern, K. *J. Am. Chem. Soc.* **2010**, *132*, 11900–11901.

(78)   Toader, M.; Knupfer, M.; Zahn, D. R. T.; Hietschold, M. *J. Am. Chem. Soc.* **2011**, *133*, 5538–5544.

(79)   Zhang, Y.; Isshiki, H.; Katoh, K.; Yoshida, Y.; Yamashita, M.; Miyasaka, H.; Breedlove, B. K.; Kajiwara, T.; Takaishi, S.; Komeda, T. **2009**, 14407–14410.

(80)   Fu, Y.-S.; Schwöbel, J.; Hla, S.-W.; Dilullo, A.; Hoffmann, G.; Klyatskaya, S.; Ruben, M.; Wiesendanger, R. *Nano Lett.* **2012**, *12*, 3931–3935.

(81)   Funk, T.; Deb, A.; George, S. J.; Wang, H.; Cramer, S. P. *Coord. Chem. Rev.* **2005**, *249*, 3–30.

(82)   Cornia, A.; Mannini, M.; Sainctavit, P.; Sessoli, R. *Chem. Soc. Rev.* **2011**, *40*, 3076–3091.

(83)   Mannini, M.; Pineider, F.; Danieli, C.; Totti, F.; Sorace, L.; Sainctavit, P.; Arrio, M.-A.; Otero, E.; Joly, L.; Cezar, J. C.; Cornia, A.; Sessoli, R. *Nature* **2010**, *468*, 417–421.

(84)   Lodi Rizzini, a; Krull, C.; Balashov, T.; Mugarza, a; Nistor, C.; Yakhou, F.; Sessi, V.; Klyatskaya, S.; Ruben, M.; Stepanow, S.; Gambardella, P. *Nano Lett.* **2012**, *12*, 5703–5707.

(85)   Lodi Rizzini, A.; Krull, C.; Balashov, T.; Kavich, J. J.; Mugarza, A.; Miedema, P. S.; Thakur, P. K.; Sessi, V.; Klyatskaya, S.; Ruben, M.; Stepanow, S.; Gambardella, P. *Phys. Rev. Lett.* **2011**, *107*, 177205.

(86)   Biswas, I.; Peisert, H.; Nagel, M.; Casu, M. B.; Schuppler, S.; Nagel, P.; Pellegrin, E.; Chassé, T. *J. Chem. Phys.* **2007**, *126*, 174704.

(87)   Hofmann, A.; Salman, Z.; Mannini, M.; Amato, A.; Malavolti, L.; Morenzoni, E.; Prokscha, T.; Sessoli, R.; Suter, A.; Spin, M.; Psi, C.-V.; Chimica, D.; Firenze, U. *ACS Nano* **2012**, *6*, 8390–8396.

(88)   Margheriti, L. Preparation and characterisation of SMM thin films obtained by UHV evaporation, University of Florence, PhD Thesis, 2010.

(89)   Malavolti, L. Single molecule magnets sublimated on conducting and magnetic substrates, University of Florence, PhD Thesis, 2013.

(90)   Klar, D.; Klyatskaya, S.; Candini, A.; Krumme, B.; Kummer, K.; Ohresser, P.; Corradini, V.; de Renzi, V.; Biagi, R.; Joly, L.; Kappler, J.-P.; Del Pennino, U.; Affronte, M.; Wende, H.; Ruben, M. *Beilstein J. Nanotechnol.* **2013**, *4*, 320–324.

(91)   Stadler, S.; Idzerda, Y. U.; Chen, Z.; Ogale, S. B.; Venkatesan, T. *Appl. Phys. Lett.* **1999**, *75*, 3384.

(92)   Li, F.; Zhan, Y.; Lee, T.-H.; Liu, X.; Chikamatsu, A.; Guo, T.-F.; Lin, H.-J.; Huang, J. C. A.; Fahlman, M. *J. Phys. Chem. C* **2011**, *115*, 16947–16953.

(93)   Biswas, I.; Peisert, H.; Casu, M. B.; Schuster, B.-E.; Nagel, P.; Merz, M.; Schuppler, S.; Chassé, T. *Phys. status solidi* **2009**, *206*, 2524–2528.

(94)   Gatteschi, D.; Sessoli, R.; Villain, J. *Molecular Nanomagnets*; Oxford University Press, 2006; p. 408.

(95)   Ganivet, C. R.; Ballesteros, B.; de la Torre, G.; Clemente-Juan, J. M.; Coronado, E.; Torres, T. *Chem. Eur. J.* **2013**, *19*, 1457–1465.

(96)   Glebe, U.; Weidner, T.; Baio, J. E.; Schach, D.; Bruhn, C.; Buchholz, A.; Plass, W.; Walleck, S.; Glaser, T.; Siemeling, U. *Chempluschem* **2012**, *77*, 889–897.

(97)   Jiang, J.; Ng, D. K. P. *Acc. Chem. Res.* **2009**, *42*, 79–88.

(98)   Mannini, M.; Bertani, F.; Tudisco, C.; Malavolti, L.; Poggini, L.; Misztal, K.; Menozzi, D.; Motta, A.; Otero, E.; Ohresser, P.; Sainctavit, P.; Condorelli, G. G.; Dalcanale, E.; Sessoli, R. *Nat. Commun.* **2014**, *5*, 4582.

(99)   Siemeling, U.; Schirrmacher, C.; Glebe, U.; Bruhn, C.; Baio, J. E.; Arnadóttir, L.; Castner, D. G.; Weidner, T. *Inorg. Chim. Acta* **2011**, *374*, 302–312.

(100)   Lozzi, L.; Ottaviano, L.; Santucci, S. *Surf. Sci.* **2001**, *470*, 265–274.

2. Assembling magnetic molecules on LSMO the electrode

3 Realization of an alternative hybrid magnetic electrode based on Tb(III) bis-phathalocyaninato.

Considering the non-conclusive attempts of using wet chemistry and sublimation to develop hybrid TbPc$_2$/LSMO systems described in the previous chapter, we decided to start testing an alternative strategy for the realisation of a spin-valve SMM-based system where, instead of using the LSMO spin injection electrode, this component is directly based on the presence of a magnetic molecular film chemically grafted on a non-magnetic surface. We selected the silicon surface and we planned to use the SMM film instead of LSMO to select the spin orientation of the charge carriers.

As starting surface we used Si(100) surface and we profited again of the collaboration with Prof. E. Dalcanale and his group to rely on a derivative of TbPc$_2$ terminating with alkene units to be able to tether silicon through the hydrosilylation reaction.[1] The selected grafting strategy offer the possibility to make robust and durable devices by forming stable Si–C covalent bonds. Moreover, the possibility of different doping of the silicon substrate can be used to influence the electronic properties of the grafted molecules[2] and the mobility of the charge carriers in the final hybrid device. Although preliminary promising results were obtained with Fe$_4$ SMMs chemically anchored on silicon through an exchange process,[3] no experiments on TbPc$_2$ were reported.

The design of a suitable TbPc$_2$ for silicon grafting requires the introduction of functionalised alkyl chains at peripheral positions of the phthalocyanine ligands (Figure 1). In a nutshell the synthesis performed in Dalcanale laboratories in Parma consists in adapting the traditional De Cian synthesis[4] for the double deckers by replacing the 1,2- dicyanobenzene with the 4-(ω-undecenyloxy)phthalonitrile in a reaction carried out at 160° with Tb^{III} acetyl-acetonate in presence of 1.8-diazabicyclo[5.4.0]undec-7-ene (DBU). The resulting TbPc$_2$(OC$_{11}$H$_{21}$)$_8$ was characterised via high resolution MALDI-ToF mass spectrometry, XPS and UV-Vis spectroscopy. The mass spectrometry revealed a unique peak centred at 2529.44 m/z that corresponds well in position and isotopic distribution to the calculated one

3. Realization of an alternative hybrid magnetic electrode based on Tb(III) bis-phathalocyaninato

for the molecular ion of $TbPc_2(OC_{11}H_{21})_8$ (Figure 2a and inset). The UV-VIS spectrum of $TbPc_2(OC_{11}H_{21})_8$ recorded in chloroform solution shown in Figure 2b, confirms the neutral π radical form of the molecule with the characteristic absorption bands of double decker phthalocyaninato complexes.[5]
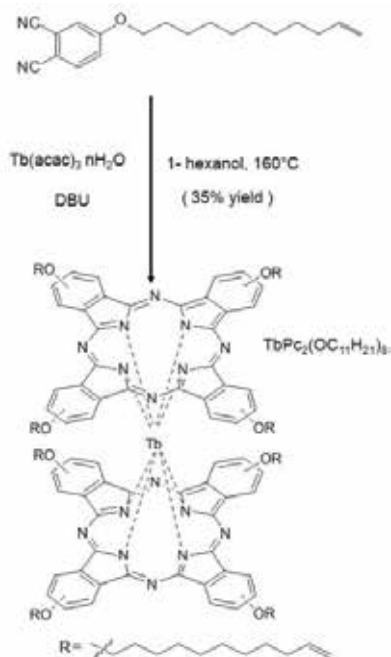
Figure 1. Synthesis of the homoleptic $TbPc_2(OC_{11}H_{21})_8$ using 4-(o-undecenyloxy) phthalonitrile as starting material.
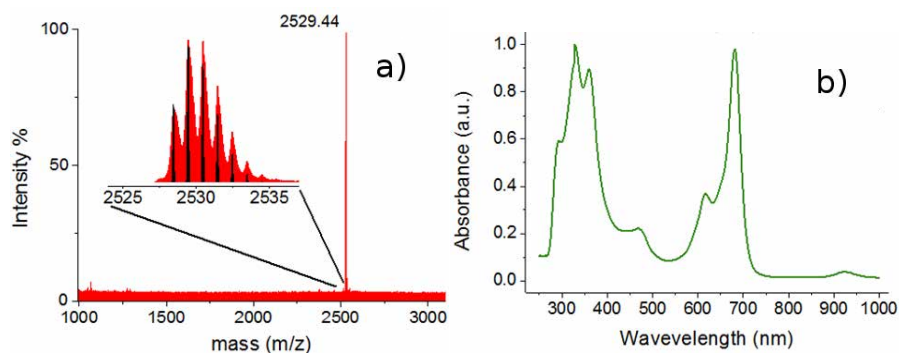
Figure 2. *a)* high resolution MALDI-ToF spectrum of $TbPc_2(OC_{11}H_{21})_8$, with experimental (red lines) versus theoretical (black) isotopic distribution pattern in the inset; b*)* UV-Vis absorption spectrum of $TbPc_2(OC_{11}H_{21})_8$ in chloroform.

3. Realization of an alternative hybrid magnetic electrode based on Tb(III) bis-phathalocyaninato

The UV-VIS spectrum (Figure 2b) was in line with what expected and on what obtained on **TbPc$_2$(PO$_3$Et$_2$)$_2$** (Chapter 2.4.5).

3.1 XPS bulk characterisations

The XPS spectra of a reference bulk phase were recorded on a thick film prepared by drop casting a diluted dichloromethane solution of the complexes on a polycrystalline gold substrate. A semi-quantitative analysis of the spectra is reported in Table 1. XPS atomic compositions of TbPc$_2$(OC$_{11}$H$_{21}$)$_8$ in a bulk deposit compared to the theoretical values for the molecule. An atomic composition of the compound in agreement, within the limits of the techniques, with the proposed formula can be deduced from this analysis, thus confirming the mass spectrometry results.

Table 1. XPS atomic compositions of TbPc$_2$(OC$_{11}$H$_{21}$)$_8$ in a bulk deposit compared to the theoretical values for the molecule.

	Tb *3d3/2*	N *1s*		C *1s*	
	%	%	N/Tb	%	N/C
TbPc$_2$(OC$_{11}$H$_{21}$)$_8$	0.5	7.5	15	92	0.08
Theoretical	0.6	9.5	16	89.9	0.1

3. Realization of an alternative hybrid magnetic electrode based on Tb(III) bis-phathalocyaninato
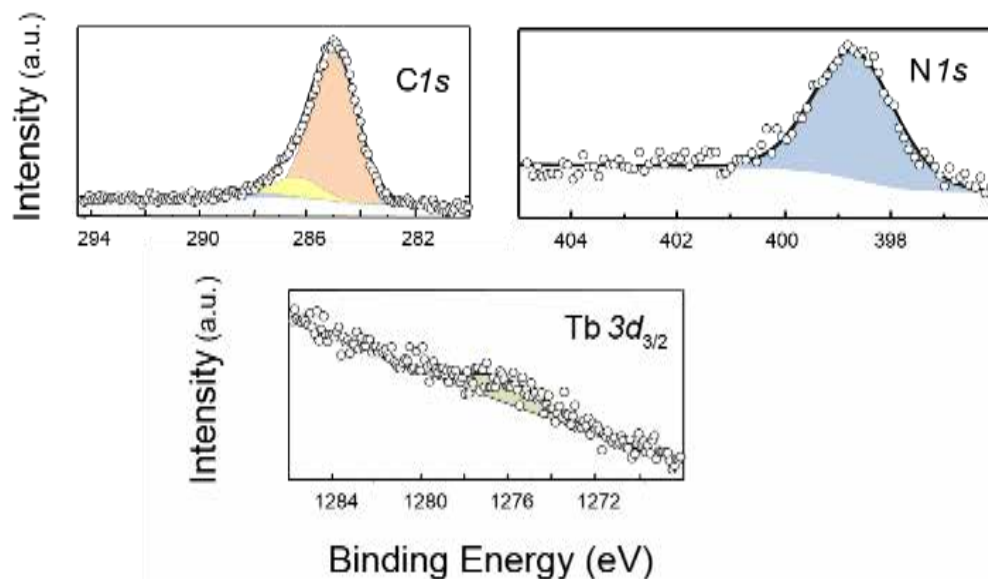
Figure 3. XPS spectra of a drop cast (thick film) of TbPc$_2$(OC$_{11}$H$_{21}$)$_8$ on Au

In Figure 3 are reported the XPS spectra of a drop cast thick film on gold. The N$1s$ features a unique peak at 398.3 eV arising from the contributions from the pyrrole-aza coordinating the metal and from the meso-bridging aza nitrogen atoms, as expected for a metal coordinated phthalocyanine.[6] The Tb$3d_{3/2}$ peak is centred at 1276.5 eV, in agreement with literature data.[7]

3.2 Magnetic characterisation of bulk TbPc$_2$(OC$_{11}$H$_{21}$)$_8$

Magnetic characterisation, performed with standard AC (Figure 4) and DC (Figure 6) magnetometric techniques clearly indicates the SMM behaviour of the complex in its bulk phase.

3. Realization of an alternative hybrid magnetic electrode based on Tb(III) bis-phathalocyaninato
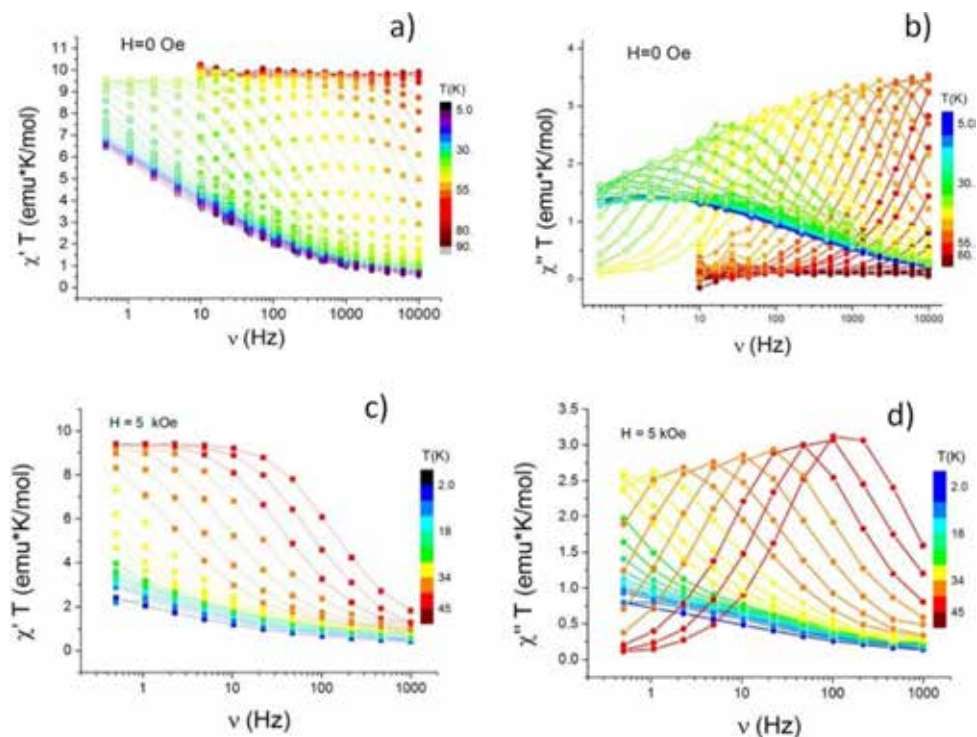
Figure 4 AC susceptibility characterisation of the bulk phase of TbPc$_2$(OC$_{11}$H$_{21}$)$_8$: in zero field (a-b) and in a *H*=5 kOe external field (c-d).

In zero static field the AC susceptibility *vs* temperature curves are characterised by a frequency dependent peak in the out-of-phase component occurring at relatively high temperatures, e.g. the maximum in χ'' at 1 kHz is observed at 47 K, that well compares with those reported for similar homoleptic substituted TbPc$_2$ systems.[8]

A more careful analysis of the frequency dependence of the AC susceptibility in a wide frequency range, 0.5 Hz - 10 kHz, was performed with the extended Debye model[9] and the relaxation time, τ, was extract using this method. In Figure 5 ln(τ) is reported *vs.* 1/*T* and in this plot and a linear trend was observed at zero static field only in the high temperature regime, i.e. *T*> 35K. Fitting the high temperature data with the Arrhenius law provided τ_0 = 5.5±0.7×10^{-12} s and Δ/k_B=811±5 K.

3. Realization of an alternative hybrid magnetic electrode based on Tb(III) bis-phathalocyaninato
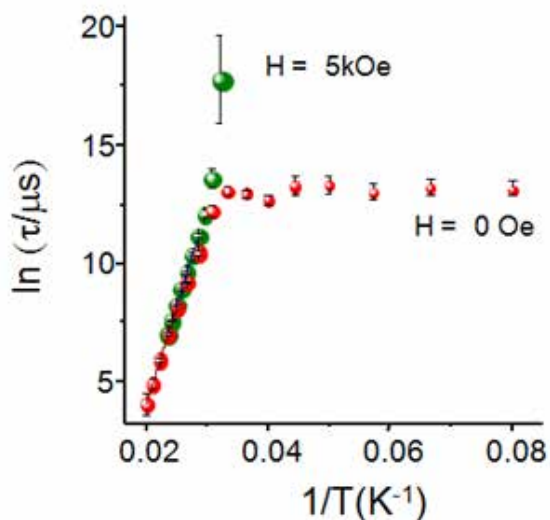
Figure 5. Arrhenius plot of data extracted from AC measurements in zero field and in 5kOe static field.

The estimated energy barrier (811 K) in the thermally activated process is bigger than that found for the $TbPc_2(PO_3Et_2)_2$ (614 K, chapter 2.4.3) but it was it was close to the value found for amorphous unfunctionalised $TbPc_2$ system (856 K).[10]

In zero field the relaxation becomes temperature independent, indicating an efficient tunnel mechanism below 35 K. The application of a static field of 5 kOe supresses the tunnelling and restores the thermally activated regime also below 35 K. with τ exceeding our time window (10 s) below 30 K. As already observed for $TbPc_2(PO_3Et_2)_2$ complex, τ was found to exhibit a single narrow distribution of in static field, where the distortions from idealised D_{4d} symmetry are not affecting the quantum tunnelling rate, while a much broader distribution was detected in 5 kOe static field.

3. Realization of an alternative hybrid magnetic electrode based on Tb(III) bis-phathalocyaninato
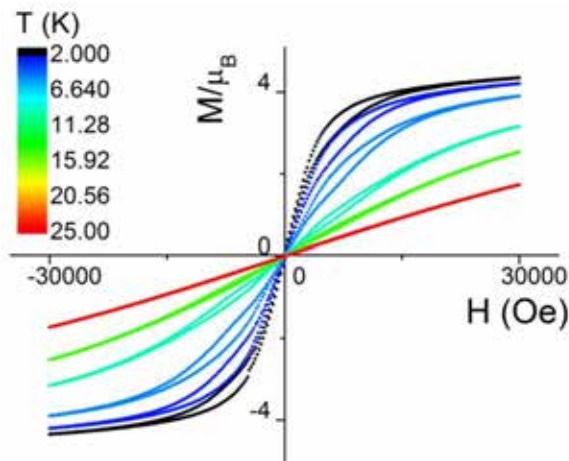
Figure 6. Magnetisation curves as a function of the temperature recorded at the field sweeping rate of 50 Oe s^{-1}.

In Figure 6 the results of magnetisation *vs.* field measurements performed at several temperatures are reported. By scanning the field between 30000 Oe and -30000 Oe at 50 Oe s^{-1} an opening in the hysteresis is evidenced below 15 K with the typical butterfly shape induced by the enhancement of quantum tunnelling in zero applied field.[11]
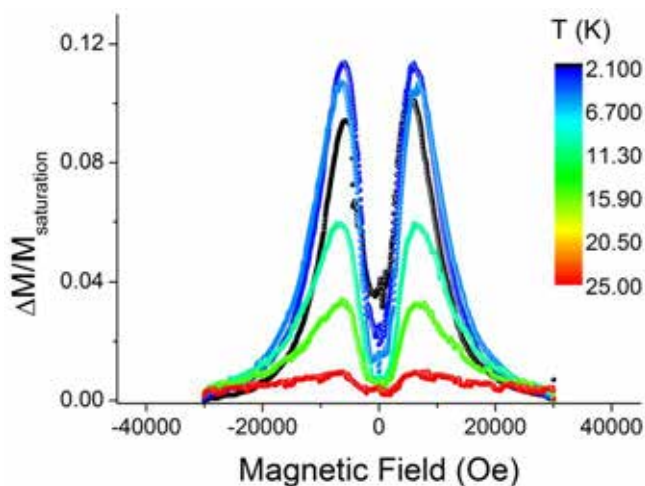
Figure 7. Hysteresis opening of a bulk sample of TbPc$_2$(OC$_{11}$H$_{21}$)$_8$ estimated as $\Delta M/M_{saturation}$ according to the procedure described in the chapter 2.4.3.

Comparing the temperature dependence of the area of the plots in Figure 7 with analogous characterisations performed on TbPc$_2$(PO$_3$Et$_2$)$_2$ and on the pristine

3. Realization of an alternative hybrid magnetic electrode based on Tb(III) bis-phathalocyaninato

[TbPc$_2$]^0 complex (Figure 8) a behaviour intermediate between the last two is found, in agreement also with the results from the Arrhenius analysis.
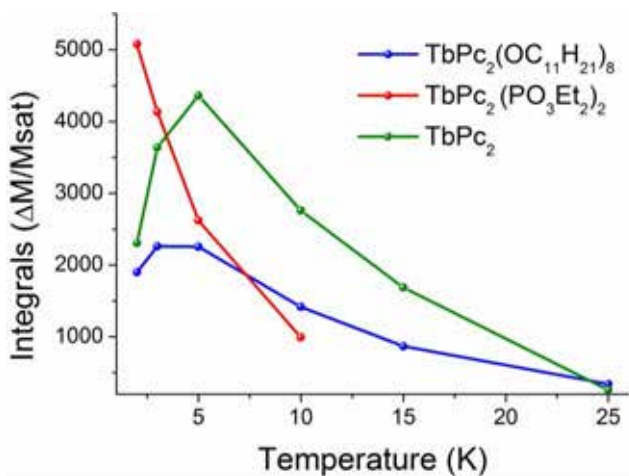
Figure 8. Comparison between the temperature dependence of area under hysteresis curves for TbPc$_2$(OC$_{11}$H$_{21}$)$_8$, TbPc$_2$(PO$_3$Et$_2$)$_2$ and for microcrystalline TbPc$_2$.[10]
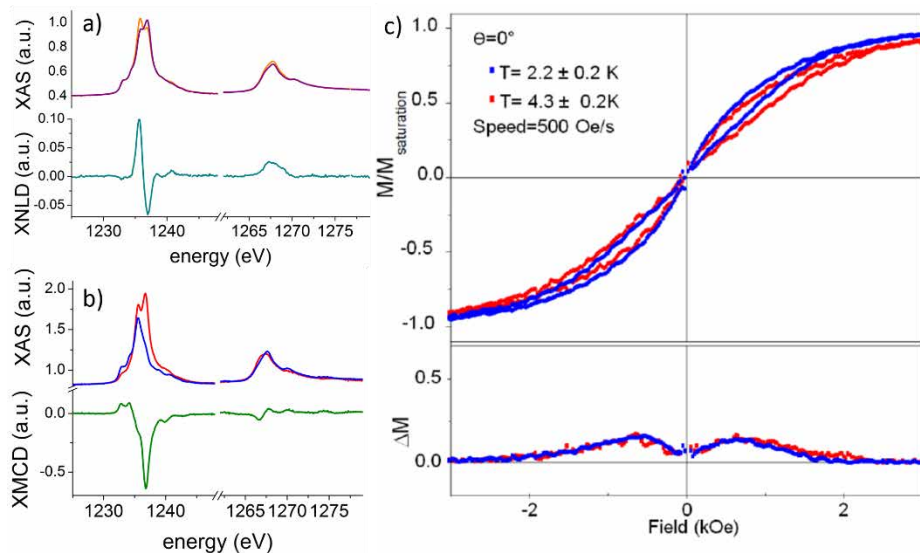
Figure 9. XAS characterisation of thick film of TbPc$_2$(OC$_{11}$H$_{21}$)$_8$ with linear polarised light (a) and circularly polarised light (b). Temperature dependence of the XMCD signal at 1236.78 eV at 2.2± 0.2 and 4.3 ± 0.2K (c).

76

3. Realization of an alternative hybrid magnetic electrode based on Tb(III) bis-phathalocyaninato

In Figure 9 are reported the results of a synchrotron-based characterisation of a drop-cast thick film of $TbPc_2(OC_{11}H_{21})_8$ on Si surface. In Figure 9a the spectra recorded with linear polarisation and the relative dichroism (XNLD) is reported. The shape of XNLD signal indicates that the molecules are preferentially oriented in the film with standing up configuration.[12] The spectra recorded with circularly polarised light (Figure 9b) show the typical XMCD signal of TbPc2 species, and of TbIII in general.[13–16] More informative is the field and temperature dependence of the XMCD signal taken at its maximum (1236.78 eV), reported in Figure 9c confirming the SMM behaviour observed by standard magnetometry (Figure 6).

3.3 Monolayer preparation.

The $TbPc_2(OC_{11}H_{21})_8$ complex has been anchored on a H-terminated Si(100) surface via thermal hydrosilylation of the double bonds according to the procedure available in the literature.[17] The hydrosilylation reaction leads to the formation of a robust Si–C bond and it occurs by placing the alkene-functionalised molecules in a 10^{-3} M mesitylene solution at 200° C in the presence of a freshly etched H-terminated Si(100) (Figure 11). After grafting, several cycles of cleaning (including the sonication of the sample in several solvents) guarantee the removal of all the physisorbed materials leaving on the surface only the monolayer of grafted molecules.
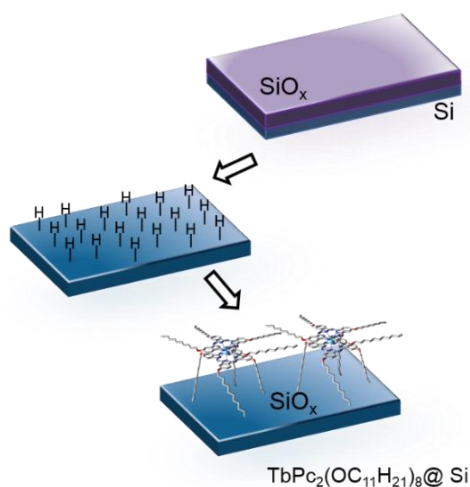
Figure 10. Sketch of the TbPc₂(OC₁₁H₂₁)₈@Si grafting procedure: step 1) etching of silicon surface in HF 2.5%; step 2) hydrosilylation at 200°C for 2h.

3.3.1 XPS TbPc$_2$(OC$_{11}$H$_{21}$)$_8$@Si characterisation

The silicon anchored complex was chemically grafted to the surface following the procedure described in the previous chapter and in Figure 10. The hybrid surface, named TbPc$_2$(OC$_{11}$H$_{21}$)$_8$@Si hereafter, was first characterised by XPS in order to verify the chemical integrity of the molecular system; only Tb$3d_{3/2}$, N$1s$ and C$1s$ signals were included in a semiquantitative estimation of the element content on surface and are reported in Table 2.

Table 2. XPS atomic composition of the monolayer of TbPc$_2$(OC$_{11}$H$_{21}$)$_8$ grafted on Si compared to the theoretical values.

	Tb $3d3/2$	N $1s$		C $1s$	
	%	%	N/Tb	%	N/C
TbPc$_2$(OC$_{11}$H$_{21}$)$_8$@Si	0.5	6.4	14	93.1	0.07
Theoretical	0.6	9.5	16	89.9	0.1

Even considering the experimental error of XPS and the presence of adventitious carbon contamination in this *ex situ* prepared sample, we can assert that the procedure of grafting assures the deposition of the intact system. Additional information on the monolayer nature can be obtained by the analysis of the N$1s$ peak shape. The comparison between the spectra of the monolayer and that of the thick film, reported in Figure 11, evidences in fact significant differences. The drop cast film features a unique peak at 398.3 eV, as mentioned above. On the contrary, the N$1s$ spectral region of the monolayer presents, in addition to this signal, a more intense component at higher energy (400.3 eV), clearly indicating that a modification occurs in the chemisorbed molecules, somehow in analogy to what observed for the TbPc$_2$(PO$_3$Et$_2$)$_2$ chemically grafted on LSMO (chapter 2.4.6).

We demonstrated in Figure 11 c that a similar shift to higher energy of the N$1s$ signal can be induced also on a thick film of TbPc$_2$(OC$_{11}$H$_{21}$)$_8$ by exposing its solution to chlorine and then preparing a drop cast deposit. The treatment with chlorine, already described in literature for Lutetium(III) bis(phthalocyaninato),[18] induces the formation of the corresponding cationic double-decker species,[19] i.e. the oxidised complex in which one of the electrons of the bis(phthalocyaninato) ligands shell has been removed. On the basis of these evidences, the energy shift can be inferred to result either from a *stabilisation effect* of the silicon surface of a cationic species

formed during the grafting reaction or from an *electron depletion* of the molecular system induced by the interaction with the surface, in analogy to similar effects experimentally observed and discussed for various phthalocyanine monolayers adsorbed on semiconducting oxides,[20–22] but never reported for double-decker complexes.
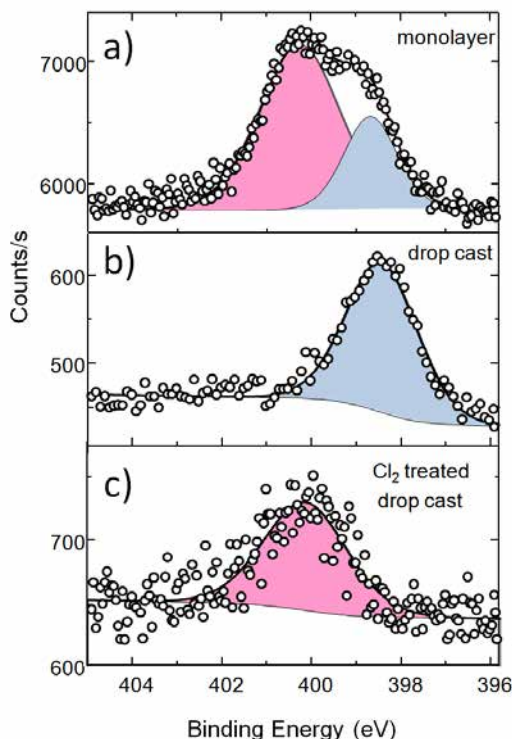
Figure 11. N 1s XPS spectra: a) TbPc$_2$(OC$_{11}$H$_{21}$)$_8$@Si monolayer, b) drop cast deposit of TbPc$_2$(OC$_{11}$H$_{21}$)$_8$ and c) drop cast sample treated with chlorine.

3.3.2 Magnetic characterisation of the TbPc$_2$(OC$_{11}$H$_{21}$)$_8$@Si monolayer

X-ray absorption experiments carried out down to 2K, under a 50 kOe magnetic field parallel to the X-ray light propagation vector, using circularly polarised light allowed to extract also the X-ray Magnetic Circular Dichroism (XMCD).

3. Realization of an alternative hybrid magnetic electrode based on Tb(III) bis-phathalocyaninato
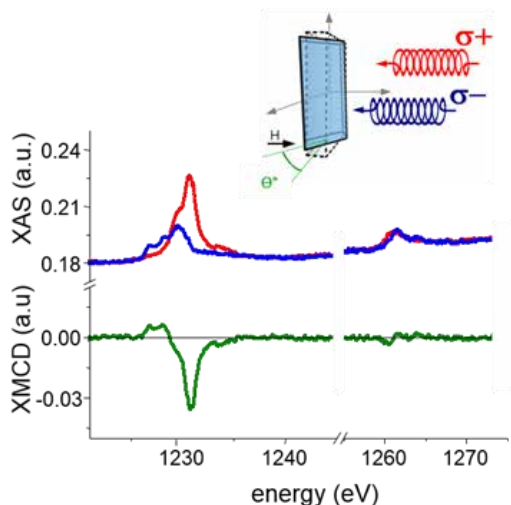
Figure 12. XMCD measurements at 2.2±0.2 K, 50 kOe, for (n,k)=60°.

The result for the monolayer is reported in Figure 12: detected features and the intensity of the dichroic signal are in line with the expected ones[12,23] for a saturated Tb^{3+} system characterised by total angular momentum J=L+S=6. Figure 13 reports the variation of the XMCD contribution at the M_5 edge, normalized to the saturation value, as a function of the applied magnetic field between -50 and 50 kOe at three different temperatures.

Profiting of the fast TEY detection setup and the stability of the experimental apparatus developed in the DEIMOS beamline, it has been possible to collect the signal as a function of the fast sweeping field, thus providing highly resolved XMCD-detected magnetisation curves clearly showing hysteretic behaviour already at 4.3±0.2 K. The opening of the hysteresis strongly depends on the temperature and also on the speed of the scanning field, confirming the dynamic character of the magnetic bistability typical of $TbPc_2$ SMMs.

3. Realization of an alternative hybrid magnetic electrode based on Tb(III) bis-phathalocyaninato
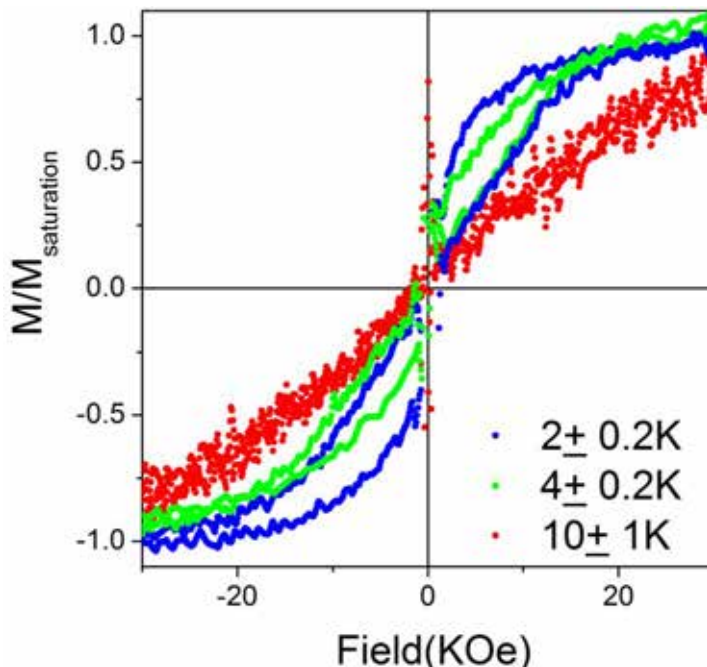
Figure 13. (a) XMCD-detected magnetisation curves for (n,k)=60° as a function of the temperature in the TbPc$_2$(OC$_{11}$H$_{21}$)$_8$@Si monolayer.

Figure 14a reports a very tiny dependence of the hysteresis on the angle (**n**,**k**) between the normal to the surface and the light propagation vector, indicating a partial orientation of the molecular film. Most important is the comparison with the behaviour of the bulk phase reported in Figure 9c. Noticeably it reveals a significantly larger opening of the hysteresis for the monolayer.

A better estimation of the changes in the hysteretic behaviour can be achieved in analogy to what reported in previous measurements by plotting the difference in the magnetisation obtained for increasing and decreasing field: $\Delta M(H)=|M(H\uparrow)-M(H\downarrow)|$. In Figure 14 b are reported the $\Delta M(H)$ curves and their area corresponds to the opening of the hysteresis loop, which results to be significantly larger in the monolayer sample than in the thick film.
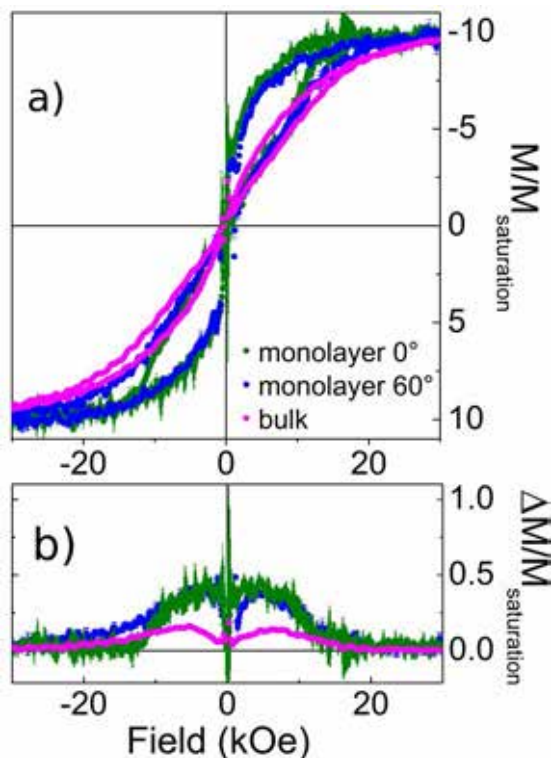
Figure 14. Comparison between the hysteresis loop (a) and $\Delta M/M_{saturation}$ (b)of the thick film and the monolayer measured for (n,k)=0° and 60°.

3.3.3 XNLD monolayer characterisation

Linear polarisation-dependent X-ray absorption experiments have been carried out on the TbPc2(OC11H21)8@Si monolayer to evaluate with the highest level of accuracy the structural properties of the assembled nanostructure.

At first, X-ray Natural Linear Dichroism (XNLD) was measured for the Tb $M_{4,5}$ edges. The sample was set so that the normal to the surface **n** and the X-ray propagation vector **k** lie in the horizontal plane with (**n,k**)=60°. The cross-sections with horizontal linear polarisation (σ_H) and with vertical linear polarisation (σ_V) were measured (Figure 15).

3. Realization of an alternative hybrid magnetic electrode based on Tb(III) bis-phathalocyaninato
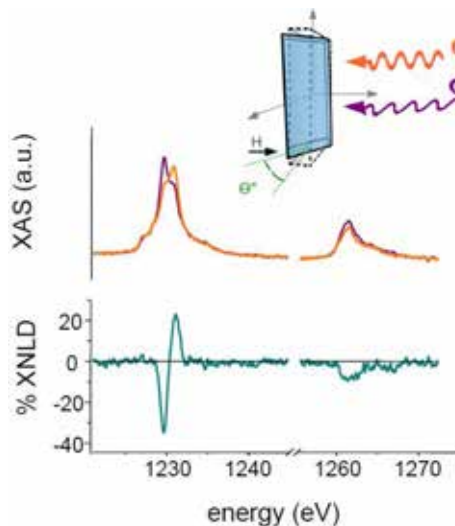
Figure 15. XNLD measurements at 2.2±0.2 K, 50000 Oe, for (n,k)=60°.

In the ideal case, where TbPc$_2$ molecules adopt a lying down configuration, that is, the phthalocyaninato C$_4$ axis is parallel to the surface normal, the electric field of the vertically polarised light is aligned perpendicular to the symmetry axis of the coordination square antiprism of the Tb^{III} ion, whereas the horizontal one forms an angle of 30° with this axis. In the opposite case, where TbPc$_2$ molecules adopt a standing configuration with no order in the plane, the electric field of the vertically polarised light can be now aligned at any angle with the symmetry axis of the molecules, whereas for the horizontal polarisation, the electric field cannot be parallel to the molecular symmetry axis. It is thus straightforward that XNLD, evaluated as (σ_V - σ_H), changes sign for the two configurations and can therefore be employed to extract information on the molecular arrangement in the monolayer.
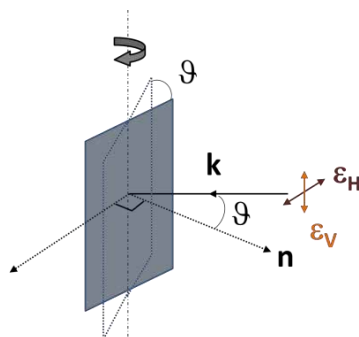
Figure 16. Sketch of the geometry of the XNLD experimental setup.

3. Realization of an alternative hybrid magnetic electrode based on Tb(III) bis-phathalocyaninato

By the comparison with experimental and theoretical reports from earlier literature[12], it is possible to assess the preferential orientation of the molecules on surface. We assume that XAS at Tb $M_{4,5}$ edges is completely described in the electric dipole approximation and that the symmetry of the sample is C∞, i.e. the sample is invariant by any rotation parallel to the normal of the sample surface. According to the work of Brouder[24] the two previous assumptions imply that the angular dependence of the cross-section is dichroic for linear polarised light. As reported in Figure 16 if ϑ is the angle between the linear polarisation vector ε and the symmetry axis **n**, then the cross section is given by:

$$\sigma(\theta) = [\cos(\theta)]^2 \sigma_{Par} [\sin(\theta)]^2 \sigma_{Perp} \qquad (1)$$

where σ_{Par} is the cross-section measured with ε parallel to **n** and σ_{Perp} is the cross-section measured with ε perpendicular to **n**. We measured cross-section with ε vertical or horizontal and using Eq. (1) we find that for vertical ε $\sigma_V = \sigma_{Perp}$, while for horizontal ε with ϑ=30° $\sigma_H = (3\sigma_{Par} + \sigma_{Perp})/4.$ Then, recalling the definition of $\sigma_{XNLD} = \sigma_V - \sigma_H$ it follows that:

$$\sigma_{XNLD} = 3/4 \, (\sigma_{Perp} - \sigma_{Par}) \qquad (2)$$

The isotropic cross-section for dichroic systems is given by:[24]

$$\sigma_{ISO} = (2\sigma_{Perp} + \sigma_{Par})/3$$

$$\sigma_{ISO} = (4\sigma_H + 5\sigma_V)/9$$

Using these definitions one can extract a percentage of the dichroic contribution with respect to the isotropic contribution and compare this result with the one calculated for a flat molecule placed in a lying down configuration and with the one experimentally measured for TbPc$_2$ unfunctionalised molecules evaporated on gold.[12] From this it is possible to estimate that about half of the molecules grafted to the silicon surface monolayer are preferentially oriented with a lying down configurations. It is interesting to notice that a reversed XNLD signal is measured in a bulk sample obtained by drop casting a solution of **TbPc$_2$(OC$_{11}$H$_{21}$)$_8$** (Figure 9a). This finding are in line with the common tendency for thick bis(phthalocyaninato) films to aggregate in a standing up configuration[12], and the observed difference between the two samples confirms that our monolayer of TbPc$_2$ does not contain physisorbed aggregates.

3. Realization of an alternative hybrid magnetic electrode based on Tb(III) bis-phathalocyaninato

The use of silicon, unprecedented for this type of SMMs, presents several interesting advantages. Our results show that TbPc$_2$ SMMs can be covalently and robustly anchored to a silicon substrate, with the deposited monolayer standing harsh treatments like sonication in dichloromethane. Si–C covalent bonds in fact guarantee a higher stability. Moreover, the pronounced magnetic bistability is not only retained at the level of the monolayer but, when quantified as the area enclosed in the hysteresis cycle, it happens to be significantly enhanced by the grafting process to silicon. More important is that this alteration correlates with changes observed in the photoelectron spectra. Although the long alkyl chains in this Tb double-decker SMM could in principle hamper a significant interaction with the substrate, their flexibility, as already observed for functionalised TbPc$_2$ molecules grafted on gold,[25] induces a preferential lying down configuration that can allow a stabilisation of an oxidised TbPc$_2$ system by the silicon substrate. It is well known that the oxidation of the Pc ligands reduces the height of the square-antiprism coordination polyhedron with a sensible enhancement of the effective energy barrier for the reversal of the magnetisation and more pronounced hysteretic behaviour.[26–28]

3. Realization of an alternative hybrid magnetic electrode based on Tb(III) bis-phathalocyaninato

Reference

(1)   Linford, M. R.; Chidsey, C. E. D. *J. Am. Chem. Soc.* **1993**, *115*, 12631–12632.

(2)   Woodruff, D. N.; Winpenny, R. E. P.; Layfield, R. A. *Chem. Rev.* **2013**, *113*, 5110–5148.

(3)   Condorelli, G. G.; Motta, A.; Fragala, I. L.; Giannazzo, F.; Raineri, V.; Caneschi, A.; Gatteschi, D. *Angew. Chem. Int. Ed.* **2004**, *43*, 4081–4084.

(4)   Cian, A. De; Moussavi, M.; Fischer, J.; Weiss, R. *Inorg. Chem.* **1985**, *24*, 3162–3167.

(5)   Jiang, J.; Ng, D. K. P. *Acc. Chem. Res.* **2009**, *42*, 79–88.

(6)   Lozzi, L.; Ottaviano, L.; Santucci, S. *Surf. Sci.* **2001**, *470*, 265–274.

(7)   Mannini, M.; Bertani, F.; Tudisco, C.; Malavolti, L.; Poggini, L.; Misztal, K.; Menozzi, D.; Motta, A.; Otero, E.; Ohresser, P.; Sainctavit, P.; Condorelli, G. G.; Dalcanale, E.; Sessoli, R. *Nat. Commun.* **2014**, *5*, 4582.

(8)   Ganivet, C. R.; Ballesteros, B.; de la Torre, G.; Clemente-Juan, J. M.; Coronado, E.; Torres, T. *Chem. Eur. J.* **2013**, *19*, 1457–1465.

(9)   Gatteschi, D.; Sessoli, R.; Villain, J. *Molecular Nanomagnets*; Oxford University Press, 2006; p. 408.

(10)   Malavolti, L.; Mannini, M.; Car, P.-E.; Campo, G.; Pineider, F.; Sessoli, R. *J. Mater. Chem. C* **2013**, *1*, 2935.

(11)   Ishikawa, N. *Polyhedron* **2007**, *26*, 2147–2153.

(12)   Margheriti, L.; Chiappe, D.; Mannini, M.; Car, P.-E.; Sainctavit, P.; Arrio, M.-A.; de Mongeot, F. B.; Cezar, J. C.; Piras, F. M.; Magnani, A.; Otero, E.; Caneschi, A.; Sessoli, R. *Adv. Mater.* **2010**, *22*, 5488–5493.

(13)   Stepanow, S.; Honolka, J.; Gambardella, P.; Vitali, L.; Abdurakhmanova, N.; Tseng, T.-C.; Rauschenbach, S.; Tait, S. L.; Sessi, V.; Klyatskaya, S.; Ruben, M.; Kern, K. *J. Am. Chem. Soc.* **2010**, *132*, 11900–11901.

(14)   Malavolti, L. Single molecule magnets sublimated on conducting and magnetic substrates, University of Florence, PhD Thesis, 2013.

(15)   Margheriti, L. Preparation and characterisation of SMM thin films obtained by UHV evaporation, University of Florence, PhD Thesis, 2010.

(16)   Lodi Rizzini, a; Krull, C.; Balashov, T.; Mugarza, a; Nistor, C.; Yakhou, F.; Sessi, V.; Klyatskaya, S.; Ruben, M.; Stepanow, S.; Gambardella, P. *Nano Lett.* **2012**, *12*, 5703–5707.

3. Realization of an alternative hybrid magnetic electrode based on Tb(III) bis-phathalocyaninato

(17)   Buriak, J. M. *Chem. Rev.* **2002**, *102*, 1271–1308.

(18)   Bufler, J.; Ziegler, C.; Göpel, W. *Synth. Met.* **1993**, *61*, 127–131.

(19)   Gonidec, M.; Davies, E. S.; McMaster, J.; Amabilino, D. B.; Veciana, J. *J. Am. Chem. Soc.* **2010**, *132*, 1756–1757.

(20)   Palmgren, P.; Nilson, K.; Yu, S.; Hennies, F.; Angot, T.; Layet, J.-M.; LeLay, G.; Gothelid, M. *J. Phys. Chem. C* **2008**, *112*, 5972–5977.

(21)   Mattioli, G.; Filippone, F.; Giannozzi, P.; Caminiti, R.; Bonapasta, A. A. *Chem. Mater.* **2009**, *21*, 4555–4567.

(22)   Yu, S.; Ahmadi, S.; Sun, C.; Adibi, P. T. Z.; Chow, W.; Pietzsch, A.; Gothelid, M. *J. Chem. Phys.* **2012**, *136*, 154703–154709.

(23)   Biagi, R.; Fernandez-Rodriguez, J.; Gonidec, M.; Mirone, a.; Corradini, V.; Moro, F.; De Renzi, V.; del Pennino, U.; Cezar, J. C.; Amabilino, D. B.; Veciana, J. *Phys. Rev. B* **2010**, *82*, 224406.

(24)   Brouder, C. *J. Phys. Condens. Matter* **1990**, *2*, 701–738.

(25)   Glebe, U.; Weidner, T.; Baio, J. E.; Schach, D.; Bruhn, C.; Buchholz, A.; Plass, W.; Walleck, S.; Glaser, T.; Siemeling, U. *Chempluschem* **2012**, *77*, 889–897.

(26)   Ishikawa, N.; Sugita, M.; Tanaka, N.; Ishikawa, T.; Koshihara, S.; Kaizu, Y. *Inorg. Chem.* **2004**, *43*, 5498–5500.

(27)   Ishikawa, N.; Sugita, M.; Okubo, T.; Tanaka, N.; Iino, T.; Kaizu, Y. *Inorg. Chem.* **2003**, *42*, 2440–2446.

(28)   Takamatsu, S.; Ishikawa, T.; Koshihara, S.; Ishikawa, N. *Inorg. Chem.* **2007**, *46*, 7250–7252.

4. Functional hybrid electrodes based on light switchable molecules.

Cobalt complexes which contains dioxolene ligands belong to the class of switchable molecules.[1,2] They are class II mixed-valence systems in the Robin's and Day's classification[2] showing a small electronic delocalization between the Co ion and the organic ligand. Namely those systems are defined as Valence Tautomers (VT), systems in which two possible molecular electronic states can be defined: one is the closed-shell diamagnetic *ls*-Co^{III}(Cat) and the other is the *hs*-Co^{II}(SQ) paramagnetic redox isomer, where Cat and SQ stand for the two forms of the dioxolene ligand, catecholate and semiquinonate, respectively.[3]

The simplest molecular systems displaying VT rely on the [CoLdiox] core, being L a tetradentate N-donating ancillary ligand and diox a chelating ligand belonging to the ortho-quinone (dioxolene) family. At low temperatures the diamagnetic *ls*-Co^{III}Cat redox isomer is the ground state, but entropy driven intramolecular electron transfer triggers a spin switch at the metal center, reversibly yielding the paramagnetic *hs*-Co^{II}SQ species upon heating the system.[4] At cryogenic temperatures the same interconversion can be induced by optical[5] and soft X-ray irradiation;[6] once removed the stimulating source, a slow decay to the *ls*-Co^{III}Cat ground state occurs with a temperature dependent lifetime.[7] The intrinsic properties of VT allows to tune the electronic properties of the two redox active centers by chemical design, giving the possibility to prepare structurally related complexes with different charge distributions.[8] Moreover, on the basis of DFT calculations it has been recently proposed that electric field switching may be achieved for surface deposits of these compounds, suggesting that detection and modulation of their magnetic state can be obtained at the single molecule level by using a Scanning Tunnel Microscopy-based architecture.[9]

Low temperatures stabilize the *ls*-Co^{III}Cat state for enthalpic reasons and upon heating, a reversible intramolecular electron transfer occurs from the ligand to the Co ion, bringing the system to switch their spin state by an intramolecular electron transfer. The transformation arise from the entropic gain induced by the higher density of vibrational and spin states in the *hs*-Co^{II}(SQ).[10] The control of the charge

distribution of the system can be tuned by varying thermodynamic parameters, like temperature,[3,11] pressure,[12,13] magnetic field.[14] The control of the charge distribution can be achieved also at cryogenic temperatures, where the irradiation, either in the visible [7] or in the soft x-rays[6] populates the metastable hs-Co^{II}(SQ) electronic state. The coupling between electronic and vibrational states with the ground ls-Co^{III}(Cat) state leads to an activation barrier and the relaxation process is temperature dependent. The optical and thermal bistabilities in both VT[15], in analogy to what observed in Spin Crossover (SCO)[16] materials, follow two mechanisms: temperature induced transitions are strictly related to environmental effects; on the other hand, the decay process of the photoinduced phase is mainly a single-molecule property, involving the variation of bond length taking place during the optically triggered transition.

4.1 Optimisation of the spectroscopic characterisations of a Valence Tautomeric system in the bulk phase

From a technological point of view these molecular properties are very promising, suggesting that bistable molecules can be used as active components for molecular devices. DFT calculations are in line with this perspective: it has been recently proposed that an STM could be used to read and change the electronic ground state of VT systems when the molecules are isolated on conductive surfaces.[9] The chemical functionalization of VT and SCO molecules with the preservation of their bistabilities features, represents a step toward the surface structuration of these systems.

For this reason, in order to understand the potentiality of VT compounds, we performed a multi-technique characterisation of a family of dinuclear Cobalt-dioxolene complexes chemically functionalised with a thioether bridge (Figure 1). The complexes have a general formula Co(Me$_n$tpa)$^{2+}$ where Me$_n$tpa are differently methylated derivatives of tris-pyridil-amine (n=0,2,3) for complexes **[CoL1-dioxo-R-dioxo-CoL1]**, **[CoL2-dioxo-R-dioxo-CoL2]** and **[CoL3-dioxo-R-dioxo-CoL3]** respectively like shown in Figure 1. These molecules are possible building blocks for the development of bistable molecular nanostructures. Complex **[CoL2-dioxo-R-dioxo-CoL2]** features a VT behaviour while complex **[CoL1-dioxo-R-dioxo-CoL1]** (and **[CoL3-dioxo-R-dioxo-CoL3]**) maintain their diamagnetic (and paramagnetic respectively) state within the range of explored temperatures in agreement with what has been reported for the archetypal Cobalt–Dioxolene Complex complexes.[7]
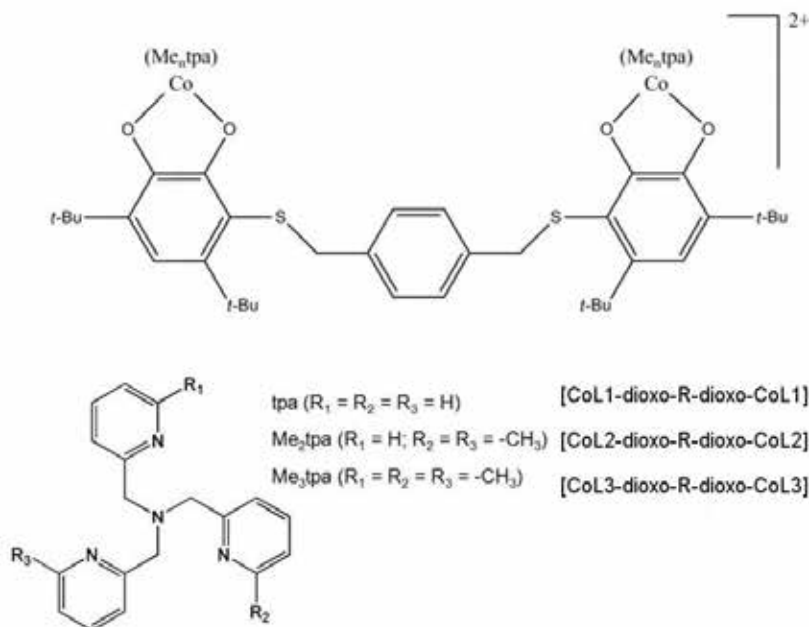
Figure 1. Schematic representation of the dinuclear Cobalt-dioxolene complexes, [CoL1-dioxo-R-dioxo-CoL1] (n=0), [CoL2-dioxo-R-dioxo-CoL2] (n=2), [CoL3-dioxo-R-dioxo-CoL3] (n=3) and the corresponding ancillary Me$_n$tpa ligands.

4.1.1 Magnetic Characterisation.

In order to follow the conversion between the diamagnetic *ls*-Co^{III}(Cat) and the paramagnetic *hs*-Co^{II}(SQ) isomers, relevant information can be extracted from temperature and light dependent magnetic measurements. In

Figure 2 is reported the temperature dependence of the $\chi_M T$ product of complexes **[CoL1-dioxo-R-dioxo-CoL1]** (blue empty circles), **[CoL2-dioxo-R-dioxo-CoL2]** (full circles of variable colour) and **[CoL3-dioxo-R-dioxo-CoL3]** (full red circles), measured by applying a 1 kOe field in the 2 – 45 K range and a 10 kOe one up to 300 K. The samples were characterized as bulk polycrystalline samples. Complex **[CoL1-dioxo-R-dioxo-CoL1]** shows a substantially diamagnetic behaviour in the 10-300 K range, its $\chi_M T$ varying from 0.02 emu K/mol at 10 K up to 0.13 emu K/mol at 300 K, in line with the expected temperature independent paramagnetism of the octahedrally coordinated *ls*-Co^{III} ion.[17] This clearly evidence a temperature independent *ls*-Co^{III}(Cat) electronic distribution in the whole investigated temperature interval. On the contrary, the room temperature $\chi_M T$ value of **[CoL3-dioxo-R-dioxo-CoL3]** (6.15

91

emu K/mol) is consistent with two non-interacting semiquinonate radical ligands (S = 1/2, g =2.0) and two *hs*-Co^{II} ions (S=3/2 with high orbital contribution) and is in the range expected for two *hs*-Co^{II}-SQ moieties (6.0 - 7.6 emuK/mol).[18]
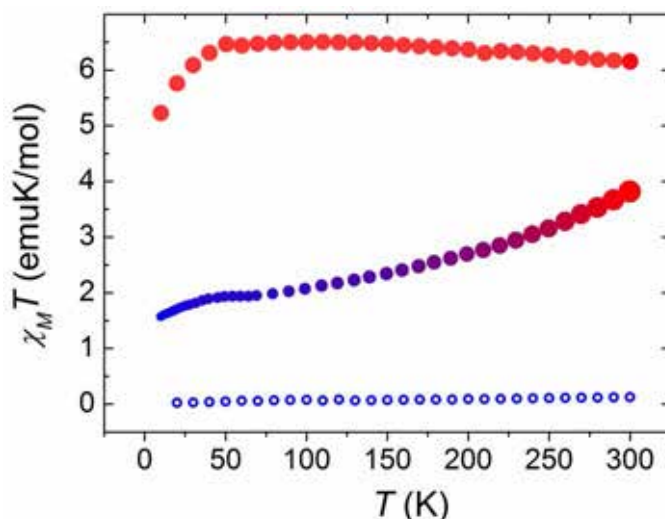
Figure 2. Temperature dependence of the $\chi_M T$ of the three investigates samples complexes [CoL1-dioxo-R-dioxo-CoL1] (blue empty circles), [CoL2-dioxo-R-dioxo-CoL2] (full circles of variable color) and [CoL3-dioxo-R-dioxo-CoL3] (full red circles).

The slight increase in $\chi_M T$ observed on lowering temperature observed for **[CoL3-dioxo-R-dioxo-CoL3]**, though surprising , has already been reported for a different dinuclear cobalt-dioxolene system.[19] This can be attributed to variable population of the excited multiplets of the $^4T_{1g}$ ground state of Co^{II} centers, which is split due to the combined effect of low symmetry distortion and spin–orbit coupling.[18,20] On the other side the temperature dependence of the $\chi_M T$ product of the complex **[CoL2-dioxo-R-dioxo-CoL2]** is completely different from **[CoL1-dioxo-R-dioxo-CoL1]** and **[CoL1-dioxo-R-dioxo-CoL1]** complexes. Indeed $\chi_M T$ product varying from 1.93 emu K/mol at 60 K to 3.82 emu K/mol at 300 K, in accordance with a thermally driven Valence Tautomeric equilibrium. Deconvolution of the magnetic signal of **[CoL2-dioxo-R-dioxo-CoL2]** using **[CoL1-dioxo-R-dioxo-CoL1]** and **[CoL3-dioxo-R-dioxo-CoL3]** as reference compositional cases for the *ls*-Co^{III}(Cat) and *hs*-Co^{II}(SQ) charge distributions, respectively, allows to estimate a *hs*-Co^{II}(SQ) molar fraction of 61 % at 300 K.

Notwithstanding its dinuclear nature no double stepped entropy driven conversion were found for complex **[CoL2-dioxo-R-dioxo-CoL2]**. This phenomenon

92

can be explained considering the structural rigidity of the thioetheric bridge, which hampers a significant vibronic coupling between the two Co-diox centers. Molecular based multistability in Co VT molecular materials, was reported for the first time by Preuss *et al.* for an amorphous film of a dinuclear Cobalt-dioxolene complex,[21] and only recently the dependance on the vibronic coupling between the two Co-diox moieties was demonstrated.[19] Below 60 K, the levelling of $\chi_M T$ of **[CoL2-dioxo-R-dioxo-CoL2]** to 1.57 emu K/mol is indicative of the presence of a *hs*-Co[II](SQ) remaining fraction at low temperature (29 % of the overall Co content). This behavior, usually observed in spin crossover complexes[21] and molecules undergoing redox isomerism,[22] is to be attributed to the trifling intermolecular cooperativity in the solid state, confirmed by the smooth profile of the entropy-driven transition.

4.1.2 Photomagnetism.

In line with other Cobalt-dioxolene complexes[23] **[CoL2-dioxo-R-dioxo-CoL2]** displays a light-induced VT transition, showing the possibility to optically trigger the *ls*-Co[III](Cat) to *hs*-Co[II](SQ) conversion. In this case the samples were prepared using a Die Kit in a mixture of **[CoL2-dioxo-R-dioxo-CoL2]** sample and dried KBr with a complex concentration of ca. 1%. Light was applied perpendicularly to the pellet surface. In Figure 3 is reported the effect of the application of 904 nm laser lightat *T*=10 K: the $\chi_M T$ value increases from 1.57 up to 1.99 emuK/mol, corresponding to an 11 % photo-conversion of the *ls*-Co[III](Cat) content.
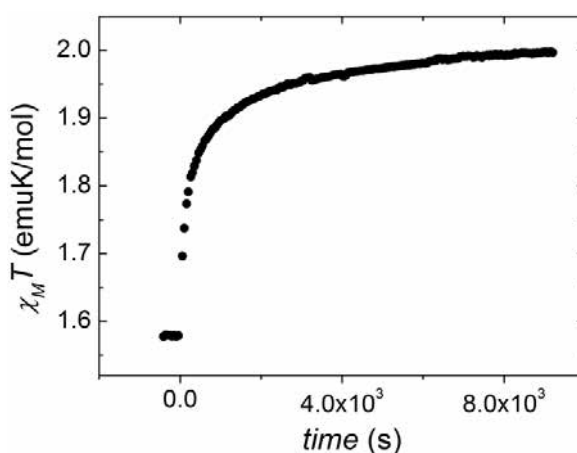
Figure 3. Time evolution of the $\chi_M T$ product of [CoL2-dioxo-R-dioxo-CoL2] after 904 nm light irradiation.

4. Functional hybrid electrodes based on light switchable molecules.

In order to characterize the relaxation dynamics of the photo-induced metastable *hs*-Co[II](SQ) molar fraction ($\gamma_{hs-Co^{(II)}SQ}$) to the *ls*-Co[III](Cat) electronic ground state for **[CoL2-dioxo-R-dioxo-CoL2]**, the time decays of the photo-induced *hs*-Co[II](SQ) were measured (Figure 4). From the data the relaxation time was extracted by fitting the curves with a stretched exponential decay:

$$\gamma_{hs}(t) = \gamma_{hs}(0)e^{-\left(\frac{t}{\tau}\right)^{\beta}} \tag{1}$$

where the β exponent takes into account the width of the distribution of relaxation times.[24] In Table 1 we report the relaxation times τ and stretching exponential factors β.

Table 1. Relaxation times τ and stretching exponential factors β extracted from the isothermal relaxation curves of the photo-induced phase of [CoL2-dioxo-R-dioxo-CoL2] .

T (K)	τ (s)	β
10	$8.3(2)\cdot10^5$	0.321(1)
20	$8.3(5)\cdot10^5$	0.315(6)
30	$3.07(3)\cdot10^5$	0.291(1)
40	$7.49(3)\cdot10^4$	0.357(1)
50	$1.317(3)\cdot10^4$	0.3822(7)
60	$5.40(2)\cdot10^3$	0.443(1)

The extracted relaxation times feature a non-linear dependence on temperature: monitoring the $\ln(\tau)$ *vs* T^{-1} plot (inset of Figure 4), it is possible to distinguish a crossover between a low temperature regime (10 - 20 K), where τ is temperature independent, and a higher temperature one (30 - 60 K), where a linear dependence of $\ln(\tau)$ with T^{-1} is clearly observed.

The fit of these points by an Arrhenius model for thermally activated relaxation

$$\tau(T) = \tau_0 e^{-\Delta E/k_B T} \tag{2}$$

resulted in a pre-exponential factor of 25(15) s and an activation barrier ($\Delta E/\kappa_B$) of 318(23) K. The height of the barrier confirms that the mixing of the metastable and ground electronic states responsible for the decay takes place mainly though the Co-O stretching vibrational mode.[8,7] Linear fit of the low temperature region (reported in Figure 4 as a dotted line) provides $8.2(1) \times 10^5$ s as estimate of the $\tau(T\rightarrow0)$.
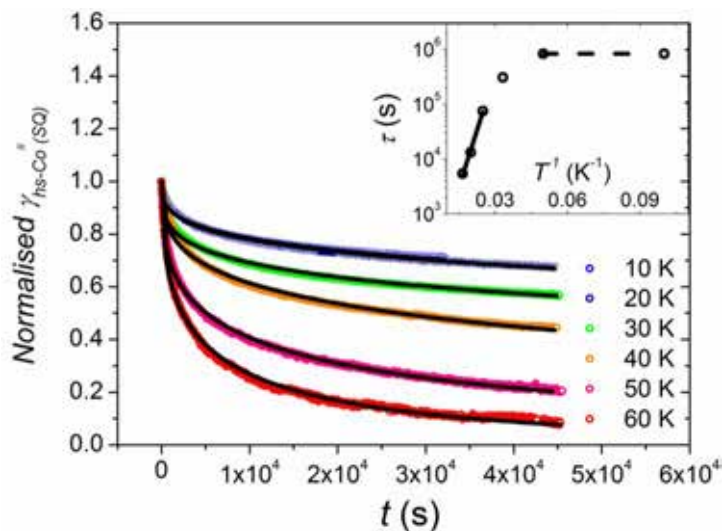
Figure 4. Isothermal time dependence of the photo-induced *hs*-Co^{II}(SQ) molar fraction of [CoL2-dioxo-R-dioxo-CoL2], measured at different temperatures after photo-excitation at 10 K. *Inset*: Corresponding Arrhenius plot.

An estimate of the energy barrier to the thermally activated relaxation of the photo-induced phase can also be obtained by analyzing the thermal dependence of its metastable molar fraction $\gamma_{hs-Co^{(II)}SQ}$ (Figure 5).
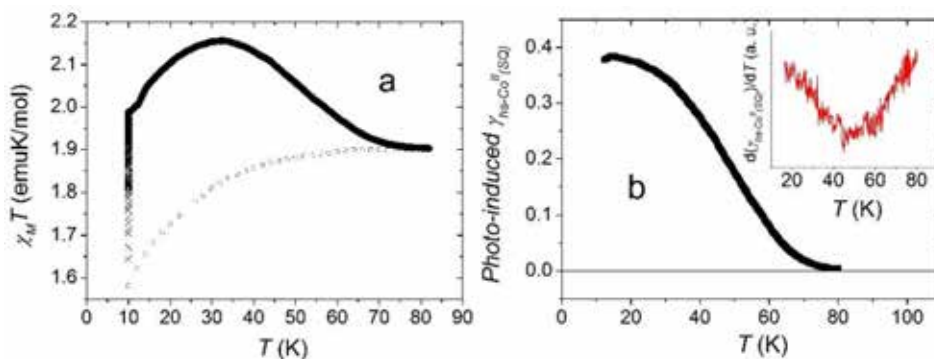
Figure 5. a) Temperature dependence of the $\chi_M T$ product before (○), during (x) and after (●) light irradiation at 10 K; b) corresponding plot of the photo-induced *hs*-Co^{II}SQ molar fraction. In the inset the temperature derivative allow to extract T$_{LIESST}$.

In Figure 5 (a) is reported the temperature dependemce of the $\chi_M T$ product where measured before during and after 904 nm irradiation at 10 K, warming the

sample after removing the irradiation at a rate of 0.3 K/min. In Figure 5 (b) is reported the corresponding plot of the photo-induced hs-Co^{II}SQ molar fraction ($\gamma_{hs-Co^{(II)}SQ}$), obtained interpolating the photo-induced $\chi_M T$ values of **[CoL2-dioxo-R-dioxo-CoL2]** using the Eq. (3):

$$\gamma_{hs-Co^{(II)}SQ}(T) = \frac{[\chi_M T(T)]_2 - [\chi_M T(T)]_1}{[\chi_M T(T)]_3 - [\chi_M T(T)]_1} \tag{3}$$

The Eq.(3) reports the procedure used to calculate the thermal evolution of the hs-Co^{II} molar fraction of **[CoL2-dioxo-R-dioxo-CoL2]** from magnetisation measurements, using the $\chi_M T$ values of **[CoL1-dioxo-R-dioxo-CoL1]** and **[CoL3-dioxo-R-dioxo-CoL3]** as representative of ls-Co^{III} and hs-Co^{II} charge distributions, respectively.

After switching off the excitation source at 10 K, the $\chi_M T$ value collapses on the non-irradiated one at 78 K. If carried out at a warming rate of 0.3 K min^{-1}, this process allows to measure the T$_{LIESST}$ parameter, *i.e.* the temperature where a minimum in the derivative d(hs-Co^{II}(SQ))/dT *vs* T plot occurs, see inset of Figure 6b.[25,26] This parameter affords an easy way to compare the stability of the photo-induced state for different optically-switchable materials. For **[CoL2-dioxo-R-dioxo-CoL2]**, the derived value of T$_{LIESST}$ is 49 K, in agreement with literature data.[7,15,19,23,27]

4.1.3 X-Ray Photoelectron Spectroscopy.

XPS has been previously used as atomically specific spectroscopic probe of oxidation and spin states in the analysis of electronic structures of molecular switchable materials, ranging from mixed valence[28] to spin crossover[29] and coordination polymeric networks.[30–33] In dioxolene-metal coordination chemistry it has allowed the determination of the charge distribution in different nickel-dioxolene adducts.[34] XPS can provide information about the chemical and the electronic structure of diluted samples like monolayers of molecules grafted to conductive surfaces. However, since the binding energy of electrons in a given orbital is dependent on both valence and spin configuration of the emitter, it is not always straightforward to address redox states when the spin state of the emitter can be switched as well.[35] By comparing the Co$2p$ XPS spectra of **[CoL2-dioxo-R-dioxo-CoL2]** with those of the limiting charge configuration cases **[CoL1-dioxo-R-dioxo-CoL1]** and

[CoL3-dioxo-R-dioxo-CoL3] it has been possible in this thesis work to achieve a reference set to estimate the charge distribution of the interconverting system.
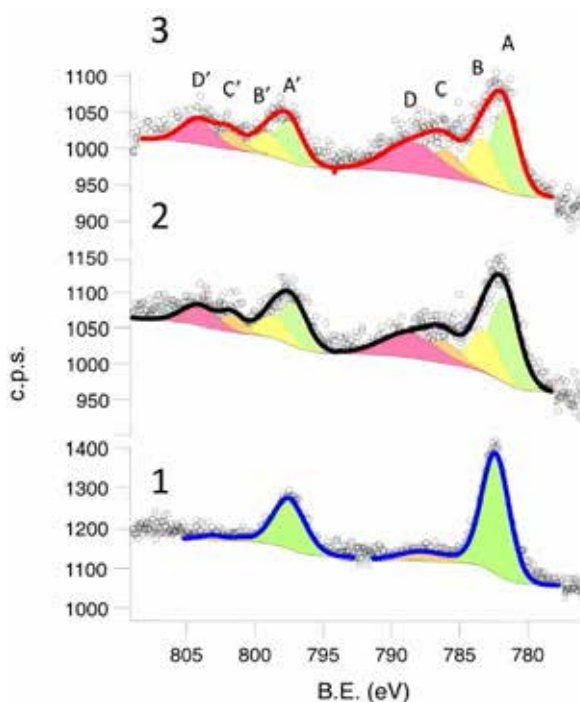
Figure 6. Co*2p* R.T. XPS spectra of compounds [CoL1-dioxo-R-dioxo-CoL1], [CoL2-dioxo-R-dioxo-CoL2] and [CoL3-dioxo-R-dioxo-CoL3] along with best fit components, as reported in Table 2.

Table 2. Results of XPS spectral fitting of [CoL1-dioxo-R-dioxo-CoL1], [CoL2-dioxo-R-dioxo-CoL2] and [CoL3-dioxo-R-dioxo-CoL3] with the procedure reported in the text, along with semi-quantitative evaluation of their chemical composition.

	Co						N		S		P		F
		A	B	C	D	S.O.[3]							
	%	B.E.[2] (%)	B.E.[2] (%)	B.E.[2] (%)	B.E.[2] (%)		Co/N	%[1]	Co/S	%[1]	Co/P	%[1]	%[1]
[CoL1-dioxo-R-dioxo-CoL1]	7.4	782.4 (89.2)	786.0 (2.5)	788.0 (8.3)	n.a. (n.a.)	15.1	0.2	**6.5**	1.1	**7.2**	1.0	**7.2**	47.2
[CoL2-dioxo-R-dioxo-CoL2]	7.6	781.6 (42.1)	783.2 (21.5)	786.2 (12.5)	788.6 (23.9)	15.5	0.3	**7.5**	1.0	**6.2**	1.2	**6.2**	48.1
[CoL3-dioxo-R-dioxo-CoL3]	7.3	781.7 (36.3)	783.3 (20.7)	786.0 (15.1)	788.4 (27.9)	15.8	0.3	**7.1**	1.0	**7.8**	0.9	**7.8**	49.8
Theor.	**7.7**						0.3	**7.7**	1.0	**7.7**	1	**7.7**	46.2

4. Functional hybrid electrodes based on light switchable molecules.

The first step of our XPS analysis involved a semiquantitative determination of the elemental composition of **[CoL1-dioxo-R-dioxo-CoL1], [CoL2-dioxo-R-dioxo-CoL2]** and **[CoL3-dioxo-R-dioxo-CoL3]** using Co$2p$ (Figure 4), N$1s$, S$2p$, P$2p$, F$1s$ (Figure 7) core levels. Carbon and oxygen contributions were discarded since they may be affected by spurious contaminations, inasmuch the samples were mounted like bulk polycrystalline samples on carbon tape to achieve higher intensity then on a drop-cast sample. This analysis confirmed the theoretical stoichiometric composition of the complexes, which is expected to be the same for the three compounds with regard to the investigated elements (see Table 2). In Table 2 are reported the molar percentage, the binding energies (B.E.) and spin-orbit splittings (S.O.) for the three systems. Component contributions are reported in brackets. The experimental ratios between the most significant contributions (Co/N, Co/S, Co/P) agree as well with the theoretical ones. Additional information can be extracted by analyzing the line shape of the Co$2p$ spectra of **[CoL1-dioxo-R-dioxo-CoL1], [CoL2-dioxo-R-dioxo-CoL2]** and **[CoL3-dioxo-R-dioxo-CoL3]**. This region was fitted following previously reported procedure for *ls*-Co^{III} and *hs*-Co^{II} complexes;[36,37] Table 2 and Figure 6 report the results of the fitting analysis. Co$2p_{3/2}$ region has been reproduced with 3 or 4 components (A-D), along with the corresponding Co$2p_{1/2}$ spin-orbit coupled contributions (A'-D'), weighted by the expected 2:1 ratio. In agreement with literature reports, the S.O. shift depends on the Co redox state and is larger for the *hs*-Co^{II} ion than for the *ls*-Co^{III} one (15.8 eV for **[CoL3-dioxo-R-dioxo-CoL3]** and 15.1 eV for **[CoL1-dioxo-R-dioxo-CoL1]**). This indicates that complex **[CoL2-dioxo-R-dioxo-CoL2]**, whose room temperature S.O. shift is 15.5 eV, is constituted mainly by *hs*-Co^{II} ions but indeed contains a relevant *ls*-Co^{III} molar fraction, in agreement with magnetometric data. Moreover, the Co$2p$ spectrum of **[CoL1-dioxo-R-dioxo-CoL1]** can be reproduced by a main peak (A) centered at 782.4 eV, with only minor contributions at higher binding energies (B, C, plus the corresponding S.O. peaks), in line with the electronic ground state expected for an octahedrally coordinated *ls*-Co^{III} ion.[38] Compounds **[CoL2-dioxo-R-dioxo-CoL2]** and **[CoL3-dioxo-R-dioxo-CoL3]**, on the contrary, display more complex spectral patterns due to the presence of shake-up components, typical of *hs*-Co^{II} systems in octahedral coordination environment and in line with previous reports about inorganic[39] and metallorganic[36] *ls*-Co^{III} and *hs*-Co^{II} compounds. This approach points out that comparison of XPS spectra of structurally related VT complexes can be used as in-house analytical tool to obtain information about their electronic charge distribution. Anyway, a quantitative description of their temperature and light

98

conversion features requires higher sensitivity techniques, like synchrotron based absorption spectroscopies.
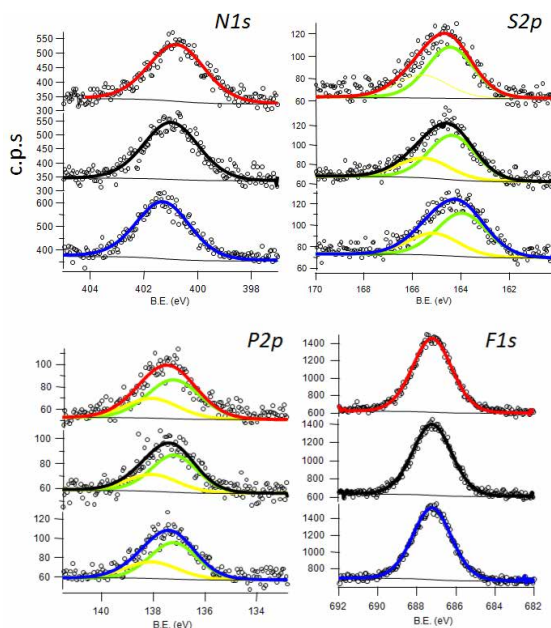
Figure 7. R.T. XPS spectra of compounds [CoL1-dioxo-R-dioxo-CoL1] (blue), [CoL2-dioxo-R-dioxo-CoL2] (black) and [CoL3-dioxo-R-dioxo-CoL3] (red) at the *N1s,* S*2p*, P*2p* and F*1s* core levels.

4.1.4 X-Ray Absorption Spectroscopy.

X-Ray Absorption Spectroscopy (XAS) has been shown to be an unmatched tool for the analysis of thermally- and optically-triggered transitions of bistable molecular materials, affording spectral analysis of the processes with atomic selectivity and sensitivity to investigate bulk and surface confined molecular assemblies.[40] XAS has been employed to study the electronic and structural features of switchable materials like polycyanometallates[41] and Fe[II] complexes[42,43] and to investigate the effect of surface confinement on their bistability.[44] In the case of VT materials, it helped in clarifying the electronic states involved in the pressure-,[45] entropy-[46] and light-driven conversions[47] and revealed that sof X-rays can act as a source of photo-conversion, though the microscopic mechanism involved in the excitation process remained to be clarified.[6] More recently, this technique provided definitive evidence

of the valence tautomeric nature of the transition in a two-centered Cobalt-dioxolene complex.[19]

Temperature and light dependent XAS at the Co $L_{2,3}$ edge was here employed to assess the charge distribution of the bulk phase of **[CoL1-dioxo-R-dioxo-CoL1]-[CoL3-dioxo-R-dioxo-CoL3]** compounds. Unlike for XPS, in XAS experiments, the sample were prepared by drop-casting the complexes from mM solutions on gold because the conduction of the sample was very important due to the employed TEY detection mode.

Figure 8 shows room temperature XAS Co L_3 edge spectra of compounds **[CoL1-dioxo-R-dioxo-CoL1]** and **[CoL3-dioxo-R-dioxo-CoL3]**, the temperature dependence of the normalised Co L_3 edge spectra of **[CoL2-dioxo-R-dioxo-CoL2]**, and the *hs*-Co[II] and *ls*-Co[III] theoretical spectra calculated for the parent complex with unfunctionalised dioxolene ligand using a Ligand Field Multiplet (LFM) approach.[6]
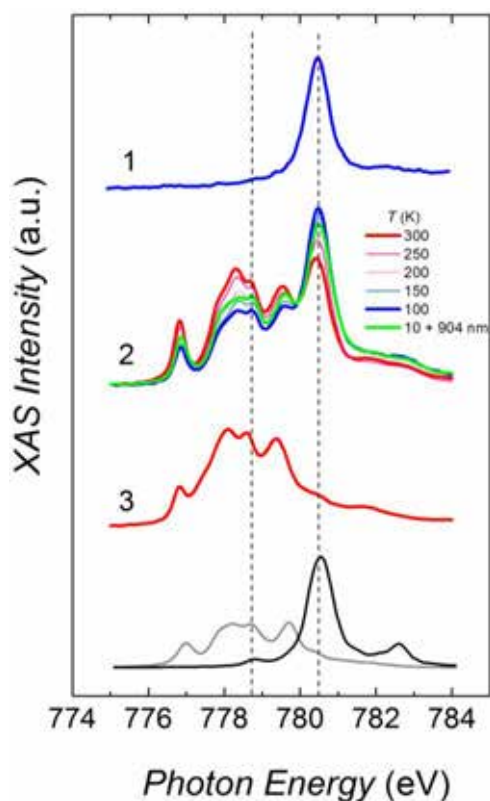
Figure 8. Co L_3 edge X-ray absorption spectra of [CoL1-dioxo-R-dioxo-CoL1], [CoL2-dioxo-R-dioxo-CoL2] and [CoL3-dioxo-R-dioxo-CoL3], along with calculated spectra for pure *hs*-Co[II] (grey line) and *ls*-Co[III] (black line) phases.

100

XAS analysis of compounds **[CoL1-dioxo-R-dioxo-CoL1]** and **[CoL3-dioxo-R-dioxo-CoL3]** confirms a temperature independent charge distribution, *ls*-Co^{III} and *hs*-Co^{II}, respectively, insensitive to the irradiation with X-ray beam. On the other hand the 300 K spectrum of **[CoL2-dioxo-R-dioxo-CoL2]** presents a superposition of signals belonging to the two redox isomeric forms. On cooling from 300 to 100 K the main feature at 781.5 eV, associated with the *ls*-Co^{III} ion, gains intensity, while the spectral band related to the *hs*-Co^{II} contribution flattens down. This indicates the occurrence of Valence Tautomeric interconversion, similarly to what was previously found for similar Co-based molecular switchable materials.[42,48,48] When lowering temperature from 100 to 10 K, XAS indicates an increase in the *hs*-Co^{II} metastable phase which is not observed by magnetometry. This strongly suggests that this is an X-ray induced effect, which can be interpreted in terms of SOXIESST (Soft X-ray Induced Excited Spin State), a reversible phenomenon previously observed for photo-switchable molecular systems.[6,49]
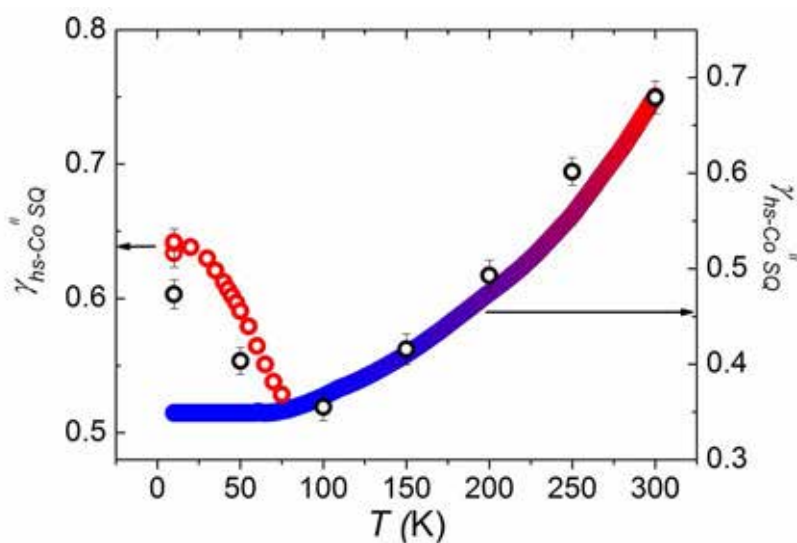
Figure 9. Thermal dependence of the *hs*-Co^{II} distribution profile obtained from deconvolution of X-ray absorption spectra (empty black circles); empty red circles display the thermally activated relaxation after 904 nm laser light. For comparison the colour band is the conversion profile obtained by rescaling magnetic measurements.

A quantitative estimation of the *hs*-Co^{II} thermal distribution profile is reported in Figure 9, as calculated from spectral deconvolution using the theoretical spectra as limiting compositional references for the electronic states of **[CoL2-dioxo-R-dioxo-CoL2]**: it displays a smooth conversion profile in the 100 – 300 K range, in accordance

with magnetometric analysis. The presence of a remaining fraction of hs-Co^{II} phase at low temperature is confirmed by this technique, corresponding to 52 % of the overall Co content, to be compared with the 39 % estimated with standard magnetometry. Beside thermal- and X-ray-driven VT, XAS spectra allowed to demonstrate the occurrence of the light induced transition, evidencing an additional increase of the hs-Co^{II} feature when the sample was irradiated with a 904 nm laser light for 30 minutes at 10 K (Figure 9, red dots). The photo-converted ls-Co^{III} percentage increases from the 11 % found by magnetometry up to the 25 % observed with XAS: such discrepancy must be related to the non-innocent nature of the X-Ray beam on the charge distribution of the sample.[6] Finally, following the procedure carried out in traditional magnetometric experiments for determining T_{LIESST}, we monitored the temperature dependence of the photo-induced hs-Co^{II} fraction after laser irradiation with XAS (Figure 10).
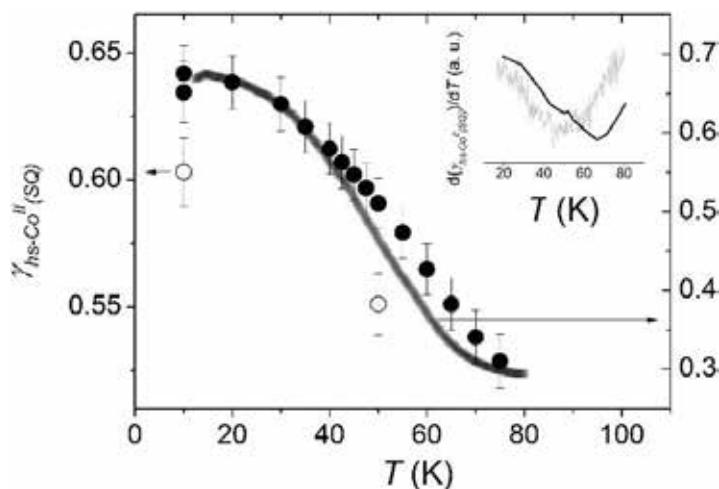
Figure 10. Temperature dependence of the hsCoII fraction of [CoL2-dioxo-R-dioxo-CoL2] measured with standard magnetometry (black fading line) and XAS before (empty circles) and after (full circles) 904 nm laser light irradiation. *Inset*: **Corresponding first derivative plots to extract T$_{LIESST}$ (grey line = magnetometry data; black line = XAS data).**

Here, the T_{LIESST} value increases from 49 to 60 K: in this case, however, differences in the temperature control setup and the non-innocence of X-rays on the low temperature electronic configuration of **[CoL2-dioxo-R-dioxo-CoL2]** may play a role in determining the minimum in the first derivative plot of the thermal distribution profile of the hs-Co^{II}(SQ) photo-induced molar fraction.

Summarizing the content of this part, temperature-dependent magnetometric analysis confirms that chemically driven tuning of the redox potential of the $[Co(Me_ntpa)]^{3+/2+}$ couple is possible in this molecular context as well: consequently, while **[CoL1-dioxo-R-dioxo-CoL1]** and **[CoL3-dioxo-R-dioxo-CoL3]** feature *ls*-Co^{III}(Cat) and *hs*-Co^{II}(SQ) temperature independent charge distributions, respectively, **[CoL2-dioxo-R-dioxo-CoL2]** displays a partial entropy-driven switchability in the temperature range investigated.

4.2 Observation of Valence Tautomerism at the nanoscale

As anticipated in the previous paragraph (4.1), switchable coordination systems featuring a reversible switching of electronic state at the molecular level promise breakthrough outcomes for information storage and processing technologies.[50] In particular, the control of length and direction of the spin in paramagnetic switchable molecules represents a key feature to be used in quantum computation and nanosized spintronic applications.[51–53] During the last few years huge research efforts have been spent investigating the effect of deposition on solid surfaces of a specific class of switchable molecular materials, the Fe(II) based Spin Crossover (SCO) coordination systems.[54] These studies revealed that thin films of SCO systems can be grown through sequential assembly or patterned on solid surface with the retention of their bulk phase switchability properties.[54,55] Lower surface coverages has been achieved by means of ultra-high vacuum sublimation techniques,[55,56] allowing the manipulation of their electronic state through scanning probe techniques.[44,57] Unfortunately, direct interaction of the thermally evaporated molecules with the metallic surface resulted in a pinning of their spin states and a capability to interconvert significantly reduced with respect to their massive phase behavior.[44,55–58]

It appears therefore of interest to deposit systems exhibiting Valence Tautomerism on conducting surfaces and investigate their thermal and optic bistability at the level of the monolayer.

4. Functional hybrid electrodes based on light switchable molecules.
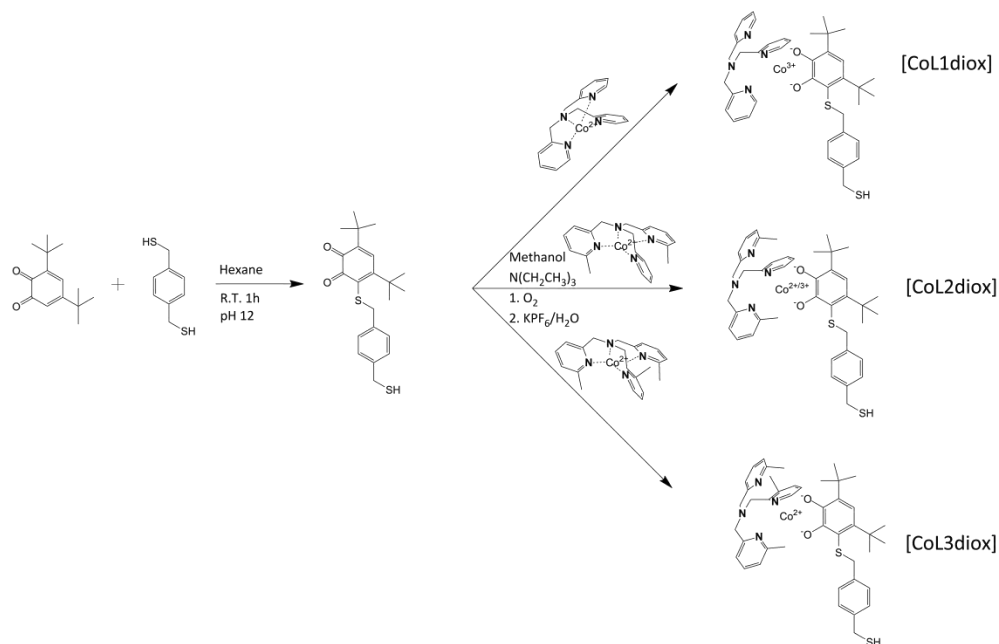
Figure 11. Synthetic pathway to the thiol-functionalised DBCatSH ligand and to the [CoL1diox], [CoL2diox] and [CoL3diox] complexes used in this study.

The **[CoLn-dioxo-R-dioxo-CoLn]** with the thioether bridge was modify to achieve a thiol terminal group in order to graft **[CoLdiox]** systems on a gold surface. We prepared a family of complexes of general formula [Co(Me$_n$tpa)DBCatSH](PF$_6$)· CH$_3$OH] (n = 0, 2, 3) for compound **[CoL1diox]**, **[CoL2diox]** and **[CoL3diox]**, respectively), where like for the **[CoLn-dioxo-R-dioxo-CoLn]** system, Me$_n$tpa are differently methylated derivatives of tris-pyridil-amine and DBCatSH is the 3,5-di-tert-butyl-catecolate ligand functionalised with a thiol moiety (Figure 11).

4.2.1 Characterisations of bulk [CoLdiox] samples

In order to characterize the massive phase of compounds **[CoL1diox]**, **[CoL2diox]** and **[CoL3diox]** we performed a bulk characterisations based on ToF-SIMS mass characterisation in order to verify the synthesis procedure and to obtain reference mass spectra to compare to those of monolayers. In addition the temperature dependence of the $\chi_M T$ product for all the compounds and the temperature dependence of $\chi_M T$ of **[CoL2diox]** after 904 nm irradiation at 10 K were measuresd, and XPS spectra recorded as a function of the temperature.

4.2.1.1 Mass characterisation of [CoLdiox] bulk samples

Figure 12 compares the positive ions mass spectra of bulk samples. A comparison among the spectrum of **[CoL2diox]** with the ones of **[CoL1diox]** and **[CoL3diox]** reported in Figure 12, points out a straightforward correlation among the spectra. This relation in the fragmentation patterns arises from the different number of methyl groups in the three complexes and evidences that the shared DBCatSH ligand is the main site of molecular fragmentation (Table 3). In all cases, due to the ionic nature of the complexes, the $(PF_6)^-$ counterion is not detected in the investigated positive spectra region while the intact $[Co(Me_n tpa)DBCatSH]^+$ cations are present in each investigated bulk sample (737.22 m/z, 765.25 m/z and 779.31 m/z for **[CoL1diox]**, **[CoL2diox]** and **[CoL3diox]**, respectively). In Table 3 a complete peak assignation is reported for bulk samples **[CoL1diox]**, **[CoL2diox]** and **[CoL3diox]** peak in each spectrum.
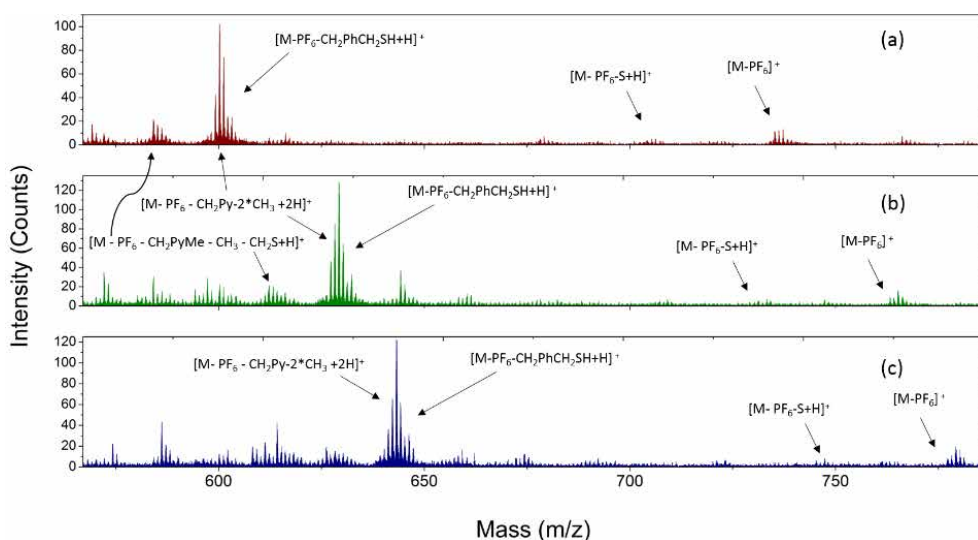
Figure 12. Positive ToF-SIMS spectra of bulk of [CoL1diox], [CoL2diox] and [CoL3diox] measured in static regime.

Table 3. **Summary of ToF-SIMS peaks expected and experimentally found for bulk samples [CoL1diox], [CoL2diox] and [CoL3diox].**

Fragment	[CoL1diox]			[CoL2diox]			[CoL1diox]		
	Theor. (m/z)	Bulk (m/z)		Theor. (m/z)	Bulk (m/z)		Theor. (m/z)	Bulk (m/z)	
$[M- PF_6]^+$	737.24	737.25	(s)	765.27	765.26	(s)	779.29	779.29	(s)
$[M- PF_6\text{-}S+H]^+$	705.27	705.30	(w)	733.30	733.29	(w)	747.31	747.30	(w)
$[M- PF_6\text{-}tbu+H]^+$	681.18	681.19	(vw)	709.20	709.20	(vw)	723.22	723.19	(vw)
$[M- PF_6\text{-}CH_2PyCH+H_3]^+$	646.20	n.d	-	660.21	660.38	(m)	674.22	674.35	(m)
$[M- PF_6 - CH_3\text{-}CH_2PyMe +2H]^+$	632.18	n.d	-	644.18	644.26	(m)	660.21	660.33	(w)
$[M- PF_6 - CH_2Py\text{-}2^*CH_3 +2H]^+$	616.15	616.23	(s)	632.18	632.31	(s)	646.19	646.31	(s)
$[M- PF_6\text{-}CH_2C_6H_4CH_2SH +H]^+$	601.20	601.23	(vs)	629.24	629.25	(vs)	643.25	643.24	(vs)
$[M - PF_6 - CH_2Py - CH_2S+H]^+$	600.21	600.22	(s)	612.21	612.20	(w)	628.24	628.26	(m)
$[M - PF_6 - CH_2PyMe - CH_3 - CH_2S+H]^+$	586.20	586.17	(m)	600.21	600.24	(w)	614.23	600.24	(m)
$[M - PF_6 -S - CH_2C_6H_4CH_2S+H]^+$	569.23	569.23	(m)	597.26	597.27	(m)	611.27	611.28	(m)

4.2.1.2 Magnetic characterisation of [CoLdiox] bulk samples.

Magnetometry data (Figure 13) evidence a room temperature charge distribution of *ls*-Co[III]Cat for **[CoL1diox]**, *hs*-Co[II]SQ for **[CoL3diox]**, and a mixture of the two for **[CoL2diox]**, as expected on the basis of what reported in section 4.1 and on similar Co-dioxolene based systems.[8,19,59] For the complex **[CoL2diox]**, the thermal evolution of the product of the molar magnetic susceptibility by the temperature, $\chi_M T$ (Figure 13a), points out a reversible interconversion between the two redox isomers in the solid state, in line with an entropy driven VT process. Using magnetic moment values of **[CoL1diox]** and **3** as references for *ls*-Co[III]Cat and *hs*-Co[II]SQ phases and using the Eq.3 chapter 4.2.1, it is possible to quantitatively describe the thermal distribution profile of **[CoL2diox]**. The VT interconversion features a remaining 40% *hs*-Co[II]SQ fraction at 10 K and occurs on a temperature range broader than the experimentally accessible one in our setup, reaching 66 % at 300 K, in analogy with different sulphur-functionalised [CoLdiox][+] switchable complexes.[60,61]
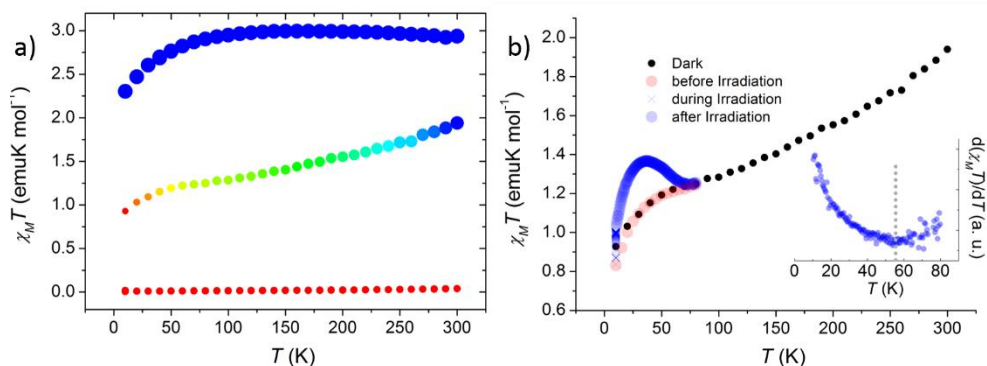
Figure 13. a): Temperature dependence of the $\chi_M T$ product of [CoL1diox] (small red circles), [CoL2diox] (full circles of variable color), and [CoL3diox] (large full blue circles); b): temperature dependence of $\chi_M T$ of 2, before (red circles), during (blue crosses) and after (blue circles) 904 nm irradiation at 10 K. In the inset the temperature derivative allow to extract T_{LIESST}.

The VT conversion of **[CoL2diox]** can also be triggered by low temperature light irradiation (Figure 13b panel): excitation of the ligand to metal charge-transfer band at 10 K turns 15 % of the *ls*-Co^{III}Cat content to the *hs*-Co^{II}SQ metastable phase. Upon heating at a 0.3 K/min rate, complete population of the ground state is recovered at 75 K, while the temperature with the highest measurable relaxation rate (T_{LIESST}) is found to be 55 K (insert panel Figure 13b). Compared with previously analysed **[CoLn-dioxo-R-dioxo-CoLn]** VT systems,[6,7,59] these data confirm that light-triggered bistability is a strictly molecular phenomenon and the switchability mechanism is strictly related to Co redox potential.

4.2.1.3 XPS characterisation of [CoLdiox] bulk samples

In Table 4 are reported the semiquantitative analysis and the stoichiometric ratios of the three complexes. These data are in accordance with the theoretical percentages and confirm ToF-SIMS data, suggesting that the starting material is suitable for the depositions on surface.

Additional information have been obtained by the XPS investigation that has been performed on bulk samples of **[CoL1diox]**, **[CoL2diox]** and **[CoL3diox]** complexes

4. Functional hybrid electrodes based on light switchable molecules.

using the same protocol of the paragraph 4.1 for the **[CoLn-dioxo-R-dioxo-CoLn]** complex family. The direct comparison of the Co 2*p* regions in the solid state of **[CoL2diox]** (Figure 14c) proves a different peak deconvolution due to a variation in temperature of the bulk sample of **[CoL2diox]**.

Table 4. Theoretical and XPS estimated atomic percentages and ratios for [CoL1diox], [CoL2diox] and [CoL3diox] complexes in bulk.

Bulk	Co	N 1s		S 2p		P 2p		F 1s	
	%	%	N/Co	%	S/Co	%	P/Co	%	F/Co
[CoL1diox]	6.7	29.2	4.3	14.0	2.1	7.6	1.1	42.6	6.3
[CoL2diox]	6.7	26.9	4.0	13.7	2.0	7.3	1.1	45.4	6.6
[CoL3diox]	7.6	27.9	3.7	11.7	1.5	6.9	0.9	45.8	6.0
theor.	7.1	28.6	4.0	14.3	2.0	7.1	1.0	42.9	6.0

So with XPS characterisation one can provide not only the semiquantitative analysis but is possible to follow also the temperature conversion of the **[CoL2diox]** complex in the bulk phase but due to its sensitivity, XPS technique could give us those type of information also for the monolayer samples. [59] The Co2*p* spectrum of **[CoL1diox]** in bulk has the typical lineshape of *ls*-Co^{III} photoemission:[59,36,62] it shows a main peak at 782.4 eV, integrating about 76 % of the overall signal area, and minor satellites at 786.7, 789.3 and 792.8 eV, with ΔE_{SO} contributions separated by 15.1 eV, in analogy to literature reference (and Figure 14).[59] Complex **[CoL3diox]**, on the other hand, presents a more structured spectrum, with high intensity satellites, as expected for *3d* ions with unquenched orbital momentum. The main peak is centred 782.3 eV and integrates about 48 % of the whole signal area, with satellites at 785.9, 788.5 and 792.0 eV, and a ΔE_{SO} of 16.0 eV, in accordance with literature data.[59,62] Both Co2*p* photoemissions do not display any temperature dependence in the 170 – 300 K range. As supposed the two complexes, **[CoL1diox]** and **[CoL3diox]**, are not affected by a temperature variation as expected because of the energy difference between redox isomers in **[CoL1diox]** and **[CoL3diox].**
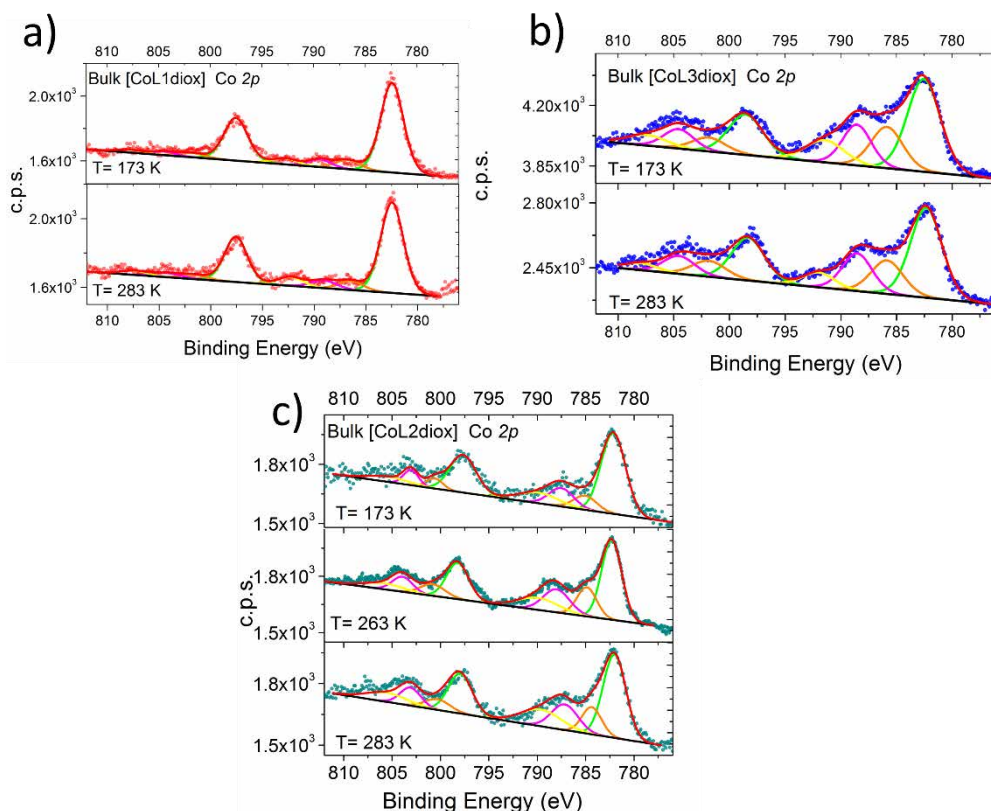
Figure 14. Co2p XPS spectra of compounds a) [CoL1diox], c) [CoL2diox] and b) [CoL3diox] along with best-fit components in function of the temperature.

The room temperature XPS Co2*p* spectral features of a bulk of **[CoL2diox]** are different from those of *ls*-Co^{III} and *hs*-Co^{II} reported above: even displaying a closer resemblance with the latter, **[CoL2diox]** shows a slightly lower ΔE_{SO} (15.9 eV), suggesting the presence of both charge distributions. Moreover, on cooling from 283 K to 173 K, an increase in the main peak contribution of the overall signal intensity (from 50% up to about 62%, respectively) parallels a reduction in the ΔE_{SO} (15.9 to 15.5 eV), indicating the presence of a thermally driven VT conversion in the bulk phase of this complex.

Particularly indicative when the chemisorption will be promoted, the formation of a Au-S bound, will be noticed as a shift in the BE of S2*p*. In the bulk phase, the S2*p* region can be reproduced using a photoemission peak centred at 162.7 eV (Figure 15), with a spin-orbit splitting (ΔE_{SO}) of 1.2 eV, as expected for the two sulphur atoms present in the molecule in very similar chemical environments.[63] All the other peaks

are at the binding energies expected for those type of compunds[59] and C*1s* deconvolution is composed by two different components attributable at different C-C and C-O chemical environment at 284.7 eV and 286.2 eV respectively. The N*1s* can be reproduced using one component due to all equivalent nitrogen chemical environment and centred at 399.8 eV. [59] P*2p* and F*1s* were in line with what expected for this type of counterion.[64]
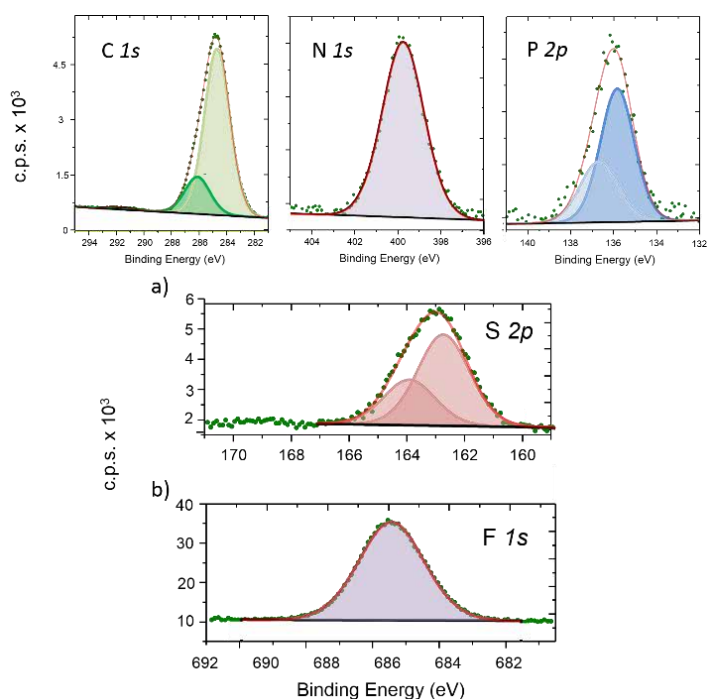
Figure 15. Massive phase C*1s*, N*1s*, P*2p*, S*2p* and F*1s* of compound [CoL2diox].

4.2.2 [CoLdiox] monolayers characterisation

Monolayers of **[CoL1diox]**, **[CoL2diox]** and **[CoL3diox]** complexes were prepared by incubation of 150 nm thick Au(111) films evaporated on mica (flame annealed with hydrogen flame before the immersion) in 2 mM dichloromethane solutions of the complexes for 18 hours at room temperature; after incubation the slides were rinsed several times with dichloromethane to leave on the surface only the chemisorbed molecules and dried with nitrogen using a portable glove-bag to minimize the air exposition. For more details see chapter 5.

4.2.2.1 Mass spectrometry characterisation of [CoLdiox] monolayers

The integrity of the surface supported molecules was first checked with time of flight-secondary ion mass spectrometry (ToF-SIMS).
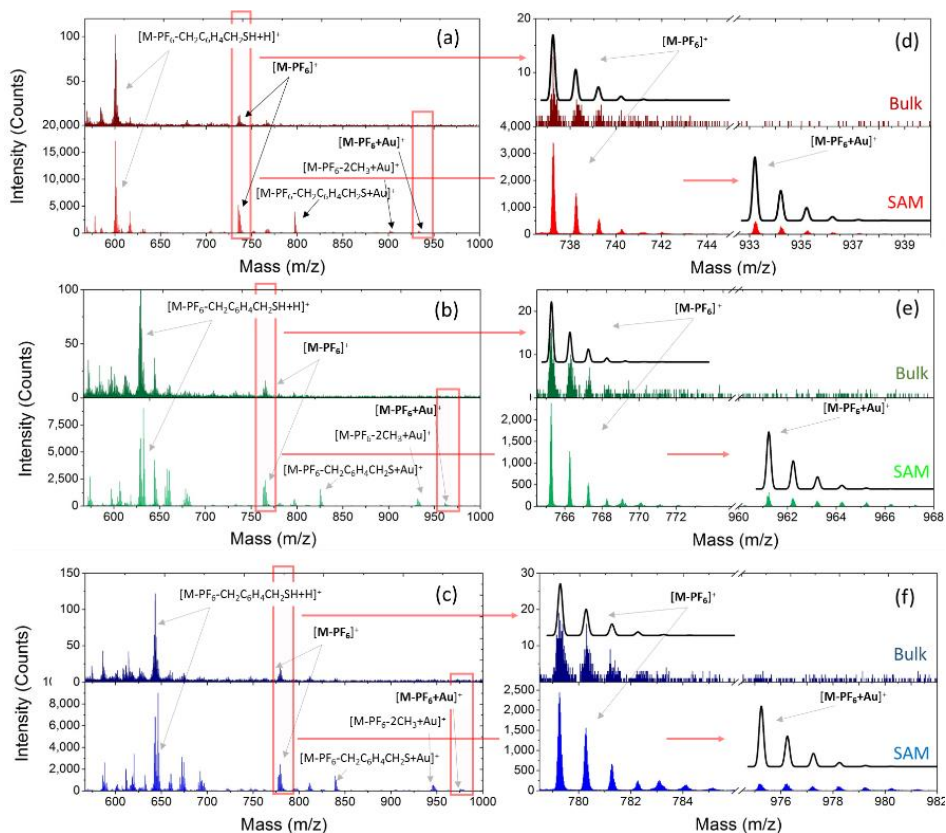
Figure 16. *Panels a-c)*: **Positive ToF-SIMS spectra of bulk and monolayer of [CoL1diox] (red line), [CoL2diox] (green line), and [CoL3diox] (blue line) Panels d-f): Magnification of the [M-PF6]$^+$ and [M-PF6-H+Au]$^+$ regions for bulk and monolayer samples of [CoL1diox], [CoL2diox] and [CoL3diox] complexes. The calculated isotopic distribution pattern expected for each fragment is reported as a black line.**

Figure 16 compares the positive ions mass spectra of bulk and monolayer samples of **[CoL1diox]**, **[CoL2diox]** and **[CoL3diox]** complexes. Clear correlations among the spectra can be easily observed in the three systems (see Figure 16). In fact in the fragmentation pattern follows the one observed in the bulk phase (4.2.2.1 section) and arises from the different number of methyl groups present in each system.

4. Functional hybrid electrodes based on light switchable molecules.

Table 5. Summary of ToF-SIMS peaks expected and experimentally found for monolayer samples of [CoL1diox], [CoL2diox] and [CoL3diox].

Fragment	[CoL1diox]			[CoL2diox]			[CoL3diox]		
	Theor. (m/z)	Monolayer (m/z)		Theor (m/z)	Monolayer (m/z)		Theor. (m/z)	Monolayer (m/z)	
$[M-PF_6+S-H+Au]^+$	965.17	965.15	(vw)	993.20	993.19	(vw)	1007.22	1007.19	(vw)
$[M-PF_6-CH_3+S-H+Au]^+$	950.14	950.16	(vw)	978.18	978.21	(vw)	992.19	992.20	(vw)
$[M-PF_6-H+Au]^+$	933.20	933.18	(w)	961.23	961.22	(w)	975.24	975.20	(w)
$[M-PF_6-CH_3+Au]^+$	918.17	918.20	(vw)	948.22	948.26	(vw)	961.23	961.24	(vw)
$[M-PF_6-2*CH_3+Au]^+$	903.15	903.20	(m)	931.18	931.24	(m)	945.20	945.25	(m)
$[M-PF_6-C(CH_3)_3+Au]^+$	8771.30	nd	-	905.17	905.13	(vw)	919.18	919.14	(vw)
$[M-PF_6-C(CH_3)_3+Au-CH_3+2H]^+$	863.12	863.12	(vw)	891.15	891.15	(vw)	905.17	905.16	(vw)
$[M-PF_6-CH_2C_6H_4CH_2S+Au]^+$	797.16	797.15	(s)	825.19	825.17	(m)	839.21	839.16	(m)
$[M-PF_6-CH_2C_6H_4CH_2S-CH_3+H+Au]^+$	783.15	783.18	(vw)	811.18	811.23	(vw)	825.19	825.20	(vw)
$[M-PF_6+S+H]^+$	769.21	769.19	(vw)	797.24	797.23	(vw)	811.23	811.23	(vw)
$[M-PF_6]^+$	737.24	737.22	(s)	765.27	765.25	(s)	779.29	779.26	(s)
$[M-PF_6-S+H]^+$	705.27	705.25	(vw)	733.30	733.28	(vw)	747.31	747.29	(vw)
$[M-PF_6-C(CH_3)_3+H]^+$	681.18	681.00	(vw)	709.20	709.20	(vw)	723.22	723.16	(vw)
$[M-PF_6-CH_2C_5H_3NCH+H_3]^+$	646.20	n.d	-	660.21	660.37	(m)	674.22	674.36	(m)
$[M-PF_6-CH_3-CH_2C_5H_3NCH_3+2H]^+$	632.18	n.d	-	644.18	644.21	(m)	660.21	660.34	(m)
$[M-PF_6-CH_2C_5H_3N-2*CH_3+2H]^+$	616.15	616.18	(s)	632.18	632.34	(vs)	646.19	646.33	(vs)
$[M-PF_6-CH_2C_6H_4CH_2SH+H]^+$	601.20	601.20	(vs)	629.24	629.23	(s)	643.25	643.22	(vs)
$[M-PF_6-CH_2C_5H_3N-CH_2S+H]^+$	600.21	600.19	(s)	612.21	612.19	(vw)	628.24	n.d.	-
$[M-PF_6-CH_2C_5H_3NCH_3-CH_3-CH_2S+H]^+$	586.20	586.20	(m)	600.21	n.d.	-	614.23	n.d.	-
$[M-PF_6-S-CH_2C_6H_4CH_2S+H]^+$	569.23	569.22	(m)	597.26	597.25	(m)	611.27	611.25	(m)

This evidence confirms that, also in monolayer samples, the shared DBCatSH ligand is the main site of molecular fragmentation and retain the same behaviour. In all cases, due to the ionic nature of the complexes, the $(PF_6)^-$ counterion is not detected while the presence of intact $[Co(Me_ntpa)DBCatSH]^+$ cations on surface is

witnessed by the observation of the corresponding $[M-PF_6]^+$ peak in each spectrum (737.22 m/z, 765.25 m/z and 779.31 m/z for **[CoL1diox]**, **[CoL2diox]** and **[CoL3diox]**, respectively). Moreover, a support to the hypothesis of formation of a single layer of molecules on surface is given by the presence of the molecular cation peak bound to a gold atom, $[M-PF_6 -H + Au]^+$, absent in bulk samples. This indicates the formation of molecule-substrate covalent bond, in analogy to what has been observed on other monolayers on Au(111).[65] A detailed and more complete fragment assignation is reported in Table 5.

4.2.2.2 XPS characterisation of [CoLdiox] monolayers

A complete XPS characterisation of the monolayers of the three complexes was confirmed because this technique allows to evaluate the stoichiometry of the molecular film deposited on surface. Moreover, accordingly to what has been reported for this complex as well as for the dimeric system presented earlier, it is possible to follow by XPS the temperature conversion of compound **[CoL2diox]** obtaining an additional confirmation of the stability of this VT system once chemisorbed.

The direct comparison of the S2p regions in the bulk sample and monolayer of **[CoL2diox]** (Figure 17a) provides further evidences of the chemisorption on Au. In the bulk phase, the S2p region can be reproduced using a photoemission peak centred (Figure 14) at 162.7 eV. In the monolayer sample, an additional signal appears at 161.7 eV, integrating 46 % of the overall S2p photopeak area: this component is directly attributed to the thiol group covalently bound to the Au surface, in analogy with previous reports on thiol based monolayers.[66,67] A minor (8%) fraction at 168.4 eV is assigned to spurious oxidation of the sulphur atoms, usually related to defects in the thiol-based molecular packing on surface.[65]

4. Functional hybrid electrodes based on light switchable molecules.
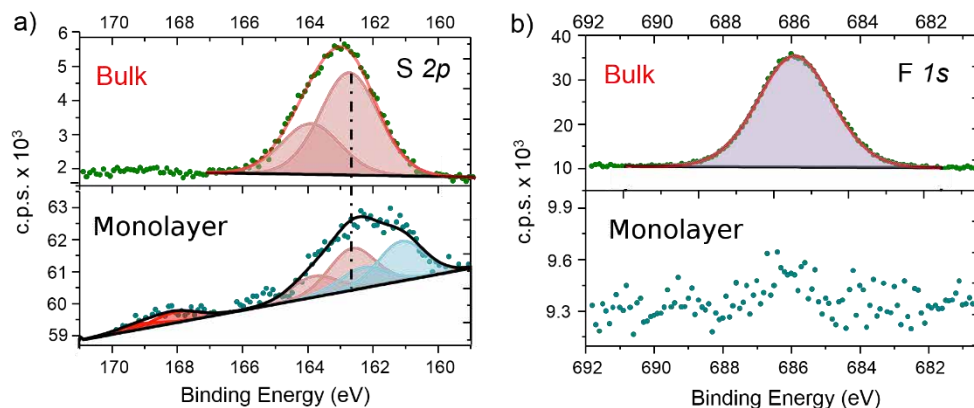
Figure 17. a) Comparison between S2*p* XPS spectra of [CoL2diox] in the massive phase and monolayer, along with best fitting lines. b) Disappearance of the F*1s* photopeak on moving from massive phase to monolayer sample of [CoL2diox].

Co2*p* XPS spectra yielded clear prints of charge distributions in Cobalt-dioxolene adducts also in the monolayers. In the following we will describe how from this analysis of monolayer samples of **[CoL1diox]**, **[CoL2diox]** and **[CoL3diox]** we qualitatively followed the VT conversion of surface deposited system by focusing on the electronic state of the metal ion (Figure 18).

At room temperature the Co2*p* spectrum of a monolayer of **[CoL1diox]** has the typical lineshape of *ls*-Co^{III} photoemission accordingly to our previous bulk analyses (Figure 14c).[59,36,62] The deconvolution shows a main peak at 781.5 eV, integrating about 50 % of the overall signal area, and minor satellites at 784.7, 788.0 and 792.2 eV, with ΔE_{SO} contributions separated by 15.1 eV, in analogy to the bulk analogue (Figure 14c and

Table 7). Complex **[CoL3diox],** as expected from bulk measurements, presents at RT a more structured spectrum, with high intensity satellites. The main peak shifts to 781.2 eV and integrates about 40 % of the whole signal area, with satellites at 785.2, 788.6 and 792.1 eV, and a ΔE_{SO} of 16.0 eV, in accordance with powder (

Table 7) and literature data.[59] Like for the bulk samples these two reference samples do not display any temperature dependence in the 170 – 300 K range. Thus, surface deposition did not affect the electronic ground states of these complexes, as expected because of the energy difference between redox isomers in **[CoL1diox]** and **[CoL3diox]**.

114

In contrast, the XPS Co2*p* spectra of a monolayer of **[CoL2diox]** features a significative temperature evolution. At RT **[CoL2diox]** shows a ΔE_{SO}=15.8 eV, intermediate between what observed in the two reference samples, suggesting an intermediate charge distributions (*ls*-Co^{III} and *hs*-Co^{II}). Cooling from 283 K to 173 K, an increase in the main peak contribution to the overall signal intensity (from 40% up to about 46%, respectively) parallels a reduction in the ΔE_{SO} (15.8 to 15.4 eV), indicating the presence of a thermally driven VT conversion also in the monolayer.
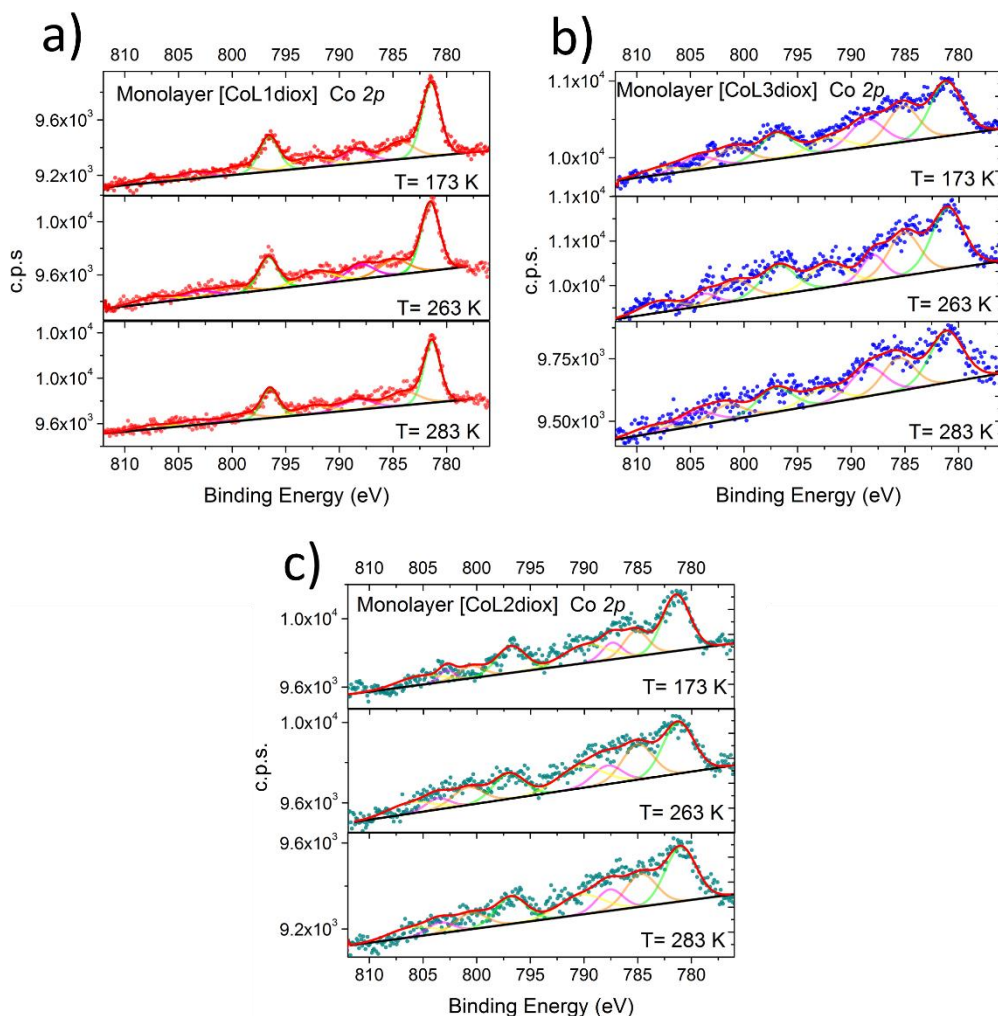
Figure 18. Comparison of XPS Co2*p* spectra of monolayers of a) [CoL1diox], c) [CoL2diox] and b) [CoL3diox] (taken at three different temperatures), along with best fitting lines.

4. Functional hybrid electrodes based on light switchable molecules.

The Co/S ratios observed in the monolayers and reported in Table 6, close to the stoichiometric one, point out that the molecule-Au linkage takes place mainly through the terminal thiol group of diox ligand. Also the N/Co ratio is close to the stoichiometric value pointing out that the molecules maintain their chemical environment and are thus intact on surface.

Table 6. Theoretical and XPS estimated atomic percentages and ratios for monolayers of [CoL1diox], [CoL2diox] and [CoL3diox].

Monolayer	Co %	N 1s %	N/Co	S 2p %	S/Co	P %	F %
[CoL1diox]	14.8	53.1	3.6	31.5	2.1	--	--
[CoL2diox]	14.9	54.6	3.7	30.5	2.0	--	--
[CoL3diox]	14.0	53.7	3.8	32.6	2.3	--	--
theor.	14.3	57.1	4	28.6	2	--	--

Table 7. Spectral components of the Co2p XPS photopeak of bulk (above) and monolayer (below) samples [CoL1diox], [CoL2diox] and [CoL3diox]. Binding energies (B.E.) are in eV. In brackets are reported the integrated area percentages of each component. ΔE_{SO} splittings are in eV.

Co *2p*					
	Components				
	A	B	C	D	ΔE_{SO}
Bulk	B.E. (%)	B.E. (%)	B.E. (%)	B.E. (%)	
[CoL1diox]	782.4, (76.2)	786.7, (8.2)	789.4, (7.4)	792.8, (8.3)	15.1
[CoL2diox], T= 173 K	782.1, (62.2)	785.0(10.3)	787.5, (14.2)	789.9, (13.4)	15.54
[CoL2diox], T= 263 K	782.3, (47.1)	784.9(16.7)	788.0, (17.8)	789.9, (18.4)	15.9
[CoL2diox], T= 283 K	782.0, (50.3)	784.4, (14.0)	787.2, (17.9)	789.7, (17.8)	15.94
[CoL3diox]	782.3, (48.0)	785.9, (19.2)	788.5, (18.9)	792.0, (13.8)	16.0
Monolayer	B.E. (%)	B.E. (%)	B.E. (%)	B.E. (%)	ΔE_{SO}
[CoL1diox]	781.5, (50.9)	784.3, (20.1)	788.3, (14.7)	792.5, (14.4)	15.1
[CoL2diox], T= 173 K	781.4, (46.5)	785.2, (18.6)	787.3, (10.2)	789.8, (24.8)	15.4
[CoL2diox], T= 263 K	781.2, (37.6)	785.0, (26.1)	787.8, (12.7)	790.2, (23.6)	15.8
[CoL2diox], T= 283 K	781.0, (40.5)	784.8, (24.4)	787.6,(13.5)	790.2, (21.6)	15.8
[CoL3diox]	781.2, (40.5)	785.2, (28.3)	788.5, (12.2)	792.2, (19.0)	16.0

Moreover, the disappearance of F*1s* photopeak in monolayer samples for the surface-supported molecules, monitored by the (Figure 17b), is a further experimental evidence of the absence of physisorbed molecules on the Au(111) surface, in analogy to what previously found for monolayer of Fe[III] complexes on Au(111).[68]

4.2.2.3 XAS characterisation of [CoL2ndiox] monolayers

To investigate the VT conversion at the nanoscale with higher accuracy, X-ray absorption spectroscopy (XAS) has been used. Standard magnetometry is not sensitive enough to detect the magnetic state of a monolayer of molecules.
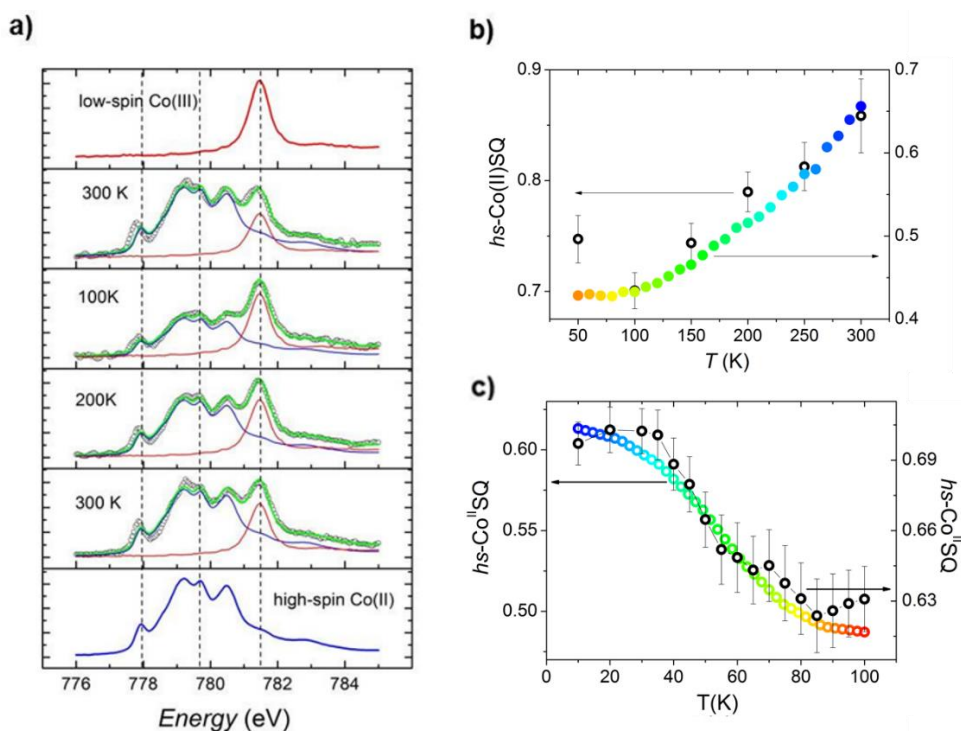
Figure 19. a) Temperature evolution of the normalized Co L$_3$ edge XAS spectra of a monolayer of [CoL2diox] (empty black dots) along with high-spin Co[II] and low-spin Co[III] spectra (blue and red line, respectively) used as reference signals for the spectral deconvolution (green lines). Broken lines are guides to the eye. b, c) *high-spin* Co[II] thermal distribution profile (empty circles) obtained from XAS spectra taken before (b)) and after (c)) laser light irradiation (black dots). Massive phase rescaled data are reported as wide coloured dots for comparison.

4. Functional hybrid electrodes based on light switchable molecules.

Like for the **[CoL2-dioxo-R-dioxo-CoL2]** system a synchrotron-based absorption techniques was employed to monitor the spin states of **[CoL2diox]** on surface. [44,57,69]

Figure 19a displays the temperature evolution of the Co L_3 edge absorption spectrum of a monolayer of **[CoL2diox]** in the 100 – 300 K range. The 300 K spectrum confirms the coexistence of *ls*-Co^{III}Cat and *hs*-Co^{II}SQ redox isomeric forms in the monolayer, closely resembling the massive phase behaviour and XPS data. Isothermal time dependence of the Co $L_{2,3}$ XAS spectra acquired on the same spot of the sample discards X-ray irreversible effects on the electronic structure of the grafted molecules and reported in Figure 20. The observed edge-jump corresponds to about 10 % of what has been observed in the bulk samples of structurally related [CoL2diox] VT systems taken in similar experimental conditions. [6,59]
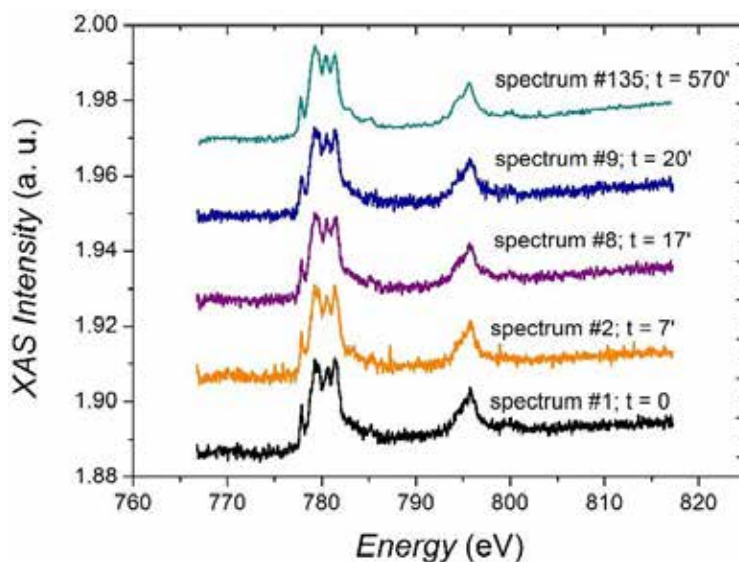
Figure 20. Isothermal time evolution of the XAS spectrum at 300 K for $L_{2,3}$ edges of a monolayer of [CoL2diox], measured on the same sample spot.

Considering that only the first few nm of a bulk sample are investigated in this type of experiments, the much weaker signal detected for the film provides an additional proof of the monolayer thickness of the studied deposit.[65] Upon cooling from 300 to 100 K the spectral features related to the *ls*-Co^{III} isomer gain intensity while the signal coming from the *hs*-Co^{II} one goes down in intensity; moreover, heating the sample back to 300 K the initial spectral lineshape is restored. These experimental evidences are in line with the occurrence of a reversible entropy driven

VT interconversion in the monolayer. In order to quantitatively analyze the *hs*-Co^{II} thermal distribution profile, the experimental Co L$_3$ spectra have been fitted using the *ls*-Co^{III} and *hs*-Co^{II} ones obtained for **[CoLn-dioxo-R-dioxo-CoLn]** in the paragraph 4.1.4 as references for the limiting redox isomeric distributions. The results, displayed in Figure 19b, evidence a VT conversion that is comparable with that observed by traditional magnetometry for the massive phase, the major difference being the 0.20(2) increase in the remaining *hs*-Co^{II} molar fraction at low temperature found for the monolayer. This feature, often documented for thin films and nanoparticles of SCO systems,[70] has been explained on the basis of different surface energies of the two interconverting phases.[68] Moreover, enthalpic and entropic changes taking place in entropy driven equilibria like SCO and VT have been shown to significantly rely on intermolecular vibrational coupling, [59,10,15] whose intensities are supposed to lower moving from a 3D network of elastic interactions (solid state) to a monolayer. Chemically induced reduction of enthalpic and entropic contributions to VT in the solid state, in fact, resulted in an increase in the low temperature *hs*-Co^{II} remaining fraction paralleling the one observed here for the monolayer.[15] Thus XPS and XAS analysis concur in pointing out that the employed chemical grafting protocol has no significant effect on the charge distribution of **[CoL1diox]**, **[CoL2diox]** and **[CoL3diox]** complexes and that it is thus possible to quantitatively retain their switchability at the monolayer level.

4.2.2.4 Characterisation of light induced interconversion of chemisorbed VT monolayers

To investigate the electronic bistability in a monolayer, we irradiated *in situ* the monolayer of **[CoL2diox]** with a 904 nm laser diode at 10 K and then measured the temperature dependence of the XAS spectra up to 100 K (Figure 21).

The coupled effect of the X-ray beam and the laser light irradiation optically populates the *hs*-Co^{II} metastable state at 10 K, reaching a *hs*-Co^{II}SQ molar fraction of 0.70(2). This value, corresponds to a 19 % overall conversion of the *ls*-Co^{III}Cat phase present a 10 K, similarly to what is found for the bulk sample (see Figure 13). Upon heating to 100 K, the *hs*-Co^{II}SQ molar fraction decreases to 0.63(3), in line with a thermally activated relaxation of the photo-induced metastable phase to the thermodynamically more stable *ls*-Co^{III}Cat. A direct comparison of the relaxation

profiles for the monolayer and bulk phase of **[CoL2diox]** points out that, in analogy to entropy driven interconversion, the possibility to optically trigger valence tautomerism of Co-dioxolene complexes is retained after they are grafted on the gold surface, and that the energy barrier to thermally activated relaxation remains substantially unaffected by surface deposition.
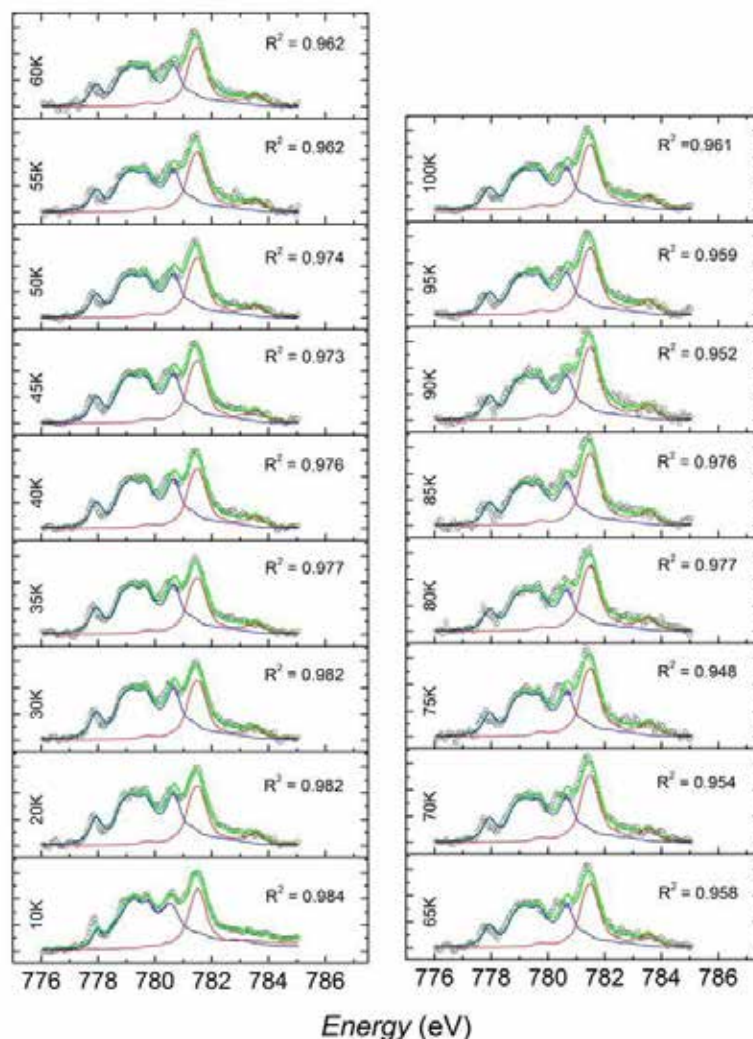
Figure 21. Thermal evolution of the normalised spectra of the Co L$_3$ edge of a monolayer of [CoL2diox] measured after 904 nm laser irradiation.

In this chapter we demonstrated that is possible to control the electronic state bulk and in a monolayer of switchable paramagnetic units using both temperature and light irradiation. This result is of paramount importance in the perspectives of

120

novel molecular-based devices that can be thermally and optically controlled, proposing Valence Tautomeric systems as potential building blocks for the construction of optically driven nanostructured hybrid devices.

4.3. Spectroscopic observation of temperature and light–induced switching of an evaporable Spin Crossover system

Spin crossover (SCO) is an intriguing phenomenon describing the switching between high and low spin states in transition metal complexes with coordination symmetry inducing *d*-orbital energy splitting.[1–7] Archetypal iron d^6 octahedral complexes can be in a paramagnetic high spin state (*HS*; S=2) or in a diamagnetic low spin state (*LS*; S=0). Spin crossover, may be observed between the HS and the LS states when these states are separated by a barrier whose height is comparable to thermal energy.[2,4,5] The SCO can be triggered via external stimuli, such as temperature,[44,71–76] pressure[8] or light irradiation,[2–4] similarly to what we have previously described for VT systems. Cooling down induces the switching of iron(II) *HS* complex to its *LS* state.[9,2,4] Light-induced excited spin-state trapping (LIESST) effect has also been observed at low temperatures in these complexes.[2,9,10] SCO has been observed by various techniques while an external stimulus was applied. [4, 25, 54,79] Thanks to the easy alteration of their spin state the implementation of SCO complexes in molecular electronics, spintronics, memory devices or sensors has been envisaged as an intriguing development of molecular magnetism.

Recently a particular class of Fe(II) complexes, namely the ([Fe(H$_2$B(pz)$_2$)$_2$phen*], pz =1-pyrazolyl; hereafter **[Fe-diaryl]**) has been proposed.[4]
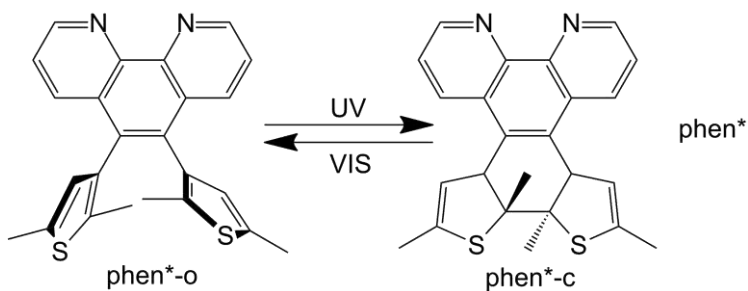
Figure 22. Diarylethene-based ligands with open (phen*-o) and closed form (phen*-c).

In this system SCO is influenced by the conformation of one of the ligand present in the molecule that can be modified through a photo-cyclization reaction (Figure 22).[4] The diarylethene unit present in the ligand can switch from the open form (phen*-o) with two functional thiophene rings to a closed form (phen*-c).[15]

Rings condensation can be triggered by irradiation with UV light (≈ 300 nm) and the reverse reaction can be induced by light in the visible range (≈ 500nm). The reversible and long-term stable photo-cyclization of the uncoordinated ligand has been successfully demonstrated in solution and in solid state.[4] The cyclization changes the ligand field at the iron core of the complex and induces SCO transition from the *HS* state of the pristine complex towards a diamagnetic *LS* state. The *LS* state can also be attained by decreasing the temperature, as schematized in Figure 23.
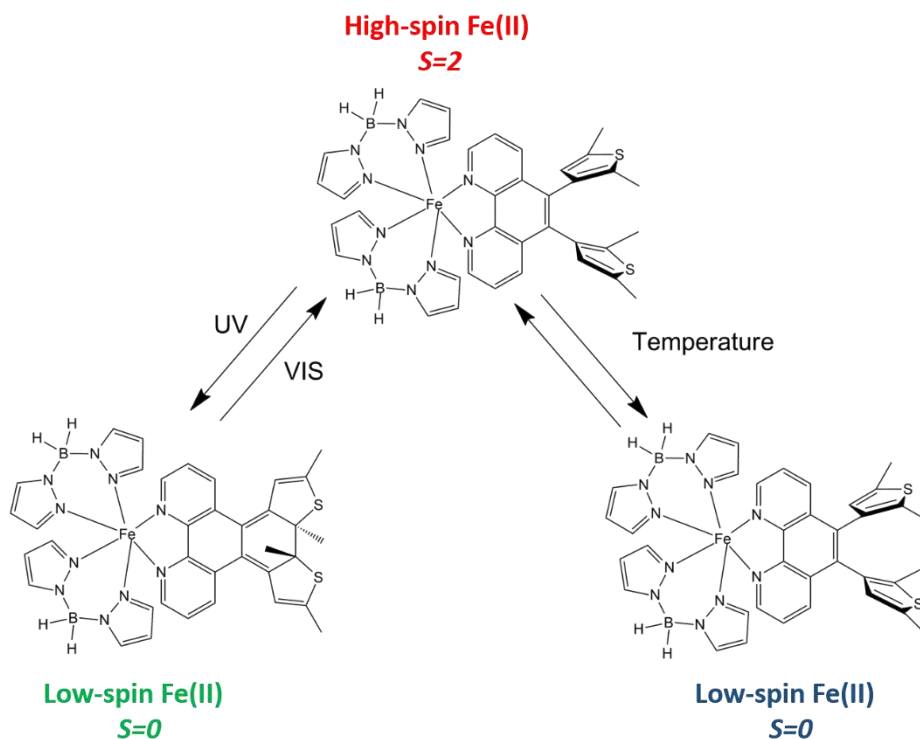
Figure 23. SCO switching with external stimuli for complex [Fe-diaryl].

This molecular system has been designed and synthetised by the group of Dr. Marat M. Khusniyarov at the Friedrich-Alexander-Universität of Erlangen and

employed in this thesis in the framework of a collaboration between our Universities and the Institut de Chimie de la Matière Condensée de Bordeaux CNRS with the aim of testing nanostructuration of this molecular material by sublimation.

4.3.1 Magnetic film characterisations

As a first step in our investigation, we analysed by magnetometry the SCO conversion properties of a thick film of the complex grown by HV sublimation on an acetate film. The sublimation temperature was 425K and the base pressure in the chamber was 10^{-7} mbar. The temperature dependence of the $\chi_M T$ product for a ≈200 nm film of **[Fe-diaryl]** is reported in Figure 24.
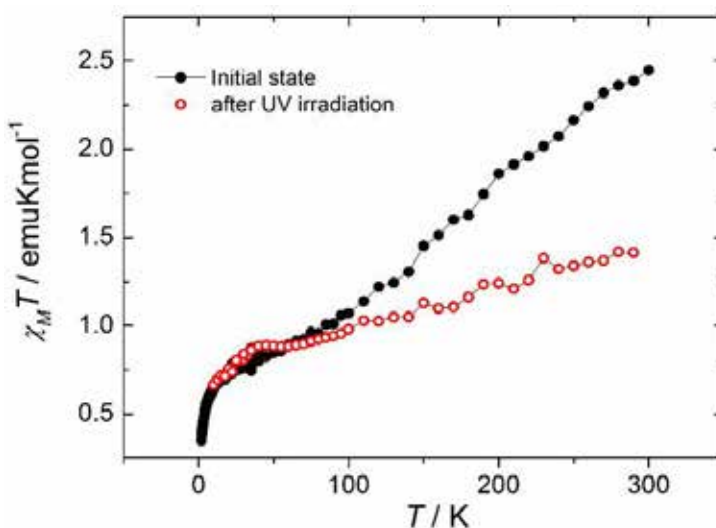
Figure 24. Temperature dependence of the product $\chi_M T$ for a thick film of [Fe-diaryl].

At room temperature, the $\chi_M T$ product of this thick film was 2.45 emuK/mol, indicating the coexistence of high spin (80 %) and low spin (20 %) Fe(II) molecules in the film. On cooling this product monotonically decreases to reach 0.75 emuK/mol at 25 K and 0.35 emuK/mol at 2 K. This behaviour has been attributed to a gradual SCO transition of the evaporated molecules, with a *HS* Fe(II) fraction of 20 % remaining unaltered at low temperature. The gradual conversion, as well as the presence of trapped *HS* fraction, have been interpreted as results of a low degree of elastic interactions among interconverting molecules in the film.[16,17] Irradiation of the film with UV light led to a decrease of the room temperature $\chi_M T$ product, reaching 1.42 emuK/mol in the photostationary state. Such a decrease is indicative

123

of the Ligand-Driven Light Induced Spin Change (LD-LISC)[18] phenomenon, already reported for the complex in solution.[4] In the film, the optically induced cyclization of the diarylethene-based ligands leads to a conversion of its high spin form to about 50 % at room temperature, a value similar to the one reported for the same compound in acetonitrile solutions.[4] This finding points out that the optically induced cyclization of the diarylethene phen* ligand is able to modify the strength of the ligand field on the Fe(II) ion even in the case of evaporated molecules on solid substrate. The remnant 30 % of unconverted high spin Fe(II) molecules keeps on displaying the original SCO behaviour on lowering the temperature.

4.3.2 Nanoscale characterisations

In order to follow the switching with temperature and with irradiation at the nanoscale, we employed XPS and UPS experiments due to the high sensitivity of those techniques in the monolayer regime. For these experiments the sample was prepared under UHV conditions and evaporated on an Au(111) single crystal with a base pressure of $1x10^{-10}$ mbar during the thermal evaporation of the complex. The gold was previously cleaned with a standard procedure involving sputtering and annealing procedure. The thermal evaporation of **[Fe-diaryl]** was carried out at 425K using the apparatus described in the chapter 5.7.3. and the nominal thickness was estimated using a quartz crystal microbalance (QCM). The XPS characterisation was performed also to verify the non-destructive thermal deposition process .

Table 8. Theoretical and XPS estimated atomic percentages and ratios for a SCO thin film (5.3 nm) evaporated on Au(111).

	Fe 2p		N 1s		B 1s		S 2p		C 1s
	%	Fe/B	%	Fe/N	%	N/B	%	N/S	%
Experimental	1.8	0.46	18.7	0.09	3.8	4.9	3.0	6.1	72.7
Theoretical	1.5	0.50	15.4	0.10	3.1	5.00	3.1	5.00	76.9

In Table 8 are reported for a film thickness of 5.3 nm the experimental percentages obtained by the estimated areas of the deconvoluted peaks. The

124

components were estimated using a fit procedure involving a Gaussian-Lorentzian line-shapes and the background in the spectra was subtracted by means of a linear function. The experimental data resulted in line with what is expected for the pristine complex, suggesting that the thermal evaporation is a non-destructive process for the depositions of this SCO complex on a surface, in agreement with previous reports on simpler Fe(II) systems.[5] Several papers have been released in the literature showing that SCO complexes can be characterised by using XPS at the Fe*2p* region, this has been observed in bulk[19,20] as well as for thick films.[21,22] The switching from *HS* to *LS* states in SCO molecules is directly observable in the line shape of the Fe*2p* region: in the *LS* configuration the Fe*2p*$_{3/2}$ peak appears narrower than in the *HS* one. The latter features a broadening of the Fe2p$_{3/2}$ peak probably due to coupling of the photoelectron with the partially-filled metal shell during the time of flight following ionization.[23] Another important fingerprint of the switching is in the spin-orbit splitting (ΔE_{SO}) of the Fe*2p*. Indeed the ΔE_{SO} changes in the two configuration due to a different orbital population: in the *HS* configuration the measured transition involves e$_g$ orbitals that are empty in the *LS* one.
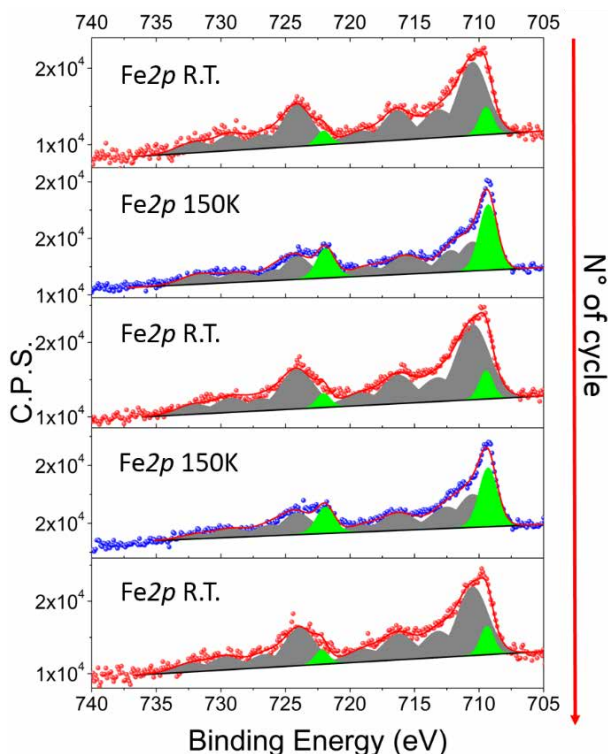
Figure 25. Reversible switching of the SCO complex in a 5.3 nm thick film in the Fe*2p* region.

In Figure 25 is reported the sequence of consecutive XPS spectra in the Fe*2p* region measured after changing the sample temperature (after one hour of thermalization). The variable temperature experiment was performed using a liquid nitrogen-based cryostat connected to the sample holder.

The variation in temperature (Figure 25) evidences a switching from the two electrons states: from *HS* (red dots) to *LS* (blue dots), going from R.T. to 150 K and *vice versa*. The reversibility of the transition is evident by looking at the shape of the Fe*2p*$_{3/2}$ peak as well as by monitoring the variation in ΔE_{SO} that is 13.4 eV in the *HS*.[19,21,24] In order to semiquantitatively follow this reversible transition a peak fitting procedure can be adopted. By monitoring the component at 709.4 eV and its relative ΔE_{SO} at 721.9 eV that have been highlighted in green, one can approximatively evaluate the LS component present in the sample depending on the temperature.
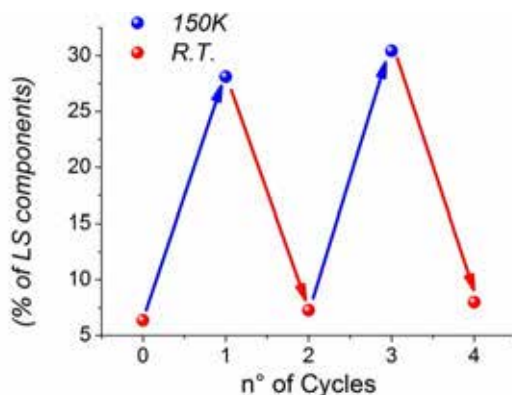
Figure 26. Percentage of green component in function of the number of thermal cycles.

In Figure 26 we report the variation of the percentage of the highlighted contribution due to the *LS* state respect to the whole Fe*2p* area. From the evolution of the component shown in Figure 26 it has been possible to demonstrate that a reversible switching of about the 20% of the molecules occurs in the explored temperature window.

Accordingly to what we mentioned above the measured process does not involve the changing of the phen* ligand, being due to the standard ligand field alteration causing the SCO effect.[4] This can be confirmed by monitoring the *S2p* region as function of the temperature (Figure 27), evidencing the absence of a parallel evolution of the S*2p* signal; this confirms that the phen* ligand retains its

conformation (phen*-o) during the thermal cycles we performed. The S$2p$ signal appears centred at 164.9 eV in agreement with literature data.[25,26]
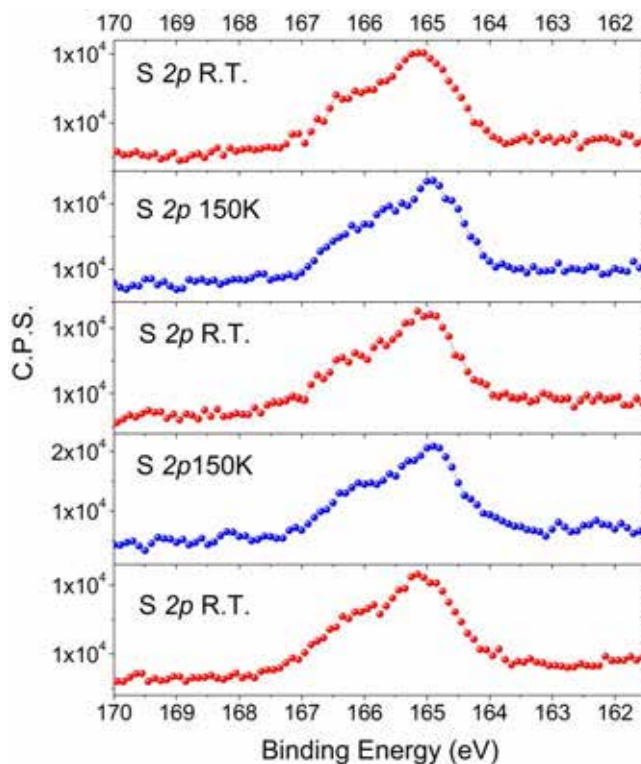
Figure 27. Variation in temperature of a SCO complex 5.3 nm thick film in the S$2p$ region.

The multi-switchability of this particular system is evident after *in situ* UV irradiation of the evaporated sample in the UHV environment. The 5.3 nm thick molecular film was exposed to UV light using a deuterium lamp (20W) directly mounted in front of a quartz viewport installed in the XPS chamber, using an optical filter with a 280.0 (+3/-0) nm band pass and with 10 ± 2 nm bandwidth in order to guarantee the irradiation with the proper wavelength to promote the cyclisation reaction. In Figure 28 are reported the spectra in the Fe$2p$ region for *HS* at RT (top, red circle), *LS* at 150K (middle, blue circle) and *HS/LS* at R.T. irradiated with UV light (bottom, green circle) configurations. From the direct comparison of the three spectra is possible to point out that a change of the lineshape is occurring in the irradiated sample that results in an intermediate situation between the 300 K and

127

the 150 K measurement. Indeed the green component, estimated using the same fitting procedure described above, resulted almost doubled respective to the one measured at RT. This evidences that a partial transition from the *HS* to the *LS* state can be promoted by UV light irradiation also in an evaporated sample accordingly to what was observed in solution for the same complex[4] and in the thick film characterized with magnetometry in paragraph 4.3.1.
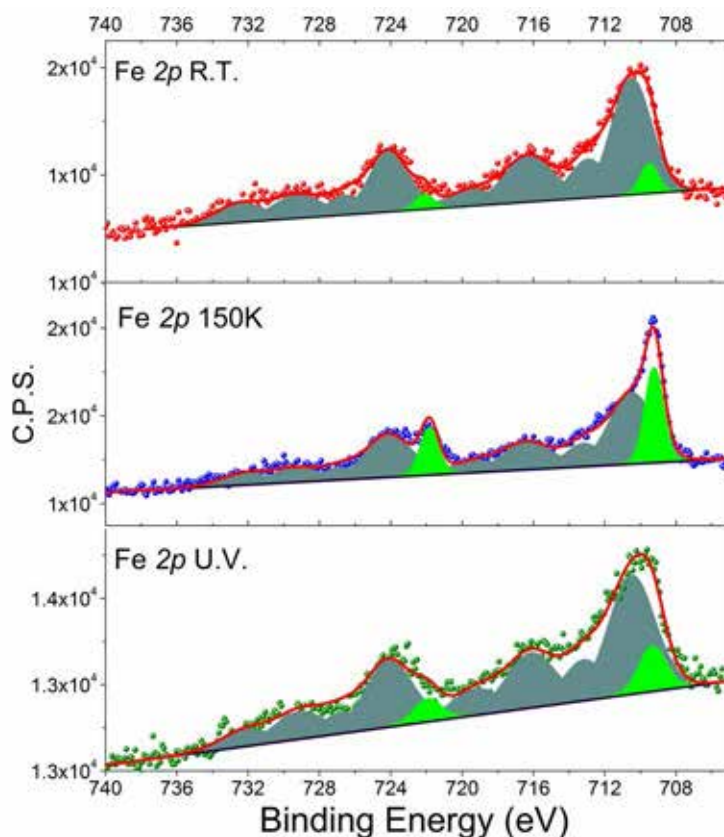
Figure 28. Comparison of Fe2p XPS spectra at R.T. (red, top), 150K (blue, middle) and at R.T. after UV irradiation (bottom, dark green).

We underline that this room temperature SCO transition is due to the alteration of the phen* ligand in **[Fe-diaryl]** molecules that goes from the open conformation (phen*-o) to a closed one (phen*-c). The occurrence of this cyclisation is confirmed by monitoring the S*2p* region (Figure 29).

The occurrence of the cyclisation of the ligand is directly observable with the appearance of a component at lower binding energy (164 eV) respective to the main

one (164.9 eV). This component accounts for 26% of the S$2p$ signal, confirming that despite the low amount of material deposited on top of the gold surface it is possible to induce SCO transition also at room temperature by light irradiation.
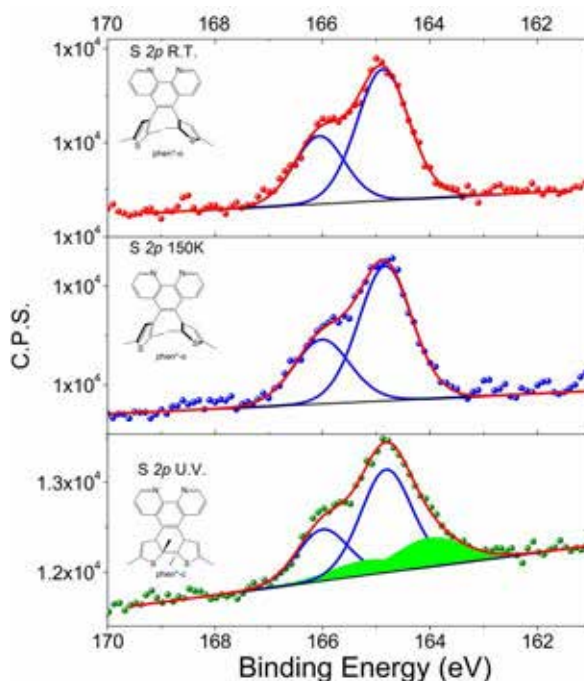
Figure 29. XPS S$2p$ spectra at R.T. (red dots), 150K (blue dots) and after UV irradiation (dark green dots).

Additional characterization of this multi-SCO switching can be performed by ultraviolet photoelectron spectroscopy (UPS). We performed a series of UPS experiments as a function of the molecular coverage starting from low coverage (0.7 nm) to a nominal thickness of 5.3 nm corresponding to about 5-6 monolayers. For this UPS characterisation we employed photons at 40.8 eV (He II). In order to ensure that all photoelectrons generated by the He II line were detected, a fixed bias of −30 V was applied to the sample. The binding energy scale was calibrated such that the Fermi level was located at 0 eV. In the spectra in Figure 30 it is possible to observe the presence of the typical features of **[Fe(II)-SCO]** systems as observed for similar compounds.[7,24,27] The spectrum acquired at room temperature for 5.3 nm thickness, shown in Figure 30, evidences contributions at -2.3 eV, -4.5 eV, -6.5 eV, and two very

broad   features   centred   for   one   at   about -9.4 eV and for the other at -14.5 eV, in line with literature reports on similar systems.[7,24,27] In Figure 30 the spectra at low coverages (0.7 nm and 2.2 nm) already show the features at -14.5 eV and at -9.5 eV. This system is thus indeed a promising candidate for the study at the sub-monolayer level due to the presence of intact molecules.
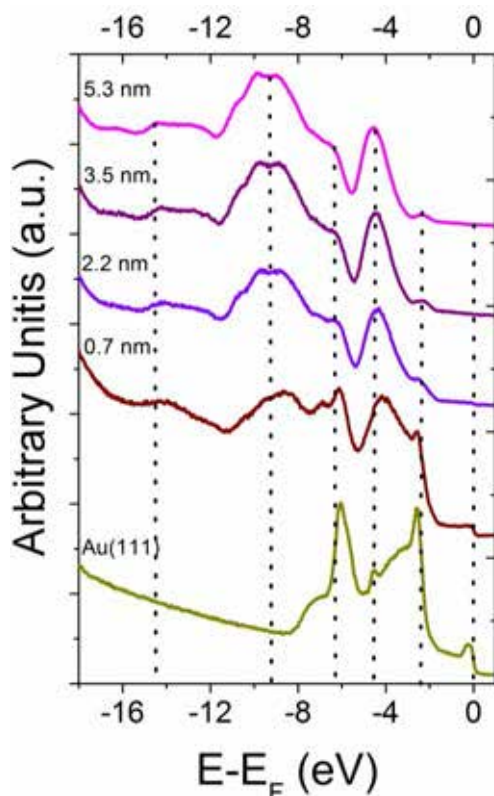
Figure 30. UPS spectra from -18 eV to 1 eV (E-E$_F$) at R.T from 0.7 nm to 5.3 nm in nominal thickness of [Fe-diaryl].

As shown in Figure 30, in the spectrum corresponding to the 5.3 nm coverage the features related to the gold substrate is absent in contrast to what reported for the for low coverages (from 0.7 to 2.2 nm) where the Fermi edge (0 eV) and the most prominent peaks of the spectra between −2 and −7 eV can be clearly identified.

Focusing on the 5.3 nm sample, the spectra reported in Figure 31 show a temperature evolution of the relative intensity of the band at -2.3 eV. The same component is altered upon UV irradiation, similarly to what observed for 1,2-Bis(5-

(2,4-diphenylphenyl)-2,4-dimethyl-3-thienyl)per-fluorocyclopentene, 1,2-bis(2-methyl-5-p-tolylthiophen-3-yl)cyclo-pent-1-ene and 1,2-bis(5-(4-hexyloxycarbonylphe-nyl)-2-methylthiophen-3-yl)cyclopent-1-ene films.[28,29] Moreover after UV light exposure the relative intensities of bands at -9.4, -6.5 and -4.5 eV change.

Focusing on the -2.3 eV band it is possible to notice that a variation in intensity is found and this can be attributed to the temperature induced switching (*LS↔HS*) by increasing the temperature: this band (blue dots) appears more intense at low temperature than in the room temperature measurement (red dots). This confirms the thermal switching as observed for similar compound, and according also to DFT calculations and experiments performed on **[Fe(H$_2$B(pz)$_2$)$_2$(bipy)]** and **[Fe(H$_2$bpz)$_2$(phen)]** deposited complexes.[7,27]
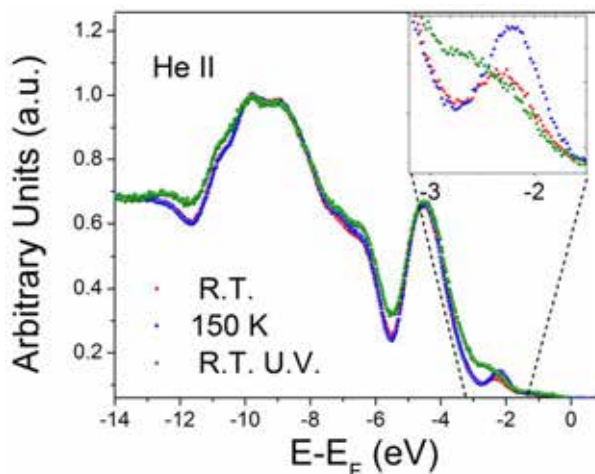
Figure 31. UPS spectra from -14 eV to 0 eV (E-E$_F$) at R.T. (red dots), 150K (blue dots) and after UV irradiation (green dots). The inset emphasizes the feature at a binding energy of -2.3 eV.

When looking more carefully, the UPS band that before the irradiation was centred at -2.3 eV appears broadened and centred at -2.4 eV after irradiation. This can be attributed to the ligand cyclisation modifying the electronic structure of the ligand and thus the electronic structure of the complex. Indeed cyclization of a diarylethene function leads the system to a different energy distribution of HOMO/LUMO orbitals, which results in a variation in UPS spectra at near Fermi energies.[28,29] Therefore the

131

band at -2.3 eV changes differently when the system is at low temperature or after UV irradiation in agreement to the different nature of the induced *LS* state.

XPS and UPS analyses confirm that it is possible to evaporate intact **[Fe-diaryl]** molecules in a UHV environment and open the possibility to study sub-monolayer coverage by XAS experiments. Due to the persistence of their SCO multi-switchability properties, it is possible to envisage the use of this particular molecular system as building block for the realization of a new family of devices for which transport properties could be externally influenced through the molecular layer by using either temperature variation or light irradiation.

4. Functional hybrid electrodes based on light switchable molecules.

Reference

(1)   Gutlich, P.; Goodwin, H. A. *Spin Crossover in Transition Metal Compounds I*; Gütlich, P.; Goodwin, H. A., Eds.; Topics in Current Chemistry; Springer Berlin Heidelberg: Berlin, Heidelberg, 2004; Vol. 233.

(2)   Robin, M. B.; Day, P. *Adv. Inorg. Chem. Radiochem.* **1968**, *10*, 247–422.

(3)   Beni, A.; Carbonera, C.; Dei, A.; Létard, J.-F.; Righini, R.; Sangregorio, C.; Sorace, L. *J. Braz. Chem. Soc.* **2006**, *17*, 1522–1533.

(4)   Boskovic, C. *Spin-Crossover Materials*; HALCROW, M. A., Ed.; John Wiley & Sons Ltd: Oxford, UK, 2013.

(5)   Sato, O.; Tao, J.; Zhang, Y.-Z. *Angew. Chem. Int. Ed.* **2007**, *46*, 2152–2187.

(6)   Poneti, G.; Mannini, M.; Sorace, L.; Sainctavit, P.; Arrio, M.-A.; Otero, E.; Cezar, J. C.; Dei, A. *Angew. Chem. Int. Ed.* **2010**, *49*, 1954–1957.

(7)   Dapporto, P.; Dei, A.; Poneti, G.; Sorace, L. *Chem. Eur. J.* **2008**, *14*, 10915–10918.

(8)   Beni, A.; Dei, A.; Laschi, S.; Rizzitano, M.; Sorace, L. *Chem. Eur. J.* **2008**, *14*, 1804–1813.

(9)   Droghetti, A.; Sanvito, S. *Phys. Rev. Lett.* **2011**, *107*, 047201.

(10)   Richardson, D. E.; Sharpe, P. *Inorg. Chem.* **1993**, *32*, 1809–1812.

(11)   Dei, A.; Gatteschi, D.; Sangregorio, C.; Sorace, L. *Acc. Chem. Res.* **2004**, *37*, 827–835.

(12)   Caneschi, A.; Dei, A.; Fabrizi de Biani, F.; Gütlich, P.; Ksenofontov, V.; Levchenko, G.; Hoefer, A.; Renz, F. *Chem. Eur. J.* **2001**, *7*, 3926–3930.

(13)   Li, B.; Yang, F.-L.; Tao, J.; Sato, O.; Huang, R.-B.; Zheng, L.-S. *Chem. Commun.* **2008**, 6019–6021.

(14)   Markevtsev, I. N.; Monakhov, M. P.; Platonov, V. V.; Mischenko, A. S.; Zvezdin, A. K.; Bubnov, M. P.; Abakumov, G. A.; Cherkasov, V. K. *J. Magn. Magn. Mater.* **2006**, *300*, e407–e410.

(15)   Dei, A.; Poneti, G.; Sorace, L. *Inorg. Chem.* **2010**, *49*, 3271–3277.

(16)   Baldé, C.; Desplanches, C.; Gütlich, P.; Freysz, E.; Létard, J. F. *Inorg. Chim. Acta* **2008**, *361*, 3529–3533.

(17)   *Magnetism: A Synchrotron Radiation Approach*; Beaurepaire, E.; Bulou, H.; Scheurer, F.; Kappler, J.-P., Eds.; Lecture Notes in Physics; Springer Berlin Heidelberg, 2006; Vol. 697.

(18)   Bencini, A.; Beni, A.; Costantino, F.; Dei, A.; Gatteschi, D.; Sorace, L. *Dalton Trans.* **2006**, 722–729.

4. Functional hybrid electrodes based on light switchable molecules.

(19)   Alley, K. G.; Poneti, G.; Robinson, P. S. D.; Nafady, A.; Moubaraki, B.; Aitken, J. B.; Drew, S. C.;
        Ritchie, C.; Abrahams, B. F.; Hocking, R. K.; Murray, K. S.; Bond, A. M.; Harris, H. H.; Sorace, L.;
        Boskovic, C. *J. Am. Chem. Soc.* **2013**, *135*, 8304–8323.

(20)   Alley, K. G.; Poneti, G.; Aitken, J. B.; Hocking, R. K.; Moubaraki, B.; Murray, K. S.; Abrahams, B.
        F.; Harris, H. H.; Sorace, L.; Boskovic, C. *Inorg. Chem.* **2012**, *51*, 3944–3946.

(21)   Hearns, N. G. R.; Korcok, J. L.; Paquette, M. M.; Preuss, K. E. *Inorg. Chem.* **2006**, *45*, 8817–8819.

(22)   Gural'skiy, I. A.; Quintero, C. M.; Molnár, G.; Fritsky, I. O.; Salmon, L.; Bousseksou, A. *Chem.
        Eur. J.* **2012**, *18*, 9946–9954.

(23)   Sato, O.; Cui, A.; Matsuda, R.; Tao, J.; Hayami, S. *Acc. Chem. Res.* **2007**, *40*, 361–369.

(24)   Chamberlin, R.; Mozurkewich, G.; Orbach, R. *Phys. Rev. Lett.* **1984**, *53*, 1025–1025.

(25)   Létard, J.-F.; Capes, L.; Chastanet, G.; Moliner, N.; Létard, S.; Real, J.-A.; Kahn, O. *Chem. Phys.
        Lett.* **1999**, *313*, 115–120.

(26)   Létard, J.-F. *J. Mater. Chem.* **2006**, *16*, 2550.

(27)   Carbonera, C.; Dei, A.; Létard, J.-F.; Sangregorio, C.; Sorace, L. *Angew. Chem. Int. Ed.* **2004**, *43*,
        3136–3138.

(28)   Ohno, Y. *J. Electron Spectros. Relat. Phenomena* **2008**, *165*, 1–4.

(29)   Mazalov, L. .; Asanov, I. .; Varnek, V. . *J. Electron Spectros. Relat. Phenomena* **1998**, *96*, 209–
        214.

(30)   Kozieł, M.; Podgajny, R.; Kania, R.; Lebris, R.; Mathonière, C.; Lewiński, K.; Kruczała, K.; Rams,
        M.; Labrugère, C.; Bousseksou, A.; Sieklucka, B. *Inorg. Chem.* **2010**, *49*, 2765–2772.

(31)   Mathonière, C.; Podgajny, R.; Guionneau, P.; Labrugere, C.; Sieklucka, B. *Chem. Mater.* **2005**,
        17, 442–449.

(32)   Tokoro, H.; Ohkoshi, S.; Matsuda, T.; Hashimoto, K. *Inorg. Chem.* **2004**, *43*, 5231–5236.

(33)   Vertelman, E. J. M.; Maccallini, E.; Gournis, D.; Rudolf, P.; Bakas, T.; Luzon, J.; Broer, R.; Pugzlys,
        A.; Lummen, T. T. A.; van Loosdrecht, P. H. M.; van Koningsbruggen, P. J. *Chem. Mater.* **2006**,
        18, 1951–1963.

(34)   Ohtsu, H.; Tanaka, K. *Chem. Eur. J.* **2005**, *11*, 3420–3426.

(35)   Joly, V.; Joy, P.; Date, S.; Gopinath, C. *Phys. Rev. B* **2002**, *65*, 184416.

(36)   Ivanova, T.; Naumkin, A.; Sidorov, A.; Eremenko, I.; Kiskin, M. *J. Electron Spectros. Relat.
        Phenomena* **2007**, *156-158*, 200–203.

(37)   Ivanova, T. M.; Shchukarev, A. V.; Linko, R. V.; Kiskin, M. A.; Sidorov, A. A.; Novotortsev, V. M.; Eremenko, I. L. *Russ. J. Inorg. Chem.* **2011**, *56*, 104–109.

(38)   Lever, A. B. P. *Inorganic electronic spectroscopy*; Studies in physical and theoretical chemistry; Elsevier, 1984.

(39)   Biesinger, M. C.; Payne, B. P.; Grosvenor, A. P.; Lau, L. W. M. M.; Gerson, A. R.; Smart, R. S. C.; St, R.; Smart, C. *Appl. Surf. Sci.* **2011**, *257*, 2717–2730.

(40)   Sessoli, R.; Mannini, M.; Pineider, F.; Cornia, A.; Sainctavit, P.; Beaurepaire, E.; Scheurer, F.; Krill, G. *Magnetism and Synchrotron Radiation*; Beaurepaire, E.; Bulou, H.; Scheurer, F.; Jean-Paul, K., Eds.; Springer Proceedings in Physics; Springer Berlin Heidelberg: Berlin, Heidelberg, 2010; Vol. 133.

(41)   Yokoyama, T.; Kiguchi, M.; Ohta, T.; Sato, O.; Einaga, Y.; Hashimoto, K. *Phys. Rev. B* **1999**, *60*, 9340–9346.

(42)   Briois, V.; dit Moulin, C. C.; Sainctavit, P.; Brouder, C.; Flank, A.-M. *J. Am. Chem. Soc.* **1995**, *117*, 1019–1026.

(43)   Lee, J.-J.; Sheu, H.; Lee, C.-R.; Chen, J.-M.; Lee, J.-F.; Wang, C.-C.; Huang, C.-H.; Wang, Y. *J. Am. Chem. Soc.* **2000**, *122*, 5742–5747.

(44)   Miyamachi, T.; Gruber, M.; Davesne, V.; Bowen, M.; Boukari, S.; Joly, L.; Scheurer, F.; Rogez, G.; Yamada, T. K.; Ohresser, P.; Beaurepaire, E.; Wulfhekel, W. *Nat. Commun.* **2012**, *3*, 938.

(45)   Roux, C.; Adams, D. M.; Itié, J. P.; Polian, A.; Hendrickson, D. N.; Verdaguer, M. *Inorg. Chem.* **1996**, *35*, 2846–2852.

(46)   Bin-Salamon, S.; Brewer, S. H.; Depperman, E. C.; Franzen, S.; Kampf, J. W.; Kirk, M. L.; Kumar, R. K.; Lappi, S.; Peariso, K.; Preuss, K. E.; Shultz, D. A. *Inorg. Chem.* **2006**, *45*, 4461–4467.

(47)   Yokoyama, T.; Okamoto, K.; Nagai, K.; Ohta, T.; Hayami, S.; Gu, Z.-Z.; Nakajima, R.; Sato, O. *Chem. Phys. Lett.* **2001**, *345*, 272–276.

(48)   Poneti, G.; Mannini, M.; Sorace, L.; Sainctavit, P.; Arrio, M.-A.; Rogalev, A.; Wilhelm, F.; Dei, A. *Chemphyschem* **2009**, *10*, 2090–2095.

(49)   Arrio, M.-A.; Long, J.; Cartier dit Moulin, C.; Bachschmidt, A.; Marvaud, V.; Rogalev, A.; Mathonière, C.; Wilhelm, F.; Sainctavit, P. *J. Phys. Chem. C* **2010**, *114*, 593–600.

(50)   Prasanna de Silva, A. *Molecular Logic-based Computation*; Monographs in Supramolecular Chemistry; Royal Society of Chemistry: Cambridge, 2012.

(51)   Baadji, N.; Piacenza, M.; Tugsuz, T.; Della Sala, F.; Maruccio, G.; Sanvito, S. *Nat. Mater.* **2009**, *8*, 813–817.

(52)   Dei, A.; Gatteschi, D. *Angew. Chem. Int. Ed.* **2011**, *50*, 11852–11858.

4. Functional hybrid electrodes based on light switchable molecules.

(53)   Wagner, S.; Kisslinger, F.; Ballmann, S.; Schramm, F.; Chandrasekar, R.; Bodenstein, T.; Fuhr, O.; Secker, D.; Fink, K.; Ruben, M.; Weber, H. B. *Nat. Nanotechnol.* **2013**, *8*, 575–579.

(54)   Bousseksou, A.; Molnár, G.; Salmon, L.; Nicolazzi, W. *Chem. Soc. Rev.* **2011**, *40*, 3313–3335.

(55)   Pronschinske, A.; Chen, Y.; Lewis, G. F.; Shultz, D. A.; Calzolari, A.; Nardelli, M. B.; Dougherty, D. B. *Nano Lett.* **2013**, *13*, 1429–1434.

(56)   Pronschinske, A.; Bruce, R. C.; Lewis, G.; Chen, Y.; Calzolari, A.; Buongiorno-Nardelli, M.; Shultz, D. A.; You, W.; Dougherty, D. B. *Chem. Commun.* **2013**, *49*, 10446–10452.

(57)   Gopakumar, T. G.; Matino, F.; Naggert, H.; Bannwarth, A.; Tuczek, F.; Berndt, R. *Angew. Chem. Int. Ed.* **2012**, *51*, 6262–6266.

(58)   Gruber, M.; Davesne, V.; Bowen, M.; Boukari, S.; Beaurepaire, E.; Wulfhekel, W.; Miyamachi, T. *Phys. Rev. B* **2014**, *89*, 195415.

(59)   Poneti, G.; Mannini, M.; Cortigiani, B.; Poggini, L.; Sorace, L.; Otero, E.; Sainctavit, P.; Sessoli, R.; Dei, A. *Inorg. Chem.* **2013**, *52*, 11798.

(60)   Tricard, S.; Costa-Coquelard, C.; Volatron, F.; Fleury, B.; Huc, V.; Albouy, P.-A.; David, C.; Miserque, F.; Jegou, P.; Palacin, S.; Mallah, T. *Dalton Trans.* **2012**, *41*, 1582–1590.

(61)   O'Sullivan, T. J.; Djukic, B.; Dube, P. A.; Lemaire, M. T. *Chem. Commun.* **2009**, 1903–1905.

(62)   Tufts, B. J.; Abrahams, I. L.; Caley, C. E.; Lunt, S. R.; Miskelly, G. M.; Sailor, M. J.; Santangelo, P. G.; Lewis, N. S.; Roe, A. L.; Hodgson, K. O. *J. Am. Chem. Soc.* **1990**, *112*, 5123–5136.

(63)   Wagner, C. D.; Naumkin, A. V.; Kraut-Vass, A.; Allison, J. W.; Powell, C. J.; Rumble, J. R. J. NIST Standard Reference Database 20, Version 4.1 (web version).

(64)   Nelson, a. J.; Glenis, S.; Frank, a. J. *J. Chem. Phys.* **1987**, *87*, 5002.

(65)   Totaro, P.; Poggini, L.; Favre, A.; Mannini, M.; Sainctavit, P.; Cornia, A.; Magnani, A.; Sessoli, R. *Langmuir* **2014**, *30*, 8645–8649.

(66)   Castner, D. G.; Hinds, K.; Grainger, D. W. *Langmuir* **1996**, *12*, 5083–5086.

(67)   Ishida, T.; Choi, N.; Mizutani, W.; Tokumoto, H.; Kojima, I.; Azehara, H.; Hokari, H.; Akiba, U.; Fujihira, M. *Langmuir* **1999**, *15*, 6799–6806.

(68)   Jacob, H.; Kathirvel, K.; Petersen, F.; Strunskus, T.; Bannwarth, A.; Meyer, S.; Tuczek, F. *Langmuir* **2013**, *29*, 8534–8543.

(69)   Warner, B.; Oberg, J. C.; Gill, T. G.; El Hallak, F.; Hirjibehedin, C. F.; Serri, M.; Heutz, S.; Arrio, M.-A.; Sainctavit, P.; Mannini, M.; Poneti, G.; Sessoli, R.; Rosa, P. *J. Phys. Chem. Lett.* **2013**, *4*, 1546–1552.

(70) Shepherd, H. J.; Molnár, G.; Nicolazzi, W.; Salmon, L.; Bousseksou, A. *Eur. J. Inorg. Chem.* **2013**, *2013*, 653–661.

(71) Gopakumar, T. G.; Bernien, M.; Naggert, H.; Matino, F.; Hermanns, C. F.; Bannwarth, A.; Mühlenberend, S.; Krüger, A.; Krüger, D.; Nickel, F.; Walter, W.; Berndt, R.; Kuch, W.; Tuczek, F. *Chem. Eur. J.* **2013**, *19*, 15702–15709.

(72) Gütlich, P.; Hauser, A.; Spiering, H. *Angew. Chem. Int. Ed.* **1994**, *33*, 2024–2054.

(73) Bressler, C.; Milne, C.; Pham, V.; Elnahhas, A.; van der Veen, R. M.; Gawelda, W.; Johnson, S.; Beaud, P.; Grolimund, D.; Kaiser, M.; Borca, C. N.; Ingold, G.; Abela, R.; Chergui, M. *Science* **2009**, *323*, 489–492.

(74) Milek, M.; Heinemann, F.; Khusniyarov, M. *Inorg. Chem.* **2013**, *52*, 11585–11592.

(75) Bernien, M.; Wiedemann, D.; Hermanns, C. F.; Krüger, A.; Rolf, D.; Kroener, W.; Müller, P.; Grohmann, A.; Kuch, W. *J. Phys. Chem. Lett.* **2012**, *3*, 3431–3434.

(76) Zhang, X.; Palamarciuc, T.; Rosa, P.; Létard, J.-F.; Doudin, B.; Zhang, Z.; Wang, J.; Dowben, P. a. *J. Phys. Chem. C* **2012**, *116*, 23291–23296.

(77) Antonangeli, D.; Siebert, J.; Aracne, C. *Science* **2011**, 64–68.

(78) Vankó, G.; Renz, F.; Molnár, G.; Neisius, T.; Kárpáti, S. *Angew. Chem. Int. Ed.* **2007**, *46*, 5306–5309.

(79) Gutlich, P.; Goodwin, H. A. *Spin crossover in transition metal compounds II*; Gütlich, P.; Goodwin, H. A., Eds.; Topics in Current Chemistry; Springer-Verlag Berlin Heidelberg New York: Berlin, Heidelberg, 2004; Vol. 233.

(80) Irie, M. *Chem. Rev.* **2000**, *100*, 1685–1716.

(81) Félix, G.; Nicolazzi, W.; Mikolasek, M.; Molnár, G.; Bousseksou, A. *Phys. Chem. Chem. Phys.* **2014**, *16*, 7358–7367.

(82) Nishino, T.; Ohshiro, T.; Umezawa, Y. *Jpn. J. Appl. Phys.* **2007**, *46*, 5519–5527.

(83) Létard, J.-F.; Guionneau, P.; Goux-CapesLaurence. *Spin Crossover in Transition Metal Compounds III*; Topics in Current Chemistry; Springer-Verlag: Berlin/Heidelberg, 2004; Vol. 235.

(84) Burger, K.; Furlani, C.; Mattogno, G. *J. Electron Spectros. Relat. Phenomena* **1980**, *21*, 249–256.

(85) Lazarus, M. S.; Hoselton, M. A.; Chou, T. S. *Inorg. Chem.* **1977**, *16*, 2549–2553.

(86) Ellingsworth, E. C.; Turner, B.; Szulczewski, G. *R. Soc. Chem. Adv.* **2013**, *3*, 3745.

4. Functional hybrid electrodes based on light switchable molecules.

(87)   Savu, S.-A.; Biswas, I.; Sorace, L.; Mannini, M.; Rovai, D.; Caneschi, A.; Chassé, T.; Casu, M. B. *Chem. Eur. J.* **2013**, *19*, 3445–3450.

(88)   Borod'ko, Y. G.; Vetchinkin, S. I.; Zimont, S. L.; Ivleva, I. N.; Shul'ga, Y. M. *Chem. Phys. Lett.* **1976**, *42*, 264–267.

(89)   Chastain, J.; Moulder, J. *Handbook of x-ray photoelectron spectroscopy: a reference book of standard spectra for identification and interpretation of XPS data*; Physical Electronics Division, P.-E. C., Ed.; 1995.

(90)   Katsonis, N.; Kudernac, T.; Walko, M.; van der Molen, S. J.; van Wees, B. J.; Feringa, B. L. *Adv. Mater.* **2006**, *18*, 1397–1400.

(91)   Ludwig, E.; Naggert, H.; Kalläne, M.; Rohlf, S.; Krçger, E.; Bannwarth, A.; Quer, A.; Rossnagel, K.; Kröger, E.; Kipp, L.; Tuczek, F. *Angew. Chem. Int. Ed.* **2014**, *53*, 3019–3023.

(92)   Tanaka, S.; Toba, M.; Nakashima, T.; Kawai, T.; Yoshino, K. *Jpn. J. Appl. Phys.* **2008**, *47*, 1215–1218.

(93)   Frisch, J.; Herder, M.; Herrmann, P.; Heimel, G.; Hecht, S.; Koch, N. *Appl. Phys. A* **2013**, *113*, 1–4.

5. Experimental methods

5.1 Magnetic characterisation

Bulk microcrystalline sample and the thick evaporated films were characterised with standard magnetometry techniques, using commercial magnetometers allowing the measurement of the magnetisation and the susceptibility of the samples. The susceptibility is defined as:

$$\chi = \frac{\delta M}{\delta H} \tag{1}$$

where *M* is the molar magnetisation of the sample and *H* is the magnetic field. The susceptibility describes the interaction between the magnetic moment of the samples and the external magnetic field. The magnetic moment, at the molecular scale, can be described as the variation in energy of the molecular system (δZ) due to the interaction with the magnetic field. The magnetic moment *m* is defined as:

$$m = \frac{\delta Z}{\delta H} \tag{2}$$

where Z is the partition function. In a system where the energy spectrum is characterized by a discrete number of levels characterized by energy E_n (n=1,2,..,n) populated according to the Boltzmann distribution, the macroscopic magnetisation can be defined by:

$$\frac{M}{N} = \frac{\sum_n \left(-\frac{\delta E_n}{\delta H}\right) e^{\frac{-E_n}{k_B T}}}{\sum_n e^{\frac{-E_n}{k_B T}}} \tag{3}$$

where *T* is the absolute temperature, k_b is the Boltzmann constant and *N* is the Avogadro's number. With this the general formula is possible to access to the macroscopic magnetic properties trough energy levels of the system. The measurement of magnetisation can be carried out by employing standard magnetometry techniques. Standard magnetometry is based on the determination of the magnetic moment through an induction effect. The variation as a function of time of the magnetic flux $d\phi/dt$ generates a current flowing in a circuit. The electromotive force is proportional to the flux variation. The detection of this electromotive force is possible using a set of coils, but also the applied magnetic field can generate a magnetic flux. The magnet flux can be cancelled by using gradiometer distribution coils that are able only to detect a magnetic field gradient. The first order

gradiometer is made up by two coils, wrapped in opposite direction, where the magnetised sample is moved from the first coil to the second one: the difference in voltage induced in the two coils is directly proportional to sample magnetisation. To achieve a better magnetic moment detection a second order gradiometer is generally used, where 2N coil are positioned between two set of N coil. The 2N coil have a different wrap direction of N coil (Figure 1).
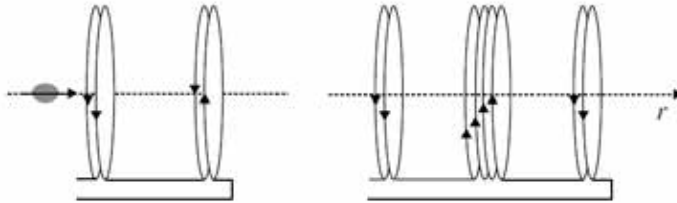
Figure 1. First (left) and second order gradiometers (right).[1]

In high sensibility magnetometer the induced current is measured coupling the gradiometer coils with a Superconducting Quantum Interference Device (SQUID). The SQUIDs are made of one superconducting ring, in which the flux is "quantized", thus allowing a precise measurement of the magnetic field in term of Josephson tunnelling of the Cooper pairs occurring in the two Josephson junctions (for a *dc*-SQUID). In Figure 2 is reported a schematic Josephson junction. The SQUID is kept in a ^{4}He bath to ensure the good superconductivity of its ring. The sample is then moved in the gradiometer and induces an electromotive force generating a new magnetic field close to the SQUID. The *dc*-SQUID measures this field in terms of the quantum interferences occurring between the two pathways that enclose the area where the magnetic flux is modified.
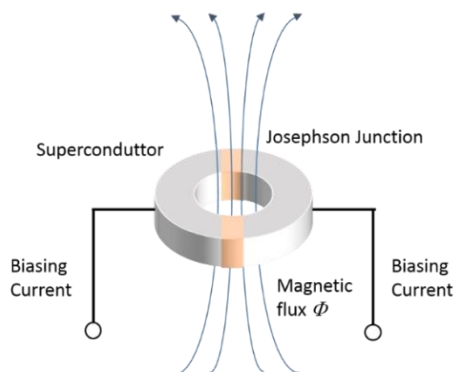
Figure 2. Scheme of a dc-SQUID. The current goes through a superconducting ring with two Josephson junctions

The current of the SQUID is therefore modulated by the flux induced in the ring. The sample is then moved through the coils and a feed–back coil is used to compensate the effect of the sample when it comes into the coils. The voltage that is needed to compensate the flux generated by the sample is proportional to its magnetization. After calibration with a known sample, it is possible to evaluate with high accuracy the magnetization of the sample. SQUID magnetometers can detect signals as low as 10^{-9} emu. This magnetometer measure the magnetisation of the sample, and the molar susceptibility χ can be calculated, with a linear approximation of the magnetisation in the field as:

$$\chi = \frac{M}{N} \cdot H \qquad\qquad (4)$$

where M is the magnetization of the sample, N is the number of molecules and H is the external field. This linear approximation is not always applicable, for instance close to phase transitions or in high magnetic fields. To have access to the real susceptibility, defined in Eq.(1), the so called *ac susceptometry* is employed. The sample is inserted inside a copper primary coil. An alternate current (*ac*) is passed through the primary coil generating a small oscillating magnetic field (in general smaller than 10 Oe). Inside the primary coil another coil, named secondary, is inserted.

Figure 3. Scheme of the coil used in an *ac* susceptometer.[1]

The magnetic moment of the sample oscillates as a response of the applied *ac* field. This oscillation is detected by the secondary coil, fixed inside of the primary one. This coil is made in two parts wrapped in opposite direction to compensate the contribution to the signal of the primary coil (see Figure 3). A first order gradiometer

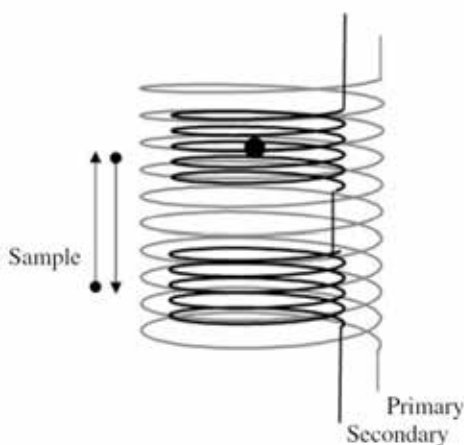is thus employed and absolute values for the susceptibility are obtained by measuring the induced voltage by the sample placed alternately at the center of the two coils of the secondary circuit.. The signal is then detected by the lock-in, in amplitude and phase. The measure can be carried out with a static magnetic field H_0 parallel to the oscillating field h and the total magnetic field H is:

$$H = H_0 + h \cos \omega t \qquad (5)$$

where ω is the frequency of the *ac* current in the primary coil. By measuring the ac susceptibility the derivative of the magnetization curve is obtained. The difference between the *dc* and *ac* susceptibility is explained easily in Figure 4.
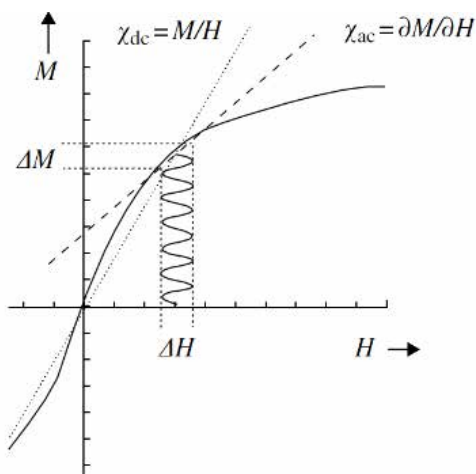
Figure 4. A schematic magnetization curve where the differences between ac and dc susceptibility are reported.[1]

Another advantage of the ac susceptibility is that the measured signal does not depend of the external static applied field but only on the weak alternating one and investigations can be done in zero static field, thus avoiding saturation effects or the smearing of phase transitions.

A further feature is that the frequency of the AC field can be varied easily over a wide range, in general about three-four order of magnitudes for a given pick-up coil. By using a phase-sensitive detection mode, i.e. a lock-in the two components of the response of the magnetisation to the oscillating field can be detected providing the complex susceptibility:

$$\chi = \chi' + \chi'' \qquad (6)$$

where χ' and χ'' are the real and imaginary part of the susceptibility. From a thermodynamic point of view we can define two limiting cases: the first, when ω is slow compared to the relaxation rate of the system, is characterized by no phase lag of the magnetization and the susceptibility and it is called the *isotherm* limit and noted χ_T. The other, when the system is not able to follow the *ac* field because it oscillates too fast compared to the relaxation rate and so the measured susceptibility is called *adiabatic* and noted χ_S. Replacing these parameters in the Eq. (6), the susceptibility becomes:

$$\chi\left(\omega\right) = \frac{\chi_T + \chi_S}{1 + i\omega\tau} \qquad\qquad (7)$$

where τ is the characteristic time of the system to come back to a thermodynamic equilibrium. The two components of the susceptibility becomes: [2]

$$\chi' = \frac{\chi_T - \chi_S}{1 + \omega^2\tau^2} + \chi_S \qquad\qquad (8)$$

and

$$\chi'' = \frac{(\chi_T - \chi_S)\omega\tau}{1 + \omega^2\tau^2} \qquad\qquad (9)$$

In Figure 5 is reported the theoretical dependence of χ' and χ'' on ω; χ'' goes to the maximum value when $\omega\tau = 1$ and is zero when $\omega \to 0$ or when $\omega \to \infty$. In contrary χ' has its largest value at low frequency and the its limits are the above mentioned χ_T and χ_S.

The Eq. (7) can be modified to take into account a distribution (or dispersion) of the relaxation times due to differently behaving components in the sample by introducing a parameter α. For a system characterised by a distribution of relaxation times the two components of the susceptibility can be calculated as:
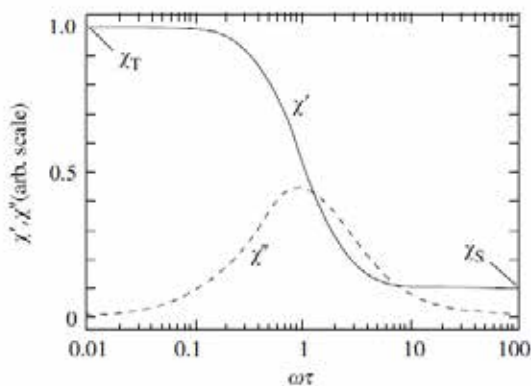
Figure 5. Scheme of the theoretical frequency dependence of the real and imaginary components of the susceptibility.[1]

$$\chi(\omega) = \chi_S + \frac{\chi_T \chi_S}{1+(i\omega\tau)^{1-\alpha}} \qquad (10)$$

and $\chi''(\omega)$ and $\chi'(\omega)$ are defined as:

$$\chi'(\omega) = \chi_S + (\chi_T - \chi_S)\frac{1+(\omega\tau)^{1-\alpha}\sin(\pi\alpha/2)}{1+2(\omega\tau)^{1-\alpha}\sin(\pi\alpha/2)+(\omega\tau)^{2-2\alpha}} \qquad (11)$$

$$\chi''(\omega) = (\chi_T - \chi_S)\frac{(\omega\tau)^{1-\alpha}\cos(\pi\alpha/2)}{1+2(\omega\tau)^{1-\alpha}\sin(\pi\alpha/2)+(\omega\tau)^{2-2\alpha}} \qquad (12)$$

when by fitting the frequency dependence of the imaginary susceptibility with Eq.(12) the relaxation time τ and the α parameter can be evaluated. α varies between 0 an 1, the larger its value the larger the width of the distribution of the relaxation times in the sample. The procedure can also be repeated using Eq. (11), although this one does not show a peak feature. By repeating the measurements at different temperatures it is possible to investigate the temperature dependence of the two parameters, τ and α. The same analysis can be repeated for different applied static fields.

By plotting $\chi''(\omega)$ versus $\chi'(\omega)$ is possible to obtain a *so*-called Argand plot that allows a direct estimation of the α parameter. When a single relaxation time is present the Argand plot is represented by a semicircle centred on the x axis. The larger is the distribution the flatter is the curve.

144

These type of magnetic measure are crucial for the investigation of the slow relaxation processes of SMM systems and for investigate the magnetization of VT and SCO.

5.2 Low Energy Ion Scattering (LEIS)

Low Energy Ion Scattering (LEIS), also called Ion Scattering Spectroscopy (ISS) is the most powerful technique to investigate the composition of the topmost layer of a surface.[3] Due to the low penetration depth of ions (at the basis of the surface sensitivity of this technique) and to the consequent need of keeping clean the investigated surface, Ultra High Vacuum (UHV) environment is mandatory to perform ISS. This technique is based on the inelastic scattering of accelerated noble gas ions (usually He and Ne) impinging the surface at energies between 500 and 10000 eV. The noble ions collide the surface topmost layer and, in first approximation, this phenomena can be described like an inelastic binary collision of a projectile of mass M_i with energy E_0 with a target atom of mass M_t as schematised in Figure 6.
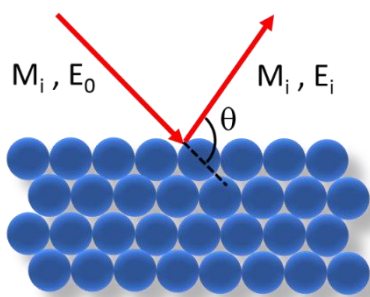
Figure 6. Schematic elastic binary LEIS process, the projectile collides the target and it is then scattered.

In the collision part of the E_0 energy of the projectile is transferred to the target atom. The energy transferred to the surface target depends on the scattering angle (θ) and on the mass of the two atoms, i.e. M_i and M_t. The projectile is then scattered with a different energy E_i and it can be collected by an ions analyser. An energy scan of the scattered ions allows to get information on the chemical composition of the surface layer. By knowing the scattering angle and the mass of the projectile, Eq. (

13) can be used to calculate the mass of the target atom or to predict the energy of the ions after the impact with a known target on the surface:[3]

$$\frac{E_i}{E_i^0} = \left\{ \frac{\pm\left[\left(M_t^2 - M_i^2 sin^2\theta\right)^{1/2} + M_i cos\theta\right]}{(M_i + M_t)} \right\}^2 \tag{13}$$

However, if the target possesses a low atomic weight, the energy and the mass of projectiles are high, the interaction of the projectiles with the surface can modify the structure of the surface.[4,5] In order to avoid such phenomenon, low energy ions are commonly used (< 1000 eV) to investigate surface composition, but accelerating the ions and using ions with larger mass, it is possible to achieve information about the "inner layers" of the sample[4] due to the occurrence of sputtering processes used ion gun.

This technique is commonly used for qualitative investigations, but with a good approximation, by estimating the differential cross sections of the investigated elements through the Thomas–Fermi–Molier interacting potential and using the "Magic Formula" by Ziegler, Biersack, and Littmark,[6] it is possible to quantify the contributions of the different elements in the LEIS spectra and then to evaluate the elemental composition. The nuclear potential is the dominant factor in the events scattering. This potential is normally written as:

$$V(r) = \frac{Z_1 Z_2 e^2}{4\pi\varepsilon_0 r} \Phi\left(\frac{r}{a}\right) \tag{14}$$

where Z_1, Z_2 are the atomic numbers of ion and atom, e is the electronic charge, r is the radius, and a is the "screening length". The screening function is unity at $r = 0$ and decreases by increasing r. Using Eq (14) the scattering angle can be calculated for each interatomic collision. The scattering of ions is thus calculated by using the empirically derived "Ziegler-Biersack- Littmark (ZBL) Universal Screening Potential":[6]

$$\Phi_U = 0.1818e^{-3.2x} + 0.5099e^{-0.9423x}$$
$$+0.2802e^{-0.4028x} + 0.2817e^{-0.2016x} \tag{15}$$

with the normalized radius:

$$x = r/a_U \tag{16}$$

and the screening length

$$a_U = \frac{0.8854 a_0}{Z_1^{0.23} + Z_2^{0.23}}$$ (17)

where a_0 is the Bohr radius. The empirical function Eq.15 is based on calculated solid-state interatomic potentials of 522 randomly chosen pairs of atoms over the range 1-82 for Z_1 and Z_2. [6]

In Chapter 2 we described the use of this technique for the study of the lanthanum strontium manganite $La_{0.7}Sr_{0.3}MnO_3$ (LSMO) topmost layers composition on a neodymium gallate ($NdGaO_3$, NGO) (100) single crystal. The four elements have quite different atomic weights thus facilitating this analysis. Moreover, varying the sputtering efficiency by changing the mass of the ions and their energy allowed to investigate the variation of the composition in the layers underneath the surface.

5.3. Time-of-Flight Secondary Ions Mass Spectrometry (ToF-SIMS).

Time-of-Flight Secondary Ion Mass Spectrometry[7] is a surface sensitive technique. With its soft ionisation mechanism, is particularly suited for the desorption of fragile molecules, such as purely organic molecules and the coordination compounds.[8,9,10,11] Molecular ions or their fragments produced with this process come from the topmost layers of the sample and only these fragments have sufficient energy to overcome the surface binding energy and leave the sample. This technique is extreme surface sensitivity due to the low mean free path of secondary ions. For this reason only the first molecular layers of the sample are involved in the ionic bombardment as well as in the subsequent desorption. The investigated sample is bombarded with a pulsed primary ions beam (Au^+ in our experiments) with energy in the range of 10-25 keV, producing fragmentation and bond breaking in the close proximity of the collision site. The obtained fragments moving into the sample. The particles loose part of their energy promoting the production of molecular fragments. This phenomenon induces the formation of neutral, positive or negative secondary particles. Only the charged ones are collected by the Time of Flight detector (ToF), revealed and analysed as a function of their m/z ratio. By placing the detector far from the sample, which means that secondary ions have a long path (see Figure 7) it is possible to get an excellent mass resolution (often exceeding 10,000 $m/\Delta m$).[12]
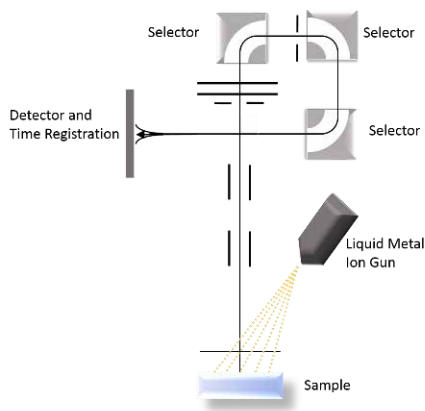
Figure 7. ToF-SIMS spectrometer simplified scheme.

A Time-of-Flight mass spectrometer is based on the measure of the time that the fragments spend to travel a distance through a medium to finally reach the spectrometer. The ions are accelerated from the surface to the instrument detector, through a sequence of electrostatic lens and selectors allowing the *m/z* selection of the produced fragments. The relation between mass and time of flight is defined by:

$$E = \frac{mv^2}{2} = \frac{mL^2}{2zt^2}$$ (18)

where *E* is the acceleration energy, *m* the mass of the flying object, *v* the velocity of the object, *L* is the length of the travel and *t* is the flight time. Is easily notable how the ToF depends on the *m/z*, on the length of the flight as well as on the acceleration energy. Ions with lower *m/z* values will have higher speed than those of higher *m/z* values.
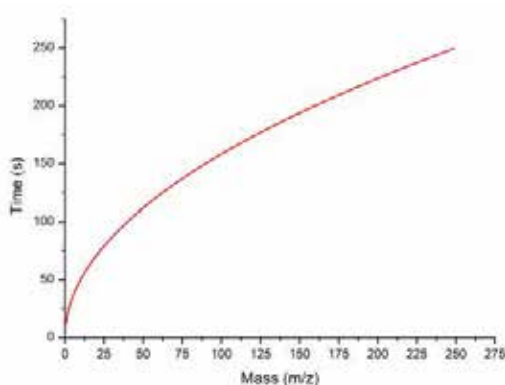
Figure 8. Flight time versus ions mass, obtaine using Eq. 18. with the experimental set-up parameters indicated in the text.

In Figure 8 is reported the trend of time of flight versus ions mass in the case of a unitary z, a potential E set to 500 eV and a length of the drift tube L = 1 m. As evident from the Figure 8 and from Eq.18 in order to obtain the best separation of ions, E must be constant and this is achieved by pulsing the primary ion source with short pulse in order to yield secondary ions with a very short time dispersion and with a very low energy dispersion. A fixed voltage then accelerates the secondary ions (that could be positive or negative) into the ToF analyser. The energy and angular dispersion of the secondary ions can be focused using electronic components like focusing lens, ion mirrors or reflectors and selectors. After separation in the ToF analyser, the secondary ions are post-accelerated with a voltage up to 15 kV. This acceleration is applied to the ions to improve the detection efficiency of the high-mass ions. In the end the ions reach the detector unit, which is typically composed by a photo-converter electrode, a channel plate, a scintillator, a photomultiplier and a counter, all in series. The complete setup of the used ToF-SIMS apparatus is sketched in Figure 7.

ToF-SIMS spectroscopy provides important and exhaustive information about molecular surface deposition processes for both evaporated system and SAM. For instance it is possible to understand if the molecules are chemically grafted or simply physisorbed on the surface, or to detect the presence of additional physisorbed layers on top of the chemisorbed one. In this thesis work, ToF-SIMS has been used to clarify SAM deposition process and to understand if the integrity of evaporate molecule occur.

5.4 Photo Electron Spectroscopies (PES)

The Photo Electron Spectroscopies (PES) are based on photoemission effect, discover for the first time by H. R. Herzt in 1887, and rationalized by Einstein in 1905.[13] Its application in spectroscopic studies was developed only in the '50s and '60s by Siegbahn that was awarded with the Noble prize in 1981. Siegbahn, noted that the PES spectra can be used for chemical analysis,[14] and developed the so called Electron Spectroscopy for Chemical Analysis (ESCA).

PES techniques are very powerful tools for the study of conducting substrate and for hybrid organic conductive substrate. The photoelectric effect requires photons with energies from a few electron-volts to over 1 MeV in elements with a high atomic number. The photoemission effect takes place when a photon transfers part of its

energy to an electron to get over the potential barrier (binding energy) holding it to the atom. The exceeding energy is given by the photon to the electron as kinetic energy. In a mono electronic approximation the process can be ascribed whit the following formula:

$$hv = E_b + E_k + \phi_s + \phi_{spec} \tag{19}$$

Knowing hv, the energy of the photon, and kinetic energy (E_k) of the photoelectron it is possible to calculate the binding energy (E_b) where Φ_s is the work function of the investigated solid and Φ_{spectr} is the work function of the spectrometer. The work function is defined as the energy difference between the Fermi and the vacuum level.

When the sample and the spectrometer are at the equilibrium and are in electrical contact their Fermi energies are equal. When photoelectrons goes from the sample to the spectrometer, due to the difference of the work functions of the two materials (Φ_s - Φ_{spec}) electrons feel a potential and they can accelerate or decelerate. Different materials have different work functions. In this approximation the two Fermi levels, of the sample and the spectrometer, are the same therefore they have different work functions.
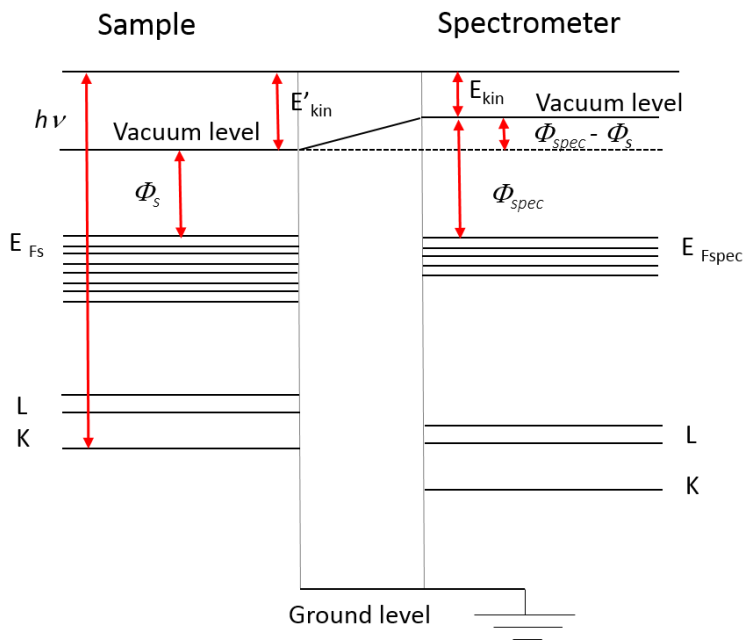

Figure 9. Sample levels scheme (left) and spectrometer levels (right).

This kind of connection between sample and spectrometer introduces a shift in the detected kinetic energy of the electrons that must be corrected to be able to compare spectra acquired with different spectrometers. Usually the correction to the kinetic energy is obtained by using an internal reference. Generally the spectra is acquired with a hemispherical analyser able to counts the number of electrons selected as a function of their kinetic energy (Figure 10). Due to the kinetic energy dependence on the radiation energy, generally it is preferred to report the binding energy in the abscissa. PES measurements allow to measure only the energy of the final state but not the initial state, because one measure only the transfer energy directly connected to the energy gap between initial and final state. The energy of initial state can be only obtained by theoretical considerations.

5.4.1 X-ray Photoelectron Spectroscopy (XPS) and Angle Resolved X-Ray Photo electron spectroscopy (AR-XPS).

Generally, in a X-ray photoelectron Spectroscopy (XPS) setup, incident photons of energies between 100 to 1500 eV are used; the common X-ray sources used in a conventional laboratory are the Al Kα (1486.6 eV) and Mg Kα (1253.6 eV). On the contrary, in synchrotron experiment it is possible to tune the frequency of incoming photons according to the interested elements. In order to compare the intensity of different XPS peaks the relative atomic photoemission cross-section (σ) must be taken into account. This parameter depends on the atomic initial state and on the photon energy.The cross-section (σ) depends on the atomic initial state and on the photon energy. A complete table of the element photoemission cross-section can be obtained from specific databases. [15]

In a good approximation the cross section allows to compare the intensity of XPS peaks originated by different atoms, thus leading to the possibility to extract information about the surface chemical composition. The tabulated values have been used in this work for the quantitative and semiquantitative interpretation of the XPS spectra. The intensity of each peak can be evaluated by integrating the corresponding area, after the subtraction of the inelastic background, and by dividing the extracted areal value by its relative cross section. In this way it is possible to estimate the surface chemical composition with an error that typically is below 10 % also in the case of very diluted elements.

Photoelectrons are generally selected by a hemispherical analyser which is able to distinguish the electrons by kinetic energy, and then counted them with a detector, that could be a single or multichannel plate (Figure 10).
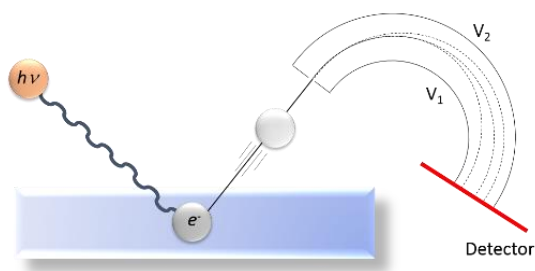
Figure 10. The X-ray photon ($h\nu$) excites the electrons of the sample which are emitted as photoelectrons. The photoelectrons are then separated in energy by means of a hemispherical analyser.

In order to understand the lineshape of a specific peak in a typical XPS spectrum several effects have to be taken into account:

- Multiplet splitting;
- Satellites (shake-off and shake-up);
- Plasmons;
- Auger peaks.

Multiplet splitting occurs when there are unfilled shells containing unpaired electrons. For instance, transition metals with unfilled *p* and *d* orbitals and rare earths with unfilled *f* orbitals all show multiplet splitting. Vacancy created by photoionization (unpaired electron left behind after ionization) couples with an unpaired electron in the originally incomplete valence shell and generates splitting of the orbital (*p*, *d* or *f* orbitals). For example iron in Fe_2O_3 has 5 unpaired electrons in the *3d* shell (Figure 11). After the photoionization in the *3s* shell, there are 2 possible final states differing in the coupling, i.e. relative spin orientation, between the unpaired electron in the core and the unpaired electrons in the valence shell. This can create a number of final states, which will be seen in the photoelectron spectrum as a multi-peak envelope.

Figure 11. Possible final state in a Fe^{3+} (d^5) system.

In addition, the total electronic angular momentum (*j*) is a combination of the orbital angular (*l*) and spin (*s*) momenta. The *j-j* coupling is equal to $|L \pm S|$ where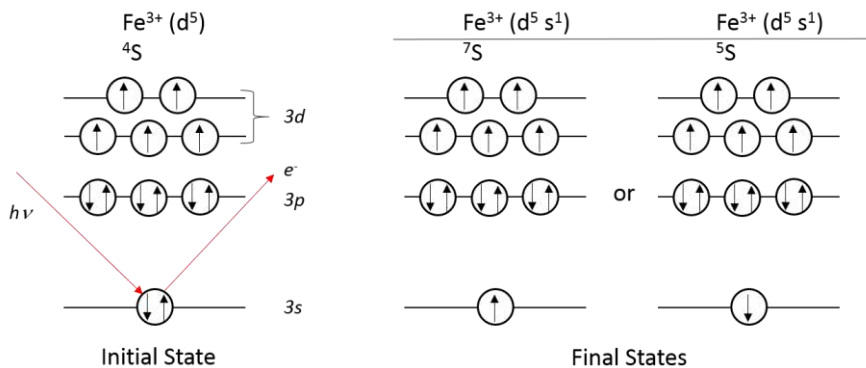 L and S are the total orbital angular and spin momenta, respectively. For angular quantum number $l \neq 0$ the line is a doublet. The splitting is given by two different final state $j_+ = l + s$ and $j_- = l - s$. For instance in p orbitals the doublet will be $p_{1/2}$ and $p_{3/2}$ because $l = 1$ and $s = \pm 1/2$ therefore $j_- = 1/2$ and $j_+ = 3/2$ and the relative intensity will be 0.5; for d orbitals, the doublet will be d_{x1} and d_{x2} because $l = 2$ and $s = \pm 1/2$ therefore $j_- = x1$ and $j_+ = x2$ and here the relative intensity will be 0.75.

Satellites are due to a sudden change in Coulombic potential as the photo-ejected electron passes through the valence band. Satellites occurs when a core electron is removed by a photoionization. There is a sudden change in the effective charge due to the loss of shielding electrons. This perturbation induces a transition in which an electron from a bonding orbital can be transferred to an anti-bonding orbital simultaneously with core ionization. Two types of satellite are detected:

- Shake-up: an ion generated by photoionization will be left in an excited energy state a few eV above the ground state and when this happens, the kinetic energy of the emitted photoelectron is reduced and this will be seen as a "shake-up" peak at a higher binding energy than the main line. Shake up broadening lines are generated by the coupling of the photoelectron with the partially-filled metal shell during the time of flight following ionization;[16]

- Shake-off: when the excitation occurs into free continuum states, leaving a double ionized atom with holes both in the core level and valence shell, the effect is denoted as a shake-off satellite. It appears as a broadening of the core-level peak or contribute to the inelastic background.
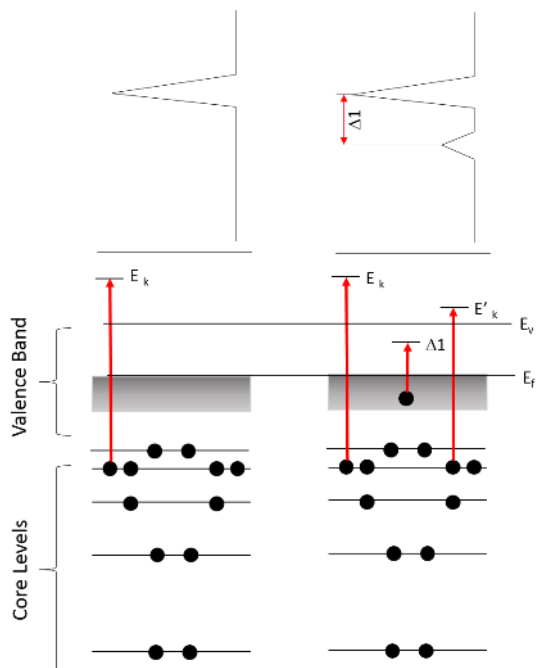
Figure 12. Scheme of shake up peaks in XPS experiments.

Shake-up satellite (Figure 12) are very useful features to get information about the chemical environment in transition metal oxides associated with paramagnetic species. Generally, the shake-up satellites have intensity and energy separations from the parent photoelectron line that depends on the chemical state of the investigated element. With transition metals, the absence of these lines is indicative of the elemental or diamagnetic states. Prominent satellites occurs with paramagnetic states.[17–20]

Photo-electrons travelling through the solid can interact with other electrons in the material. These interactions can result in the photoelectron exciting an electronic transition, thus losing part of its energy (inelastic scattering process). Most common features are due to interband or plasmons effects. The satellites due to plasmon loss are rarely sharp in insulators but very prominent in the metals. The plasmon effect is normally observed as additional oscillations at higher binding energy respect to the main peak of lower intensity but with the same splitting in energy of the main feature. More than one set of plasmon satellites can be observed in case when the surface and the bulk are characterized by different plasmons.

Also Auger electrons emission occurs when X-rays impinge a sample. Auger electron is initiated by the photoemission, with the creation of an ion with an inner shell vacancy. Auger electrons are emitted during the non-radiative relaxation of the excited ion: an electron from a higher lying energy level decays in the inner shell vacancy promoting the simultaneous emission of an Auger electron. It is thus a ***three-electron*** process.

We have already seen that in order to perform quantitative and semiquantitative analysis it is important to know the elements cross-section (σ). This depends not only on the atomic initial state and on the photon energy but also on the inelastic mean free path (λ). The inelastic mean free path is defined as the average distance that an electron with a given energy can travel through successive inelastic collisions. One λ is defined as the 32% of all photoelectrons coming from the surface without collisions, while the majority of photoelectrons (98%) will come from 3 λ. For most core electrons excited by Al Kα X-rays this depth is in the order of a few nm. On the basis of this, it is possible to estimate the thickness of a film deposited on top of a substrate by tilting the sample orientation with respect to the analyser. In an Angle-Resolved XPS (AR-XPS) is thus possible to collect information about thin surface layers composition and also about segregation in complex matrices. The effective inelastic mean free path is given by the following formula

$$\lambda = E_k \left(\left[28.8 \sqrt{\frac{N_v \rho}{M}} \right]^2 \left\{ \beta \ln(\gamma E_k) - C E_k^{-1} + D E_k^{-2} \right\} \right)^{-1} \qquad (\,20\,)$$

where E_k is the kinetic energy of the involved electron, N_v is the number of valence electrons per atom/molecule of the matrix, ρ is the density of solid, M is the molecular weight and β, γ, C and D are material parameters (depending on the electronic structure of the material).
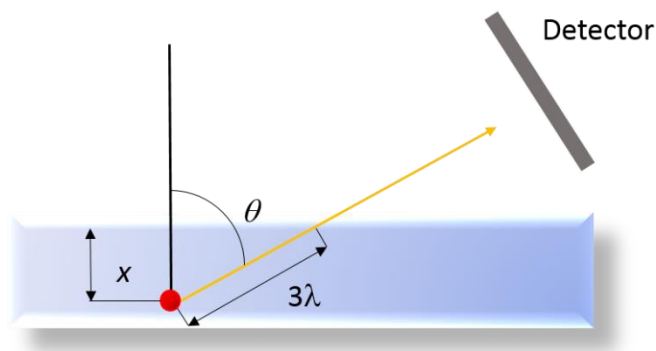
Figure 13. Schematic representation of AR-XPS.

The distance *x* that the electrons have to travel through the sample is crucial in determining their probability of escape from the material without inelastic scattering. It is given by:

$$x = 3\lambda sin\theta \qquad\qquad (21)$$

where θ is the collecting angle between the normal to the surface and the collection angle. Therefore knowing the λ of the sample the XPS sampling depth can give important information like:

- the thickness of a layer of material deposited on a substrate by the attenuation of the intensity of the substrate signal;
- the profile of the stoichiometry by measuring at different collection angles, because on increasing θ the distance that the electron has to travel increases thus reducing the sampled thickness.

This particular evolution of XPS, was used in addition with LEIS, to investigate LSMO topmost layers, estimating a possible element segregation and define atomic concentration profiles for this system.[4]

5.4.2 Ultraviolet-Photoelectron Spectroscopy (UPS)

Ultraviolet-Photoelectron Spectroscopy (UPS) is the most powerful and versatile technique to study the electronic structure of the valence bands in atoms, solids and molecules (ionization energy of molecules, HOMO). This PE process depends on parameters such as Emission angles, Spin polarization, Photon energy (hv).

Commonly the used energy range is between 16.6 and 40.8 eV, being the most common ionization sources Ne(I) at 16.6eV, Ne(II) at 26.8eV and He(I) at 21.2eV, He(II) at 40.8eV. These lines are produced by cold cathode capillary discharge causing the excitation of the gas. Each line is due to the resonance fluorescence produced when the gas is excited by the discharge and then decays back to its ground state. The nomenclature refers to light emitted from neutral atoms, i.e. He(I) and to light emitted by singly ionized atoms, i.e. He(II). The resonance line produced by transition from the first excited state to the ground state is usually the most intense one (called raie ultime).
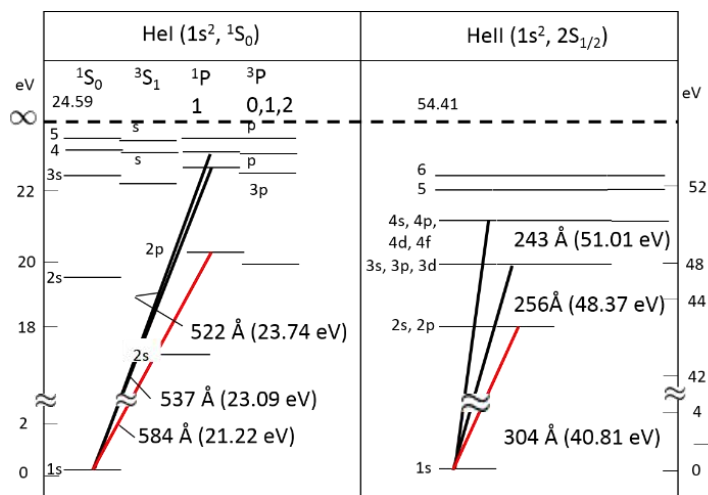
Figure 14. Grotian diagram for He(I) and He(II).

In Figure 14 the strongest resonance lines of He are reported, where 98% of the emission intensity is given by the line at 21.22 eV and the residual 2% is given by the other lines present in a He discharge (23.09 eV, 23.74 eV and 40.81 eV). UPS, allowing the study of the valence band, provides useful information about the electronic structure of the surface and of molecular films. By comparison of the UPS spectrum at different sample temperature, it has been possible to follow the temperature conversion from the high-spin or low-spin state in a Spin Cross-Over molecule, deposited with thermal evaporation procedure. Generally, it is possible, by comparison of the UPS spectrum with the calculated Density Of State (DOS) of the isolated molecule, to evaluate the intactness of the molecules and the extent of interaction with the substrate.

5.5 X-ray synchrotron radiation based experiments

An electromagnetic radiation can be efficiently generated by the deviation of an electron beam accelerated at relativistic energies: the energy loss involved in this process is released to give a continuous spectrum, this concept is exploited in a synchrotron light facility.

In a synchrotron electrons are produced by an electron gun and accelerated by a linear accelerator up to several tens of MeV. Then "bunches" of electrons are then moved into the so called "booster ring", where their energy is increased up to the GeV range, and subsequently they are passed into a "storage ring". Once introduced in this higher diameter ring, linear trajectory of electrons is deviated by means of magnetic fields, this process leads to the emission of electromagnetic radiation along the tangent to the electrons trajectory that can be used for a very large range of experiments. Depending on the specific purpose a portion of the electromagnetic radiation can be selected by adopting specific "curved sections". When intense and monochromatic radiation is required like in XMCD experiments "insertion devices" are used. Those devices are made by periodic arrays of magnets placed above and below the electron pathway (Figure 15). The insertion devices are divided in two classes the *wigglers* and the *undulators*.
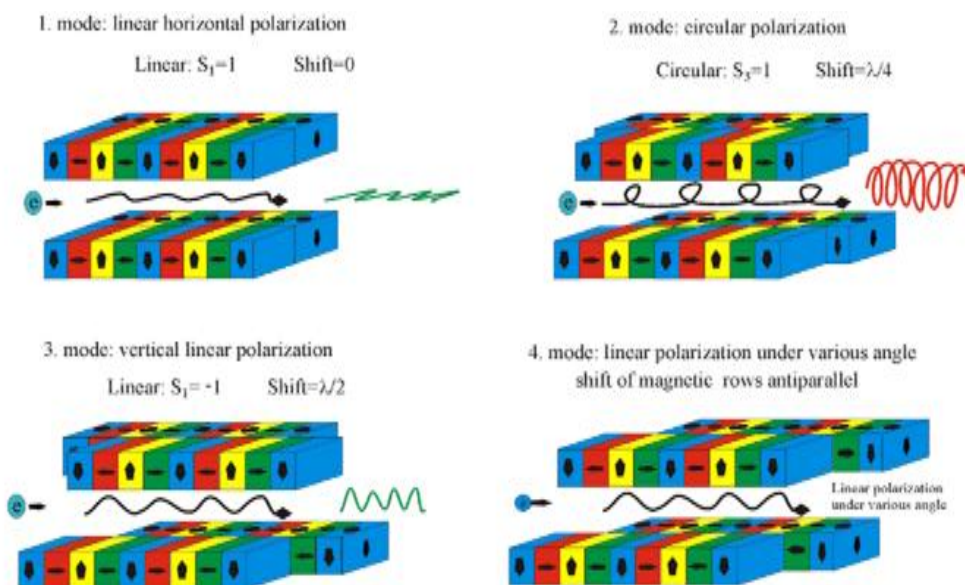

Figure 15. Schematic representation of an insertion device. In the *undulator* the gap distance between the two rows can be modified to tune the spectral emission

Wigglers are composed by several magnetic sections causing a large oscillation amplitude of the electrons, due to high static magnetic fields. These deviations leads to an overall high energy emission of light (10-20KeV) that is poorly collimated and which polarisation (linear horizontal or vertical) depends on the distance from the horizontal plane of the ring plane. In *undulators* the magnetic field of each section is weaker thus electrons are less deviated (induced oscillation are smaller in amplitude). This results in a narrow emitted radiation cone and a smaller spectral width. In these devices, by changing the distance between the upper and lower rows of magnets (Figure 15) the energy interval can be tuned into the appropriate range. Moreover, both circularly and linearly polarisations of X-ray radiation can be easily achieved by a relative horizontal displacements of the upper and lower rows of magnets thus allowing polarised-light dependent experiments.

In this thesis all synchrotron-based measurements where obtained using Total Electron Yield (TEY) detectors. This type of detection mode is based on the measurement of the drain current originated when absorption occurs: absorption, induces the emission of electrons due to the following relaxation processes; thus TEY, by indirectly measuring this effect results proportional to the number of photons absorbed by the sample at a given energy. We notice that the sampling depth of TEY measurements is limited by the mean free path of the electrons that are emitted in the absorption process. These secondary electrons have limited energy thus limiting the escape depth of an electron to 5-10 nm depending on the involved excitation radiation. For this reason TEY-based spectroscopies result surface sensitive techniques. In certain cases the combination of TEY measurements with more depth sensitive fluorescence yield measurements can be used to provide a more complete picture of the electronic structure of a material.

5.5.1 X-ray Absorption Spectroscopy (XAS)

X-ray Absorption Spectroscopy (XAS) is an experimental technique that yields information concerning the local electronic structure of the sample, as well as about the magnetism and the structure of investigated materials. In particular, in this thesis XAS has been exploited to understand structural and magnetic features of metalorganic systems in bulk as well as at the nanoscale. This information can be extracted once measurements are made using polarized X-rays.

XAS is based on the selective excitation of core electrons to unoccupied electronic states by means of photons, according to the dipole selection rules. If the incident photons have an energy equal or larger than the difference in energy between the initial state and the unoccupied final electronic state, X-rays are absorbed. The fine structure of the obtained spectrum recorded is a fingerprint of the atomic species present as well as of the oxidation state and the coordination geometry of the absorbing atom. The phenomenon of X-ray absorption is useful in the investigation of metalorganic compounds due to its unique atomic selectivity, the high sensitivity to charge state, as well as to the sensitivity to spin state. It also provides a direct insight on the coordination symmetry of the investigated atoms. Moreover, by using circularly polarised light it is possible to selectively promote transitions involving only spin up or spin down electrons that can be used to gain insight of the local magnetism of the absorber, by simply evaluating the dichroism (XMCD), i.e. the difference between the absorbed light using left and right polarizations. On the other hand, by using linearly polarized light it is possible to collect information about the anisotropy of the charge distribution around the absorbing atom, recovering information about the orientation of the orbitals and thus the orientation of the molecules assembled on a surface. This can be done by simply evaluating the natural linear dichroism (XNLD) extracted as the difference between vertically and horizontally polarised light.

The above mentioned description of X-rays absorption by matter is defined as the "one electron approximation".[21] This treatment is also referred as the "active electron approximation",[21] being all other electrons in the atom ignored and considered passive during the excitation process. Such description has the advantage of being intuitive even if cannot be used to describe rigorously the XAS process. In fact, electrons not directly involved in the excitation are not actually passive, but rather influence the active electron. This oversimplification for this reason cannot be used to treat on a quantitative basis the spectra of metal ions. A more correct way to describe the phenomenon is the *configuration picture*.[21] Transitions involved in soft X-ray absorption are governed by the dipole selection rules where configurations can be described by their total angular momentum (J) which can be calculated with the (j-j) coupling scheme. The rules place limits on the excited states that can be created via the absorption of a photon in absorption measurements. The dipole selection rules are described in terms of the allowable changes in the various quantum numbers, and are summarized in Table 1.

Table 1. Dipole selection rules

Quantum Number	Selection Rule
Δn	(not constrained)
Δl	± 1
Δs	0
Δj	0, ± 1
Δm_j	0, ± 1; $m_j = 0$ to $m_j' = 0$ are forbidden if $\Delta j = 0$

These selection rules mean that only certain electronic states contribute to the measured spectra, thus the measurements are not indicative of the total density of states but rather of a partial density of states. In general, an absorption process, causing the excitation of a particular core level will involve transitions to an excited states of only one type.

Table 2. Notation used in soft X-ray spectroscopy

X-ray notation	Atomic Notation	Quantum Numbers		
n	nl_j	N	l	j
K	$1s$	1	0	1/2
L_1	$2s$	2	0	1/2
$L_{2,3}$	$2p_{1/2,\ 3/2}$	2	1	1/2 , 3/2
M_1	$3s$	3	0	1/2
$M_{2,3}$	$3p_{1/2,\ 3/2}$	3	1	1/2 , 3/2
$M_{4,5}$	$3d_{3/2,\ 5/2}$	3	2	3/2, 5/2

X-ray absorption spectra are most often described with atomic notation, using the quantum numbers of the core electron, in the format nl_j. For instance K-shell absorption denotes the complete set of measurements involving the creation of a $1s$ core level. The notation used to describe several relevant absorption edges is summarised in Table 2.

The phenomenon of X-rays absorption by matter can be rationalised as a time dependent perturbation of the atomic levels (described by the stationary Hamiltonian containing electron/nucleus and electron/electron interactions).[21]
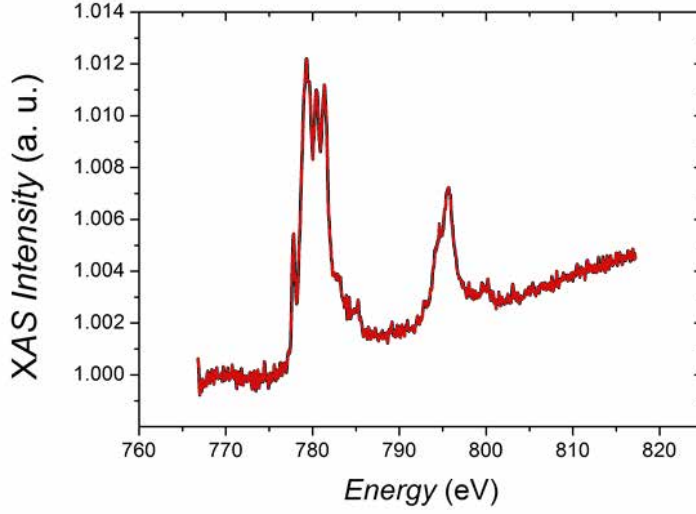
Figure 16. Co L$_{2,3}$ spectrum of a monolayer of Cobalt Valence Tautomer.

In a non-relativistic approach, the transition probability T_{if} for this process can thus be expressed using the formalism developed by Dirac [22] as:

$$T_{if} = \frac{2\pi}{\hbar}\left|\langle f|\mathcal{H}_{int}|i\rangle + \sum_n \frac{\langle f|\mathcal{H}_{int}|n\rangle\langle n|\mathcal{H}_{int}|i\rangle}{\varepsilon_i - \varepsilon_n}\right|^2 \rho(\varepsilon_f)d(\varepsilon_i - \varepsilon_f) \qquad (22)$$

where ε_f and ε_i are the energy of the final and the initial state respectively, $\rho(\varepsilon_f)$ is the density of the final state per unit of energy, and $\mathcal{H}_{int}$ is defined by

$$\mathcal{H}_{int} = \frac{e}{m_c}\vec{p}\cdot\vec{A} \qquad (23)$$

The Hamiltonian is related to the interaction between the excited electron of rest mass m_c, charge e and momentum p and the electromagnetic field of the radiation, of potential vector A. Just to clarify the electric field of the radiation can be obtained from A according to $\vec{E} = \frac{\delta\vec{A}}{\delta t}$. The explicit equation describing the X-ray absorption cross section (σ), which, after an integration in the domain of energies, will provide the intensities of the transitions:

$$\sigma = \frac{T_{if}}{\Phi_0} = 4\pi\alpha|\langle b|\vec{r}\cdot\vec{\varepsilon}|a\rangle|^2\eth[\hbar\omega - (E_b - E_a)]\rho(E) \qquad (24)$$

where

$$\alpha = \frac{e^2}{4\pi\varepsilon_0\hbar c} \approx \frac{1}{137} \qquad (25)$$

The calculation of the transition matrix element depends on the wave functions $|a\rangle$ and $|b\rangle$.

XAS has been used in this thesis for all *in situ* thermal evaporations of SMM, and *ex situ* deposited SMM and VT to verify the integrity of the molecular systems as well as to follow the temperature dependence of the VT phenomenon.

5.5.2 X-ray magnetic Circular Dichroism (XMCD)

X-ray magnetic circular dichroism (XMCD) is an experimental technique that enables quantitative determination of the magnitude, direction of the spin and orbital moments of each investigated element.[23] Noticeably, if again associated to TEY detection mode, this technique allows the magnetic characterisation of very diluted samples including ultrathin magnetic films and two dimensional arrays of magnetic nanostructured samples. The XMCD technique relies on spin selective photon excitation from the spin orbit split core electronic levels.[21]

Considering the left circular polarisation, σ^+, the one with the helicity pointing to the photon propagation direction and the reverse for the right polarisation, σ^-, r the XMCD spectrum is given by the subtraction of spectrum registered at σ^- minus the spectrum registered at σ^+:

$$XMCD = \sigma^- - \sigma^+ \qquad\qquad (26)$$

Circularly polarized X-ray light is used here to transfer the photon angular momentum $\hbar$ to the sample along the magnetization direction. This leads to consider XMCD as a vector magnetometry, the dichroic intensity being proportional to **k·M**.

According to the dipole selection rules, using circular light, transitions from the $2p_{3/2}$, and $2p_{1/2}$ initial states to the empty *3d* levels are allowed with spin selectivity. The unbalance of the empty *3d* final states caused by the exchange splitting of the *3d* final state leads to a spin selective absorption process and yields information about the spin polarization of the *3d* states. The spin moment (m_s) is simply given by the difference between the number of spin up (N$^+$) and spin down (N$^-$) *3d* holes, reflected in the intensity of the *2p* $_{3/2}$, and 2p $_{1/2}$ white lines. [24,25]

The absorption in the exchange split valence states is different for circularly polarized light. According to the previously mentioned XAS selection rules we have:

$$\Delta j = 0, \pm1 \; ; \Delta s = 0; \; \Delta m = +1 \text{ (left circular)} -1 \text{ (right circular)}$$

Considering the $L_{2,3}$ edges (the transition within $2p_{3/2}$ and $2p_{1/2}$ and $3d$ levels) the XMCD experiment can be described in the "one electron approximation" using a two-step picture.[26]

In the first step photoelectron are excited by X-rays absorption. If the photoelectron originates from a spin-orbit split level, like the $2p_{3/2}$ level, the angular momentum of the photon can be partially transferred to the spin through the spin-orbit coupling ($j = l \pm s$). For this reason right circularly polarized photons will transfer the opposite momentum to the electrons respect to the one excited by left circularly polarized photons. Photoelectrons with opposite spins are created in the two cases: since the $2p_{1/2}$ (L_2) and $2p_{3/2}$ (L_3) levels have opposite spin-orbit coupling, the spin polarization will be opposite at the two edges. For this reason, in the absorption process, "spin-up" and "spin-down' are defined in respect to the photon helicity, which is parallel (right) or antiparallel (left) to the X-ray propagation direction.
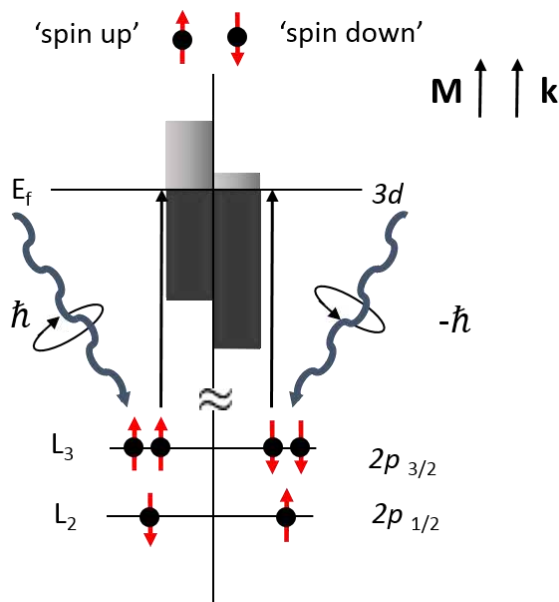

Figure 17. Schematic representation of the circular polarised light absorption. The different probability of the two transitions gives rise to the XMCD signal.

After the excitation of photoelectron the spin-split *d* valence shell acts as a detector for the spin of the excited photoelectron. If the *d* states possesses an orbital momentum electrons can also act as orbital momentum detector allowing to separate the spin and orbital contribution to the magnetic moment. The quantification of the two contributions can be achieved by using the *sum rules.* As illustrated in Figure 17 we shall denote the differences of intensities recorded with right and left circular polarization for metals, e.g. the XMCD intensities.

The strong dichroism at the $L_{2,3}$ edges of transition-metal ions and $M_{4,5}$ edges of rare-earth ions provides information about their ground-state magnetic properties. Exploiting the chemical sensitivity of X-ray absorption edges contributions from different transition-metal and rare-earth ions within the molecule can be easily separated. In XMCD technique the maximum dichroism is observable when the polarization of the light lays on the same direction of the magnetisation direction. In this thesis the XMCD technique has been used in order to confirm the SMM behaviour after the deposition process and to get information about the easy axis magnetization direction of adsorbed molecules in respect to the surface.

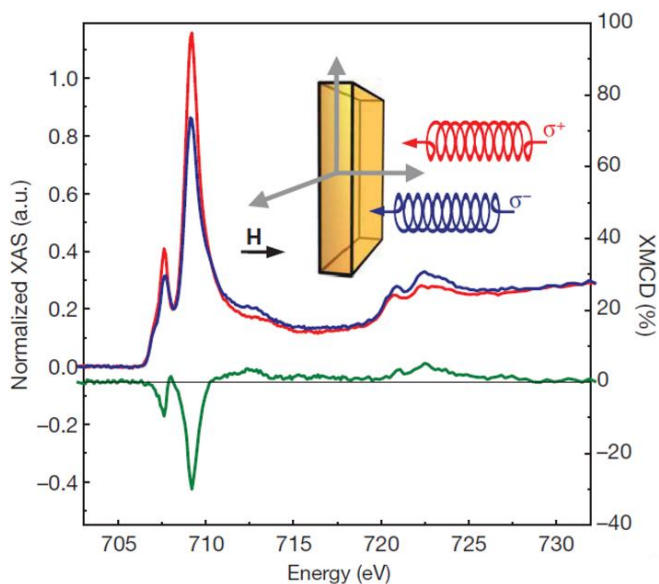**Figure 18. Circularly polarized XAS (red, σ^+; blue, σ^-) and XMCD (green) spectra of the Fe_4C_5 monolayer at the iron $L_{2,3}$ edges (T=650(50) mK, H=30 kOe). a.u., arbitrary units. In the inset the geometry of the experiment is presented.**[27]

5.5.3 X-ray Natural Linear Dichroism (XNLD)

X-ray Natural Linear Dichroism or XNLD is defined as the difference between XAS measured with vertical (σ_V) and horizontal (σ_H) light polarisation and is due to an anisotropic charge distribution.

$$XNLD = \sigma_V - \sigma_H \qquad (27)$$

This information can be useful to locate a preferential orientation in molecules lying on surfaces.[28,29] The easiest way to visualize the polarization dependence underlying XNLD is the "*search light effect*".[21,30] This effect*t* can be demonstrated for the case of K- and L-edges, where the electronic transitions involve $1s \rightarrow 2p$ and $2p \rightarrow 3d$ core to valence excitations. From the spatial charge distribution of the empty valence states involved in the transitions it is possible to picture the valence states by p and d orbitals. In a cubic ligand field d orbitals form the e_g and t_{2g} irreducible representations, the sum of the orbitals within each representation is spherically symmetric while p orbitals are not split in cubic symmetry and their sum is also spherically symmetric. Therefore, in the cubic symmetry the X-ray absorption intensity in nonmagnetic materials is independent from the orientation of *E*-vector relative to the sample. It is clear that the charge distribution of the *individual p* and *d* orbitals is asymmetric in space, and therefore as the symmetry is lowered below cubic, transitions to individual p and d orbitals will depend on the orientation of the *E*-vector relative to the *x, y, z* coordinate system of the crystal. This is the origin of the natural linear dichroism effect. For the K-edge it is possible to recognise the foundation of the search light effect, since the p orbitals have directions of maximum charge density and perpendicular nodal planes where the charge density is zero. The X-ray absorption intensity is maximum when *E* is aligned along the orbital and is zero when *E* lies in the *nodal plane*. The photoelectron is ejected from the spherically symmetric core state along the direction of the *E*-vector. The *E*-vector "search light" then detects the hole density of the valence orbital. If the density in the direction of *E* is zero the transition intensity vanishes. In general, the transition intensity scales directly with the orbital density along *E*. For L-edges the transition intensity is zero if the *E*-vector lies along the d orbital *nodal axis*, which is the intersection of two nodal planes.
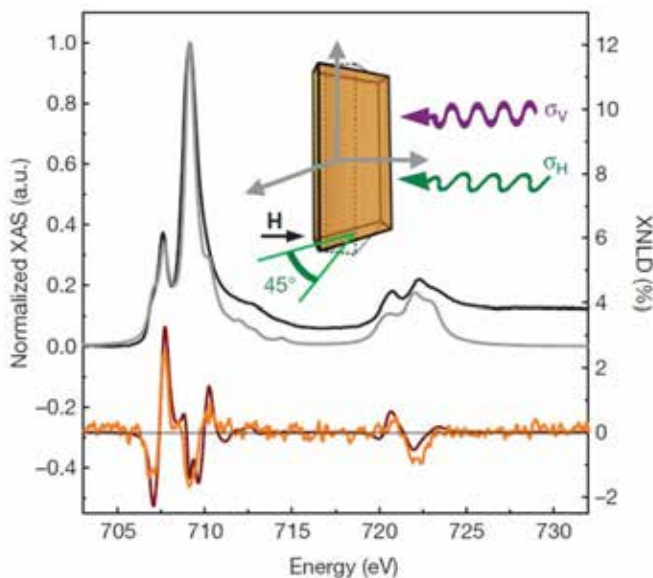
Figure 19. Experimental (black) and calculated (grey) isotropic XAS ($1/3\sigma_V+2/3\sigma_H$) of the Fe$_4$C$_5$ monolayer at the iron L$_{2,3}$ edges together with the experimental (orange) and calculated (dark red) XNLD spectra (σ_V-σ_H), normalized to the isotropic signal (T=10(1) K, H=20 kOe). As shown in the insets, the photon propagation vector is collinear with the applied field (H) and lies at 45u to it.[27]

5.6 Scanning Probe Microscopy

The Scanning Probe Microscopy (SPM) techniques are the main tools for the study of morphology of surfaces with high spatial resolution. Using a local probe that interact with the sample is possible to achieve sub-Å spatial resolution. The type of interaction between the probe and the surface, defines the specific SPM. Scanning Tunnelling Microscopy (STM) and Atomic Force Microscopy (AFM) are among the most utilised techniques to obtain morphological information at the nanoscale and are based on quantum electrical tunnelling effect and tip/surface interaction forces respectively. Starting from these two techniques several other SPMs have been released allowing to get more specific and *local* information depending on the specific interaction between the probe and the sample.[31]

Piezoelectric scanners are usually employed to guarantee the probe (or the sample) displacements. By changing the voltage applied to the piezoelectric material, the relative tip-sample position can be controlled. By applying a voltage to

the different electrodes on the piezotube scanner is possible to produce a scanning (raster) motion in *x* and *y* thus obtaining the point by point 2D image acquisition. The *z* component of each point depends to the type of the specific interaction used in the SPM. By using a feedback controlled acquisition the z value corresponds to the one imposed to maintain constant the interaction within the probe and the surface. By excluding the feedback circuit is instead possible to directly monitor the variation of the specific interaction intensity at constant height that can be locally mapped for each point of the image.

5.6.1 Scanning Tunnelling Microscopy (STM)

STM microscopy is one of the most powerful imaging technique for surface morphological characterization, reaching atomic and sub-molecular resolution. By using this technique it is possible to achieve lateral resolution of the 0.1 Å order and 0.01 Å in *z*. The impulse imposed to nanotechnologies by the STM is unquestionable being both vertical and lateral sub-nanometric resolution achievable even in a "low-cost" setup. In the STM technique a bias voltage is applied between a sharp metal tip and a conductive sample; when the tip is "near" the surface of the sample (5-15Å) electrons tunnel from the tip to the surface or *vice-versa* depending on the sign of the applied bias voltage. In STM measurement is possible to work in *constant current mode* using the feedback loop system described above or in *height constant mode* excluding the feedback loop circuit. STM contrast is based on the tunnelling current variation. Constant current mode is the operative mode allowing rough surfaces investigations reducing the probability of tip crashing. Constant height mode requires an atomically flat surface in order to prevent tip crashing. This latter technique allows higher lateral resolutions.

The electron tunnelling cannot be described using classical physics: an electron cannot pass through a potential barrier if its energy E is smaller than the potential ϕ describing the barrier. On the other hand, by using a quantum mechanics approach, is possible to predict the existence of an exponential decay solution depending on the length (*d*) of the barrier describing the electron wave function out of the barrier. In a mono-dimensional model (see Figure 20) where the electrons can be described by the following wave equation:

$$\boldsymbol{\Psi(d) = \Psi(0)e^{-kd}} \qquad\qquad (\, 28 \,)$$

where $\Psi(d)$ is the solution of Schrondinger's equation outside a solid and $\Psi(0)$ the solution inside the solid, while k can be expressed as:

$$k = \frac{\sqrt{2m(\phi - E)}}{\hbar} \qquad (29)$$

where m is electron mass, ϕ is the electron energy and E is the energy barrier. The probability to find an electron out of the barrier is thus:

$$W(d) = |\Psi(d)|^2 = |\Psi(0)|^2 e^{-2kd} \qquad (30)$$

The probability, i.e. electron density, to find an electron at a distance d from the barrier, decays exponentially increasing the distance (d).
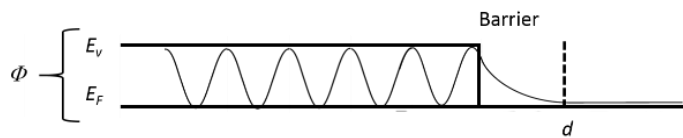

Figure 20. Scheme of a potential barrier.

If two identical metals are take very close each other and $\phi_1 = \phi_2$ (Figure 21) the current must be the same in each direction.
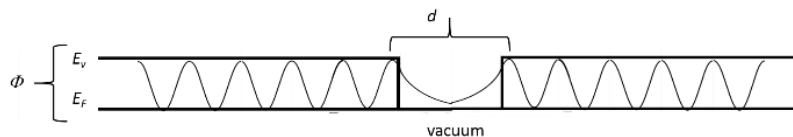
Figure 21. Scheme of a two metallic surfaces keep in quasi-contact at the same energy

By appling a potential V to an electron of one of the two metal, tunnelling occurs from filled states within in metal to an empty states in metal 2.
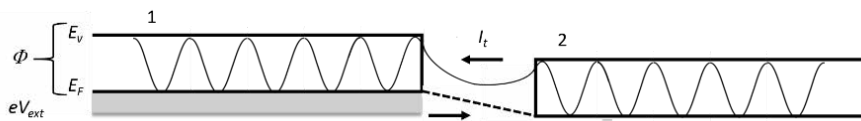

Figure 22. Two very close metallic surface.

The electron flux direction depends on the sign of applied voltage on metal "1",[32] i.e. when it is negative the electron comes from "filled" states of metal "1" (with

lower Fermi energy) to "empty" states of metal "2" where the energy is higher than Fermi. The opposite scenario is possible with a positive applied voltage. Depending on applied voltage is thus possible study "empty" states or "filled" states namely by moving electrons from sample to tip and *vice-versa*.

The tunnelling from a metallic tip to a sample constituted by a metallic surface can be described using a simple model. The barrier is expressed by using an approximated work function obtained as the average of the tip and sample:

$$\Phi' \approx \frac{(\Phi_{tip} + \Phi_{sample})}{2} \qquad (31)$$

If the applied potential $eV \ll \Phi'$, k, from Eq. (29) can be described as:

$$k \approx \sqrt{(2m\Phi')}/\hbar \qquad (32)$$

and the tunnelling current can be described as:

$$I \propto \sum_{E_N=E_F-eV}^{E_f} |\Psi(d)|^2 e^{-2kd} \qquad (33)$$

One can note that by using a low current set point (below 1 pA) the distance between tip and sample is larger than the distance obtained by imposing a high current constrain (nA). For this reason working with surfaces decorated with molecules, a low current-based setup is mandatory to avoid the damaging of the molecular sample. We notice that, in the more complex case of an hybrid molecular-inorganic sample an STM characterization can provide information about the local density of states involved during the tunnelling process thus leading to information related to the molecular orbitals of molecules.[33]

5.7 Sample Preparations

Here below we briefly describe the main preparation protocols adopted during this thesis work.

5.7.1 Gold substrates

Polycrystalline gold surfaces have been used as substrate for several molecular depositions. These substrates ware obtained using a *home-made* evaporation chamber operating in HV conditions (10^{-7} mbar). The chamber is equipped with a

heating filament to anneal the substrates and with a QCM to estimate the deposition rate. High purity gold pellets (99.999%) were mounted in molybdenum crucible and brought to evaporation temperature, by varying the current flowing through the crucible deposition rate is optimised.
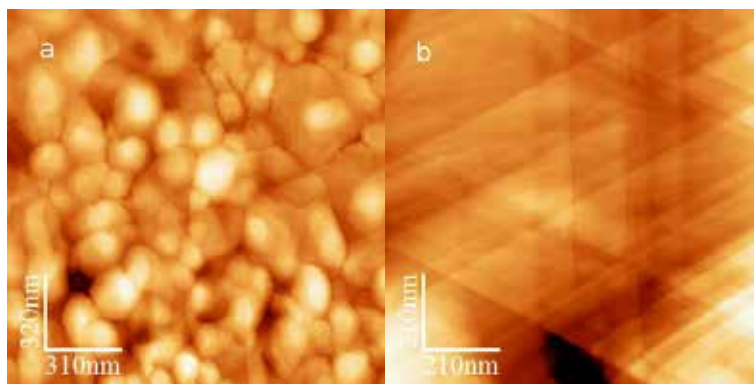

Figure 23. STM images of the same surface before (a) and after (b) annealing procedure (Bias = 0.4 V, I = 0.4 nA).

Gold is annealed using a hydrogen flame immediately before the use; the gold coated substrates are then rinsed in ethanol and dried under nitrogen to avoid contamination. This annealing process is useful to eliminate surface impurity and to have an atomically flat surface (see Figure 23). All the gold substrates employed in this work were approximately 120 nm and have been obtained with a deposition rate of 1.7 Å/min estimated by the QCM.

5.7.2 Self-Assembling Monolayer

A chemisorption process allows a high control of the deposition process where molecules chemically linked to a surface can form a high order monolayer. When this process is carried out using specific conditions this technique take the name of Self-Assembling Monolayer (SAM) technique[34] and permits to assemble molecules on the surface with a significant bidimensional ordering. These molecules need a particular chemical structure with a linker group specifically selected to promote a chemical interaction with a desired surface. In particular we employed sulphur family and phosphonic family linker groups to promote the specific chemisorbtion on gold and metal-oxide surfaces respectively. All the SAM were incubated using clean glassware with standard procedure. All preparation was performed in a portable glove bag to avoid the air exposure.

5.7.3 Thermal evaporations

As alternative sample preparation for epitaxial molecular deposition we employed thermal sublimation under UHV conditions (down to 10^{-10} mbar). The extreme conditions guarantee a higher quality of the final monolayer deposit respect to the SAM preparation even if longer preparation procedure are requested. All the thermal sublimations were performed using home-made cells formed by a quartz crucible surrounded by a tantalum wire acting as heating component and with a K thermocouple to monitor the temperature. The K thermocouple is connected to a molybdenum foil inserted inside the crucible in order to guarantee a proper measurement of the temperature of the molecular powders. The system is assembled on DN20 feedthrough and it can be connect to UHV systems (see Figure 24).

By applying a voltage on the tantalum wire, the powder sample can be heated up controlling the temperature. The electron flowing process is controlled by using a standard power-supply. The film preparation is thus achieved by heating up the powder to the sublimation temperature while the surface is directly exposed to the incoming flux of molecules.
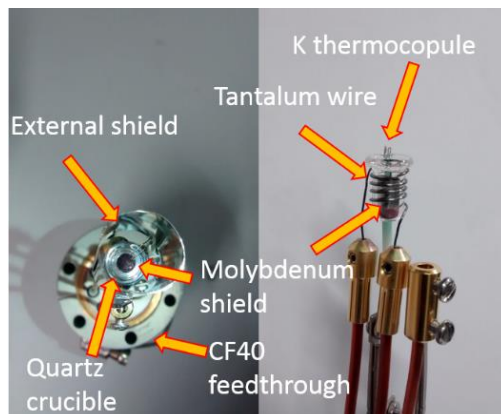
Figure 24. Scheme of the home made sublimating system.

The unique limitation of thermal sublimation is the stability of the molecules to the thermal treatment. Only a few SMMs are stable enough to be sublimated in UHV, as in the case of the $TbPc_2$ system[35] and Fe_4 *star-shaped* family[36,37,38] SMMs. The big advantage of using thermal sublimation respect to the SAM technique is the possibility to deposit the same molecule on different substrates, including particular surfaces which are not stable in ambient conditions or in solution. With SAM only a

monolayer can be achieved but using thermal sublimation there is the possibility of controlling the thickness of deposited molecules, from sub-monolayer sample that can be investigated by SPM techniques to thick films that can be studied with traditional bulk characterization tools.

Reference

(1)   Gatteschi, D.; Sessoli, R.; Villain, J. *Molecular Nanomagnets*; Oxford University Press, 2006; p. 408.

(2)   Casimir, H. B. G.; du Pré, F. K. *Physica* **1938**, *5*, 507–511.

(3)   Brongersma, H. H.; Draxler, M.; de Deridder, M.; Bauer, P. *Surf. Sci. Rep.* **2007**, *62*, 63–109.

(4)   Poggini, L.; Ninova, S.; Graziosi, P.; Mannini, M.; Lanzilotto, V.; Cortigiani, B.; Malavolti, L.; Borgatti, F.; Bardi, U.; Totti, F.; Bergenti, I.; Dediu, V. A.; Sessoli, R. *J. Phys. Chem. C* **2014**, *118*, 13631–13637.

(5)   Brongersma, H. H.; Carrere-Fontaine, M.; Cortenraad, R.; Denier van der Gon, A. W.; Scanlon, P. J.; Spolveri, I.; Cortigiani, B.; Bardi, U.; Taglauer, E.; Reiter, S.; Labich, S.; Bertrand, P.; Houssiau, L.; Speller, S.; Parascandola, S.; Ünlü-Lachnitt, H.; Heiland, W. *Nucl. Instruments Methods Phys. Res. Sect. B Beam Interact. with Mater. Atoms* **1998**, *142*, 377–386.

(6)   Ziegler, J. F.; Biersack, J.; Littmark, U. *Treatise on Heavy-Ion Science*; Bromley, D. A., Ed.; Springer US: Boston, MA, 1985.

(7)   Vickerman, J.; Briggs, D. *ToF-SIMS: Materials Analysis by Mass Spectrometry 2nd Edition*; Vickerman, J. C.; David, B., Eds.; IM Publications, 2013; p. 732.

(8)   Pineider, F.; Mannini, M.; Danieli, C.; Armelao, L.; Piras, F. M.; Magnani, A.; Cornia, A.; Sessoli, R. *J. Mater. Chem.* **2010**, *20*, 187.

(9)   Mannini, M.; Sorace, L.; Gorini, L.; Piras, F. M.; Caneschi, A.; Magnani, A.; Menichetti, S.; Gatteschi, D. *Langmuir* **2007**, *23*, 2389–2397.

(10)   Totaro, P.; Poggini, L.; Favre, A.; Mannini, M.; Sainctavit, P.; Cornia, A.; Magnani, A.; Sessoli, R. *Langmuir* **2014**, *30*, 8645–8649.

(11)   Tencer, M.; Nie, H.-Y.; Berini, P. *Appl. Surf. Sci.* **2011**, *257*, 4038–4043.

(12)   Purbrick, M. D. *Polym. Int.* **1994**, *34*, 119–119.

(13)   Einstein, A. *Ann. Phys.* **1905**, *17*, 132.

(14)   Nordling, C.; Sokolowski, E.; Siegbahn, K. *Phys. Rev.* **1957**, *105*, 1676–1677.

(15)   Yeh, J. J.; Lindau, I. *At. Data Nucl. Data Tables* **1985**, *32*, 1–155.

(16)   Borod'ko, Y. G.; Vetchinkin, S. I.; Zimont, S. L.; Ivleva, I. N.; Shul'ga, Y. M. *Chem. Phys. Lett.* **1976**, *42*, 264–267.

(17)   Poneti, G.; Mannini, M.; Cortigiani, B.; Poggini, L.; Sorace, L.; Otero, E.; Sainctavit, P.; Sessoli, R.; Dei, A. *Inorg. Chem.* **2013**, *52*, 11798.

174

(18)   Burger, K.; Furlani, C.; Mattogno, G. *J. Electron Spectros. Relat. Phenomena* **1980**, *21*, 249–256.

(19)   Pronschinske, A.; Bruce, R. C.; Lewis, G.; Chen, Y.; Calzolari, A.; Buongiorno-Nardelli, M.; Shultz, D. A.; You, W.; Dougherty, D. B. *Chem. Commun.* **2013**, *49*, 10446–10452.

(20)   Ellingsworth, E. C.; Turner, B.; Szulczewski, G. *R. Soc. Chem. Adv.* **2013**, *3*, 3745.

(21)   Stöhr, J.; Siegmann, H. *Magnetism: from fundamentals to nanoscale dynamics*; 2007.

(22)   Dirac, P. a. M. *Proc. R. Soc. A Math. Phys. Eng. Sci.* **1929**, *123*, 714–733.

(23)   Chen, C.; Idzerda, Y.; Lin, H.-J.; Smith, N.; Meigs, G.; Chaban, E.; Ho, G.; Pellegrin, E.; Sette, F. *Phys. Rev. Lett.* **1995**, *75*, 152–155.

(24)   Sessoli, R.; Mannini, M.; Pineider, F.; Cornia, A.; Sainctavit, P.; Beaurepaire, E.; Scheurer, F.; Krill, G. *Magnetism and Synchrotron Radiation*; Beaurepaire, E.; Bulou, H.; Scheurer, F.; Jean-Paul, K., Eds.; Springer Proceedings in Physics; Springer Berlin Heidelberg: Berlin, Heidelberg, 2010; Vol. 133.

(25)   Stöhr, J. *J. Magn. Magn. Mater.* **1999**, *200*, 470–497.

(26)   Stöhr, J.; Padmore, H. A.; Anders, S.; Stammler, T.; Scheinfein, M. R. *Surf. Rev. Lett.* **1998**, *05*, 1297–1308.

(27)   Mannini, M.; Pineider, F.; Danieli, C.; Totti, F.; Sorace, L.; Sainctavit, P.; Arrio, M.-A.; Otero, E.; Joly, L.; Cezar, J. C.; Cornia, A.; Sessoli, R. *Nature* **2010**, *468*, 417–421.

(28)   Cornia, A.; Mannini, M.; Sainctavit, P.; Sessoli, R. *Chem. Soc. Rev.* **2011**, *40*, 3076–3091.

(29)   Mannini, M.; Bertani, F.; Tudisco, C.; Malavolti, L.; Poggini, L.; Misztal, K.; Menozzi, D.; Motta, A.; Otero, E.; Ohresser, P.; Sainctavit, P.; Condorelli, G. G.; Dalcanale, E.; Sessoli, R. *Nat. Commun.* **2014**, *5*, 4582.

(30)   Stöhr, J. *NEXAFS Spectroscopy*; Springer Series in Surface Sciences; Springer Berlin Heidelberg: Berlin, Heidelberg, 1992; Vol. 25.

(31)   Wiesendanger, R. *Scanning probe microscopy and spectroscopy: methods and applications*; Cambridge University Press, 1994; p. 660.

(32)   Tersoff, J.; Hamann, D. R. *Phys. Rev. Lett.* **1983**, *50*, 1998–2001.

(33)   Lu, X.; Grobis, M.; Khoo, K.; Louie, S.; Crommie, M. *Phys. Rev. Lett.* **2003**, *9*, 096802.

(34)   Ulman, A. *Chem. Rev.* **1996**, *96*, 1533–1554.

(35)   Margheriti, L.; Chiappe, D.; Mannini, M.; Car, P.-E.; Sainctavit, P.; Arrio, M.-A.; de Mongeot, F. B.; Cezar, J. C.; Piras, F. M.; Magnani, A.; Otero, E.; Caneschi, A.; Sessoli, R. *Adv. Mater.* **2010**, *22*, 5488–5493.

5. Experimental methods

(36)   Ninova, S.; Lanzilotto, V.; Malavolti, L.; Rigamonti, L.; Cortigiani, B.; Mannini, M.; Totti, F.; Sessoli, R. *J. Mater. Chem. C* **2014**, *2*, 9599–9608.

(37)   Rigamonti, L.; Piccioli, M.; Malavolti, L.; Poggini, L.; Mannini, M.; Totti, F.; Cortigiani, B.; Magnani, A.; Sessoli, R.; Cornia, A. *Inorg. Chem.* **2013**, *52*, 5897–5905.

(38)   Margheriti, L.; Mannini, M.; Sorace, L.; Gorini, L.; Gatteschi, D.; Caneschi, A.; Chiappe, D.; Moroni, R.; de Mongeot, F. B.; Cornia, A.; Piras, F. M.; Magnani, A.; Sessoli, R. *Small* **2009**, *5*, 1460–1466.

6. Conclusions

In this thesis I summarised the most relevant results I obtained during my PhD activity that has been focused on the nanostructuration of several molecular systems with relevant magnetic properties. The studied systems belong to the families of Nitronyl Nitroxide Radicals (NNRs), Single Molecule Magnets (SMMs), Valence Tautomers (VTs) and Spin-crossovers (SCOs). The aim of this wide range activity was to explore the possibilities of organising magnetic molecules on solid surfaces in order to advance in the preparation of novel devices based on these fragile molecules for spintronic purposes.

A NNR was functionalized with phosphonate linker group to be chemically grafted on the LSMO surface, one of the most employed ferromagnetic spin injection electrode used in molecular spin valves. By XPS and ToF-SIMS techniques we investigated massive phase deposits and monolayers of this system confirming the presence of intact NNRs on surface. On the basis of this evidence we proceeded toward the realization of a first spin valve based on NNR-LSMO hybrid surface evidencing the occurrence of a remarkable magneto-resistance effect on this new device. This result indicates that the presence of paramagnetic species at the spin-injection interface is not detrimental for application purposes thus increasing the interest on this type of surface modifications.

We then moved to the TbPc$_2$ complexes, featuring interesting SMM properties and considered as one of the best candidates to alter the spin injection interface in molecular spin valve. We demonstrated that magnetic properties of this mononuclear system are strongly influenced by the surface and by the deposition processes. Our study has been focused on depositing TbPc$_2$ on top of the LSMO and on silicon surfaces. The results presented here suggest that no significant polarisation of the TbPc$_2$ magnetic moments is induced by the LSMO substrates. On the other hand the Si(100) seems to stabilise the oxidised form of the TbPc$_2$ complex inducing to an enhancement of the magnetic properties of the chemisorbed SMM. Magneto-transport experiments on devices embedding TbPc$_2$ molecules at LSMO interface and a new family of molecular spin valve devices based on TbPc$_2$ molecules on silicon are likely to be the focus of this research in the near future.

6. Conclusions

The third class of magnetic molecules we explored is constituted by cobalt-catecholate (Co-cat) complexes featuring a VT behaviour. Deposition of these VT systems on surfaces opens the possibility to create an hybrid interface in which is possible to modulate molecular properties with temperature and with light irradiation. Initially we tested a Co-cat system in the massive phase with synchrotron light experiments and the comparison with in house XPS experiments validated the latter as a precious tool to investigate thin films of these bistable materials. Subsequently we modified the Co-cat system in order to promote their chemisorption on Au(111) surface. The temperature induced conversion of a monolayer film was demonstrated by in house experiments qualitatively observing the behaviour of the massive phase. Additionally synchrotron has been used to confirm these data and to be able to demonstrate that also light induced switching is achievable at the nanoscale.

The last series of experiments were carried out on a particular class of Fe(II)-based spin-crossover (SCO) system with a "multi-functional" behaviour. In this system the SCO conversion can be induced both by temperature as well as by light. This system was thermally evaporated on cellulose acetate in HV retaining its switchability accordingly to our DC magnetometry investigations. Moreover, by reducing the thickness of the evaporated deposit, the thermal and light switchability was confirmed via XPS without synchrotron experiments. Our characterisation has allowed to address the switchability at the nanoscale thus providing also in this case a good strategy to assemble new multifunctional devices for spintronic purposes.

Concluding with this thesis work the panorama of magnetic molecules that can be deposited by wet chemistry of via UHV compatible approaches (maintaining intact their magnetic properties) has been extended, thus extending the playground for developing new hybrid molecular devices opening the way to new series of experiments in the field of molecular spintronics.